Zinc oxide based nano-composites for multifunctional applications

A thesis submitted in fulfilment of the requirements for degree of

Doctor of Philosophy (Applied chemistry)

Ahmad Esmaielzadeh Kandjani

BSc (Materials science and engineering)

MSc (Materials science and engineering)

School of Applied Sciences

RMIT University

August 2014

Declaration

I certify that except where due acknowledgement has been made, the work is that of author alone; the work has not been submitted previously, in whole or in part, to qualify for any other academic award; the content of this thesis is the result of work which has been carried out since the official commencement data of approved research program; and any editorial work, paid or unpaid, carried out by third party is acknowledged.

Ahmad Esmaielzadeh Kandjani

Acknowledgement

Many people have guided and supported me, in one way or another while completing this thesis and I take this opportunity to express my deepest gratitude to all of them. My PhD like most others had number of ups and downs, achievements and failures. However, during this journey I have learnt that when I have wonderful colleagues and friends like the ones mentioned here, research can be fun.

First and foremost, I would like to thank my PhD supervisors. The opportunity to start my research at RMIT initiated by applying to Prof. Suresh Bhargava for PhD position in his research group. I would like to thank him for the trust to invite me half-way around the world as his PhD student. I am grateful for his supervision, mentorship and guidance throughout my time at RMIT University. His passion and encouragement to always strive for excellence motivated me during my research at RMIT. His multidisciplinary research platform, Centre of Advanced Materials and Industrial Chemistry (CAMIC) gave me unique opportunity to work with many people and make my research innovative and directed towards problem solving. I'd especially like to thank Assoc. Prof. Vipul Bansal for his warm encouragement and experienced guidance. He has given me the greatest freedom to do research independently and at the same time has provided me with insightful discussions and suggestions. I am very grateful for guidance, discussions, ideas, and support of his direct supervision. Dr. Bansal would be always my mentor, and I cannot thank him enough for all his help and support. This research could not be possible without their helps and I've learnt a lot from them and I can only hope that someday I can pass on the values and the dreams that they have given me.

I would also like to thank Dr. Ylias Sabri and Dr. PR. Selvakannan for their encouragement and constructive feedback on my thesis. I appreciate the time they have spent on reading and suggesting changes to my thesis. Furthermore, they have been great inspiration and support during my PhD. I have learnt a lot from them, especially Dr. Sabri who has helped me not only during my PhD with his scientific inputs, but also he has been a true friend and support during good and bad days of my research. My grateful thanks also go to Dr. Samuel Ippolito for his constant support and help during my PhD, especially his electronic and software engineering inputs during my research. I'd also like to thank Dr. Rajesh Ramanathan and Dr. Mahsa Mohammadtaheri for their help and support on different

steps of this project. Also, I'd like to thank Mrs. Zahra M. Davoudi, not only for being a big help during my research and teaching me several technical laboratory protocols and tricks, for being also be an excellent patient friend during my research.

Many additional collaborative partners were involved in various projects that I could contribute to during my PhD, and I highly appreciated all the contributions and help from Dr. Hemant K. Daima, Mr. Matthew Griffin, Miss Akshi Thakkar, and Mr. Hussein Nilli.

There are also many people working behind the scenes in research and this research could not have been possible without their collaboration. I would like to acknowledge their support during my PhD. From Department of Chemistry, this includes, Mr. Karl Lang, Mrs. Dianne Mileo, Mrs. Zahra M. Davoudi, Mrs. Nadia Zakhartchouk, Mrs. Ruth Cepriano-Hall, Mrs. Pegah Ghobadi and Mr. Howard Anderson. I'd also like to thank Mr. Frank Antolasic for providing training and assistance with a number of the characterisation instruments, as well as, Mr. Paul Morrison for operating the ICP-MS instrument for my work. From the Physics Department, I'd like to thank the technical staff of the RMIT Microscopy and Microanalysis Facility (RMMF), including Mr. Phil Francis and Mr. Peter Rummel, as well as several duty microscopists. From the School of Electrical and Computer Engineering, I'd like to thank Mr. Paul Jones and Mr. Yuxun Cao for providing me access to the clean-room facilities and for performing the e-beam depositions used in this work. Thanks are due to my fellow members of CAMIC for their support. My sincere thanks to Dr. Lisa Dias for helping me out with all of my formal documentation processes. I would also like to thank all my friends who supported me during my PhD and I will always treasure our friendship. I want to thank Dr. Ylias Sabri, Dr. Samuel Ippolito, Dr. Rajesh Ramanathan, Dr. Blake Plowman, Dr. Lathe Jones, Dr. Sarvesh Soni, Dr. Emma C. Goethals, Dr. Hemant K. Daima, Dr. Mahsa Mohammadtaheri, Dr. Hailey Reynolds, Dr Mohammad Amin, Dr Mohammad Alkobaisi and Mr. Hussein Nilli as well as many other friends who supported me during my PhD journey.

I would also like to gratefully acknowledge the financial support provided to me by the College of Science Engineering and Health together along with School of Applied Sciences at RMIT University. In addition, I would like to acknowledge the other funding bodies, including The Deputy Pro Vice-Chancellor Research and Innovation Postgraduate Research International Conference Award for allowing me to travel and present my work at AMWC (2013) Izmir, Turkey. The Prof. CNR Rao Postgraduate Research Excellence Award which was awarded to me in Materials Science as the most outstanding postgraduate research student working in the field of materials science (2014) is also acknowledged, as it has given me the opportunity to travel to India and work with Prof. CNR Rao's Group for 45 days. The

Perkin Elmer Prize for postgraduate student making the most outstanding contribution to the field of vibrational spectroscopy is also appreciated and duly acknowledged.

I also wanted to thank my father and mother. It was them who supported me in my early education. I am also thankful to my wife Negar Ilchizadeh. It was my wife who accompanied me and experienced all the hardships in my course of pursuing the PhD and I would like to dedicate this thesis to her for her 10 years of support and unquestionable love. Last but not least, I thank the Almighty for giving me strength, health and patience for carrying on during all different phases of my life so that today I can stand proud and happy.

This thesis is dedicated to:

My wife, Negar Ilchizadeh whose support, encourage and love have been an inspiration to my life. I am eternally grateful for all your unquestionable love.

Love you more than anything imaginable.

Table of Contents

Declaration **i**

Acknowledgement **ii**

Table of Contents **vi**

List of Figures **xi**

List of Tables **xx**

List of Abbreviations **xxi**

Chapter I: Introduction **2**

1.1. Introduction **3**

1.2. Photocatalysis **3**

1.2.1. A short journey to the world of semiconductor **3**

1.2.2. Semiconductor junctions **8**

1.2.2.1. Semiconductor/metal junctions **8**

1.2.2.2. Semiconductor/semiconductor junctions **11**

1.2.3. Photocatalysis **16**

1.3. Surface enhanced Raman spectroscopy **20**

1.3.1. Fundamentals of local surface plasmon resonance (LSPR) **20**

1.3.2. Surface enhancement Raman spectroscopy (SERS) **22**

1.3.3. Enhancement mechanisms in SERS **24**

1.4. SERS: difficulties and applications-road to multifunctionality **26**

1.5. Zinc oxide **29**

1.5.1. Properties **29**

1.5.2. Synthesis of ZnO nano-arrays **31**

1.5.3. Optical applications **33**

1.6. Research motivation **34**

1.7. Thesis Outline **35**

References **37**

Chapter II: Analytical and characterisation techniques **47**

2.1. Introduction **48**

2.2. Scanning Electron Microscopy (SEM) **48**

2.3. Atomic Force Microscopy (AFM) **50**

2.4. UV-Visible Spectroscopy (UV-Vis) **51**

2.5. Raman spectroscopy **52**

2.6. X-Ray Diffraction (XRD) **53**

2.7. Energy Dispersive X-ray (EDX) **53**

2.8. X-ray Photoelectron Spectroscopy (XPS) **54**

2.9. Inductively Coupled Plasma Mass Spectrometry (ICP-MS) **55**

References **56**

Chapter III: A novel approach towards a better background correction of Raman signals **58**

3.1. Introduction **59**

3.1.1. A short survey to background correction methods **59**

3.1.2. Raman spectroscopy and its background issues **61**

3.1.3. A brief introduction to Wavelet transform **62**

3.2. Aim and goals **65**

3.3. Methods **66**

3.3.1. Generating simulated spectra **66**

3.3.2. Generating calibration curve **67**

3.3.3. Background correction method **69**

3.3.4. Testing the accuracy of current algorithm **76**

3.3.5. Experimental data **76**

3.4. Results and discussion **77**

3.4.1. Calibration curve **77**

3.4.2. Estimating signal to noise ratio **80**

3.4.3. 2nd derivative and end effect **83**

3.4.4. Reasons for adding helping points based on the degree of separation **85**

3.4.5. Background correction **86**

3.4.6. Testing the accuracy of proposed algorithm **88**

3.4.7. Experimental results **93**

3.5. Conclusion **94**

References **95**

Chapter IV: Fabrication of ZnO and ZnO/Ag nano-arrays for SERS biosensing **98**

4.1. Introduction **99**

4.2. Materials and methods **100**

4.3. Zinc oxide nano-arrays **104**

4.3.1. Mechanism **104**

4.3.2. Effect of hydrothermal conditions **106**

4.3.3. Effect of seed layer **106**

4.4. Silver decoration **113**

4.4.1. Mechanism **113**

4.4.2. Silver decoration via photoreduction **116**

4.4.3. Silver decoration via Tollens method **120**

4.5. Conclusion **129**

References **130**

Chapter V: Hg(II) sensing with ZnO/Ag nano-arrays **134**

5.1. Introduction to mercury pollution **135**

5.2. Mercury ions sensing and removal **137**

5.3. Materials and methods **139**

5.4. Results and discussion **142**

5.5. Conclusion **153**

References **153**

Chapter VI: ZnO/AgTCNQ as a novel p/n junction photocatalyst **158**

6.1. Introduction to surface patterning: necessities and applications **159**

6.1.1. Synthesis of monodispersed polymer beads **159**

6.1.2. Colloidal particles at the air/water interface **161**

6.1.3. Close-pack colloidal arrays and colloidal lithography **163**

6.2. Silver tetra-cyanoquinodimethane (AgTCNQ) **164**

6.3. Materials and methods **166**

6.4. Formation of PS monolayers and ZnO/Ag nano-star patterns **168**

6.5. ZnO/AgTCNQ arrays **173**

6.6. Conclusion **179**

References **179**

Chapter VII: Conclusion and Future Works **184**

7.1. Summary of work **185**

7.1.1. Designing novel background correction technique for SERS sensing **186**

7.1.2. Fabrication of ZnO/Ag nano-arrays for SERS based sensors **187**

7.1.3. Controlling the junction place and formation in inorganic/organic p/n hetero junction of ZnO/AgTCNQ **188**

7.2. Future work **188**

7.2.1. Designing novel background correction technique for SERS sensing **189**

7.2.2. Fabrication of ZnO/Ag nano-arrays for SERS based sensors **189**

7.2.3. Controlling the junction place and formation in inorganic/organic p/n hetero **190**

junction of ZnO/AgTCNQ

Appendices **192**

A. Supporting information for chapter III **193**

B. Curriculum vitae **204**

List of Figures

Figure 1.1. Conduction and valence band diagram of **a)** direct and **b)** indirect band-gap semiconductors. **4**

Figure 1.2. Schematic representation of energy bands in different type of materials. **5**

Figure 1.3. Density of states (*N(E)*), Fermi distribution (*f(E)*) and carrier concentration (n or p) for intrinsic, n-type and p-type semiconductors in thermal equilibrium. **6**

Figure 1.4. Band structures of metal–semiconductor junctions for **(a,b)** an n-type semiconductor and **(c,d)** a p-type semiconductor in thermodynamic equilibrium. **11**

Figure 1.5. **a)** Band structure of a p-type and an n-type semiconductor before joining, **b)** band structure of a p-n homojunction, **c)** structural change in the depletion layer of a p-n homojunction, **d)** charge profile in the depletion layer and **e)** electric field profile in the depletion layer (maximal at the junction). **12**

Figure 1.6. Different semiconductor heterojunctions based on their band edge offsets in the flat band condition for: **a)** Straddling, **b)** Offset and **c)** Broken gaps. **14**

Figure 1.7. **a)** Band structure of a p-type and an n-type semiconductor before joining, **b)** band structure of a p-n heterojunction, **c)** structural change in the depletion layer of a p-n heterojunction, **d)** charge profile in the depletion layer and **e)** electric field profile in the depletion layer (maximal at the junction). **15**

Figure 1.8. Schematic illustration of the principle of semiconductor photocatalysis: (I) the generation of an electron/hole pair via photo-excitation; (II) the volume recombination of electron and hole; (III) Consumption of electron in the broken ligands and defects located at the surface (surface recombination); (IV) the initiation of a reductive pathway by a conduction-band electron; (V) the initiation of an oxidative pathway by a valence-band hole. **17**

Figure 1.9. Photocatalytic mechanism in Ag/ZnO heterojunction nanocrystals. **18**

Figure 1.10. Band structure of $Ag_2O/Bi_2O_2CO_3$ p-n heterojunction **a)** before forming junction (*V vs. NHE*), **b)** in the dark **c)** under illumination. **20**

Figure 1.11. Schematic illustration of surface plasmon resonance in a spherical particle. **21**

Figure 1.12. Quantum mechanical model of Raman scattering. **23**

Figure 1.13. Enhancement factor (*EF*) distribution in the region of the gap between **a)** two gold colloids (radii = 30 nm) for polarization along the vertical axis of the dimer; **b)** gold tip on top of a gold surface. **25**

Figure 1.14. Structure of Wurtzite zinc oxide. **30**

Figure 1.15. A collection of ZnO nanostructures. **31**

Figure 2.1. Interaction between electron beam and mater. **49**

Figure 2.2. AFM **a)** Contact and **b)** Tapping modes; **c)** Force between tip of AFM cantilever and surface of the sample in different modes. **51**

Figure 2.3. The mechanism for EDX. **54**

Figure 2.4. Schematic of photo-ionization of the electron from 1s orbital in XPS. **55**

Figure 3.1. **a)** Simulated spectrum with 10 peaks without noise and background; **b)** Same spectrum after adding white noise with *SNR*=25; **c)** Linear background; **d)** Spectrum generated from adding linear background shown in **c** to spectrum **b**; **e)** Sigmoidal background; **f)** Spectrum generated from adding Sigmoidal background shown in **e** to spectrum **b**; **g)** Sinusoidal background and **h)** Spectrum generated from adding Sinusoidal background shown in **g** to spectrum **b**. **68**

Figure 3.2. General Flowchart for estimating background. **70**

Figure 3.3. Endpoint effects for (Subclass=1 and 4), wherein **a)** shows the full original spectrum before adjusting the endpoints, and **b)** and **c)** show the magnified regions of the starting and the finishing points, respectively, after adjusting the endpoints. **74**

Figure 3.4. Endpoint effects for (Subclass=2 and 5), wherein **a)** shows the full original spectrum before adjusting the endpoints, and **b)** and **c)** show the magnified regions of the starting and the finishing points, respectively, after adjusting the endpoints. **75**

Figure 3.5. Endpoint effects for (Subclass=3 and 6), wherein **a)** shows the full original spectrum before adjusting the endpoints, and **b)** and **c)** show the magnified regions of the starting and the finishing points, respectively, after adjusting the endpoints. **75**

Figure 3.6. A Gaussian peak with different *SNR* values. **78**

Figure 3.7. Variation of correlation coefficients with *SNR* and *CWT* scales. **79**

Figure 3.8. Calibration curve for signals in Figure 3.6. **79**

Figure 3.9. The effect of peak width on Best-Scale in different *SNR* values. **80**

Figure 3.10. *SNR* estimation steps: **a)** Simulated Raman spectrum with 10 peaks randomly distributed on the signal with sigmoidal background, wherein shaded section represents window size for calculating *LSTD*; **b)** *STD* in different divided ranges of the spectrum; **c)** Spectrum in minimum *LSTD*, wherein red line shows linear fitting of the spectrum in selected region to find background; **d)** Estimated noise profile by subtracting linear background and spectrum; and **e)** Different smoothing levels of the spectrum. **81**

Figure 3.11. Testing of *SNR* estimation algorithm: **a)** *SNR* variation with smoothing level; **b)** effect of background intensity on *SNR* estimation, wherein the intensity ratio is the ratio between intensity of the highest peak in initial background-free signal and max intensity of the added background; and **c)** Comparison between estimated *SNR* values and initially added *SNR* of signal. **82**

Figure 3.12. **a)** Synthetic spectrum (*SNR*=20, 10 peaks); **b)** 2^{nd} derivative (wavelet transform, *Best-Scale*=17); **c)** Added points based on slopes of the spectrum at ending points; and **d)** 2^{nd} derivative (wavelet transform, *Best-Scale*=17) with end point correction. **84**

Figure 3.13. **a)** Synthetic spectrum with (*SNR*=20, 10 peaks); **b)** Numerical 2^{nd} derivative; **c)** 2^{nd} derivative (wavelet transform, *Best-Scale*=17); and **d)** Squared 2^{nd} derivative to suppress noises. **85**

Figure 3.14. Overlapping Gaussian peaks and their second and third derivatives: **a)** R=0.37; **b)** R=1.11; **c)** R=2.6; and **d)** R=3.34. **87**

Figure 3.15. **a)** Spectrum with starting and finishing points of background; **b)** Starting condition of the spectrum (Subclass=0); **c)** Ending condition of the spectrum (Subclass=4); **d)** Background points and their fittings, wherein green dashed and magenta curves relate to starting fitting curve and corrected background after 314 loops, respectively; and **e)** Original spectrum with the background corrected one. **88**

Figure 3.16. **a)** Root mean squared error (*RMSE*) variation during testing 900 times **89**

random spectra with 10 peaks; and **b)** Distribution of *RMSE* with number of tests.

Figure 3.17. Variation of *RMSE* with peak numbers in the spectrum. Dot points show median of *RMSE*, and upper and lower error bars are related to *STD* of points with higher and lower *RMSE*, respectively. **90**

Figure 3.18. Variation of *RMSE* with *SNR* in the spectrum. Dot points show median of *RMSE*, and upper and lower error bars are related to *STD* of points with higher and lower *RMSE*, respectively. **90**

Figure 3.19. **a)** Raman spectrum without any background with 30 peaks and no noise, **b)** spectrum in **(a)** after introducing noise corresponding to *SNR*=60, **c)** spectrum in **(b)** after introducing a sigmoidal background, and **d)** background corrected spectrum of that shown in **(c)**. The rectangular boxes shown in **(b)** and **(d)** highlight the errors introduced during the background correction step. **91**

Figure 3.20. **a)** Raman spectrum without any background with 10 peaks and no noise, **b)** spectrum in **(a)** after introducing noise corresponding to *SNR*=5, **c)** spectrum in **(b)** after introducing a sigmoidal background, and **d)** background corrected spectrum of that shown in **(c)**. The rectangular boxes shown in **(b)** and **(d)** highlight the errors introduced during the background correction step. **92**

Figure 3.21. **a)** Raman spectrum without any background with 30 peaks and no noise, **b)** spectrum in **(a)** after introducing noise corresponding to *SNR*=5, **c)** spectrum in **(b)** after introducing a sigmoidal background, and **d)** background corrected spectrum of that shown in **(c)**. The rectangular boxes shown in **(b)** and **(d)** highlight the errors introduced during the background correction step. **93**

Figure 3.22. Examples of application of the current algorithm for experimentally obtained real Raman spectra: **a)** Serine amino acid; **b)** Rhodamine B; **c)** methyl red and **d)** crystal violet. **94**

Figure 4.1. Schematic representation of fabrication of ZnO/Ag nano-arrays on a Si substrate which involves (1) hydrothermal growth of ZnO nano-arrays onto Si wafer spin-coated with ZnO thin film, (2) photocatalytic reduction of AgNPs using UV irradiation. **101**

Figure 4.2. Schematic representation of fabrication of ZnO/Ag nano-arrays on a Si substrate which involves (1) hydrothermal growth of ZnO nano-arrays onto Si wafer spin-coated with ZnO thin film, (2) sensitization **102**

of ZnO nano-arrays with Sn and Pd, followed by (3) electroless plating of AgNPs onto ZnO nano-arrays.

Figure 4.3. Schematic for 1) detection and 2) Photocatalytic removal of organic marker for regeneration of SERS sensor. **104**

Figure 4.4. Hydrothermally grown ZnO nano-arrays on sputtered ZnO thin film (400 nm) for 6 h at 95 °C with initial $Zn(NO_3)_2$ concentrations of **a)** 1, **b)** 3, **c)** 5, **d)** 10, **e)** 12.5, **f)** 25, **g)** 50 and **h)** 100 mM. **108**

Figure 4.5. Hydrothermally grown ZnO nano-arrays on sputtered ZnO thin film (400 nm) at 95 °C with initial $Zn(NO_3)_2$ concentrations of **a)** 12.5 and **b)** 25 mM for 1) 1.5, 2) 3, 3) 4.5 and 4) 6 h. **109**

Figure 4.6. Edge effects in **a)** sol-gel and **b)** sputtered ZnO seed layers; red dashed lines show the position of the edge of the samples. **110**

Figure 4.7. Effect of cycles of coating of ZnO seed layer on the hydrothermally grown ZnO nano-arrays for **a)** 1, **b)** 3 and **c)** 5 cycles of coatings [1) Top view and 2) angle (30°) view]. **110**

Figure 4.8. Effect of sol-gel concentration on the hydrothermally grown ZnO nano-arrays for **a)** 1, **b)** 10 and **c)** 100 mM of $Zn(AC)_2$ [1) Top view and 2) angle (30°) view]. **111**

Figure 4.9. Effect of calcination temperature of the seed layer at **a)** 70, **b)** 150, **c)** 300, **d)** 450, **e)** 600 and **f)** 750 °C [Top view]. **112**

Figure 4.10. Effect of calcination temperature of the seed layer at **a)** 70, **b)** 150, **c)** 300, **d)** 450, **e)** 600 and **f)** 750 °C [Tilt (30 °C) view]. **113**

Figure 4.11. Effect of calcination temperature of the seed layer at **a)** 150, **b)** 450 and **c)** 750 °C [Side view]. **113**

Figure 4.12. Effect of silver ion concentration on the decoration of ZnO nano-arrays for 2 h for samples prepared with **a)** 150, **b)** 15, **c)** 1.5, **d)** 0.15 mM and **e)** and **f)** 0.1 mM Ag^+ ions. **117**

Figure 4.13. Silver decoration [0.15 mM, 2 h] of ZnO nano-arrays with different seed layer heat treated at **a)** 70, **b)** 150, **c)** 450 and **d)** 750 °C. **118**

Figure 4.14. UV-visible absorbance spectra of RB with increasing illumination time in the **a)** absence and **b)** presence of ZnO/Ag prepared using 450 °C calcinated ZnO nano-arrays decorated with 0.15 mM AgNPs, **c)** photodegradation efficiency of ZnO and ZnO/Ag nano-arrays and **d)** **119**

SERS spectra for pure ZnO and ZnO/Ag nano-arrays.

Figure 4.15. SEM images of ZnO/Ag composite nanorod arrays fabricated by reaction of ZnO nano-arrays with **a)** 1, **b)** 10, **c)** 100 and **d)** 1000 mM diaminesilver(I) complex for (**a1**, **b1**, **c1** and **d1**) 1 min, (**a2**, **b2**, **c2** and **d2**) 3 min and (a3, b3, c3 and d3) 6 min. Scale bars correspond to 1 μm. **121**

Figure 4.16. Additional SEM images of ZnO/Ag nano-arrays prepared using **a)** 1, **b)** 10, **c)** 100 and **d)** 1000 mM diaminesilver complex for 3 min reaction. **122**

Figure 4.17. SEM images of ZnO/Ag nano-arrays prepared using 100 mM diaminesilver complex for 3 min reaction **a)** side-view, **b)** top-view, **c)** perspective-view at 10° sample tilt, and **d)** low magnification top-view images. **122**

Figure 4.18. XRD patterns obtained from ZnO/Ag nanorod arrays **a)** as a function of diaminesilver concentration of (i) 1, (ii) 10, (iii) 100 and (iv) 1000 mM for 3 min reaction, and **b)** as a function of reaction time for (i) 1, (ii) 3 and (iii) 6 min for 1000 mM diaminesilver concentration. The lattice planes corresponding to Ag are indicated, while other peaks correspond to wurtzite phase of ZnO. **123**

Figure 4.19. XPS spectra arising from ZnO/Ag nanorod arrays during different stages of Ag decoration **a)** general area scans from each synthesis step, **b)** Sn $3d_{5/2}$ core level from ZnO-Sn, **c)** Pd 3d core level from ZnO-Sn-Pd and **d)** Ag 3d core level from ZnO-Sn-Pd-Ag (ZnO/Ag). **124**

Figure 4.20. SERS spectra of RB molecules obtained from ZnO/Ag nano-arrays prepared by exposing ZnO substrates **a)** for 3 min to (i) 0, (ii) 1, (iii) 10, (iv) 100 and (v) 1000 mM diaminesilver complex and **b)** to 100 mM diaminesilver complex for (i) 0, (ii) 1, (iii) 3 and (iv) 6 min; **c)** relative intensity of the characteristic RB Raman band at 1355 cm^{-1} as a function of silver precursor concentration and AgNPs decoration time and **d)** 30 overlapping SERS spectra of RB molecules randomly collected from a single ZnO/Ag substrate prepared using 1 mM diaminesilver complex for 3 min. **127**

Figure 4.21. SEM images of ZnO nano-arrays at **a)** lower and **b)** and **c)** higher magnification, wherein **b**) shows the top-view image and **c**) shows a perspective image at 10° sample tilt. **127**

Figure 4.22. UV-visible absorbance spectra of RB with increasing illumination time in the **a)** absence and **b)** presence of ZnO/Ag prepared using 1 **129**

mM diaminesilver complex for 3min, **c)** photodegradation efficiency of different ZnO/Ag nano-arrays prepared after 3 min of AgNPs deposition and **d)** recyclability studies showing SERS spectra of RB on a single ZnO/Ag nano-array substrate through three cycles of SERS detection and substrate photo-cleaning.

Figure 5.1. Hg emission contributors around the world. **135**

Figure 5.2. Mercury pollution - transport and cycle. **136**

Figure 5.3. Detailed (**a**) synthesis and (**b**) sensing, removal and regeneration processes, starting with **a1**) synthesizing ZnO seed layer via sol-gel technique, **a2**) ZnO hydrothermal array growth, **a3**) decoration of the nano-arrays with palladium nanoparticles by charge exchange between Sn^{2+} and Pd^{2+} at the surface of the ZnO nano-arrays, **a4)** performing silver electroless plating decorating the ZnO arrays; followed by, **b1)** adsorption of Hg^{2+} ions on ZnO/Ag nano-arrays and subsequent adsorption of Raman marker on the arrays, **b2)** Raman detection of marker on mercury-contaminated ZnO/Ag nano-arrays, **b3)** photocatalytic degradation of marker dye and finally, **b4)** removing mercury contamination from the ZnO/Ag nano-arrays by using heat treatment under vacuum as the regeneration step. **143**

Figure 5.4. **a)** ZnO nano-arrays; **b)** Silver decorated ZnO nano-arrays; **c)** and **d)** low magnification of the obtained arrays; **e)** and **f)** side view of the obtained arrays. **144**

Figure 5.5. XRD patterns of ZnO (JCPDF 36-1451) and ZnO/Ag (JCPDF 04-0783) nano-arrays. **145**

Figure 5.6. **a)** ICP-MS analysis of mercury ions removed from a solution containing 10 ppm Hg^{2+} tested in dark and under UV irradiation and **b)** SERS spectra of RB collected from a ZnO/Ag nano-arrays based substrate following its exposure to a 10 ppm Hg^{2+} solution in dark and under UV irradiation for a period of 0.5 h and 2 h. **146**

Figure 5.7. **a)** ICP-MS data showing Hg^{2+} ion removal efficiency of ZnO/Ag nano-arrays having geometric surface areas (GSA) of 1 cm^2 and 0.25 cm^2 from a solution contaminated with 10 ppm Hg^{2+} ions; and **b)** relative intensity of the characteristic RB Raman band at 1358 cm^{-1} as a function of Hg^{2+} ion concentration (10, 50, 100, 500, 1000, 5000 and 10000 ppb) using ZnO/Ag nano-arrays based SERS substrates (GSA=0.25 cm^2). **148**

Figure 5.8. **a)** Raman mapping for scanning area of 150 × 150 μm^2 based on the characteristic RB Raman band at 1358 cm^{-1} from a sensor device having a **149**

geometric surface area (GSA) of 0.25 cm^2 of the ZnO/Ag nano-arrays without Hg^{2+} exposure; **b)** after exposing to a Hg^{2+} concentration of 1 ppm.

Figure 5.9. **a)** Photodegradation efficiency of RB using blank (no photocatalyst), ZnO and ZnO/Ag systems and **b)** UV-Vis absorbance spectra of RB by increase in the illumination time in the presence of ZnO/Ag nano-arrays. **150**

Figure 5.10. **a)** Hg 4f and **b)** Ag 3d XPS spectra of ZnO/Ag nano-arrays after RB degradation followed by heat treatment in vacuum. **151**

Figure 5.11. **a)** SERS enhancement of RB for developed substrates before and after Hg^{2+} exposure (5 ppm) and after removing RB and amalgamated mercury from the system with three successful regeneration cycles and **b)** Overlayed SERS spectra of one sample after three complete regeneration cycles without any background corrections being applied. **152**

Figure 5.12. Selectivity of the ZnO/Ag nano-arrays towards Hg^{2+} (on the characteristic RB Raman band at 1358 cm^{-1}) in the presence of other metal ion species in a solution containing 1 ppm of each cation for an exposure period of 1 h. **152**

Figure 6.1. Schematic model for growth of monodispersed polystyrene microspheres. **160**

Figure 6.2. **a)** Geometry of particle float on the interface; **b)** accumulation of the surface charge on the suspended particles which particles dispersed; **c)** formation of attractive capillary forces. **162**

Figure 6.3. Structure of TCNQ and its ionic forms. **165**

Figure 6.4. Synthesis procedure for controlled ZnO/AgTCNQ nano-arrays: 1) synthesis of ZnO thin film via Sol-gel method; 2) Monolayer of PS nano-arrays on ZnO thin film; 3) E-beam evaporation of silver layer; 4) Lift-off of PS arrays and formation of Ag star-shape patterns on ZnO thin film; 5) CVD growth of AgTCNQ nano-arrays and formation of ZnO/AgTCNQ heterojunction. **168**

Figure 6.5. SEM images of the synthesized **a)** 500 nm and **b)** 1500 nm polystyrene monodispersed spheres. **169**

Figure 6.6. SEM images of the monolayer formed by **a)** 500 nm and **b)** 1500 nm PS beads. **169**

Figure 6.7. Schematic shows the cross section for formation of star shaped islands. **170**

Figure 6.8. SEM images of the produced ZnO/Ag nano-star patterns using **a)** 500 nm **170**

and **b)** 1500 nm packed PS masks.

Figure 6.9. AFM images and height profiles of ZnO/Ag nano-star patterns using **a)** 500 nm and **b)** 1500 nm packed PS masks. **171**

Figure 6.10. AFM phase image of ZnO/Ag nano-star patterns using 500 nm. **172**

Figure 6.11. EDX linear profile and spectrum of ZnO/Ag nano-star patterns using **a)** 500 nm and **b)** 1500 nm packed PS masks. **173**

Figure 6.12. Effect of CVD temperature on the formation of AgTCNQ from nano-star patterns (500nm PS mask): **a)** 160 °C, **b)** 180 °C and **c)** 200 °C for 1h. **174**

Figure 6.13. Growth of AgTCNQ at 200 °C for 1h from nano-star patterns **a)** 500 nm and **b)** 1500 nm PS masks: 1) Low magnification 2) origin of the nanowires and 3) AgTCNQ wires. **175**

Figure 6.14. a1) SEM image of ZnO-Ag nan-ostar pattern fabricated from 500nm PS mask; **a2)** EDX mapping of the **(a1)** surface for Ag Lα ; **a3)** EDX mapping of the a1 surface for Si kα; **a4)** EDX spectrum from surface of **(a1)**; **b1)** SEM image of ZnO-AgTCNQ of same surface at 200 °C for 1h; **b2)** EDX mapping of the **b1** surface for Ag Lα ; **b3)** EDX mapping of the **b1** surface for N kα; **b4)** EDX spectrum from surface of **b1**. **176**

Figure 6.15. Raman spectra of **a)** TCNQ powder, **b)** Zno-AgTCNQ 160°C, **c)** Zno-AgTCNQ 180 °C and **c)** Zno-AgTCNQ 200 °C fabricated from 500 nm Ag nano-stars and **d)** Zno-AgTCNQ 200 °C fabricated from 1500 nm Ag nano-stars. **177**

Figure 6.16. XPS spectra of different materials showing **a)** Zn 2p and **b)** N 1s. **178**

Figure 6.17. UV-visible absorbance spectra of RB with increasing illumination time in the **a)** absence of any photocatalytic surfaces, **b)** ZnO thin film, **c)** ZnO-Ag nano-star pattern, **d)** ZnO-AgTCNQ [160 °C, 2h] , **e)** ZnO-AgTCNQ [180 °C, 2h] , **f)** ZnO-AgTCNQ [200 °C, 2h] and **g)** corresponding photodegradation efficiency of the samples. **179**

List of Tables

Table 3.1. Classification of BCMs based on the required prior signal information. **60**

Table 6.1. Synthesis conditions for producing 500 and 1500 nm monodispersed PS spheres. **167**

List of Abbreviations

AFM	Atomic Force Microscopy
BCM	Background Correction Methods
BE	Binding Energy
CE	Chemical Enhancement
CL	Colloidal Lithography
CT	Charge Transfer
CVD	Chemical Vapour Deposition
CWT	Continuous Wavelet Transform
EDX	Energy Dispersive X-ray
EM	Electromagnetic enhancement
FWHM	Full Width at Half Maximum
GSA	Geometric Surface Area
HMTA	Hexamine
ICP-MS	Inductively Coupled Plasma Mass Spectrometry
LSPR	Local Surface Plasmon Resonance
LSTD	Local Standard Deviation
MOF	Metal Organic Frame
NP	Nanoparticles
ppb	Parts Per Billion
ppm	Parts Per Million
PS	Polystyrene beads
RMSE	Root Mean Squared Error
rpm	Revolution Per Minute
RSD	Relative Standard Deviation
sccm	Standard Cubic Centimetre per Minute
SEM	Scanning Electron Microscopy
SERS	Surface Enhanced Raman Spectroscopy
SNR	Signal to Noise Ratio
SPR	Surface Plasmon Resonance
SRM	Signal Removal Method
TCNQ	Tetracyanoquinodimethane
UV-Vis	UV-Visible Spectroscopy
WTM	Wavelet Transform Method
XPS	X-ray Photoelectron Spectroscopy
XRD	X-ray Diffraction

CHAPTER I

INTRODUCTION

This chapter provides an overview of the thesis starting with a short survey on semiconductors, photocatalysis, metal nanoparticles, surface plasmon resonance, surface enhanced Raman scattering, followed by their applications in catalysis and sensing. Material parameters as well as the effect of heterojunction structures of a semiconductor device that can influence the photocatalytic activities were briefly reviewed. As zinc oxide is the main inorganic semiconductor used in the research presented in this thesis, an introduction is provided to show its properties and optical applications. The conceptual development of multifunctional materials, which can integrate photocatalysis and sensing for the development of renewable molecular and heavy-metal ion SERS sensors were further discussed.

1.1. Introduction

Catalytic processes are chemical reactions where the rate of the reaction is modified by the presence of a catalyst. In most of the catalytic processes, chemical reaction can only happen in the presence of the catalyst, which significantly reduces the activation energy; otherwise, the rate of the reaction would be slow in the absence of the specific catalyst. Photocatalysis is a unique branch of catalysis, wherein the catalyst can only become activated when it is illuminated with the light with appropriate energy through excitation of the electronic states of the catalyst. These photocatalytic reactions can be carried out in homogeneous and heterogeneous phases. In homogeneous photocatalysis, both the catalyst and the reactants in the chemical system are in the same phase[1], whereas in heterogeneous catalysis, the catalyst is in a different phase from the reactants[2-3]. Most of the inorganic and organic semiconductors have been demonstrated as very good photocatalysts for many chemical reactions. In particular, high photocatalytic activities of the wide band-gap semiconductor based heterogeneous photocatalysts (e.g. TiO_2[4-6], ZnO[7-8], SnO_2[9], WO_3[10], etc.) have attracted researchers' attention. Functionalizing semiconductors with metal nanostructures to create metal-semiconductor junctions can alter the photocatalytic activity of the semiconductors as well as may provide a multifunctionality using optical properties of the metallic structures such as SERS hot spots for multifunctional device fabrication, which is the major focus of this thesis. Thus an introduction about semiconductor, their properties, metal nanostructures, SERS and device fabrication are given in the following sections.

1.2. Photocatalysis

1.2.1. A short journey to the world of semiconductor

Semiconductor energy band

Semiconductors belong to a special class of materials where their conductivity ranges between that of a metallic conductor like silver and gold and that of an insulator such as quartz. The differences in their electrical conductivity can be understood by studying their electronic band structures. The simplified version of the band diagram can be considered to explain these differences. The highest band occupied by electron, and the lowest almost-empty band are known as valence and conduction bands, respectively. These two bands

mainly dominate the behaviour of a semiconductor. The energy gap between the maximal energy point of valence band and the minimal energy point of conduction band is known as band-gap (E_g). This band-gap energy is not as large as in insulators which does not allow the excitation of the electrons from valence bands to the conduction band. The energy band-gap is a major characteristic of a semiconductor. Based on the materials structures, semiconductors can be in the form of inorganic (e.g. Ge, Si, ZnO, etc.) or organic (e.g. tetrathiafulvalene (TTF) and tetracyanoquinodimethane (TCNQ)) materials[11-12].

There are two different types of semiconductors in regard to their band structures: direct and indirect band-gap semiconductors as shown in **Figure 1.1**. If the momentum of electrons and holes is the same in the valence and conduction band, the minimum energy point of the conduction band aligns with the maximum energy point of the valence band. This is the case with direct band-gap materials. In an indirect band-gap this alignment does not exist and thus for transferring an electron from the valence band to the conduction band, momentum of the electron should be changed. In direct semiconductors, the electron transfer between valence band and conduction band can easily happen if enough energy equal to or higher than band-gap energy of the semiconductor is provided to the system[13].

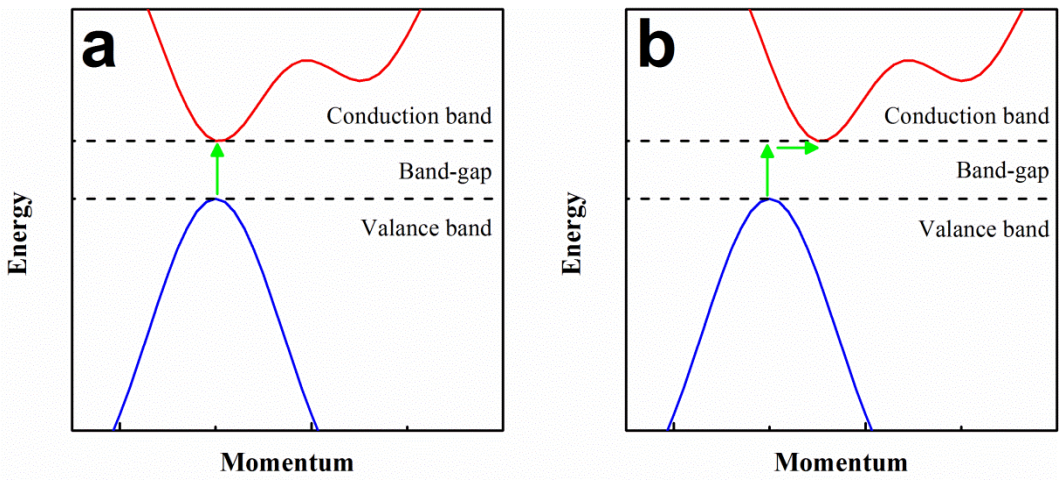

Figure 1.1. Conduction and valence band diagram of **a)** direct and **b)** indirect band-gap semiconductors.

When a direct band-gap semiconductor is exposed to a photon with energy equal or higher than its band-gap energy, this energy is absorbed by semiconductor and used to excite an electron from the valence band to the conduction band, creating electron/hole pairs. On the other hand, in indirect semiconductors, the momentum change should be provided by absorbing an additional phonon. Thus in most of the optical phenomena, applications are

based on the direct band-gap semiconductors where only photon interaction is required for these applications[14].

Electron distribution in semiconductors

As indicated before, in a solid, electrons occupy a series of bands. For a band with energy of (ε) the probability that an electron can occupy the band in an equilibrium temperature of T can be estimated through Fermi-Dirac distribution $f(\varepsilon)$ as:

$$f(\varepsilon) = \frac{1}{e^{\frac{(\varepsilon-\mu)}{k_B T}} + 1} \qquad 1.1$$

Where μ is energy of the state and k_B is the Boltzmann constant. With this equation an average number of electrons that can occupy the state of μ can be calculated. The location of the μ in a solid is important in characterizing the electronic structure of the solid. If valence and conduction bands are considered, μ would be called as E_f or Fermi level. The location of E_f in different materials is shown in **Figure 1.2**. In an insulator, E_f lies between a large band-gap between conduction and valence bands. In metallic structures, E_f lies within the valence band where there are a large number of active states available nearby. In this case, the bands are overlapped to each other as shown in **Figure 1.2**. In an intrinsic semiconductor, E_f lies between valence and conduction band.

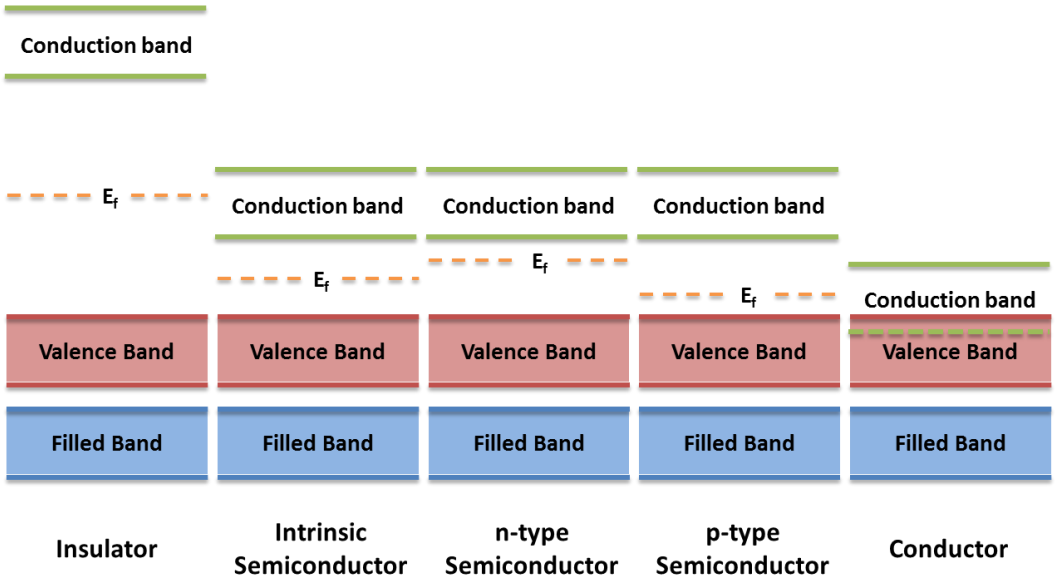

Figure 1.2. Schematic representation of energy bands in different type of materials.

Electrons excited to the conduction band in a semiconductor can make the electron flow and contribute to the conduction similar to metals. However, there is a difference between conduction in the metals and semiconductors. As shown in **Figure 1.2,** the conduction band and valence bands are separated from each other in the semiconductor. Thus, to observe conductivity, an electron should be transferred to the conduction band. This excitation and electron transfer, leaves an empty space in the valence band which is called as ***hole***. As electrons located in the valence band can be relocated in this empty space, the holes move in the opposite direction of the electrons movement. Thus, hole is considered as an individual component with positive charge in the quantum mechanics with specific characteristic. In a semiconductor, by controlling impurities (doping) and also defects in the crystallite of the semiconductor, the type of the semiconductor can be controlled to be as ***n-type*** (electron as majority carriers) or ***p-type*** (hole as majority carrier). A single semiconductor crystal can have many p- and n-type regions, the majority of each region determining the type of a semiconductor.

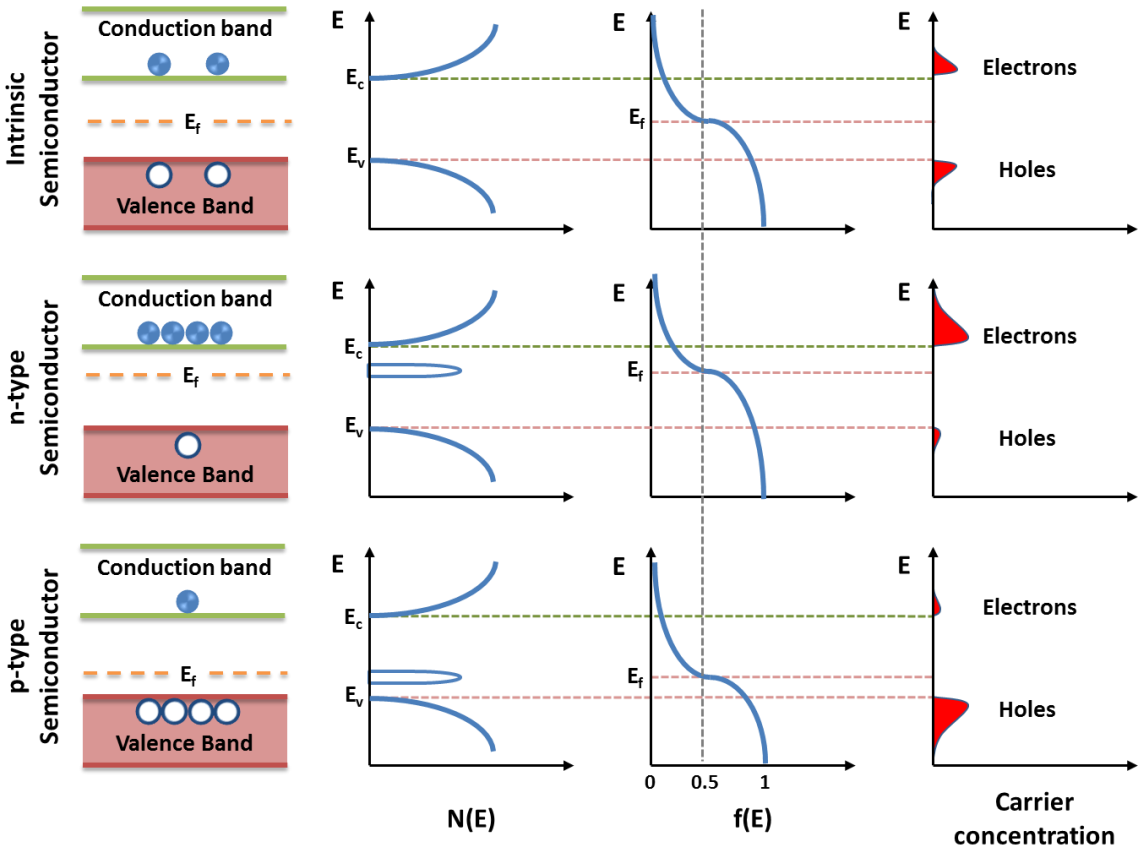

Figure 1.3. Density of states (*N(E)*), Fermi distribution (*f(E)*) and carrier concentration (n or p) for intrinsic, n-type and p-type semiconductors in thermal equilibrium.

As the exponential part of *Eq.1.1* is much higher than unity, this equation can be simplified as:

$$f(\varepsilon) \approx \exp(-\frac{E - E_f}{k_B T}) \quad 1.2$$

As the charge transfer carriers in the conduction and valence bands are electrons and holes, respectively, the density of the carriers can be shown as:

$$n_{e^-} = N_C \exp\left(-\frac{E_C - E_f}{k_B T}\right) \quad 1.3$$

$$n_{h^+} = N_V \exp\left(-\frac{E_f - E_V}{k_B T}\right) \quad 1.4$$

N_C and N_V are the density of the state at conduction and valence bands, respectively, which are equal to:

$$N_C = 2\left[\frac{2\pi m_e^* k_B T}{h^2}\right]^{3/2} \quad 1.5$$

$$N_V = 2\left[\frac{2\pi m_h^* k_B T}{h^2}\right]^{3/2} \quad 1.6$$

Where h is the Plank's constant, m_e^* is the effectiveve mass of electron and m_h^* is the effective mass of hole. In an intrinsic semiconductor the number of n_{e^-} and n_{h^+} are same and equal to n_i. Considering this fact by multiplying *Eq.1.3* and *Eq.1.4* to each other:

$$n_i{}^2 = N_C N_V \exp\left(-\frac{E_C - E_V}{k_B T}\right) = N_C N_V \exp\left(-\frac{E_g}{k_B T}\right) \quad 1.7$$

Now that $n_{e^-} = n_{h^+} = n_i$, and by considering *Eq.1.3* and *Eq.1.7*:

$$E_f = \frac{1}{2}(E_V + E_C) + \frac{1}{2}\left(k_B T ln\left(\frac{N_V}{N_C}\right)\right) \quad 1.8$$

By considering *Eq.1.5* and *Eq.1.6*:

$$E_f = \frac{1}{2}(E_g) + \frac{3}{4}\left(k_B T ln\left(\frac{m_h^*}{m_e^*}\right)\right) \quad 1.9$$

By considering that the second term is relatively small as it depends logarithmically on the ratio of hole and electron's effective masses in the bands, E_f in an intrinsic semiconductor is located in the middle of the energy gap, as shown in **Figure 1.3**.

In semiconductors with structural impurities, such as those in n-type or p-type semiconductors, the majority of the carrier would either be electrons or holes, respectively. The relative positions of the Fermi level and also band edges in these semiconductors are highly depended on the impurities level. These impurities, ***Donor*** (D) or ***Acceptor*** (A), can only stay in the lattice in an ionized form. These impurities can produce a dopant state within the band-gap. Due to the existence of additional electrons or holes due to impurities, if the dopant energy of the state is close enough to the thermal energy units (i.e. k_BT) of the band edge, electrons or holes in these dopant states can be easily migrated into the bands (acceptor levels are proximal to the valence band and donor levels are close to the conduction band). Thus, the Fermi energy in an n-type and p-type could be considered as:

$$E_f = E_C + k_B T ln\left(\frac{n_{e^-}}{N_C}\right) \quad 1.10$$

$$E_f = E_V + k_B T ln\left(\frac{N_V}{n_{h^+}}\right) \quad 1.11$$

Thus, the position of the E_f in a semiconductor highly depends on the type of the semiconductor. If a semiconductor is an n-type, the density of the states in the conduction band filled with electron is higher and thus E_f is near to the conduction band; while in the p-type the population of the holes in the valence bands are higher in the semiconductor, which make the E_f locates near to the valence band[13-17].

Even in 'chemically pure' semiconductors, deviation from stoichiometry can introduce some defect states, and thus these semiconductors may act as n-type or p-type in their pure non-stoichiometric form, e.g. CuI[18-19] (p-type) and ZnO[20-21] (n-type).

1.2.2. Semiconductor junctions

1.2.2.1. Semiconductor/metal junctions

Fermi level in a solid indicates the chemical potential of the lowest energy of free electron or the highest energy of free hole. When two semiconductors are attached to each other to form junctions, there will be a change in the chemical potential that brings the

interface in a thermodynamically non-equilibrium state due to the difference in their potentials. Subsequently, there will be an exchange of either matter or energy at the interface to equilibrate the chemical potential of the interfaces in order to make the system attaining the equilibrium state. This can be called as ***Fermi energy alignment*** in the heterojunction combination of the semiconductors with other materials[13]. When metals form contact with the semiconductors, two different kinds of contacts can be established, namely Schottky and Ohmic contacts[22]. The work function of the metal and semiconductor are the two major parameters that control the nature of contact between the metal and the semiconductor. The work function is the minimum energy needed to remove an electron from a solid to a point in the vacuum outside the solid surface free from the nuclei of the originated atom. The work function of a metal ($e\Phi_m$) is the energy difference between vacuum energy and the Fermi level of the metal (E_{Fm}) (as Fermi level is located in the band). However, for a semiconductor, the work function ($e\Phi_s$) is described as the energy required removing an electron from the semiconductor to the free vacuum level; thus, it can be considered as the energy difference between the Fermi level (E_{Fs}) and the vacuum level. In addition, the energy difference between the conduction band and vacuum level is known as the electron affinity ($e\chi_s$). Based on the differences between $e\Phi_s$ and $e\Phi_m$ and also considering the type of the semiconductor, four different junction can be realised at the metal/semiconductor interface, as shown in **Figure 1.4**. Regardless of the type of the junction, all these junctions attain the equilibrium state by the electron or hole exchange between the semiconductor and metals[14, 22].

In the case of n-type semiconductor/metal junction with $e\Phi_m > e\Phi_s$; due to transferring of electrons from the semiconductor to the metal, equilibrium and alignment in the Fermi levels occur. When few electrons are transferred from the semiconductor, the Fermi level or the band profile of the metal does not change. This is mainly due to the fact that metals have enormous free electron densities. As a result of electron transfer from the semiconductor to the metal side, positively charged fixed dopants are left in the semiconductor region which produces a dipole region at the interface. This charge transfer leaves a layer of the positively charged region (Depletion layer (W)) in the semiconductor. This dipole region can make a built-in potential between the charged area of the semiconductor and metallic structure in the junction interface. In the ideal Schottky barrier, the height of the barrier ($e\Phi_b$) at the junction is defined as the difference between conduction band of the semiconductor structure and Fermi level of the metal structure at the junction:

$$e\phi_b = e\phi_b - e\chi_s \quad (1.12)$$

The potential eV_{bi} is called the built-in potential of the junction and is given by

$$eV_{bi} = -(e\phi_m - e\phi_s) \quad (1.13)$$

Thus the electrons transferring from the semiconductor to the metal side face a barrier of eV_{bi} (***Forward bias***). On the other hand, due to existence of this barrier at the junction, the reverse translation (***Reverse bias***) needs more energy to move from the metallic to the semiconductor[14, 17].

In p-type semiconductor, if $e\Phi_m<e\Phi_s$ then similarly barrier can form during for hole transport. In this case, electrons can be transferred from metal to the semiconductor in the junction and make a negative charge depletion layer. The bands bend in such a way to make a barrier for hole transport. In this case the built-in potential would be:

$$eV_{bi} = e\phi_s - e\phi_m \quad (1.14)$$

In n-type semiconductor if $e\Phi_m<e\Phi_s$ then the junction can act as an ***Ohmic junction***. In this case, there would be no barrier between metallic and semiconductor structures. In this case, the junction acts only as a resistor and electrons can be easily transferred from the metal to semiconductor. This case can also be considered in the p-type semiconductor, if $e\Phi_m>e\Phi_s$. In both of these cases, the barrier does not exist but metallic structure can produce more free space for charge transfer and can act as charge traps[16-17].

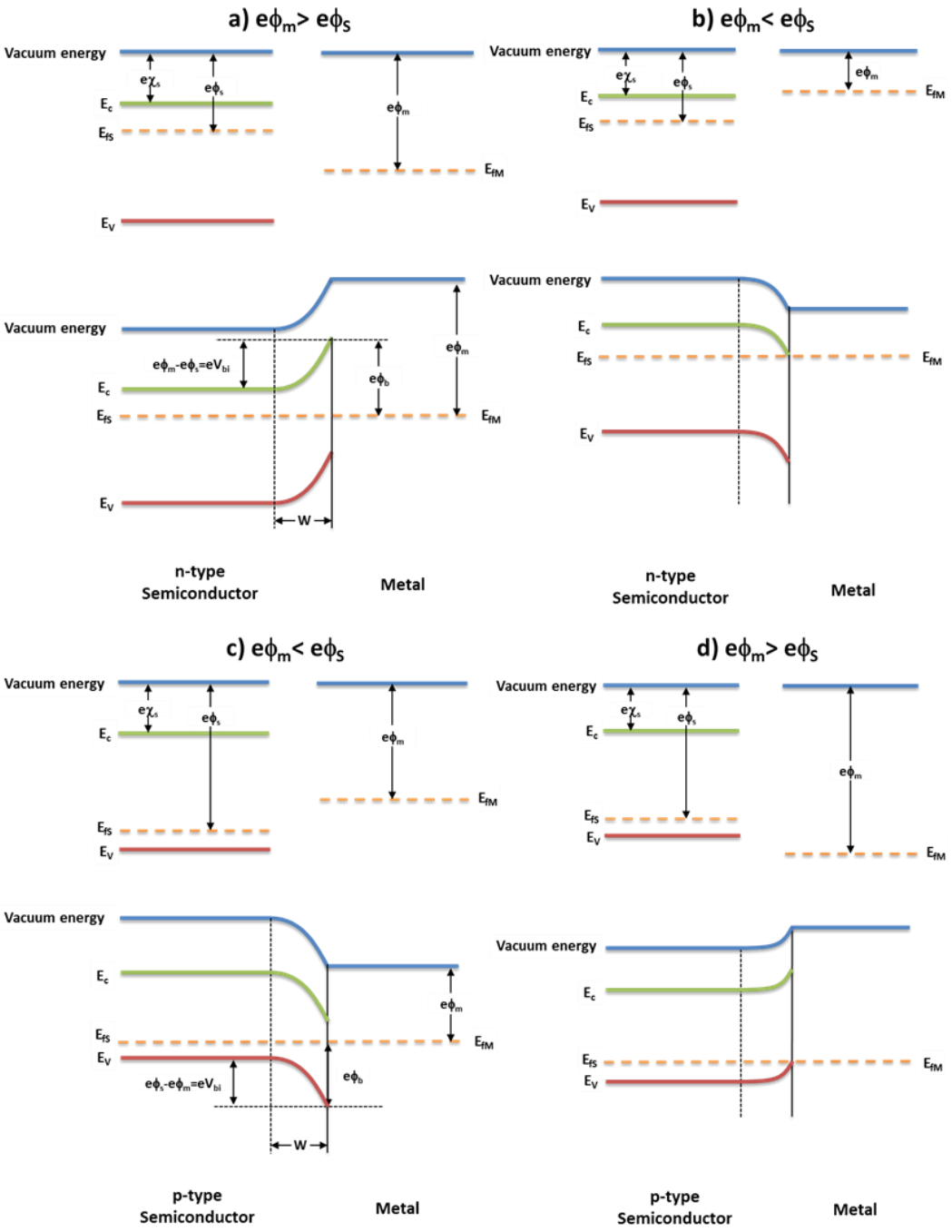

Figure 1.4. Band structures of metal–semiconductor junctions for **(a,b)** an n-type semiconductor and **(c,d)** a p-type semiconductor in thermodynamic equilibrium.

1.2.2.2. Semiconductor/semiconductor junctions

p-n homojunction

When two semiconductors of same composition with different dopants, making one p-type and the other n-type, come together they form a junction called p-n junction. As

explained in *Section 1.2.1*, the Fermi levels of these semiconductors are completely in different positions (**Figure 1.5a**). The n type semiconductor has a large number of electron carriers, whereas in the p-type the majority charge carrier belongs to holes with positive charges.

Due to the doping of the semiconductor, the majority of the carriers on the n-type side are electrons, while very few mobile electrons are available on the p-type region. Due to the random thermal motion of the free electrons and differences in their concentration in the p region and n region, electrons from the n-type side start to ***diffuse*** into the p-type side. Similar condition happens for holes. There are large numbers of mobile holes in the p-type region as they are major carriers in a p-type semiconductor, on the other hand, on the n-type side holes are just minority carriers. Therefore, a diffusion of the holes from the p-type region across into the n-type region occurs (**Figure 1.5b**). Most of the electrons recombine with holes during simultaneous diffusion of electron and holes in opposite directions. As a result, a region of ***depleted*** mobile carriers is formed at the junction (**Figure 1.5c**)[17].

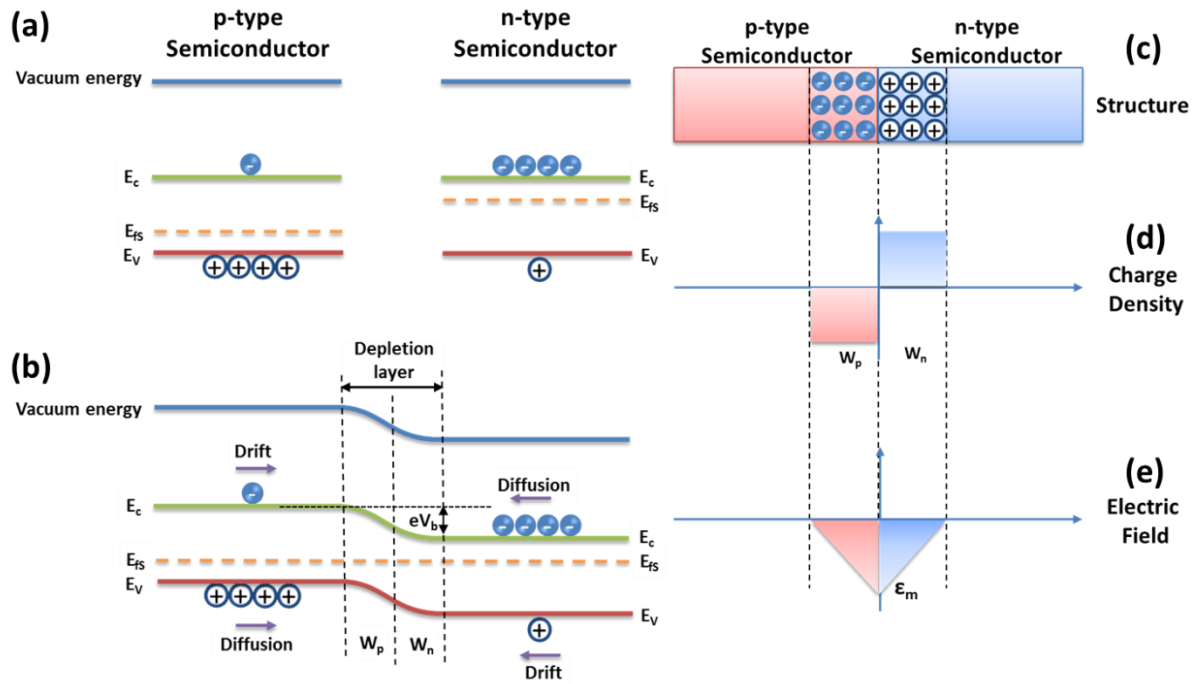

Figure 1.5. a) Band structure of a p-type and an n-type semiconductor before joining, **b)** band structure of a p-n homojunction, **c)** structural change in the depletion layer of a p-n homojunction, **d)** charge profile in the depletion layer and **e)** electric field profile in the depletion layer (maximal at the junction).

An electric field in the depletion layer is produced due to coexisting of positive charge in the n-side and negative charge in the p-side which sweeps out any electrons and holes that enter the region (**Figure 1.5d** and **e**). A ***drift*** current is created at the junction after attainment of equilibrium, that counter balances the diffusion current (**Figure 1.5b**). Since the structure after diffusion should reach to the equilibrium, Fermi levels of the p- and n-type materials get aligned in the structure. The above exchange of carriers occurs on a very short time scale. So the whole process can be thought of as instantaneous. As a result aligning the Fermi levels of the p and n type semiconductors, between the n-side and the p-side, a built-in voltage, V_{bi}, is produced. As indicated in **Figure 1.5b**, the built-in voltage is given by:

$$eV_{bi} = Eg - (E_{Cn} - E_{fn}) - (E_{fp} - E_{Vp}) \quad 1.15$$

By solving the Poisson equation, the width of the depletion region for the junction under no applied bias can be estimated as:

$$W_p(V_{bi}) = \left\{\frac{2\epsilon V_{bi}}{q}\left[\frac{N_d}{N_a(N_a+N_d)}\right]\right\}^{1/2} \quad 1.16$$

$$W_n(V_{bi}) = \left\{\frac{2\epsilon V_{bi}}{q}\left[\frac{N_n}{N_d(N_a+N_d)}\right]\right\}^{1/2} \quad 1.17$$

Where, N_a and N_d are the uniform doping densities for the acceptors and donors for p-n structure; ϵ is permittivity and q is the magnitude of the electron charge. Thus the width of the depletion layer in each region is highly depended on the concentration of the dopants.

The electric field is non-uniform in the depletion region; where it reaches to its maximal amounts at the junction (**Figure 1.5.f**). The maximum value can be calculated as[13]:

$$\varepsilon_m = -\frac{qN_dW_n}{\epsilon} = -\frac{qN_aW_p}{\epsilon} \quad 1.18$$

p-n heterojunction

If two different semiconductor materials are used to form a junction, the junction is called heterojunction. In this case based on the band-gaps and also the position of the bands based on the vacuum energy levels, three different band diagrams as *Straddling*, *Offset* and *Broken gaps* can be produced as shown in **Figure 1.6**[13, 23].

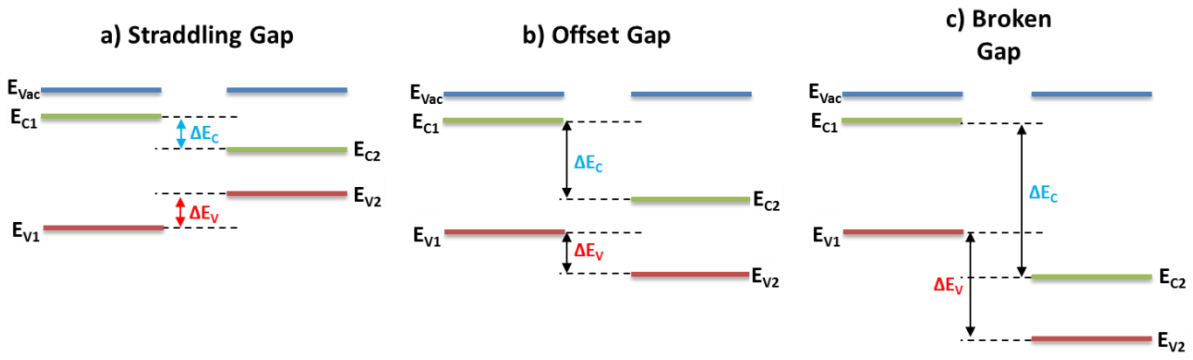

Figure 1.6. Different semiconductor heterojunctions based on their band edge offsets in the flat band condition for: **a)** Straddling, **b)** Offset and **c)** Broken gaps.

Based on the type of the semiconductors, the heterojunction can be categorised into four different types. **Anisotype** heterojunctions in which n-P or N-p junctions are formed; where the capital letter indicates the larger band-gap material. If the same semiconductor type is used in the junction it will be known as **isotype** heterojunction which includes n-N and p-P. There are some "rules of thumb" in analysing the band diagram of heterojunction:

- *Linearity*: The band-gap and the band edge positions cannot be changed by joining the semiconductors to each other.
- The common anion rule: When two semiconductors with same anion (As in GaAs and InAs) make heterojunction, the bending in the conduction band edge is always greater than the valence band edge ($\Delta E_V < \Delta E_C$).
- The common cation rule: When two semiconductors with same cation (Ga in GaAs, GaP and GaSb) make heterojunction the valence band edge energies scale with the anion electronegativities.

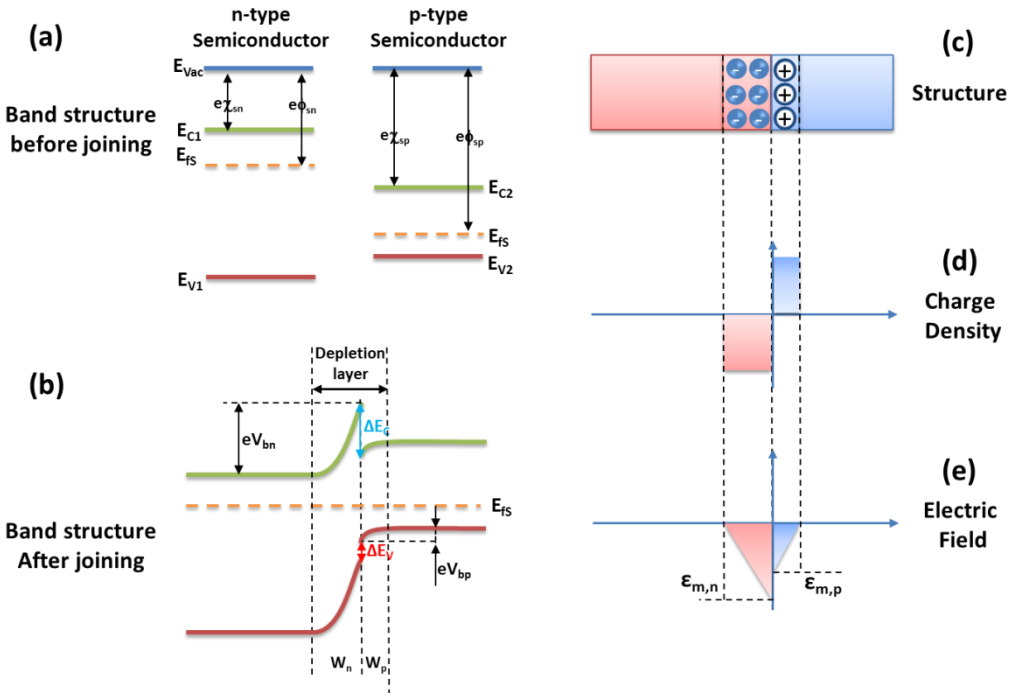

Figure 1.7. a) Band structure of a p-type and an n-type semiconductor before joining, **b)** band structure of a p-n heterojunction, **c)** structural change in the depletion layer of a p-n heterojunction, **d)** charge profile in the depletion layer and **e)** electric field profile in the depletion layer (maximal at the junction).

Band bending as in homojunctions can be resulted in heterojunctions due to the alignment of Fermi energies to attain equilibrium. In the case of n-type wide band-gap semiconductor attached to the low band-gap p-type semiconductor, Fermi levels should be flat to reach an equilibrium state. In this case, like homojunction, p-n junction diffusion and drift of the carriers happen. This generates the depletion layer in the interface (**Figure 1.7**).

One of the main and significant features of the semiconductor heterojunction is the discontinuity in the band edge. The discontinuities result from the fact that not only the doping and the electron density are changing across the interface of a p-n heterojunction, but that the atoms themselves are changing. This results in the formation of a step function in electron potential. One of the remarkable discontinuity-related effects is the formation of spike in the interfacial regions. In this case, the charge carriers are trapped in the spike[13]. This discontinuity highly depends on the structures of the materials. It can only happen if the materials are completely changed by passing the interfaces of the junction from one semiconductor to another. In other word, two materials that have little or no solid solubility in each other will form an abrupt interface (e.g. Si and ZnSe)[24]. Abrupt interface will not form

in the junctions where the semiconductors have large solid solubilities (e.g. GaAs and AlAs)[13].

1.2.3. Photocatalysis

General description

The interaction of light and a semiconductor photocatalyst is shown in **Figure 1.8**, schematically. When a semiconductor is excited by light with appropriate energy (*hv>Eg*), an electron is excited from valence band to the conduction band, creating an electron-hole pair. The holes have enough positive potential to convert the water molecules attached to their surfaces into •*OH* radicals. These •*OH* radicals are strongly oxidizing radicals present on the surface of the semiconductor. Conversely, the electrons react with dissolved oxygen molecules in the water to form superoxide anion, $O_2^{\bullet -}$. The electrons on the surface can create reduction sites on the surface of the semiconductors. However, the formation of the electron-hole pair is not a stable phenomenon[25-26].

Absorption of a photon results in the excitation of an electron from the valence band to the conduction band that leaves a hole in the valence band. When the excited electron returns to the valence band from the conduction band, it ***recombines*** with the generated hole. The excitation-recombination (depends on the structure and defects of a semiconductor) is a nanosecond length phenomenon. As the formation of the radicals highly depends on the availability of the electron and hole in the excited semiconductor, therefore, the life-time of the electron-hole pair in a semiconductor becomes a very critical parameter to control its photocatalytic activities[25]. The fast recombination makes the life-time of an electron-hole pair shorter and subsequently decreases the amount of the radicals formed on the semiconductor and reduces the efficiency of the photocatalytic reactions. Presence of any radical scavenger or crystalline defect can facilitate the recombination rate via trapping the electron or the hole in the semiconductor structure (***volume recombination***). Therefore, the population of the trapping states and recombination sites can be reduced by providing photocatalysts with a better crystallinity. This can be resulted into an increase in the efficiency of a photocatalyst by increasing the life time of electron-hole pairs[4, 6]. At the interface of a semiconductor material with the media, the termination of the periodic structure of a semiconductor at its free surface can form surface-localized electronic states within the semiconductor band-gap and/or a double layer of charge, known as a surface dipole. Surface atoms with no upper atom to bind can lead to formation of **dangling bonds.** These dangling bonds can form different

charge characteristics at the surface of the semiconductor. Furthermore, the topology of the semiconductor can charge in the surface (there is no completely flat surface) which is due to steps and kinks at the surface of the semiconductors. These phenomena at the surface can make recombination sites for trapping and consumption of electron and hole pairs formed via photoexcitation (***surface recombination***)[27].

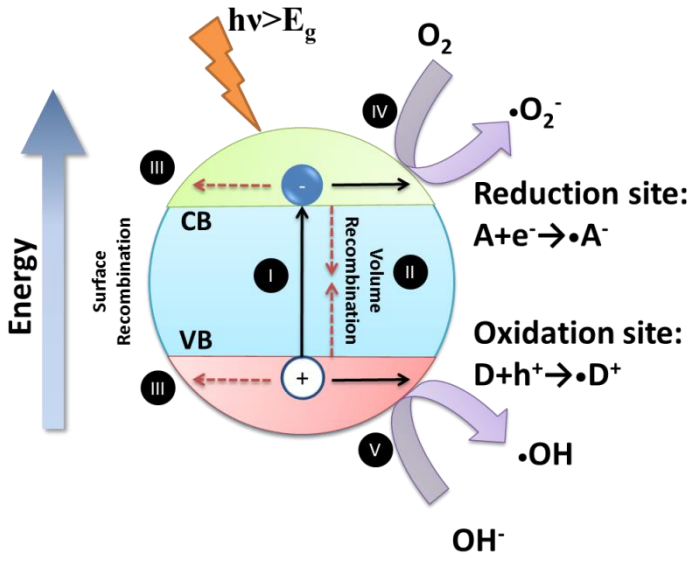

Figure 1.8. Schematic illustration of the principle of semiconductor photocatalysis: (I) the generation of an electron/hole pair via photo-excitation; (II) the volume recombination of electron and hole; (III) Consumption of electron in the broken ligands and defects located at the surface (surface recombination); (IV) the initiation of a reductive pathway by a conduction-band electron; (V) the initiation of an oxidative pathway by a valence-band hole.

Increasing efficiency

To obtain optimum photocatalytic efficiency, the electron and the hole should be efficiently separated from each other, and the photo-generated charges should be rapidly transferred across the surface/interface to avoid the recombination. To improve the photocatalytic performance, the approach that has generally been applied is to form a semiconductor junction by coupling with a secondary substance (noble metal, other semiconductors)[23, 28].

As mentioned in *Sections 1.2.2.1* and *1.2.2.2*, the formation of the junction between a semiconductor and metallic or semiconducting materials can form junctions with an ability to separate the electron and hole. Semiconductor/metal junction can have two different forms.

First, if the heterojunction forms Schottky barrier, photo-excited electron is transferred to the metallic structure, which allows the separation of the electron and hole. Furthermore, formation of the electric field in the depletion layer can help electron-hole separation as the excited electron cannot easily come back to the semiconductor to recombine with the hole. These phenomena increase the life-time of electron-hole pairs. On the other hand, when Ohmic junction forms, the transfer of the charge into the metallic structure, like the situation in the Schottky junction, can increase the lifetime of the electron-hole as the metallic structure acts as electron sink[29-31]. Although the barrier does not exist in this form, but the bending of the conduction band and the differences in the Fermi levels of the metal, and the semiconductor makes the return of the electron to the semiconductor harder, and thus helps the separation of the electron-hole pairs. As an example, the photocatalytic reaction using silver decorated zinc oxide is presented in **Figure 1.9**[7, 32-33]**.**

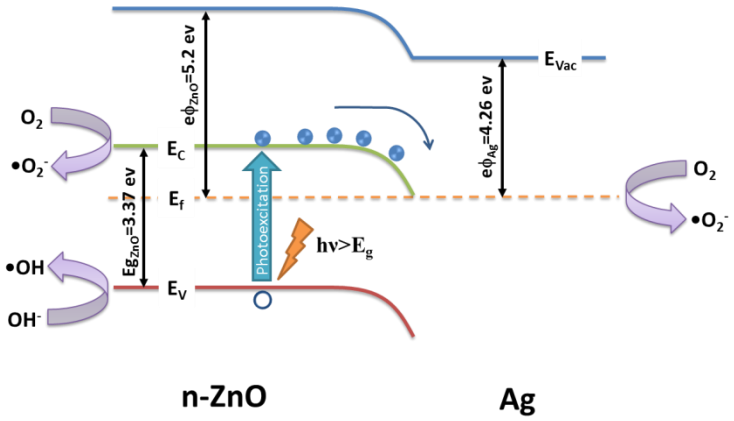

Figure 1.9. Photocatalytic mechanism in Ag/ZnO heterojunction nanocrystals.

In the case of ZnO/Ag, the work function of the semiconductor is larger than the Fermi level of the junction, thus the photo-excited electrons can be transferred from ZnO to silver metal due to the higher energy of the conduction band of the ZnO. These electrons can generate $\bullet O_2$ radicals while the holes in the ZnO structures can generate $\bullet OH$ radicals. Thereby, existence of the silver metal on the surface of zinc oxide can increase the rate of the charge transfer due to lower Fermi levels than conduction band of the zinc oxide, which leads to the separation between photo-generated electron and hole pairs[33-34].

Another type of junction to increase the life time of an electron-hole pair is semiconductor-semiconductor junctions, wherein the band-gap of both semiconductors are significantly different [23, 28, 35-36]. There are two reasons for using these structures. First, using

semiconductors with different band-gaps, wider wavelength ranges of the light can be harvested for generating electron-hole pairs. If a wide band-gap semiconductor is used for instance, it needs short wavelength light with energies high enough to overcome its band-gap. Thus, in most of the wide band-gap semiconductors like ZnO[8, 37] and TiO_2[5-6], UV source is needed for their photo-excitation. As the UV region is the small portion of the solar light, it is advantageous to integrate lower band-gap semiconductors with wide band-gap semiconductor to harvest broad region of solar light spectrum. Therefore, the use of n-n heterojunctions like CdS/ZnO[38-40] and CdSe/TiO_2[41-43] have become one of the major attractions of the semiconductor heterojunctions. On the other hand semiconductor-semiconductor junction can be formed as p-n junctions[44-45]. The main efforts are focused on the heterojunctions. In this way not only the fabricated photocatalyst can harvest larger areas of the solar light, but it can also make the electron-hole separation more effectively. In p-n junction, due to formation of charged depletion layer at the junction, the electric field does not allow the electron hole recombination. Also, in the heterojunction, formation of the spikes in the band structure can act as electron or hole traps, furthermore, assist with electron-hole separation. For instance, the Ag_2O (p-type) and $Bi_2O_2CO_3$ (n-type) semiconductor's junction can be taken as an example to show band structures and the photocatalytic mechanisms, as shown in **Figure 1.10**[46].

As discussed in the *Section 1.2.2.2*, under dark the Fermi levels are aligned and a depletion layer is formed at the interface. After generation of an electron-hole pair upon light absorption, the system attains a non-equilibrium state by creating a bend in the Fermi level of the junction. The system behaves like p-n diode under forward bias. In this regards, the electrons formed in Ag_2O drift into the depletion layer of $Bi_2O_2CO_3$, while the holes generated in $Bi_2O_2CO_3$ are transferred to the Ag_2O structure. Then these separated electron and holes can be consumed to form free radicals of $\bullet OH$ or $\bullet O_2$. Thus formation of the p-n junction can cause efficient separation between electrons and hole, thereby, increasing the efficiency of the photocatalytic reactions[46].

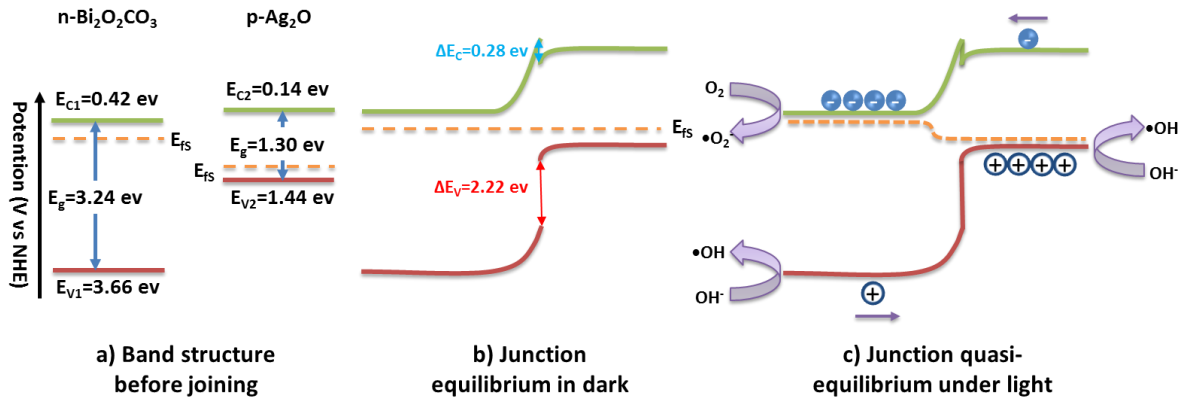

Figure 1.10. Band structure of $Ag_2O/Bi_2O_2CO_3$ p-n heterojunction **a)** before forming junction (*V vs. NHE*), **b)** in the dark **c)** under illumination.

Photocatalysis cannot only be done with inorganic semiconductors, but also there are some reports on the use of the organic semiconductor photocatalysts. Major disadvantage in this case is the stability of the organic semiconductor itself because the produced radicals may degrade the organic semiconductor. Recently, the use of AgTCNQ and CuTCNQ, two well-known narrow band-gap p-type charge transfer semiconductors, with/without metal junctions, for the degradation of environmental pollutants have been reported[47-48]. These materials have shown a good stability in the presence of the photocatalytically generated radicals. One of the main attempts of this thesis is to utilize the semiconducting p-n junctions between ZnO and AgTCNQ as inorganic-organic heterojunction to increase the photocatalytic efficiency of the ZnO nanostructures.

1.3. Surface enhanced Raman spectroscopy

1.3.1. Fundamentals of local surface plasmon resonance (LSPR)

Plasmons are considered, in a classical picture, as the collective oscillation of the free-electron gas density in a conducting material such as metal. When the electrons in the metal interact with light having frequencies less than the plasma frequency, the light is reflected. On the other hand, for frequencies of light higher than plasma frequency of the metal, the electrons of the metal particles cannot respond to the electromagnetic field fast enough and thus the light transmitted[49]. When an electromagnetic wave interacts with a metal particle, conduction electrons of the metal set into oscillations and they are displaced with respect to their equilibrium positions. The attractive forces are exerted by the cationic cores that act as a

restoring force that enables the electron oscillations around their equilibrium positions. As the size of the metal is reduced below the mean free path of the electron in a metal, these dipolar oscillations become quantized and the force on the surface electrons results into a unique resonance frequency that matches the oscillations[50]. This phenomenon generates collective charge oscillations on the surface of the metal particles known as surface plasmon resonance (*SPR*) as shown in **Figure 1.11**. Most of the metals such as Pb, In, Hg, etc. have plasma frequencies in UV parts of the spectra, thus there is no color effect that could be observed in these materials. Conversely, Cu, Ag and Au show their *SPR* frequencies in the visible spectral ranges. *SPR* results in efficient absorption and scattering of light at specific frequencies depending on the particle shape, size, and composition[49, 51-54].

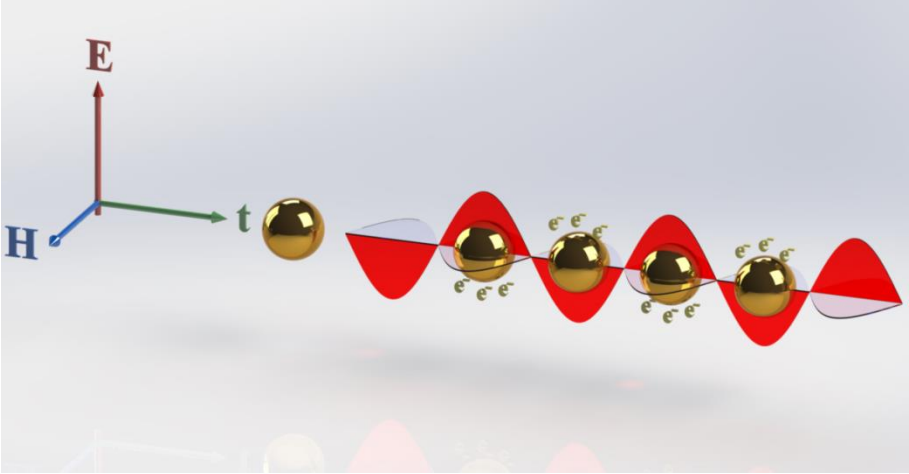

Figure 1.11. Schematic illustration of surface plasmon resonance in a spherical particle.

The quasi-static approximation assumes that the phase of the electric field of the incident light is essentially constant over the length of the nanoparticle. Thus, for nanoparticles with sizes smaller than the incident wavelength of the light, by using the quasi-static approximation, the particle is treated as a single dipole and thus the produced dipole momentum can be estimated as:

$$p = 4\pi\varepsilon_0\varepsilon_m a^3 \frac{\varepsilon - \varepsilon_m}{\varepsilon + 2\varepsilon_m} E_0 \qquad 1.19$$

Where ε_0 is the vacuum permittivity, ε_m is the dielectric constant of the medium, a is the partiradius; ε is the complex dielectric function of metal, and E_0 represents the incident field. The polarizability, α of the particle then can be defined as[55]:

$$p = \varepsilon_0 \varepsilon_m \alpha E_0 \quad (1.20)$$

From *Eq. 1.19* and *Eq.1.20*:

$$\alpha = 4\pi a^3 \frac{\varepsilon - \varepsilon_m}{\varepsilon + 2\varepsilon_m} \quad (1.21)$$

As could be seen from *Eq.1.21*, if the term $(\varepsilon + 2\varepsilon_m)$ reaches to its minimal point, the polarizability of the particles would be maximized. Dielectric function consists of real (ε_r) and imaginary parts(ε_i). Based on the Fröhlich theory, when $\varepsilon_r = -2\varepsilon_m$ then absorption and scattering of incident light on the particle are greatly enhanced at these frequencies[55]. As ε_i is small and relatively constant, the *LSPR* is determined by real part of dielectric constant of the metallic particles and the dielectric constant of the media. The sum of the scattering and absorption of the light by metallic materials is known as extinction. Mie theory can estimate the extinction for spherical particles as:

$$E(\lambda) = \frac{(1+\chi)^2 8\pi^2 N a^3 (\varepsilon_m)^{3/2}}{3\lambda \ln(10)} \left[\frac{\varepsilon_i(\lambda)}{(\varepsilon_r(\lambda) + \chi\varepsilon_m)^2 + (\varepsilon_i(\lambda))^2} \right] \quad (1.22)$$

Where, χ is a shape factor ($\chi = 2$ for spherical particles), *N* is the density of particles, a is particle radius, ε_m is the dielectric constant of the surrounding media, ε_r and ε_i are real and imaginary part of the metal dielectric function. With this theory, we can predict the position and shape of the plasmon absorption spectrum for spherical and spheroidal metal particles[56-57].

1.3.2. Surface-enhanced Raman scattering (SERS)

Raman scattering

Raman scattering is an inelastic scattering of a light photon by a molecule as discovered by C. V. Raman in 1928[58]. The inelastically scattered photon has the vibrational fine structure of the molecule that scatters the photon, and the vibrational fine structure forms the ***fingerprint*** of each molecule. This ability in distinguishing the molecules using this technique as a promising analytical tool is called Raman spectroscopy[59-60].

Figure 1.12 shows the different types of scattering mechanisms schematically. Photon with the energy of $h\nu_0$ excites the molecule into a virtual energy state. During the energy relaxation, if the photon does not interact with the molecule, the relaxation results in the

formation of re-radiation of the photon with the same frequency. This scattering is an ***elastic scattering***, which is known as ***Rayleigh scattering***. However, there are some photons that interact with the molecular vibrational/rotational motions; therefore, their frequency after scattering is reduced from the incident photon frequency. These types of scattering which include the change in the energy of the initial photon are known as ***Stokes*** and ***Anti-Stokes scatterings*** which are the basics of ***Raman scattering***. ***Stokes scattering*** is in which case that the scattered photon has lower energy than the initial photon. Raman scattering is an extremely weak process and only 1 photon in 10^6-10^9 photons are scattered inelastically. Therefore the intensity of Raman scattering is quite weak and has a number of drawbacks in terms of using it as an analytical technique.

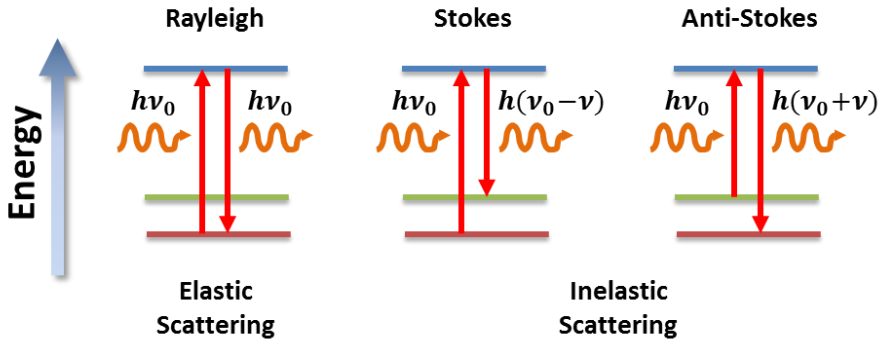

Figure 1.12. Quantum mechanical model of Raman scattering.

Surface-enhanced Raman scattering (SERS)

When a molecule locates close enough (r) to the metallic nanoparticle, there will be an enhancement in the Raman signal of the molecule which is known as ***Surface-enhanced Raman scattering (SERS).*** The induced *LSPR* from interaction of metallic particles with light occurs at the surface of the particles and then generates the amplified electromagnetic field. Subsequently, it results into difference in the electromagnetic fields inside (E_{in}) and outside (E_{out}) of the particles, which can be calculated by the Maxwell's equations as[61]:

$$E_{in} = \frac{3\varepsilon_M}{\varepsilon_m(\lambda) + 2\varepsilon_M} E_0 \qquad 1.23$$

$$E_{out} = E_0 Z - \alpha E_0 \left[\frac{Z}{r^3} - \frac{3Z}{r^5}(Zz + Xx + Yy)\right] \qquad 1.24$$

Where ε_M and ε_m are dielectric functions of media and metallic nanoparticles, respectively; E_0 represents the incident field; α represents polarizability of metallic particles described in *Eq.1.21*; *r* is the radius distance; *x,y* and *z* are Cartesian coordinates and *X,Y* and *Z* are the unit vectors. It could be seen from these equations that the E_{out} is the strongest when excitation and scattered fields are in resonance with *LSPR*.

There are two main enhancement reasons known that relate to the SERS phenomenon: ***electromagnetic enhancement (EM)*** and ***chemical enhancement (CE)*** mechanisms[62].

1.3.3. Enhancement mechanisms in SERS

Electromagnetic enhancement (EM)

The resonance excitation of plasmon oscillation in the surface of the metal nanoparticle is the main reason for electromagnetic enhancement (*EM*). The resonance excitation of *LSPR*, as shown in *Eq.1.24*, makes (i) an amplified electric field in the vicinity of its originated metallic surface and also (ii) provides the radiation enhancement due to the modified Raman dipole[63].

The electromagnetic field of the incident light (E_{Inc}) at the incident frequency of ω is different in the magnitude as well as orientation with the local electromagnetic field (E_{Loc}) at the molecule. The local field intensity enhancement factor (M_{Loc}) can be estimated by:

$$M_{Loc}(\omega_L) = \frac{|E_{Loc}(\omega_L)|^2}{|E_{Inc}|^2} \qquad 1.25$$

Typically, the gap (***hot spots***) between two metallic objects has the highest local field intensity enhancement. As shown in *Eq.1.24*, the local field intensity enhancement exists at the distances near to the metallic surface, and is associated with a coupling to *LSPR*, Thus, M_{Loc} should be a function of the incident wavelength[64].

The radiation enhancement factor is also dependent on the Raman scattering processes. Thus, the total SERS-EM ***enhancement factor*** (EF) is the accumulated result of these two phenomena, the local field enhancement and radiation enhancement:

$$EF \approx M_{Loc}(\omega_{Loc})M_{Rad}(\omega_{Rad}) \approx |E_{Loc}|^4 \qquad 1.26$$

As could be seen, in SERS the signal is enhanced by a factor proportional to the fourth-power of the electric field enhancement. Thus, since the M_{Loc} arising from the

plasmonic excitation can be very large, the EM is the main dominant mechanism in the enhancement of the Raman signals[62].

The control in making nanoparticles of desired optical properties and the ability to be excited by different wavelengths led to an enhanced sensitivity of the Raman scattering into such an extent that the vibrational features of a single molecule could be captured. Single-molecule SERS (SM-SERS) can be generated in special case, where the analyte sandwiched between nanoscale gaps between adjacent SERS active nanoparticles which are presented in aggregate structure. These gaps are named as ***hot spots*** because the SERS electromagnetic enhancement in these regions are predicted to exceed (10^8) [65]. The formation of the enhanced electric field between particles can be simulated using Finite-difference time-domain (*FDTD*) modelling method. As shown in **Figure 1.13**, if the distances between the particles exceed 10 nm, the enhancement factor in the electric field generated between particles is decreased drastically[63, 66-67]. If hot spots are properly designed, the SERS can be used as a tool to study single molecule phenomena [68-71].

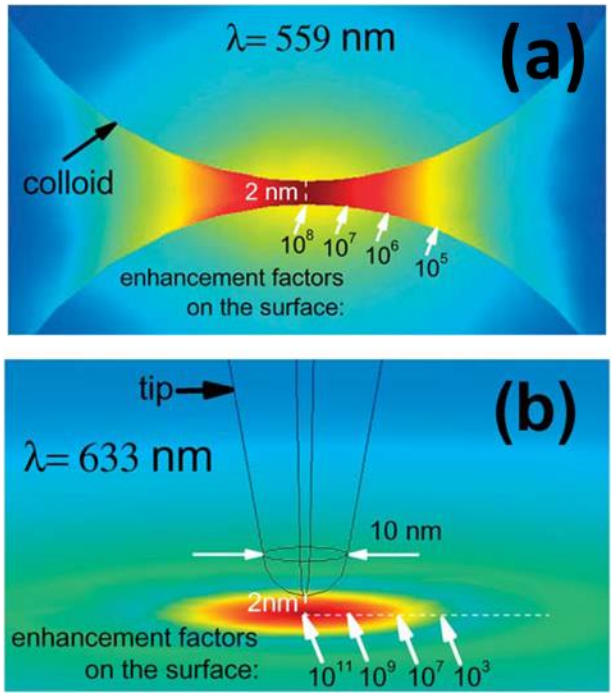

Figure 1.13. Enhancement factor (*EF*) distribution in the region of the gap between **a)** two gold colloids (radii = 30 nm) for polarization along the vertical axis of the dimer; **b)** gold tip on top of a gold surface[63].

Chemical enhancement (CE)

Charge transfer (*CT*) between metallic particles and adsorbed marker molecule can lead to another type of Raman enhancement known as chemical enhancement. In the case of charge transfer, due to *LSPR*, an electron from the metal can inject into the molecule and perturb its potential, hereby inducing a change in the charge cloud of the molecule. When the electron transfers into the metal again, the molecule returns to the ground state. This charge transfer can facilitate the excitation of the Raman scattering of the molecule[72].

Recently, Musumeci et al, have shown strong Raman enhancement of biologically active enediol molecules adsorbed on the surface of TiO_2 NPs. Two different situations were considered to explain SERS here: *CT* from excited semiconductor to molecule and *CT* from the molecule to semiconductor, where the latter reported to have larger enhancement effect. The most important point in this type of charge transfer is the selective of its Raman enhancement in different modes of the molecule as Raman features. It has been shown that based on the distinct binding and orientation of the adsorbed molecules on the semiconductor surface the modes which are appearing in the Raman signal of the molecule can be changed [73-74].

It is known that *EM* enhancement shares major part of the Raman scattering enhancement using SERS materials; however, it has been shown that some of SERS materials have selectivity toward different molecules. This is due to the difference in charge transfer between different molecular structures and the SERS substrate. Also, the marker molecule should bind to the SERS metallic structure in order to make any charge transfer. Thus, the charge transfer mechanism explains the additional enhancement which cannot be explained alone by the *EM* mechanism. As these two phenomena always occur simultaneously, mechanistic study of the SERS is still a practical challenge[75-77]. A recent study by Selvakannan et. al. showed the importance of *CT* mechanism in SERS enhancement[78].

1.4. SERS: difficulties and applications-road to multifunctionality

As discussed in the previous section, if properly designed, SERS is an interesting technique for not only structural analysis of the materials, but also it can be a powerful technique for chemical and biological sensing platforms. Although, there are many reports on the usage of SERS materials for sensing of materials but still there are a number of debates to make it acceptable as an analytical spectroscopy approach. As SERS is highly dependent on the *LSPR* effects of the metallic structures, any factor that changes the *LSPR* properties can change the SERS enhancement factor. Thus, to be accepted as an analytical tool, the

reproducibility of the SERS samples should be addressed. In addition, the formation of hot spots in the SERS samples is highly important as they have the highest enhancement on the Raman intensities of the molecules' signals due to higher *EM* enhancement in the hot spots[77]. To have the same hot spot concentrations and formats, the synthesis, assembly and orientation of the metallic structure should be controlled. There are two different major approaches for controlling the hot spots in a SERS material[76]. First method in context of NPs, is based on the approaches controlling their assembly and distances from each other; while second category regards to surface based SERS where hot spots are controlled via adjusting the topology and roughness of the nanostructured surfaces. First method is mainly based on controlling the materials assembly in solutions via passive methods like adjusting the concentration of the solution or via active method like assembly through magnetic or electrophoresis methods. On the other hand for surface based SERS platforms, the most optimum controllable way of fabrication of SERS hot spots is based on lithography[79], specially electron beam lithography (*EBL*) techniques[65,80]. As these techniques are expensive, time-consuming and can be done only in small areas, there is a high interest to find alternative ways of designing homogenous and well controlled metallic structures. Colloidal lithography showed an alternative method to *EBL*, but still it is a highly expensive method as fabrication of the sacrificing materials as a monolayer in these methods is highly challenging[76, 81]. Using templates with repeated topologies as a base for SERS applications is another approach for controlling SERS hot spots. In this case, highly reproducible nano-arrays of Si, TiO_2, ZnO, etc. have been shown as good substrates for fabricating well defined nanoscale patterns for SERS applications[82-86].

Besides the aforementioned challenges, researchers recently have been focusing on enhancing the sensing application of the SERS materials by merging it with other applications to produce multifunctional materials. As SERS has been shown a powerful technique to detect low concentration of different organic species, using SERS based sensing and combining it with other applications for monitoring of different chemical and/or biological reactions has become a field of interest. Briefly, these areas can be divided into three major categories:

Magnetic/SERS material combination: is one of the fields where the functionality of the magnetic core and SERS sensing comes together for different applications. There are three main reasons for using this type of combination:

- ***Controlling the assembly:*** In this case, magnetic cores are used for controlling the assembly of the Magnetic/SERS core/shell materials. In this way, the distance between the SERS active particles can be controlled. Also, this method shows the ability to control the assembly not only in a powder form, but also the assembly of the magnetic SERS nanoparticles on a surface. In this case the assembled film obtained via magnetic field can be used for other sensing approaches like electrochemical sensing as well as SERS sensing platform which adds the functionality of multimodal sensing platforms[87-90].
- ***Magnetic resonance imaging (MRI):*** It is well known that magnetic nanoparticles can be used as MRI imaging contrast. Using MRI imaging combined with SERS gives the multi functionality in bimodal imaging of the cancer cells[91-94].

Metallic/SERS material combination: For metallic/SERS combination, two major applications have been reported. Briefly, these multifunctionalities can be summarized as:

- ***Multi modal imaging:*** In this method the SERS active metallic material is designed in a way that it could show more functionalities than pure SERS. For example gold nanorods have been shown to have *SPR* excitation near infrared regions of the light spectra. This property gives the ability of infrared imaging besides the SERS sensing for these materials[90, 95-97].
- ***Photothermal ablation:*** Metallic nanoparticles with *SPR* peaks in near-infrared regions in addition to some of the non-metallic structures like graphene oxide[98] have been used for photothermal ablation of bacteria and cancer cells. In this platform, the cancer cells are detected via specially designed marker loaded on SERS particles and after detection, they are killed via photothermal properties of the materials[90, 99].

Semiconductor/SERS material combination: The application for the semiconductor/SERS junctions are mainly reported in two categories:

- ***Chemiluminescence sensing***: This is a new field where the semiconductor substrate is used for electro-generated chemiluminescence (*ECL*), while being decorated with SERS active metals. In this composition, the dual sensing of the organic materials can be achieved, which can help in understanding reaction mechanism of organic molecules and quantitative analysis with the combined methods of SERS, optical spectroscopy and electrochemistry[100].

- ***Recyclable SERS sensors:*** The major application of semiconductor/SERS composites relies on the photocatalytic activities of the semiconductors. As mentioned before making a reliable SERS platform is an expensive and challenging task. As in most of the applications the sensing platform is for a single use only, the SERS method is a highly expensive spectroscopy method. SERS is mainly used for detecting trace organic materials. These organic materials can be in the form of organic molecules like dyes and organic chemicals or in the form of biological species. As in all cases the formed materials are organic they are susceptible to degradation via photocatalytic reactions. There are a numbers of reports where the combination of the photocatalysis and SERS has been successfully used for the fabrication of the recyclable SERS sensors[82-83, 101-108]. The first reports on semiconductor/SERS was related to using sputtered silver decorated ZnO nano arrays to monitor the degradation of the dye on the surface via SERS rather than UV-Vis spectroscopy. The application of self-cleaning effect of semiconductor to be used in combination of recyclable SERS materials started in 2010, through a report on the formation of TiO_2 nanotube arrays composed with chemically decorated Au nanoparticles[101]. Since then, this field has attracted many researchers attention, as they have used this method to fabricate different interesting combinations of semiconductor/SERS platforms such as: single monolayer of semiconducting photocatalytic monolayer with SERS coatings[108], semiconducting/magnetic cores for recycling and separation[87-88], recyclable semiconducting flexible substrates[109] and using decorated SERS nano-arrays with semiconductors[84, 101-103].

1.5. Zinc Oxide

Zinc oxide thin films and nano-arrays are the main semiconductor surfaces used in this thesis. As this material is main part of the thesis, in this section, a brief introduction is provided for the most important properties and application of one dimensional nano-arrays of zinc oxide.

1.5.1. Properties

Zinc oxide (ZnO) is one of the most widely reported direct wide band-gap II-VI materials that has a large exciton-binding energy of 60 meV and wide band-gap energy of 3.37 eV at room temperature in bulk form[110]. The main stable structure of ZnO in room

temperature is wurtzite crystal structure as shown schematically in **Figure 1.14**. Wurtzite belongs to the space group P63mc. This structure in an ideal form possesses two lattice parameters $a = 3.2495$ Å and $c = 5.2069$ Å with a ratio of $c/a = 1.633$. The non-centrosymmetry of the wurtzite crystal structure of ZnO leads to piezoelectricity which arises from atomic scale polarization[111]. When a piezoelectric material is squeezed, twisted or bent, electric charges assemble on its surfaces. This charge can change the characteristics of the band-gaps, especially in junction with other materials, which could be used as a secondary source for modifying the final properties of a device[112-113]. As major defects of the zinc oxide crystals are oxygen vacancies, this semiconductor has n-type characteristics in the non-doped form. There are many reports on fabricating p-type ZnO structures, however, p-type semiconductor ZnO is still an open challenge for the researchers as the modelling and experimental methods do not converge into same conclusion which could enable researchers to provide a global method to fabricate p-type ZnO materials[20, 114-116].

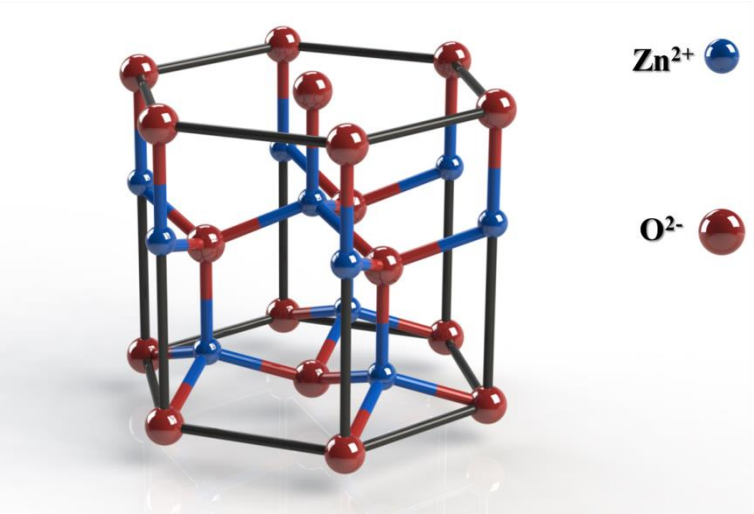

Figure 1.14. Structure of Wurtzite zinc oxide.

One of the special ability of the zinc oxide in nanoscale is the ability of the materials to change its morphology. ZnO is one of the materials showing highest number of various morphologies. Some of these morphologies are shown in **Figure 1.15**. Among these morphologies, zinc oxide nano-arrays have been used widely in many applications. There are many different reasons in the use of this morphology. From structural point of view, this material is a one-dimensional single crystal material, thus providing fewer defects and recombination sites in the structure, which makes it highly applicable for optoelectronic applications. The synthesis process results in high yield and it is highly controllable in

manner of the size, orientation and also coverage of different substrates from silicon wafer up to textiles[117-118].

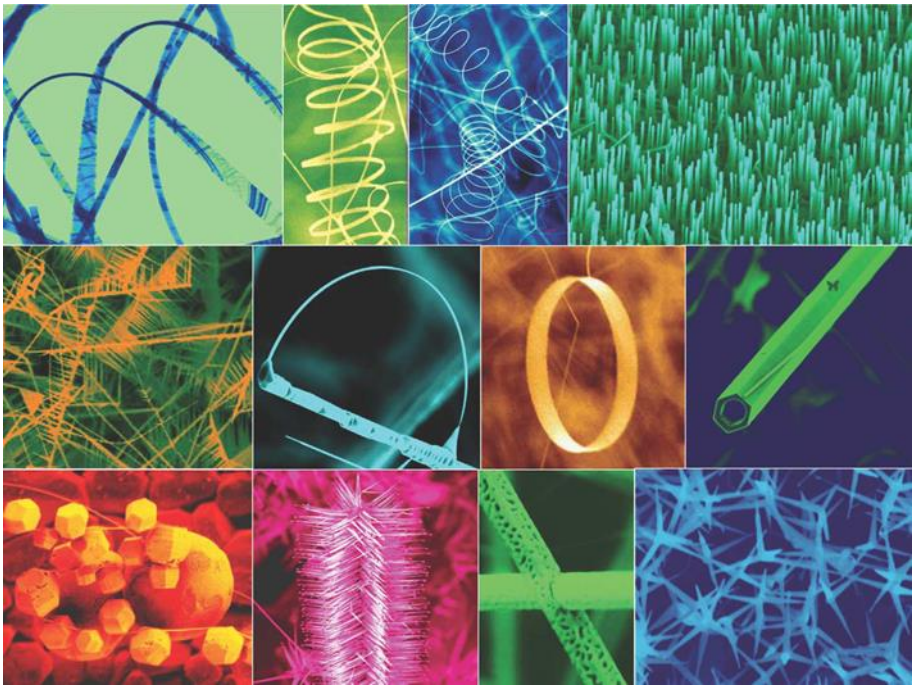

Figure 1.15. A collection of ZnO nanostructures[113].

1.5.2. Synthesis of ZnO nano-arrays

Vapour-Liquid-Solid (VLS) deposition:

This is the first method reported for fabricating ZnO nano arrays in 2001[119-120]. Huang et. al., have reported a simple fabrication process for fabricating well aligned ZnO nano array grown on a sapphire substrate. They reported use of Au thin film as a catalyst for epitaxial single crystal growth of ZnO nano-arrays[121]. They have shown that uniform nano-arrays of ZnO can be formed via controlled ZnO and C evaporation in high temperatures. By adjusting the temperature, synthesis time, Ar gas flow rate and substrate position (temperature of substrate) the ZnO nano arrays can be formed evenly on the substrate. Overall reaction can be summarized as Zn vapour is generated by carbothermal reduction of ZnO and transported to the substrates where ZnO nanowires grow[122]. They have shown that due to the small diameter of the rods, in the electroluminescence and photoluminescence conditions, these materials can generate UV light lasing in their structures[120]. Since then many other researchers have used this method for fabrication of well aligned ZnO nano-arrays[121, 123-124]. For examples, as this method uses Au as catalysis, there some other research that looked for alternative

catalysts like Cu and also tried to fabricate novel structures using the patterned catalytic surfaces[125]. Also, Yuan et. al. has modified this method in order to dope the ZnO nano-arrays which show the ability of this method to control the doping and also the type of the produced semiconductor[126].

Electrochemical deposition:

By electrochemical deposition, ZnO nano-arrays can be produced with high uniformity and in large areas. The technique uses the external electrical driving force for the reaction on an electrode. The electrode could be any type of conductive material with proper crystal structure similarity, like STO, Au or even ZnO itself. The ZnO can be produced only on the cathode of D.C. power source[127].

In this process generally, a three electrodes system of Pt counter electrode, Ag/AgCl as reference and conductive substrate as a cathode is used. The reaction rate is controlled by current in constant voltage[128]. It has been reported that most of the zinc salts can make zinc nano-arrays but the aspect ratio and also the orientation of the arrays would be different. The most reported zinc salt is $ZnCl_2$ as it has been shown that Cl^- can be adsorbed preferentially on the Zn-terminated (0001) planes of ZnO, where, like VLS, the ZnO rods is grown along their c-axis (0001)[129]. Furthermore, this method shows a high ability in doping ZnO nano-arrays. The concentration of the anion and cation can change the morphologies from nano-arrays of nano-rods to nano-arrays of plates[130-131].

Another alternative method in electrochemical growth of aligned ZnO nano-arrays, is the use of sacrificial templating materials. Polycarbonate template is the most used template material where anodic aluminium oxide (AAO) cannot be used as most of the etchants of AAO can etch ZnO as well. The reports showed that this method can produce a high aspect ratio ZnO arrays[132]. Although his method can produce nano-arrays but the application of this method is limited, as the materials produced with templating techniques are either amorphous or polycrystalline consisting of small domains with an abundance of defects[118, 133].

Low temperature hydrothermal deposition:

This method is one of the most common methods in fabricating well-aligned ZnO nano-arrays[118, 134-139]. In this method, ZnO nano-arrays are hydrothermally generated from $Zn(NO_3)_2$ as Zn source and hexamethylenetetramine (HMTA) as oxidizer in water[140]. One of the main advantages of this method is that the ZnO nano-arrays with high alignment can be

produced on arbitrary substrates, such as Si wafer, paper, organic substrates, etc. This method needs a seed layer that can be produced via different methods such as sputtering of ZnO thin films[138], ZnO nanoparticles, ZnO sol-gel derived thin films, etc[139]. The aspect ratio of the ZnO materials can exceed over 100 where the alignment of the ZnO nano-arrays is highly depended to the seeding layer and can be adjusted by controlling of the crystallinity the seed layer[118]. The synthesis method and related chemical background of this method is explained in detail in *Chapter 4, Section 4.3*.

1.5.3. Optical applications

Due to its wide band-gap and large binding energy of 60 meV at room temperature, ZnO is considered as a potential candidate for UV emitting devices. Large-scale capability of fabrication of ZnO nano-arrays and single crystalline nature of the produced nano-arrays makes this material as an exciting candidate for optoelectronics applications. Four main optical applications reported in the literatures are photoluminescence, UV-lasing pumps, light emitting diode (LED) and photocatalysis.

- *Photoluminescence (PL):* The UV excited PL characteristic of ZnO nano-arrays usually shows two major emission bands at room temperature[141]. First peak appearing in UV region regards to its near-band edge representative of its band-gap[141]. The visible peak regards to its intrinsic and surface point defects like oxygen vacancies, which make deep level transitions inside the band-gap of ZnO[142]. These defects are usually generated during the synthesis procedure and cannot be eliminated completely. In photoluminescence applications, these two emission bands have been used to enhance the photoluminescence intensity of other materials as a composite[143].
- *Lasing pump:* There are three major reasons, which make ZnO nano-arrays as interesting candidates for room temperature lasing. First, ZnO has a wide band-gap and large binding energy, which is larger than room temperature thermal energy. So the excitation is independent of the ambient temperature and thus emission is stable. Moreover, the perpendicular top and bottom of the nanorods in the array act as a mirror (Fabry-Perot cavities). Finally as the reflective index of the ZnO is 2.45, the emitted light can be laterally confined inside of the nanorods and in this case nanorods act as a waveguide[120, 144].
- *Light emitting diodes:* In this case, a p-n junction has been fabricated between ZnO nano-arrays and p-type semiconducting material. The p-type materials can be

homojunction[145], inorganic, organic or hybrid in the nature. As the ZnO is in the form of single crystal nanorods, the non-radiative recombination sites inside of the ZnO nano-arrays are confined, and the radiative recombination mostly happens in the p-n junction regions where it increases the efficiency of the produced LED devices. The concentration of non-radiative recombination sites is highly depended on the crystallinity of the ZnO nano-arrays which are arisen from its synthesis conditions[146-148].

- *Photocatalytic applications:* Due to high surface area and the ability to grow on different substrates, ZnO nano-arrays have attracted attentions of many researchers for photocatalytic uses. This material, due to its wide band-gap, is competitive to the commercially available UV photocatalysts like TiO_2[149]. Zhou et .al. showed that the size of the arrays has a critical effect on the activity of the nano-arrays of ZnO photocatalysts[150]. They showed that if the diameter of the rods became smaller than a critical value, the redox potentials will increase, and therefore, the photo-generated electrons and holes will have higher photocatalytic efficiency. Additionally, as the facets of the ZnO have different dangling bond configurations, the photocatalytic properties are unlike on different facets of the nano-arrays. Studies indicated that the polar faces have higher photocatalytic activities than non-polar surfaces[151].

1.6. Research motivation

The work presented in this thesis focuses on fine-tuning the morphology of ZnO semiconductors and preparing functional materials such as ZnO-metal and ZnO-organic semiconductor hybrids. Applications of these materials in photocatalytic degradation of environmental pollutants and sensing of ecotoxic chemical species are the major focus of the thesis.

Most of the spectroscopic and other analytical sensing technologies get frequently interfered from the instrumental noise and background in the spectra. Especially scattering based technique such as SERS, where the Raman scattering signal component often has significant contribution from the background and noise, therefore, need a proper removal of these unfavourable components from the signals. As the sensing technique in this thesis was based on SERS method, in this research, a new methodology has been introduced to answer the needs for more reliable background correction for ultrahigh sensitive nanosensing applications.

Photocatalytic activities of zinc oxide nano-arrays and ability of integrating this property with the other useful applications like biological and chemical sensing can bring a variety of novel applications. The controllable synthesis of this material with desired physical parameters, different substrates and also their ability to form heterojunction with the highest controllability are some of the advantages of using these nanostructures for various applications. These arrays have shown a good reproducibility and morphological control during synthesis procedure, which makes them interesting materials to be used as SERS based sensing substrates in order to obtain higher reproducibility and sensitivity. Also, as zinc oxide is a photocatalyst, using this material can give broader functionality to the sensing platform. Not only it can make the sensor regenerable, but also, it can be used for removing the heavy metal ions from the water. The combination of ZnO/Ag nano-arrays can make dual sensing ability of biological sensing and selective Hg^{2+} sensing abilities.

Organic semiconductors have attracted many researchers' attentions as they are easy to control based on their band-gap and thus opening new applications where the inorganic semiconductors fail to operate. In addition, the heterojunction formation between organic and inorganic semiconductors can bring more possibilities and opportunities for developing new optoelectronics devices. In this regards, decorating silver nanostructures on the surface of an inorganic semiconductor can bring other functionalities to n-type ZnO nanostructures as Ag can be easily changed to metal-organic semiconductor molecule of AgTCNQ. The method for fabricating reproducible and simple approach to syntheses of inorganic-organic hybrids of AgTCNQ-ZnO (p-n heterojunction) was another aim of this research. In this thesis, this heterojunction has been synthesized and studied for increasing the activities of ZnO photocatalyst, where proposed method can be extended for synthesis of other controlled heterojunctions.

1.7. Thesis Outline

The work presented in this thesis can be divided into three major sections: (i) designing a novel background correction algorithm to analyse the Raman data collected from SERS samples; (ii) Synthesis of ZnO/Ag nano-arrays with high Raman signal enhancement and photocatalytic activities and finally (iii) improving photocatalytic activities of n-type ZnO thin films via using controlled decoration of p-type AgTCNQ nano-arrays.

The chapter breakdown of the thesis is as follows:

In **Chapter II** a short survey of techniques used in this research for the characterization of the materials is provided. The characterization methods used in this thesis include: Scanning Electron Microscopy (SEM), Atomic Force Microscopy (AFM), UV-visible spectrometry (UV-vis), Raman Spectroscopy (Raman), X-Ray Diffraction (XRD), Energy Dispersive X-ray (EDX) spectroscopy, X-ray Photoelectron Spectroscopy (XPS) and Inductively coupled plasma mass spectrometry (ICPMS).

In **Chapter III**, the process for designing a new smoothing-free method for background correction is shown, which has been developed by merging continuous wavelet transform and signal removal methods, which in combination, could be applied to noisy signals without smoothing. Wavelet transformation has been used for suppressing the side effects of noise and extracting derivative of the studied spectra, while signal removal method has been applied for eliminating peaks of signals from the spectrum, thereby providing spectral sections purely related to the background to be used in the background correction process. A range of statistical analyses were applied to test the performance of this algorithm, wherein a low deviation in background correction procedure was observed. Additionally, when this algorithm was used for experimentally obtained Raman spectra, it showed good capability in background correction of noisy signals without the requirement of a smoothing process. This algorithm was used as a basic method for surface enhanced spectroscopy data analysis presented in **Chapters IV** and **V** of this thesis.

In **Chapter IV**, the effect of synthetic parameters on the formation of ZnO nano-arrays was studied thoroughly. After finding proper synthetic condition for synthesizing well controlled and reproducible ZnO nano-arrays, different approaches were carried out for decorating the obtained ZnO nano-arrays with silver nanoparticles. This study employed facile soft chemical synthesis strategies to fabricate Raman-active and recyclable ZnO/Ag nanorod arrays as highly reproducible surface enhanced Raman scattering (SERS) substrates. Arrays of ZnO nanorods on silicon wafer were synthesized using hydrothermal method, which was followed by controllable decoration of ZnO nano-arrays with silver nanoparticles (AgNPs). By controlling the AgNPs deposition parameters, the uniform density of SERS-active hot-spots on ZnO nano-arrays could be controlled on a large 1 cm × 1 cm substrate. These ZnO/Ag nano-arrays showed outstanding reproducibility towards acquiring SERS spectra of Rhodamine-B as a probe molecule at 30 random locations on a single substrate. The photocatalytic nature of ZnO/Ag semiconductor-metal heterojunction was exploited to endow these SERS substrates with reusability characteristics. The study shows that by

controlling optimal metal loading on a semiconductor surface, high photocatalytic activity and SERS performance can be integrated within a single package to obtain high quality, reproducible, stable and recyclable SERS substrates.

Mercury being one of the most toxic heavy metals has long been a focus of concern due to its gravest threats to human health and environment. Although multiple methods have been developed to detect and/or remove dissolved mercury, many require complicated procedures and sophisticated equipment. In **Chapter V**, a simple surface enhanced Raman spectroscopy (SERS) active ZnO/Ag nano-arrays is described, which can detect Hg^{2+}, remove Hg^{2+} and can be fully regenerated, not just from Hg^{2+} contamination when heat-treated, but also from the SERS marker when exposed to UV as a result of the self-cleaning ability of this heterojunction photocatalyst. The sensors are as well highly selective because of the unique way mercury (among other chemicals) interacts with Ag nanoparticles, thus reducing its SERS activity.

Controlling the position of a junction and also the population of the junction can alter the activities of the heterojunction semiconductor devices. In **Chapter VI**, organic-inorganic heterojunction combinations of ZnO-AgTCNQ were synthesized to form a p-n heterojunction system. With use of colloidal lithography the position of the AgTCNQ nano-wires on the zinc oxide thin films were completely controlled. AgTCNQ nano-arrays were grown using the chemical vapour deposition (CVD) technique on the designed silver nano-spots. The temperature effect on the growth of AgTCNQ nano-arrays on ZnO thin films was studied thoroughly, and the synthesized heterojunction nano-arrays were studied for their photocatalytic activities.

Chapter VII provides a summary of the research completed during this PhD candidature and provides a scope for future possible research in the areas studied.

References

1. Andreozzi, R.; Marotta, R., *Water Res.* **2004,** *38* (5), 1225-1236.
2. Kudo, A.; Miseki, Y., *Chem. Soc. Rev.* **2009,** *38* (1), 253-278.
3. Litter, M. I., *Applied Catalysis B: Environmental* **1999,** *23* (2–3), 89-114.
4. Nakata, K.; Fujishima, A., *Journal of Photochemistry and Photobiology C: Photochemistry Reviews* **2012,** *13* (3), 169-189.
5. Fujishima, A.; Zhang, X.; Tryk, D. A., *Surf. Sci. Rep.* **2008,** *63* (12), 515-582.

6. Fujishima, A.; Rao, T. N.; Tryk, D. A., *Journal of Photochemistry and Photobiology C: Photochemistry Reviews* **2000,** *1* (1), 1-21.
7. Zheng, Y.; Chen, C.; Zhan, Y.; Lin, X.; Zheng, Q.; Wei, K.; Zhu, J.; Zhu, Y., *Inorg. Chem.* **2007,** *46* (16), 6675-6682.
8. Li, D.; Haneda, H., *Journal of Photochemistry and Photobiology A: Chemistry* **2003,** *155* (1–3), 171-178.
9. Esmaielzadeh Kandjani, A.; Farzalipour Tabriz, M.; Arefian, N. A.; Vaezi, M. R.; Halek, F.; Sadrnezhaad, S. K., *Water Sci. Technol.* **2010,** *62* (6), 1256-1264.
10. Sclafani, A.; Palmisano, L.; Marcí, G.; Venezia, A. M., *Sol. Energy Mater. Sol. Cells* **1998,** *51* (2), 203-219.
11. Ahmad, S., Organic semiconductors for device applications: current trends and future prospects. In *J. Polym. Eng.*, **2014**; Vol. 34, p 279.
12. Myers, J. D.; Xue, J., *Polymer Reviews* **2012,** *52* (1), 1-37.
13. Rockett, A., *The Physics of Solids*. Springer US: **2008**.
14. Grundmann, M., *Introduction*. Springer Berlin Heidelberg: **2010**.
15. Yu, P.; Cardona, M., *Introduction*. Springer Berlin Heidelberg: **2010**.
16. Hamaguchi, C., *Energy Band Structures of Semiconductors*. Springer Berlin Heidelberg: **2010**.
17. Mishra, U.; Singh, J., *Structural Properties of Semiconductors*. Springer Netherlands: **2008**.
18. Meng, L. r.; Mo, R.; Zhou, H.; Wang, G.; Chen, W.; Wang, D.; Peng, Q., *Crystal Growth & Design* **2010,** *10* (8), 3387-3390.
19. Ng, C. H. B.; Fan, W. Y., *The Journal of Physical Chemistry C* **2007,** *111* (26), 9166-9171.
20. Özgür, Ü.; Alivov, Y. I.; Liu, C.; Teke, A.; Reshchikov, M. A.; Doğan, S.; Avrutin, V.; Cho, S.-J.; Morkoç, H., *J. Appl. Phys.* **2005,** *98* (4), -.
21. Ozgur, U.; Hofstetter, D.; Morkoc, H., *Proceedings of the IEEE* **2010,** *98* (7), 1255-1268.
22. Potje-Kamloth, K., *Chem. Rev.* **2008,** *108* (2), 367-399.
23. Wang, Y.; Wang, Q.; Zhan, X.; Wang, F.; Safdar, M.; He, J., *Nanoscale* **2013,** *5* (18), 8326-8339.
24. Xiwei, Z.; Xiujuan, Z.; Liu, W.; Yiming, W.; Yan, W.; Peng, G.; Yuanyuan, H.; Jiansheng, J., *Nanotechnology* **2013,** *24* (39), 395201.
25. Ângelo, J.; Andrade, L.; Madeira, L. M.; Mendes, A., *Journal of Environmental Management* **2013,** *129* (0), 522-539.

26. Ohtani, B., *Journal of Photochemistry and Photobiology C: Photochemistry Reviews* **2010,** *11* (4), 157-178.
27. van de Krol, R.; Goossens, A.; Schoonman, J., *J. Electrochem. Soc.* **1997,** *144* (5), 1723-1727.
28. Calow, J. T.; Deasley, P. J.; Owen, S. J. T.; Webb, P. W., *Journal of Materials Science* **1967,** *2* (1), 88-96.
29. Ikeda, S.; Sugiyama, N.; Pal, B.; Marci, G.; Palmisano, L.; Noguchi, H.; Uosaki, K.; Ohtani, B., *Phys. Chem. Chem. Phys.* **2001,** *3* (2), 267-273.
30. Subramanian, V.; Wolf, E. E.; Kamat, P. V., *JACS* **2004,** *126* (15), 4943-4950.
31. Ansari, S. A.; Khan, M. M.; Ansari, M. O.; Lee, J.; Cho, M. H., *RSC Advances* **2014**.
32. Wang, X.; Kong, X.; Yu, Y.; Zhang, H., *The Journal of Physical Chemistry C* **2007,** *111* (10), 3836-3841.
33. Zheng, Y.; Zheng, L.; Zhan, Y.; Lin, X.; Zheng, Q.; Wei, K., *Inorg. Chem.* **2007,** *46* (17), 6980-6986.
34. Zheng, Y.; Chen, C.; Zhan, Y.; Lin, X.; Zheng, Q.; Wei, K.; Zhu, J., *The Journal of Physical Chemistry C* **2008,** *112* (29), 10773-10777.
35. Zhou, P.; Yu, J.; Jaroniec, M., *Adv. Mater.* **2014,** *26* (29), 4920-4935.
36. Wang, H.; Zhang, L.; Chen, Z.; Hu, J.; Li, S.; Wang, Z.; Liu, J.; Wang, X., *Chem. Soc. Rev.* **2014,** *43* (15), 5234-5244.
37. Maeda, K.; Domen, K., *Chem. Mater.* **2009,** *22* (3), 612-623.
38. Kundu, P.; Deshpande, P. A.; Madras, G.; Ravishankar, N., *J. Mater. Chem.* **2011,** *21* (12), 4209-4216.
39. Tak, Y.; Kim, H.; Lee, D.; Yong, K., *Chem. Commun.* **2008,** (38), 4585-4587.
40. Lingampalli, S. R.; Gautam, U. K.; Rao, C. N. R., *Energy & Environmental Science* **2013,** *6* (12), 3589-3594.
41. Hensel, J.; Wang, G.; Li, Y.; Zhang, J. Z., *Nano Lett.* **2010,** *10* (2), 478-483.
42. Yang, L.; Luo, S.; Liu, R.; Cai, Q.; Xiao, Y.; Liu, S.; Su, F.; Wen, L., *The Journal of Physical Chemistry C* **2010,** *114* (11), 4783-4789.
43. Lo, S.-C.; Lin, C.-F.; Wu, C.-H.; Hsieh, P.-H., *J. Hazard. Mater.* **2004,** *114* (1–3), 183-190.
44. Zhang, Z.; Shao, C.; Li, X.; Wang, C.; Zhang, M.; Liu, Y., *ACS Applied Materials & Interfaces* **2010,** *2* (10), 2915-2923.
45. Jung, S.; Yong, K., *Chem. Commun.* **2011,** *47* (9), 2643-2645.

46. Liang, N.; Wang, M.; Jin, L.; Huang, S.; Chen, W.; Xu, M.; He, Q.; Zai, J.; Fang, N.; Qian, X., *ACS Applied Materials & Interfaces* **2014,** *6* (14), 11698-11705.
47. Nafady, A.; O'Mullane, A. P.; Bond, A. M., *Coord. Chem. Rev.* **2014,** *268*, 101-142.
48. Pearson, A.; O'Mullane, A. P.; Bansal, V.; Bhargava, S. K., *Inorg. Chem.* **2011,** *50* (5), 1705-1712.
49. Lu, X.; Rycenga, M.; Skrabalak, S. E.; Wiley, B.; Xia, Y., *Annu. Rev. Phys. Chem.* **2009,** *60* (1), 167-192.
50. Kelly, K. L.; Coronado, E.; Zhao, L. L.; Schatz, G. C., *The Journal of Physical Chemistry B* **2002,** *107* (3), 668-677.
51. Murphy, C. J.; Sau, T. K.; Gole, A. M.; Orendorff, C. J.; Gao, J.; Gou, L.; Hunyadi, S. E.; Li, T., *The Journal of Physical Chemistry B* **2005,** *109* (29), 13857-13870.
52. Sun, Y.; An, C., *Frontiers of Materials Science* **2011,** *5* (1), 1-24.
53. Wiley, B.; Sun, Y.; Mayers, B.; Xia, Y., *Chemistry – A European Journal* **2005,** *11* (2), 454-463.
54. Maier, S. A.; Brongersma, M. L.; Kik, P. G.; Meltzer, S.; Requicha, A. A. G.; Atwater, H. A., *Adv. Mater.* **2001,** *13* (19), 1501-1505.
55. Moores, A.; Goettmann, F., *New J. Chem.* **2006,** *30* (8), 1121-1132.
56. Halperin, W. P., *Reviews of Modern Physics* **1986,** *58* (3), 533-606.
57. Ghosh, S. K.; Pal, T., *Chem. Rev.* **2007,** *107* (11), 4797-4862.
58. Raman, C. V.; Krishnan, K. S., *Nature* **1928,** *121* (3048), 501-502.
59. Wang, Y.; Yan, B.; Chen, L., *Chem. Rev.* **2012,** *113* (3), 1391-1428.
60. Agrawal, G. K.; Timperio, A. M.; Zolla, L.; Bansal, V.; Shukla, R.; Rakwal, R., *Journal of Proteomics* **2013,** *93* (0), 74-92.
61. Schwartzberg, A. M.; Zhang, J. Z., *The Journal of Physical Chemistry C* **2008,** *112* (28), 10323-10337.
62. Jensen, L.; Aikens, C. M.; Schatz, G. C., *Chem. Soc. Rev.* **2008,** *37* (5), 1061-1073.
63. Etchegoin, P. G.; Le Ru, E. C., *Phys. Chem. Chem. Phys.* **2008,** *10* (40), 6079-6089.
64. Kleinman, S. L.; Frontiera, R. R.; Henry, A.-I.; Dieringer, J. A.; Van Duyne, R. P., *Phys. Chem. Chem. Phys.* **2013,** *15* (1), 21-36.
65. Banaee, M. G.; Crozier, K. B., *ACS Nano* **2010,** *5* (1), 307-314.
66. Wei, H.; Xu, H., *Nanoscale* **2013,** *5* (22), 10794-10805.
67. Stoerzinger, K. A.; Lin, J. Y.; Odom, T. W., *Chemical Science* **2011,** *2* (8), 1435-1439.
68. Le Ru, E. C.; Etchegoin, P. G., *Annu. Rev. Phys. Chem.* **2012,** *63* (1), 65-87.
69. Willets, K. A., *ChemPhysChem* **2013,** *14* (14), 3186-3195.

70. Wang, Y.; Irudayaraj, J., *Philosophical Transactions of the Royal Society B: Biological Sciences* **2013,** *368* (1611).
71. Lee, H. M.; Jin, S. M.; Kim, H. M.; Suh, Y. D., *Phys. Chem. Chem. Phys.* **2013,** *15* (15), 5276-5287.
72. Guerrini, L.; Graham, D., *Chem. Soc. Rev.* **2012,** *41* (21), 7085-7107.
73. Musumeci, A.; Gosztola, D.; Schiller, T.; Dimitrijevic, N. M.; Mujica, V.; Martin, D.; Rajh, T., *JACS* **2009,** *131* (17), 6040-6041.
74. Wang, X.; Shi, W.; She, G.; Mu, L., *Phys. Chem. Chem. Phys.* **2012,** *14* (17), 5891-5901.
75. Campion, A.; Kambhampati, P., *Chem. Soc. Rev.* **1998,** *27* (4), 241-250.
76. Banholzer, M. J.; Millstone, J. E.; Qin, L.; Mirkin, C. A., *Chem. Soc. Rev.* **2008,** *37* (5), 885-897.
77. Lin, X.-M.; Cui, Y.; Xu, Y.-H.; Ren, B.; Tian, Z.-Q., *Analytical and Bioanalytical Chemistry* **2009,** *394* (7), 1729-1745.
78. Selvakannan, P. R.; Ramanathan, R.; Plowman, B. J.; Sabri, Y. M.; Daima, H. K.; O'Mullane, A. P.; Bansal, V.; Bhargava, S. K., *Phys. Chem. Chem. Phys.* **2013,** *15* (31), 12920-12929.
79. Bhuvana, T.; Kulkarni, G. U., *Small* **2008,** *4* (5), 670-676.
80. Chirumamilla, M.; Toma, A.; Gopalakrishnan, A.; Das, G.; Zaccaria, R. P.; Krahne, R.; Rondanina, E.; Leoncini, M.; Liberale, C.; De Angelis, F.; Di Fabrizio, E., *Adv. Mater.* **2014,** *26* (15), 2353-2358.
81. Yang, S.; Hricko, P. J.; Huang, P.-H.; Li, S.; Zhao, Y.; Xie, Y.; Guo, F.; Wang, L.; Huang, T. J., *Journal of Materials Chemistry C* **2014,** *2* (3), 542-547.
82. Zhou, Y.; Chen, J.; Zhang, L.; Yang, L., *Eur. J. Inorg. Chem.* **2012,** *2012* (19), 3176-3182.
83. He, X.; Wang, H.; Zhang, Q.; Li, Z.; Wang, X., *Eur. J. Inorg. Chem.* **2014**, n/a-n/a.
84. Tan, E.-Z.; Yin, P.-G.; You, T.-t.; Wang, H.; Guo, L., *ACS Applied Materials & Interfaces* **2012,** *4* (7), 3432-3437.
85. Zhang, B.; Wang, H.; Lu, L.; Ai, K.; Zhang, G.; Cheng, X., *Adv. Funct. Mater.* **2008,** *18* (16), 2348-2355.
86. Tang, H.; Meng, G.; Huang, Q.; Zhang, Z.; Huang, Z.; Zhu, C., *Adv. Funct. Mater.* **2012,** *22* (1), 218-224.
87. Zhang, X.; Zhu, Y.; Yang, X.; Zhou, Y.; Yao, Y.; Li, C., *Nanoscale* **2014,** *6* (11), 5971-5979.
88. Cai, W.; Tang, X.; Sun, B.; Yang, L., *Nanoscale* **2014,** *6* (14), 7954-7958.

89. Ding, Q.; Ma, Y.; Ye, Y.; Yang, L.; Liu, J., *Journal of Raman Spectroscopy* **2013,** *44* (7), 987-993.
90. Song, J.; Zhou, J.; Duan, H., *JACS* **2012,** *134* (32), 13458-13469.
91. Lou, L.; Yu, K.; Zhang, Z.; Huang, R.; Zhu, J.; Wang, Y.; Zhu, Z., *Nano Research* **2012,** *5* (4), 272-282.
92. Shen, J.; Zhu, Y.; Yang, X.; Zong, J.; Li, C., *Langmuir* **2012,** *29* (2), 690-695.
93. Zhang, L.; Xu, J.; Mi, L.; Gong, H.; Jiang, S.; Yu, Q., *Biosens. Bioelectron.* **2012,** *31* (1), 130-136.
94. Amendola, V.; Scaramuzza, S.; Litti, L.; Meneghetti, M.; Zuccolotto, G.; Rosato, A.; Nicolato, E.; Marzola, P.; Fracasso, G.; Anselmi, C.; Pinto, M.; Colombatti, M., *Small* **2014,** *10* (12), 2476-2486.
95. Zong, S.; Wang, Z.; Yang, J.; Wang, C.; Xu, S.; Cui, Y., *Talanta* **2012,** *97* (0), 368-375.
96. Jiang, L.; Qian, J.; Cai, F.; He, S., *Analytical and Bioanalytical Chemistry* **2011,** *400* (9), 2793-2800.
97. Wang, Y.; Chen, L.; Liu, P., *Chemistry – A European Journal* **2012,** *18* (19), 5935-5943.
98. Lin, D.; Qin, T.; Wang, Y.; Sun, X.; Chen, L., *ACS Applied Materials & Interfaces* **2013,** *6* (2), 1320-1329.
99. Lu, W.; Singh, A. K.; Khan, S. A.; Senapati, D.; Yu, H.; Ray, P. C., *JACS* **2010,** *132* (51), 18103-18114.
100. Xu, C.; Geng, H.; Bennett, R.; Clayton, D. A.; Pan, S., *The Journal of Physical Chemistry C* **2012,** *117* (4), 1849-1856.
101. Li, X.; Chen, G.; Yang, L.; Jin, Z.; Liu, J., *Adv. Funct. Mater.* **2010,** *20* (17), 2815-2824.
102. Tao, Q.; Li, S.; Zhang, Q. Y.; Kang, D. W.; Yang, J. S.; Qiu, W. W.; Liu, K., *Mater. Res. Bull.* **2014,** *54* (0), 6-12.
103. Chen, J.; Su, H.; You, X.; Gao, J.; Lau, W. M.; Zhang, D., *Mater. Res. Bull.* **2014,** *49* (0), 560-565.
104. Ding, Q.; Zhang, L.; Yang, L., *Mater. Res. Bull.* **2014,** *53* (0), 205-210.
105. Zou, X.; Silva, R.; Huang, X.; Al-Sharab, J. F.; Asefa, T., *Chem. Commun.* **2013,** *49* (4), 382-384.
106. Yibing, X.; Yanyan, J.; Yingzhi, Z.; Yong, W., *Appl. Surf. Sci.*, **2014**, 313, 549-557.
107. Xu, S. C.; Zhang, Y. X.; Luo, Y. Y.; Wang, S.; Ding, H. L.; Xu, J. M.; Li, G. H., *Analyst* **2013,** *138* (16), 4519-4525.

108. Li, X.; Hu, H.; Li, D.; Shen, Z.; Xiong, Q.; Li, S.; Fan, H. J., *ACS Applied Materials & Interfaces* **2012,** *4* (4), 2180-2185.
109. Li, S.-K.; Yan, Y.-X.; Wang, J.-L.; Yu, S.-H., *Nanoscale* **2013,** *5* (24), 12616-12623.
110. Kołodziejczak-Radzimska, A.; Jesionowski, T., *Materials* **2014,** *7* (4), 2833-2881.
111. Anderson, J.; Chris, G. V. d. W., *Rep. Prog. Phys.* **2009,** *72* (12), 126501.
112. Qin, Y.; Wang, X.; Wang, Z. L., *Nature* **2008,** *451* (7180), 809-813.
113. Wang, Z. L., *Mater. Today* **2004,** *7* (6), 26-33.
114. Chavillon, B.; Cario, L.; Renaud, A.; Tessier, F.; Cheviré, F.; Boujtita, M.; Pellegrin, Y.; Blart, E.; Smeigh, A.; Hammarström, L.; Odobel, F.; Jobic, S., *JACS* **2011,** *134* (1), 464-470.
115. Herring, N. P.; Panchakarla, L. S.; El-Shall, M. S., *Langmuir* **2014,** *30* (8), 2230-2240.
116. Pearton, S. J.; Norton, D. P.; Ip, K.; Heo, Y. W.; Steiner, T., *Prog. Mater Sci.* **2005,** *50* (3), 293-340.
117. Udom, I.; Ram, M. K.; Stefanakos, E. K.; Hepp, A. F.; Goswami, D. Y., *Mater. Sci. Semicond. Process.* **2013,** *16* (6), 2070-2083.
118. Xu, S.; Wang, Z., *Nano Research* **2011,** *4* (11), 1013-1098.
119. Huang, M. H.; Wu, Y.; Feick, H.; Tran, N.; Weber, E.; Yang, P., *Adv. Mater.* **2001,** *13* (2), 113-116.
120. Huang, M. H.; Mao, S.; Feick, H.; Yan, H.; Wu, Y.; Kind, H.; Weber, E.; Russo, R.; Yang, P., *Science* **2001,** *292* (5523), 1897-1899.
121. Kong, Y. C.; Yu, D. P.; Zhang, B.; Fang, W.; Feng, S. Q., *Appl. Phys. Lett.* **2001,** *78* (4), 407-409.
122. Podzemsky, J.; Schade, W. In *Vapor-liquid-solid growth of ZnO nanostructure*, Electronics Technology, 2009. ISSE 2009. 32nd International Spring Seminar on, 13-17 May 2009; **2009**; pp 1-4.
123. WangWang; Summers, C. J.; Wang, Z. L., *Nano Lett.* **2004,** *4* (3), 423-426.
124. Geng, C.; Jiang, Y.; Yao, Y.; Meng, X.; Zapien, J. A.; Lee, C. S.; Lifshitz, Y.; Lee, S. T., *Adv. Funct. Mater.* **2004,** *14* (6), 589-594.
125. Li, S. Y.; Lee, C. Y.; Tseng, T. Y., *J. Cryst. Growth* **2003,** *247* (3–4), 357-362.
126. Yuan, G. D.; Zhang, W. J.; Jie, J. S.; Fan, X.; Zapien, J. A.; Leung, Y. H.; Luo, L. B.; Wang, P. F.; Lee, C. S.; Lee, S. T., *Nano Lett.* **2008,** *8* (8), 2591-2597.
127. Skompska, M.; Zarębska, K., *Electrochim. Acta* **2014,** *127* (0), 467-488.
128. Elias, J.; Tena-Zaera, R.; Lévy-Clément, C., *J. Electroanal. Chem.* **2008,** *621* (2), 171-177.

129. Tena-Zaera, R.; Elias, J.; Wang, G.; Lévy-Clément, C., *The Journal of Physical Chemistry C* **2007,** *111* (45), 16706-16711.
130. Tena-Zaera, R.; Elias, J.; Lévy-Clément, C.; Bekeny, C.; Voss, T.; Mora-Seró, I.; Bisquert, J., *The Journal of Physical Chemistry C* **2008,** *112* (42), 16318-16323.
131. Elias, J.; Tena-Zaera, R.; Lévy-Clément, C., *The Journal of Physical Chemistry C* **2008,** *112* (15), 5736-5741.
132. Zhou, H.; Wong, S. S., *ACS Nano* **2008,** *2* (5), 944-958.
133. Li, Y.; Yang, X.-Y.; Feng, Y.; Yuan, Z.-Y.; Su, B.-L., *Crit. Rev. Solid State Mater. Sci.* **2012,** *37* (1), 1-74.
134. Xu, S.; Adiga, N.; Ba, S.; Dasgupta, T.; Wu, C. F. J.; Wang, Z. L., *ACS Nano* **2009,** *3* (7), 1803-1812.
135. Teng, M.; Min, G.; Mei, Z.; Yanjun, Z.; Xidong, W., *Nanotechnology* **2007,** *18* (3), 035605.
136. Li-An, M.; Tai-Liang, G. In *Hydrothermal growth and field emission properties of ZnO nanotube arrays*, Nanotechnology Materials and Devices Conference (NMDC), 2010 IEEE, 12-15 Oct. 2010; **2010**; pp 380-382.
137. Sunandan, B.; Joydeep, D., *Science and Technology of Advanced Materials* **2009,** *10* (1), 013001.
138. Liu, S.-Y.; Chen, T.; Wan, J.; Ru, G.-P.; Li, B.-Z.; Qu, X.-P., *Appl. Phys. A* **2009,** *94* (4), 775-780.
139. Baruah, S.; Dutta, J., *J. Sol-Gel Sci. Technol.* **2009,** *50* (3), 456-464.
140. Vayssieres, L., *Adv. Mater.* **2003,** *15* (5), 464-466.
141. Lyu, S. C.; Zhang, Y.; Ruh, H.; Lee, H.-J.; Shim, H.-W.; Suh, E.-K.; Lee, C. J., *Chem. Phys. Lett.* **2002,** *363* (1–2), 134-138.
142. Tam, K. H.; Cheung, C. K.; Leung, Y. H.; Djurišić, A. B.; Ling, C. C.; Beling, C. D.; Fung, S.; Kwok, W. M.; Chan, W. K.; Phillips, D. L.; Ding, L.; Ge, W. K., *The Journal of Physical Chemistry B* **2006,** *110* (42), 20865-20871.
143. Zhou, H.; Chen, X.; Wu, G.; Gao, F.; Qin, N.; Bao, D., *JACS* **2010,** *132* (6), 1790-1791.
144. Pauporte, T.; Lincot, D.; Viana, B.; Pelle, F., *Appl. Phys. Lett.* **2006,** *89* (23), 233112-233112-3.
145. Look, D. C.; Claflin, B.; Alivov, Y. I.; Park, S. J., *physica status solidi (a)* **2004,** *201* (10), 2203-2212.
146. ul Hasan, K.; Sandberg, M. O.; Nur, O.; Willander, M., *Advanced Optical Materials* **2014,** *2* (4), 326-330.

147. Xu, S.; Xu, C.; Liu, Y.; Hu, Y.; Yang, R.; Yang, Q.; Ryou, J.-H.; Kim, H. J.; Lochner, Z.; Choi, S.; Dupuis, R.; Wang, Z. L., *Adv. Mater.* **2010,** *22* (42), 4749-4753.
148. Zhang, X.-M.; Lu, M.-Y.; Zhang, Y.; Chen, L.-J.; Wang, Z. L., *Adv. Mater.* **2009,** *21* (27), 2767-2770.
149. Hernandez-Alonso, M. D.; Fresno, F.; Suarez, S.; Coronado, J. M., *Energy & Environmental Science* **2009,** *2* (12), 1231-1257.
150. Anthony, S. P.; Lee, J. I.; Kim, J. K., *Appl. Phys. Lett.* **2007,** *90* (16), 169902-169902-1.
151. Jang, E. S.; Won, J. H.; Hwang, S. J.; Choy, J. H., *Adv. Mater.* **2006,** *18* (24), 3309-3312.

CHAPTER II

ANALYTICAL AND CHARACTERISATION TECHNIQUES

This chapter provides a short survey to the characterization techniques employed in this thesis.

2.1. Introduction

Main goal for this thesis is to develop multifunctional materials via compositing the semiconductor (inorganic and organic) and metallic nanostructures. These nanostructures can be used in photocatalytic as well as electronic applications. In order to determine the properties of the developed materials, the designed materials should be tested via various characterization methods. This chapter is designed to explain basic principles related to the characterization techniques used in this project. These techniques include Scanning Electron Microscopy (SEM), Atomic Force Microscopy (AFM), UV-visible spectrometry (UV-Vis), Raman Spectroscopy (Raman), X-Ray Diffraction (XRD), Energy Dispersive X-ray (EDX) spectroscopy, X-ray Photoelectron Spectroscopy (XPS) and Inductively coupled plasma mass spectrometry (ICPMS).

2.2. Scanning Electron Microscopy (SEM)

It is known that the properties of nanostructures are highly dependent to their structure, size and shape. Due to the size of nano-materials imaging of these materials requires the use of electron microscope. Due to the wavelength of the visible light and also lens aberration, optical microscopy can be used for the materials with micron size features. To image the submicron materials the light beam is replaced by an electron beam with much smaller wavelength and optical lenses are replaced with magnetic lens. Using electron beam gives the advantage of controlling the wavelength of the beam by controlling voltage used to accelerate electron in the microscope column. As the wavelength of an electron beam is always in Angstrom orders, the resolution of the image would make theses types of microscopes an excellent candidate for imaging nano-materials.

Scanning electron microscope (SEM) is one of the electron microscopy techniques, which can provides information about the surface of the materials for morphological studies. In SEM electron beam is emitted from an electron gun which could be either a thermionic emitter or a field emission gun (FEG). Emitted electron beam with energy ranging from 0.2 to 40 keV is focused by passing through microscope column containing several condenser lenses to nm range sizes. Finally, a deflector lens is used to control the position of the electron on the sample and give the ability of scanning the surface of the sample in a raster scanning. The incident electron can have different interactions as shown in **Figure 2.1**. As the

electron interacts with the mater based on the energy of the electron and also interacting materials, elements can go through either elastic or inelastic interactions. Electron interaction with materials can result into different phenomena, including heat, visible light, x-ray emissions, backscattered electrons, diffracted backscattered electrons and low-energy secondary electrons. Among these, backscatter and secondary electrons are the most common techniques used for imaging via pseudo 3-dimensional SEM images.

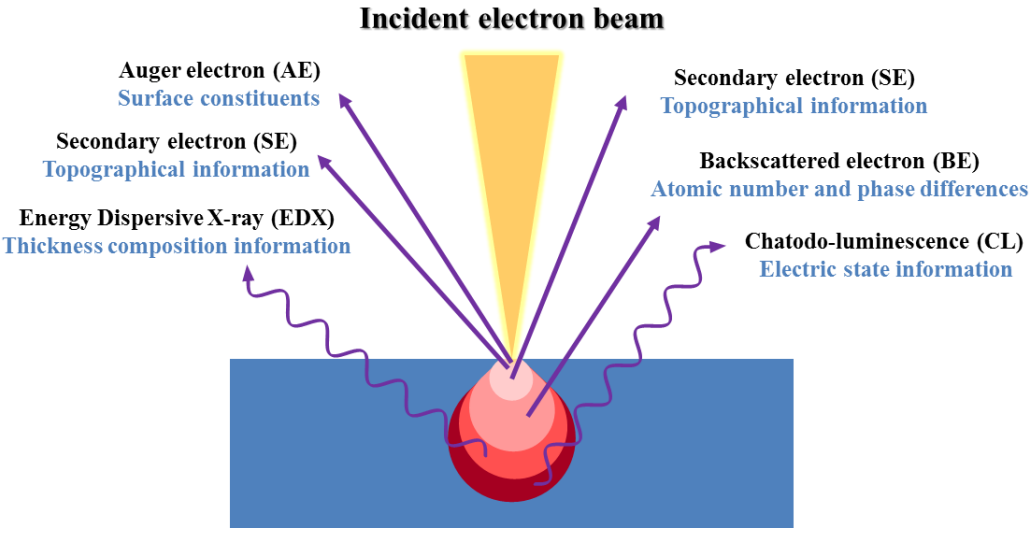

Figure 2.1. Interaction between electron beam and mater.

The incident electron beam can be reflected or back-scattered out of the interaction region with elastic scattering. This scattered high-energy beam is known as backscattered electron beam and since the heavier elements backscatter electrons more strongly than lighter ones this technique could be used for imaging. Chemical compositions of the scanned material can be achieved as a brighter area in a picture is related to heavier element in the backscattered image[1].

When an electron beam is scattered in the material, a part of the incident electrons can pass near the atoms and can impart some of its energy to the electron in the atom with lower energy and can thereby ionize the electron in the atom. This ionized electron can leave the atom with very small kinetics (5ev). One incident high energy electron has enough energy to make several ionized electrons during its interaction. The electron beam generated from this inelastic interaction is known as secondary electrons. Due to the low kinetic energy, these electrons have a short free path. Thus only part of the secondary electrons related to the atoms located near the surface can exit the sample and be examined. Thus, this technique is highly topology depended. These electrons are collected through a “collector” with positive

charge placed in front of the detector to be able to count the generated secondary electron to build image via pseudo 3-dimensional SEM images[2].

In this thesis, SEM analysis of all samples was performed on a FEI NovaSEM, operating at an accelerating voltage of 15 kV, with a spot size of 3.5 nm and a working distance of 5 mm.

2.3. Atomic Force Microscopy (AFM)

In addition to SEM, topological information of a surface can be determined via using Atomic Force Microscopy (AFM) technique. Unlike the electron microscope, which provides a two-dimensional projection or a two-dimensional image of a sample, the AFM provides a three-dimensional surface profile. The AFM operates by sweeping an atomic sharp tip (few nano-meter radii of curvature) across the surface of a sample. This tip could have a pyramid or a conical shape and locates on the top of a cantilever made from silicon or silicon nitride. The surface of the materials is raster scanned using piezoelectric controller to produce a 3d image of the analysed surface. As the tip of the cantilever is brought close to the surface of the material, the interaction between the tip and the surface deflects the tip. There are numerous imaging modes for the AFM but the two main modes are contact mode and tapping mode.

In contact-mode, the change in cantilever deflection is constantly scanned across the sample surface during monitoring. These deflections are monitored across the sample surface to collect the image.

In tapping mode AFM, similar information is measured via a different mechanism. Tapping mode operates by scanning a tip oscillating near the response frequency of cantilever (ranging from 20 to 100 nm) by small piezoelectric element mounted in the AFM tip. The oscillating tip “taps” on the sample surface where interaction forces between surface of the sample and the tip changes the amplitude of the oscillation. Imaging the force of the intermittent contacts of the tip with the sample surface is measured to produce AFM image of the surface of a sample. There are several advantages in tapping mode in comparison with contact mode. This mode can be used for soft materials, whereas in contact mode, the contact between tip of the cantilever and the surface of soft materials can damage the material which is under study. In addition, a reduction in lateral and normal forces being applied to the sample surface can be achieved using tapping mode. The schematic picture of different

modes as well as change in the atomic force between the tip of the cantilever and surface of the material are shown in **Figure 2.2.**[3]

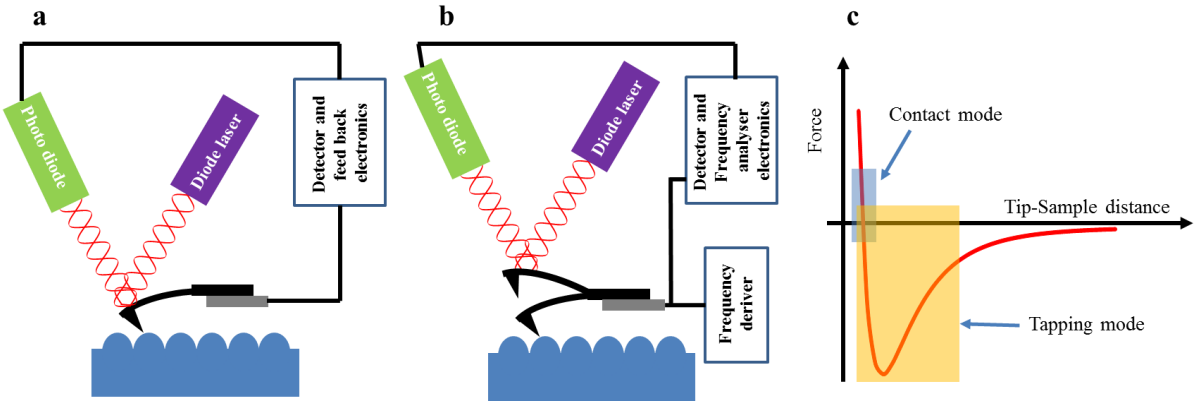

Figure 2.2. AFM **a)** Contact and **b)** Tapping modes; **c)** Force between tip of AFM cantilever and surface of the sample in different modes.

Although the data achieved about topology of the materials is more in detail in AFM rather than SEM but major drawbacks for AFM are a smaller area of the scan, longer time for scanning and limitation on the shape detection due to dependence of the final data to the tip shape and sharpness.

Atomic force microscopy (AFM) was carried out on this project in tapping mode using an AFM-Bruker D3100 in order to assess the surface roughness of samples.

2.4. UV-Visible Spectroscopy (UV-Vis)

There are multiple phenomena in the interaction of light with materials. When light is passed through a solution, the intensity of illuminated light is always different from the intensity of the emerging radiation. This could be partly related to reflection or scattering or emission in the sample, but mainly depends on absorption by the matter.

When light is absorbed by a material, it can make excitation and electronic transition within the material. Photon with proper energy can excite an electron from a bonding or non-bonding orbitals to an anti-bonding orbital. Thus, there should be a relation between adsorbed energy by the matter and also energy of the initial light beam. As the energy of the photon is dependent on the wavelength of the beam, the energy necessary for making an electronic transition from the ground state to the excited state can be measured by detecting the wavelength of the incident light beam as:

$$\Delta E = h\nu = \frac{hc}{\lambda} = hc\bar{\nu} \quad 2.1$$

Where ΔE is the energy required to induce a transition from the ground state to the excited state; λ and ν relate to frequency and wavelength of the light, h is the Planck's constant (6.626×10^{-34} J.s); c is the velocity of the light and $\bar{\nu}$ is wavenumber.

When single photon absorption can be explained through the *Beer-Lambert* law relating the intensity of the incident light, I_0, to the intensity of transmitted light through the sample, I, with the equation of:

$$log_{10}\left(\frac{I_0}{I}\right) = \varepsilon cl = A \quad 2.2$$

Where ε, c, l and A are related to the molar extinction coefficient of the sample, molar concentration, sample thickness and absorbance or optical density of the materials, respectively[4].

As absorbance is directly related to the concentration of the sample, by a simple UV-Vis spectroscopy and extracting standard curve for a dye, concentration of an unknown sample can be determined. Thus, this can be a quantitative technique for understanding the pollutant concentration in environmental studies, which are presented in this thesis.

In the following thesis, UV-Visible spectra were obtained on a Cary 50 Bio spectrometer, operating at a resolution of 1 nm over a wavelength range of 200-800 nm.

2.5. Raman spectroscopy

This technique is another vibrational spectroscopic technique, which is complimentary to FTIR technique. In contrast to FTIR where dipole momentum change during vibration is the main phenomenon, in Raman spectroscopy in order to have a "Raman active" molecule, polarizability of the molecule during the vibration should be changed (positional change in the electron cloud of the molecule). Also Raman uses monochromatic laser as electromagnetic light source. In Raman spectroscopy when electromagnetic beam interacts with a molecule, an inelastic scattering occurs which make a net effect where the frequency of the scattered electron is altered slightly. This slight change can be used as analytical approaches for spectroscopy. The energy shift could be categorised into red (absorbing energy) and blue (losing energy) shift which are known as Stokes and anti-Stokes

shifts. These interactions and energy shifts are correlated to the specific molecular functional groups and could be used for detection of different molecules in Raman spectroscopy[5].

Raman spectroscopy was obtained on Perkin Elmer Raman Station 400F. All samples were carried out with best Raman focus and 100% laser (785 nm) power with 5 sec exposure time and 10 acquisitions averaged with the background correction feature disabled. The obtained spectra were further background corrected using software developed in this project as explained in details in *Chapter III* of this thesis.

2.6. X-Ray Diffraction (XRD)

X-ray diffraction is one of the powerful spectroscopy techniques for studying crystal structures. X-ray beam (λ=0.1 to 3 angstrom) is produced in a hot cathode tube at high vacuum where emitted electrons produced by thermionic effect from a filament (cathode) are accelerated due to the high-voltage difference between cathode and anode and the impact of the electron with the anode generates X-ray. When X-ray beam interacts with crystalline materials with regular atomic structure, these atoms based on their formation, structure and also orientation can go through elastic scattering of X-ray waves. Some of these waves cancel each other through destructive interference, but based on the crystallite lattice groups and structure of the materials, other wave can have a constructive interference. These constructive interferences can be determined by Bragg's law[6]:

$$2d \sin\theta = n\lambda \qquad 2.3$$

Where d refers to diffracting crystallite plane spacing, θ is X-ray incident angle, n is an integer and λ is the wavelength of the X-ray. As for any crystal planes because of the size and type of the atoms and crystallite structure of them, each crystallite atomic structure diffracts X-ray in a unique characteristic pattern.

X-ray Diffraction experiments were performed using a Bruker AXS D8 Discover with a General Area Detector Diffraction System (GADDS) micro diffraction instrument operating at 40 kV and 40 mA over a 2θ range of 15-85°.

2.7. Energy Dispersive X-ray (EDX)

As shown in **Figure 2.1**, when an electron-beam interact with a material, electron in the beam has enough energy to force the electron at the inner orbitals of the atoms to eject from their allocated orbitals to the conduction band of the atoms. The vacancy produced from

ejection of the electron from inner orbital creates a low-energy vacancy where an electron from outer shell with higher energy fills the vacancy. The difference between the higher energy shell and lower energy shell can be released in the form of X-ray. This process is shown schematically in **Figure 2.3**.

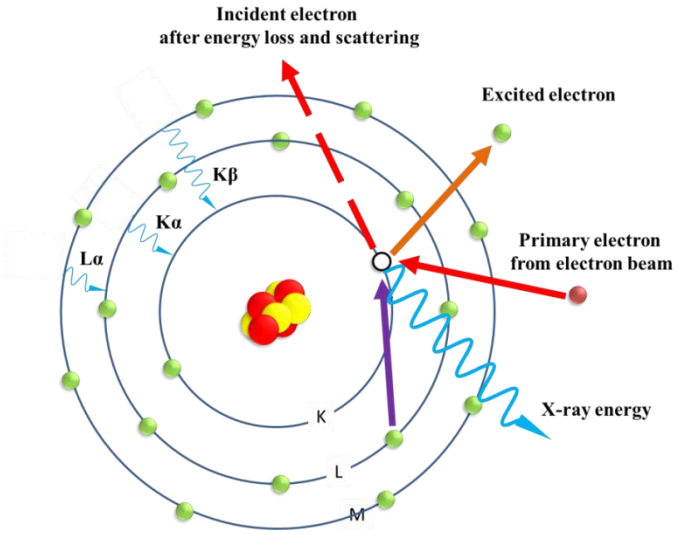

Figure 2.3. The mechanism for EDX.

The energies of emitted X-ray are characteristic energy between electron transferred shells, and the element which they are emitted from. This allows atomic composition analysis of the sample to be obtained. As EDX provides information from the focused point of the incident electron beam from the SEM emitter, by a raster scanning of the surface, it can provide a composition map of the materials under study. Additionally, EDX can be used for semi-quantitative analysis of the sample as the mass fractions or weight percents of the elements present in the sample can be calculated in EDX[7].

EDX analysis conducted in the body of work was performed on a FEI Nova NanoSEM instrument coupled with an Oxford Instruments, X-MaxN detector.

2.8. X-ray Photoelectron Spectroscopy (XPS)

XPS is one of the semi-quantitative surface spectroscopy techniques for estimation of the elemental composition and chemical or electronic state (oxidation state) of the element on the surface. This device uses high-energy X-ray photons under ultra-high vacuum (UHV) to excite “core” electrons in the near-surface region of the materials as shown in **Figure 2.4**. This is a surface spectroscopy technique and the depth of the information obtained from this

technique cannot typically be more than 10 nm. This is due to the fact that the excited photoelectrons from deeper parts of the samples cannot make it out of the solid due to the scattering phenomena below the surface of the material.

Number and kinetic energy (KE) of the photoelectrons collected from the surface of the materials are measured during XPS analysis. From KE of the electrons, binding energy (BE) of the electron can be obtained, which reflects the oxidation state of the elements on the surface[8].

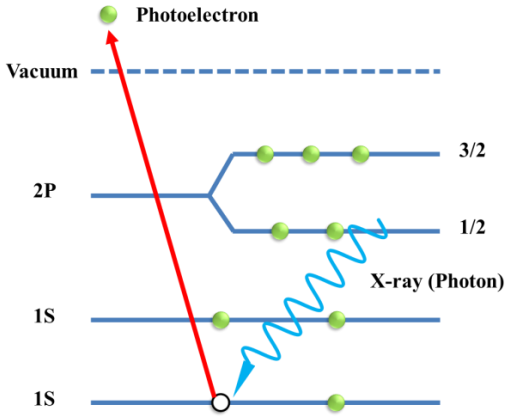

Figure 2.4. Schematic of photo-ionization of the electron from 1s orbital in XPS.

X-ray photoelectron spectroscopy (XPS) surface analyses were carried out by a Thermo Scientific K-Alpha instrument using un-monochromatized Mg Kα radiation (photon energy 1253.6 eV) under vacuum better than 10^{-9} Torr at pass energy of 50 eV and electron take off angle of 90°. The core level spectra were background corrected using Shirley algorithm. XPS core levels were aligned to the adventitious C 1s binding energy (BE) of 285 eV. The overall resolution was 0.1 eV for XPS measurements.

2.9. Inductively Coupled Plasma Mass Spectrometry (ICP-MS)

This spectroscopy method is a combination of easy sample injection and quick analysis of ICP with high resolution and accuracy of mass spectroscopy techniques. The equipment is capable of detecting trace metal multi-elements within levels of part per trillion (PPT). In ICP-MS samples are decomposed to neutral elemental form using high-temperature argon plasma and analysed based on their mass to charge ratios. An ICP-MS contains four main processes. First aqueous sample is introduced into a small nozzle (nebulizer) where with argon flow support it is sprayed as an aerosol, then generated aerosol is ionized by argon plasma source. After that the mass spectrometer ions are removed from the plasma chamber

via pumping. In this section, the removed ions are separated based on their specific mass to charge value using a DC/AC filtering system which only allows a specific ion reaching to the detector. This discrimination is mostly carried out using quadrupole mass filter system. The last section of the systems is the detector, where in most of the system it is a chaneltron multiplier. When an ion passes by or hits a surface, the detector records either the charge induced or the current produced. The produced signal versus the place of the scan will produce a mass spectrum[9].

Inductively coupled plasma mass spectrometry (ICP-MS) analysis were carried out using Agilent 7700 series ICP-MS for measuring the amount of ions in different solutions in this thesis.

References

1. De Harven, E., *Ultrastructural Pathology* **1987,** *11* (5-6), 711-721.
2. Cazaux, J., *J. Electron Microsc.* **2012,** *61* (5), 261-284.
3. Johnson, D.; Hilal, N.; Bowen, W. R., *Atomic Force Microscopy in Process Engineering*, Bowen, W. R.; Hilal, N., Eds.; Butterworth-Heinemann: Oxford, **2009**.
4. Zhang, C., *Fundamentals of Environmental Sampling and Analysis*; John Wiley & Sons, Inc., **2006**.
5. Zhang, S.-L., *Raman Spectroscopy and its Application in Nanostructures*; John Wiley & Sons, Ltd, **2012**.
6. Waseda, Y.; Matsubara, E.; Shinoda, K., *X-Ray Diffraction Crystallography*; Springer Berlin Heidelberg, **2011**.
7. Anderhalt, R., *Scanning Microscopy for Nanotechnology*, Zhou, W.; Wang, Z., Eds.; Springer New York, **2007**.
8. Hofmann, S., *Auger- and X-Ray Photoelectron Spectroscopy in Materials Science*; Springer Berlin Heidelberg, **2013**; Vol. 49, 409-449.
9. Thomas, R., *Practical Guide to ICP-MS*; CRC Press, **2003**.

CHAPTER III

A novel approach towards a better background correction of Raman signals

Noise removal is considered a primary and inevitable step for background correction in experimentally obtained Raman spectra. Employing an appropriate algorithm for a smoothing-free background correction technique not only increases the speed but also eliminates unwanted errors from the smoothing algorithms. Herein, the process for designing a new smoothing-free method for background correction is shown, which has been developed by merging continuous wavelet transform and signal removal method, which in combination, could be applied to noisy signals without smoothing. Wavelet transformation has been used for suppressing the side effects of noise and extracting derivative of the studied spectra while signal removal method has been applied for eliminating peaks of signals from the spectrum, thereby providing spectral sections purely related to the background to be used in the background correction process. A range of statistical analyses were applied to test the performance of this algorithm, wherein a low deviation in background correction procedure was observed. Additionally, when this algorithm was used for experimentally obtained Raman spectra, it showed good capability in background correction of noisy signals without the requirement of a smoothing process. This algorithm was used as a basic method for surface enhanced spectroscopy data analysis presented in *Chapters IV* and *V* of this thesis.

Part of the work presented in this chapter has been published in:

a) **Kandjani, A.E.**, Griffin, M.J., Ramanathan, R., Ippolito, S.J., Bhargava, S.K. and Bansal, V.; A new paradigm for signal processing of Raman spectra using a smoothing free algorithm: Coupling continuous wavelet transform with signal removal method; *Journal of Raman Spectroscopy*, 2013, 44, 608-621.

b) Bansal, V., **Kandjani, A. E.**, Griffin, M.J., Ramanathan, R.; A background correction method for a spectrum of a target sample; *PCT/AU2013/001472*.

3.1. Introduction

3.1.1. A short survey to background correction methods

In analytical spectroscopy, in addition to the desired signal, a spectrum always contains undesirable elements such as noise, spike and background features. Thus, for most of the analytical studies, extracting the real signal from the other unwanted features becomes necessary. The reasons for removing unwanted elements are highly application dependent, which could vary from simple presentations to quantification and subsequent numerical studies. Since all spectra need to be interpreted into a digital format to enable post processing of the results, there are several different algorithms that have been introduced for correcting the background of experimental spectra. These algorithms are mainly different in accuracy, modes of failure, computation time and mathematical processes. Although there are numerous algorithms available for background correction, there is no actual standard algorithm that can be applied to all the different types of spectra. This is mainly due to the fact that signals in different spectroscopy techniques have various types of elements and the different nature of the signals makes it impossible to provide a global background solution for all spectroscopy techniques. Therefore, understanding the reasons behind the background generation and also the shape of different signal components is an inevitable step to obtain background corrected spectra accurately.

Initial attempts to address background correction issues started in 1969[1]. Since then, several background correction methods have been introduced. Most of these methods have been developed during the time when the process of the algorithm design has been accelerated by improving the computer's performance. This improvement allowed programmers to design better algorithms enabling processing of a vast amount of data in short time and high precision[2]. After emergence of high-performance computers, the enormous amount of the produced data to be processed made the researchers to design automated signal processing methodologies.

The spectrum itself, in the most simplified format, always consist of four major components, including, desired signal, background, noise and spectroscopy blurring

effects. Thus, separating these components of an analytical spectrum is an essential step with background correction being one of the intermediate goals of this process. A sampled signal can be considered as an array (S) that can be given as:

$$S = (PS + B) + N \tag{3.1}$$

where, PS, B and N are the noiseless signal without background (pure spectrum), background and noise, respectively.

An alternative way for analysing components of a spectrum is based on frequency analysis of its components. In this method, background and noise are taken to comprise low frequency and high-frequency features, respectively. The signal component of a spectrum is considered to lie between the background and noise frequencies. This suggests that if a signal is decomposed based on their frequencies and the noise and background components are filtered, a pure noiseless and background corrected signal can be obtained.

All of the background correction methods (BCMs) need some initial information about the spectrum features to be able to performing the background correction algorithm. Therefore, background correction techniques can be categorized based on the type of initial information needed to be known before applying them into a spectrum. **Table 3.1** lists the different famous BCMs and the initial information needed to estimate the background feature of the signals.

Table 3.1. Classification of BCMs based on the required prior signal information[1].

Class	Requirements	Method
a.	PS, B and N	Noise median method (NMM)
		First derivative method (FDM)
b.	B	Threshold-based classification (TBC)
		Signal removal methods (SRM)
		Composite (linear-sine-cosine) baseline method (CBM)
		Spectral shift methods (SSM)
c.	B and N	Manual methods (MM)
d.	PS, B and N	Maximum entropy method (MEM)
e.	Frequency	Fourier transform method (FTM)
		Wavelet transform method (WTM)

Each of the aforementioned categories has some associated disadvantages. One of the major limitations of the group of BCMs requiring information about signal components is that the existing noise in the signal makes denoising and smoothing an inevitable process before engaging in any background removal. This is because most methods in these categories (e.g. SRM[3] or TBC[4]) essentially employ the derivative of the signal that is estimated numerically, which may be rather overwhelming to calculate without employing a smoothing process in advance. Additionally, applying a smoothing procedure in the early stages can inject unwanted errors into the signals depending on the form of denoising methodology. An erroneous denoising process can further result in peak shifts or even peak suppression in the case of low signal to noise ratio (*SNR*s)[5]. On the other hand, the frequency based method requires signals to be transformed into frequency domain and subsequently the signal components can be extracted based on their frequencies, which can sometimes be rather daunting. This is generally due to the fact that components in real signals do not have constant frequencies, i.e. the frequency component is not a single rigid value but consists of a range of frequencies, making selection of thresholds a challenging endeavour. Therefore, decomposing the spectrum into different frequencies followed by rebuilding the final spectrum could leave traces of noise or background[6].

Therefore, there is a need to address background correction of a spectrum considering advantages and disadvantages of the BCMs. In addition, a combinatory approach could give the advantages to increase efficiency and also accuracy of the background correction methods by combining different BCM methodologies.

3.1.2. Raman spectroscopy and its background issues

Raman spectroscopy, due to its ability to provide information about the physical and chemical characteristics of materials, finds its application in many different branches of science from biology to chemistry and materials science[7-8]. It is a non-destructive technique, which is routinely used to qualitatively and quantitatively analyse materials by identifying their native structures and structural impurities[9-11]. Raman spectroscopy can also be used for investigating the thermodynamical aspects and phase equilibrium of different materials[12]. Raman spectroscopy has also attracted significant attention in bio-imaging wherein different biological components could be differentiated due to the differences in their

resonance nature, especially by the position of peaks in Raman spectra as well as their relative intensities that is related to the quantity of each molecular structure, thus, making Raman spectroscopy a strong candidate for mapping biological objects[13].

One of the major problems associated with employing Raman spectroscopy, especially for biological samples, is that due to the sensitivity of the biological samples to the incident wavelength of the laser, Raman signals from biological samples typically have lower signal to noise ratios and high magnitude of background which arises mainly from auto-fluorescence. Since the existence of the background suppresses the main spectrum, the interpretation becomes very difficult. Therefore, it is essential for a background correction method to be applied to the spectrum before performing detailed analysis of the spectra obtained from Raman spectroscopy.

Most of the application provided in chapter IV and V of this project are mainly based on the surface enhanced Raman spectroscopy (SERS) techniques. In addition, as Raman spectroscopy was one of the major spectroscopy techniques in the project discussed in chapter VI, a novel algorithm with a high precision for background correction was initially designed. The proposed technique for background correction is based on extracting the derivative of a spectrum without applying any smoothing procedures. Subsequently after detecting derivative of the spectrum, SRM could be used to estimate the background of the spectrum. As mentioned before, smoothing of the spectra could inject some unwanted errors to the system however, there are limited reports wherein the background correction is carried out without smoothing. This algorithm is based on combining certain strengths of signal removal method (*SRM*) and continuous wavelet transform (*CWT*) methodologies. Specifically, *CWT* is initially employed to calculate the approximate 2^{nd} derivative of the noisy signal which leads to the identification of signal peak positions in the experimental spectrum. This is followed by using SRM to remove the signal peak component of the spectrum and fitting the reminiscent spectrum to find the background, which is then subtracted from the original spectrum to obtain a background-corrected signal.

3.1.3. A brief introduction to Wavelet transform

As mentioned above, a spectrum could be analysed based on the frequencies of its components. A spectrum is a sequence of data points, a series of time (as X axis) and amplitude (as Y axis) values which is known as ‘time series’. Typically, the

process of signal processing transforms a time-domain signal into another domain for extracting more detailed information from the spectrum which cannot be observed in time series domain. There are two major transformations in signal processing in analytical chemistry namely, Fourier Transform (FT) and Wavelet Transform (WT) methods. In a FT method a signal in time series domain transforms to frequency domain via a linear operator. This linear operator is a combination of sine and cosine functions which is favoured when considering the fact that any periodic function can be decomposed using a sine and cosine waves. The biggest disadvantage of the FT is that this transformation does not provide any information about the time of the frequency changes[14].

In most of the applications where the frequency changes with time the FT, cannot be an answer as it provides information only about overall frequency values but not the timing of the frequency change. To address this issue FT can be analysed by using segments of a spectrum which is otherwise known as window. This technique is known as Windowed Fourier Transform (WFT) where analysis is carried out in the small sections of the signal at a certain time and the window sweeps to transform the spectrum into frequency domain while giving information on the time of the frequency change based on the position of the sweeping window[15]. Unfortunately, this method has some disadvantages in real applications as the size of the window is fixed and thus precision of the time would be limited[16]. The solution for this disadvantage can be carried out by analysing the time series signal with a series of transforming functions having variable window sizes. The various window sizes, known as scales, can then provide better precision in the time of the frequency changes as well as information on the frequency values. This method is the basic core of the wavelet transformation.

Wavelets transforms (WT) like Fourier transforms (FT) are a convolution between a wavelet function ($\psi(t)$) and signal ($\chi(t)$). The major difference between FT and WT is that in FT, the wavelet has a sine or cosine form that specifically provides information in the frequency domain; while in WT, the mother wavelet could have any function if it has zero-mean oscillation behaviour. A mother wavelet could produce families of waves through[17]:

$$\psi_{a,b}(t) = \frac{1}{\sqrt{a}}\psi\left(\frac{t-b}{a}\right) \tag{3.2}$$

where *b* is the parameter for transition and *a* represents dilation (that is always a positive integer). If (*1/a*) is considered as representing an average frequency, then *b* indicates the position of wavelet window. Hence, in employing WT, information on both time and frequency can be extracted from a spectrum. It is important to note that although, both WT and FT provide information on frequency; they are not a replacement for each other[18].

WT can be divided into two main categories viz. Continuous Wavelet Transform (*CWT*) and Discrete Wavelet Transform (*DWT*) which can be defined as:

$$Wf(a,b) = \int_{-\infty}^{+\infty} f(t)\cdot\psi^{*}{}_{a,b}(t)dt \tag{3.3}$$

where the asterisks (*) represents complex conjugation. This equation can also be given as:

$$Wf(a,b) = f(b)\otimes\psi_{a}^{*}(b) \tag{3.4}$$

where $\otimes$ represents convolution[17].

Although wavelet transformation has been studied extensively for processing spectroscopic data[14, 18], this technique has recently being used for calculating the approximate derivative of a signal[19-20]. This was substantiated by showing that the n^{th} order derivative of a signal could be achieved in a specific dilation (scale) by applying an appropriate mother wavelet[19, 21]. Furthermore, the mother wavelet was chosen in a way that its derivative still had a wavelet nature. For instance, if the Gaussian function is considered as a mother wavelet, it's 2^{nd} derivative commonly referred to as 'Mexican Hat' or 'Marr' with a minus sign can also be used as a wavelet[22]. In the present case, the nth derivative of a signal can be estimated using 'Gaussian' wavelet applied *n* times to the spectrum or a proper n^{th} derivative of the Gaussian function. As outlined before, noise and spectrum have different frequencies where lower frequency components are related to the higher dilation (scale) numbers. Thus the side effects of the noise of the transformed signal can be extremely suppressed by increasing the dilation. This enables finding the approximate derivative of a noisy spectrum by reducing the influence of noise.

Spectroscopic techniques commonly employ derivative calculations as a resolution enhancement technique[23-24], especially the 2nd order derivatives for extracting peak characteristics such as position and starting-finishing point from a signal[25]. In order to obtain high resolution enhancement, higher-order derivatives can be used for locating and de-convoluting overlapping peaks. With the 2nd order derivative, peaks can be mined from a spectrum where the remaining points of the spectra would be the representative segments of background that can be further used for background estimations. However, the presence of noise in these signals can be a serious drawback in finding peaks and calculating derivatives of experimental signals. One of the most common techniques employed for calculating the derivative is 'Numerical Calculation'. Due to the random nature of noise in these spectra, numerical derivative would result in noisy signals especially in those with low *SNR*s, which makes spectral smoothing an essential process. However, by applying proper *CWT* method, the derivative format of a noisy spectrum can be obtained without requiring any further de-noising processes.

3.2. Aim and goals

As most of the data presented in the current thesis uses Raman spectroscopy as a sensing platform or as a spectroscopic technique, development of reliable background correction software appeared critical for this thesis. In this chapter, a new algorithm is provided for a highly efficient background correction of Raman spectra, which is based on combining certain strengths of *SRM* and *CWT* methodologies. Specifically, in the current study, initially *CWT* is employed to calculate the approximate 2nd derivative of the noisy signal which leads to the identification of signal peak positions in the experimental spectrum. This is followed by using *SRM* to remove the signal peak component of the spectrum and fitting the reminiscent spectrum to find the background, which is further subtracted from the original spectrum to obtain a background-corrected signal. It is notable that *CWT* was chosen over *DWT* in the current study as the former is a tool for analysis, feature determination and approximate derivative calculation, while the latter is the preferred technique for data compression and denoising. Application of the current algorithm for background correction of four different noisy experimental systems (L-serine, rhodamine B, methyl red and crystal violet) showed a good performance of this

algorithm, wherein the end effect errors were found considerably less than the commonly reported studies. Notably, the major strength of the current algorithm is that it does not involve any smoothing step, avoiding which is a major challenge in obtaining background-corrected spectra.

3.3. Methods

3.3.1. Generating simulated spectra

All experimental steps in the current study were investigated utilizing MATLAB for MS Windows, version 7.11(R2010b). In this study, Raman peaks were simulated using a Gaussian function given by:

$$f(x) = a \cdot e^{\left(\frac{-0.5\cdot(x-c)^2}{\sigma^2}\right)} \tag{3.5}$$

where a is the intensity controller, c and σ are median and variance, respectively, of the Gaussian peak. The program creates simulated Gaussian peaks of variable quantity with random positions, intensity and width distributed in the spectrum with three main backgrounds as linear, sigmoid and sinusoid forms (**Figure 3.1**) and variable background constants. The general formulae for backgrounds are:

Linear background:

$$Background = a \cdot x + b \tag{3.6}$$

where a and b are the slope and scope of line, respectively.

Sigmoidal background:

$$Background = \frac{1}{1+\exp\left(-a(x-c)\right)} I + O \tag{3.7}$$

where a is the gradient at the inflection point, c is the location of the inflection point, I is the intensity controller (since sigmoid function results in numbers between 0 and 1) and O is an offset.

Sinusoidal background:

$$Background = x^{1.5} Sin(\frac{x}{a}) \cdot I + O \tag{3.8}$$

where *a* is the frequency controller, *I* is the intensity and *O* is the offset. Noise is considered as white Gaussian noise and added based on calculated SNR_{dB}.

3.3.2 Generating calibration curve

As outlined in the introduction, the 2nd derivative of a spectrum can be estimated with *CWT* using *'Mexican hat'* as a mother wavelet[19]. This can be followed by choosing the appropriate scale to reduce the effects of noise in the 2nd derivative. An increase in the scale (i.e. towards lower frequencies) results in a decrease in the influence of noise. This increase correspondingly results in broadening of the wavelet (i.e. widening of transformed peaks), which in turn reduces the resolution of the derivative spectrum due to merging of peaks at higher dilation numbers. Therefore, to overcome this issue and to select the *Best-Scale*, which is representative for the derivative of noiseless spectrum, *SNR* of the spectrum must be considered during calculations. For this reason, *correlation coefficient (r)* was used as a factor to select the *Best-Scale*:

$$r = \frac{\sum_{i=1}^{N} x_i y_i - \frac{1}{N}\left(\sum_{i=1}^{N} x_i\right)\left(\sum_{i=1}^{N} y_i\right)}{\sqrt{\sum_{i=1}^{N} x_i^2 - \frac{1}{N}\left(\sum_{i=1}^{N} x_i\right)^2} \cdot \sqrt{\sum_{i=1}^{N} y_i^2 - \frac{1}{N}\left(\sum_{i=1}^{N} y_i\right)^2}} \tag{3.9}$$

where x_i and y_i represent the i^{th} element of vectors *X* and *Y*, respectively, where *(r)* could have values between 0 and 1, and if *r=1*, vectors *X* and *Y* would be completely similar to each other.

If the spectrum has a signal without noise, its 2nd derivative can be easily calculated numerically. Now, if noise with a known *SNR* is added to this signal, by using the *CWT* method, its transformed spectrum can be calculated at different scales. Thereafter, by comparing the resultant spectrum of each scale with noiseless 2nd derivative of the signal and calculating the respective correlation coefficient values, one can find the variation of correlation coefficient with increase in *SNR*.

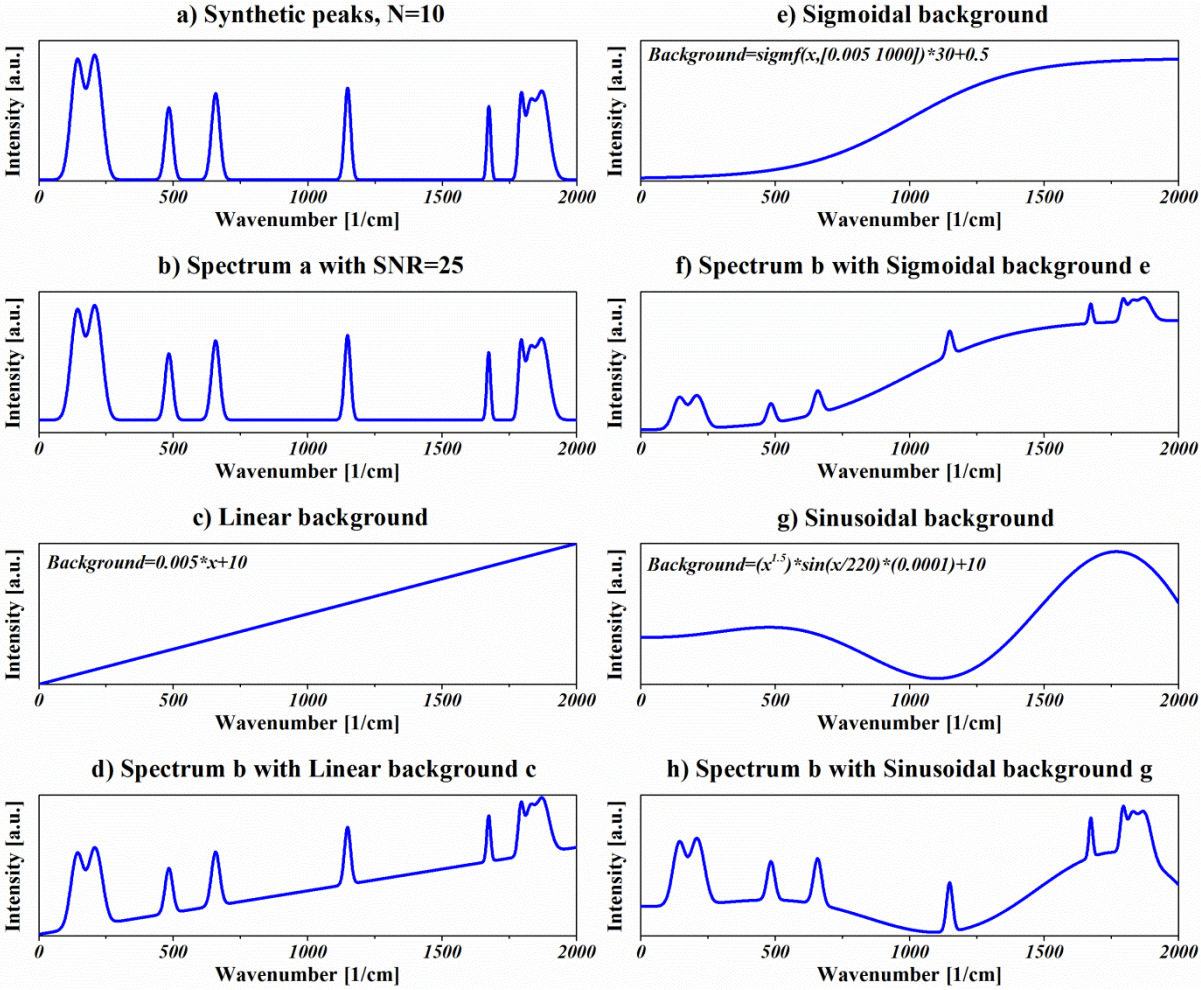

Figure 3.1. a) Simulated spectrum with 10 peaks without noise and background; **b)** Same spectrum after adding white noise with *SNR*=25; **c)** Linear background; **d)** Spectrum generated from adding linear background shown in **c** to spectrum **b**; **e)** Sigmoidal background; **f)** Spectrum generated from adding Sigmoidal background shown in **e** to spectrum **b**; **g)** Sinusoidal background and **h)** Spectrum generated from adding Sinusoidal background shown in **g** to spectrum **b**.

In this study, several spectra with each containing a single Gaussian peak of similar intensities and positions; however, with different widths and *SNRs* were synthesized. The numerical 2nd derivatives of these noiseless spectra were determined before adding a white Gaussian noise to these spectra. Thereafter, the correlation coefficients between the numerically derived 2nd derivative and wavelet transformed spectra with different *SNRs* at different scales were calculated. Transformed spectra in scales with highest correlation coefficients were chosen for each *SNR* and named as the *Best-Scale*s. Following the determination of the *Best-Scales* for signals with different *SNR*s, these parameters were

plotted for each of the signal widths and the respective calibration curves were estimated by fitting a function to these points. This allowed estimation of the *Best-Scale* values by knowing *SNR* and the width of a signal. A flowchart outlining the estimation of the *Best-Scale* is shown in the Appendix A.

3.3.3. Background correction method

The underlying principles for background correction employed in the propeosed method are as follows:

- Estimating Signal to Noise ratio (*SNR*)
- Calculating 2nd derivative of the spectrum using *CWT* in the *Best-Scale* using estimated *SNR*
- Finding the starting and finishing points of peaks in the spectrum through estimated 2nd derivative
- Finding points related to background by removing peaks from the spectrum
- Fitting a 9th order polynomial function to background points and adjusting fittings
- Background correction by subtracting the fitted spectrum from the spectrum

The overall algorithm is shown in **Figure 3.2**, and the detailed flowchart for each section is provided in *Appendix A.*

Data processing

This program allows the ability to cut the regions of interest in a particular spectrum, thereby (i) increasing the visual resolution, (ii) increasing the accuracy due to the decrease in the amount of calculation, and (iii) minimizing unexpected errors due to the abrupt change of background or impurities from other erroneous peaks. This function was incorporated as often only a section of the spectrum is required for spectral analysis.

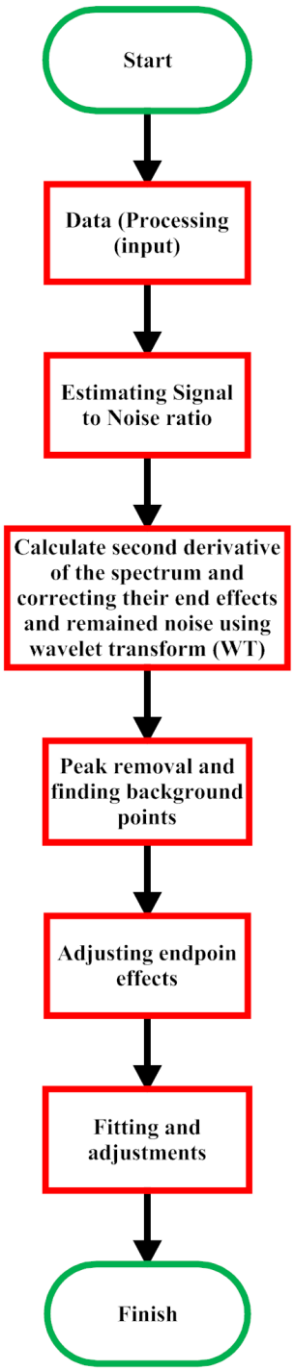

Figure 3.2. General Flowchart for estimating background.

Estimating Signal to Noise Ratio (SNR)

The *SNR* equation used in this program is in (logarithmic decibel) *dB* mode and is given by:

$$SNR_{dB} = 20 \cdot \log_{10}\left(\frac{RMS(Signal)}{RMS(Noise)}\right) \tag{3.10}$$

where *RMS* represents the *root mean square*.

For estimating the noise profile, initially, the spectrum is divided into 30 scanning windows with equal lengths (X-axis), and each of these 30 windows are used independently to estimate the *local standard deviation* (*LSTD*) in each of the scanned sections. Minimum *LSTD* is used as a region for estimating noise profile and calculating the *RMS* of the noise of the whole spectrum. In order to calculate *RMS* of the signal, the spectrum is smoothed using *Savitzky-Golay filter* at different levels from 0.1 to 0.9, followed by subtracting them individually from the main spectrum. Thereafter, *SNRs* of all the temporary background corrected signals are calculated using Equation (3.10). The average of these SNRs is then used by the user to choose the *Best-Scale* by input of peak width.

Calculating 2nd derivative of the spectrum (SDS)

It is well known that due to the discrete nature of a spectrum, artificial peaks are typically generated at both the ends of the transformed signals during transformation. To address this issue, points were added to the start and the end of the original spectrum that subsequently shifted and restricted this erroneous effect. After transformation, these erroneous areas could easily be removed from the signal and the 2nd derivative. It should be noted that the points were added in a way that there would be minimal discontinuities or changes in the slope of the spectrum as this would have considerably generated some unwarranted artificial peaks in the derivative spectrum. Additionally, as noise does not follow the same frequency as in the experimental data, there were still some remanent traces of noise in the *Best-Scale*. These reminiscent traces always have a smaller intensity in comparison with the peaks related to the signal. In order to eliminate the effect of residual noise in the 2nd derivative completely, this spectrum was squared to enhance the signals (*SSDS*).

Peak removal and finding background points

The method for background correction in this algorithm is based on *Signal Removal Methods* (*SRM*). In this technique, the first step involves the isolation of peaks from the signal (the residual corresponds to background). During isolation, starting and finishing points of the peaks (signals) were identified using the 2nd derivative as explained in *Section 3.3.6*, which allowed calculation of the zero crossing that corresponded to the starting and finishing points. Based on the zero crossing, the spectrum could then be divided into different sections with clear starting and finishing point pairs. Thereafter, the areas of each section within the 2nd derivative spectrum of a particular signal sandwiched between zero crossing

pairs were calculated, followed by the selection of the minimum (i.e. largest negative) local area corresponding to the largest and the sharpest peak. In order to select areas related to background a simple threshold is considered as:

$$Thershold = \sqrt{abs(\min(local\ area))} \tag{3.11}$$

Any local areas smaller than this threshold were considered as background. These background points were saved into fitting arrays of *FIT_X* (wavenumber) and *FIT_Y* (intensity). Furthermore, the next derivative of *SSDS* (endpoints corrected 2nd derivative of the spectrum) was calculated through *CWT* using '*Gauss1*' as mother wavelet, which produced 3rd derivative of the spectrum. In the case of a positive area surrounded with two negative areas in *SSDS*, the former was scanned for the minimum extremum points, which correspond to zero crossing points of the first derivative of *SSDS* with negative slopes. These points were then added to the fitting arrays *FIT_X* (wavenumber) and *FIT_Y* (intensity) to bring the fitted background closer to the real peak minima.

Adjusting endpoint effects

Estimation of the background using signal-deprived spectrum is based on fitting of residual points with a 9th order polynomial function. In the case where no background points exist at the start and finish of the spectrum, the fitting could select any arbitrary conditions in these areas, thereby failing to have a correct background correction towards these endpoints. The most commonly employed approach to address this problem is to continue the minimum of the nearest background point as a horizontal line[26]. However, this approach produces an artificial offset at the ends of the spectrum. In order to resolve this issue, 100 points were fitted each from the starting and the finishing parts of the spectrum with a cubic polynomial. This process decreases the effect of noise in the selected sections of the spectrum.

Based on the location of the starting and finishing background points and the slopes of the spectrum at endpoints, seven different conditions may occur. These conditions relate to the endpoints of the spectrum and can be divided into four main categories incorporating subclasses 0-6. These subclasses are determined based on *FIT_X(1), X(1), FIT_Y(1), Y(1)* and *SlopeS* that relate to the first point of fitting arrays (wavenumber), first point of spectrum (wavenumber), first point of fitting arrays (intensity), first point of spectrum (intensity) and the slope of the fitted cubic polynomial in initial 20 points, respectively. In the following

section, only the starting point relating to different subclasses are explained and the same can then be extrapolated to the finishing points.

Condition 1. *If FIT_X(1)=X(1)*; (*Subclass=0*): In this condition, starting or finishing points of the spectrum exist in a fitting array. Hence no modification is required as they are already included in the background.

Condition 2. *If FIT_X(1)≠X(1) and FIT_Y(1)>Y(1) and SlopeS>0;* (*Subclass=1 for starting and 4 for finishing points*): In this condition, the end points of the fitting array have intensities higher than the end points of signal (**Fig. 3.3**). The unfinished Gaussian peaks at the start and the end of the spectrum are cut from the last 25 points and based on *SlopeS*, a 2^{nd} order polynomial is fitted to these points, following which the minimum point of this polynomial is determined. Thereafter, 10 additional points are added as background from the location of minima to outside of the spectrum.

Condition 3. *If FIT_X(1)≠X(1) and FIT_Y(1)<Y(1)and SlopeS>0;* (*Subclass=2 for starting and 5 for finishing points*): This condition is quite similar to the previous subclass. The only difference is that *FIT_Y(1)<Y(1)* and therefore, there is no need to cut the spectrum at end points (**Figure 3.4**).

Condition 4. *If FIT_X(1)=X(1) and FIT_Y(1)>Y(1)and SlopeS<0;* (*Subclass=3 for starting and 6 for finishing points*): In this condition it is extremely difficult to determine the finishing point of the signal (**Figure 3.5**). Hence, 10 additional points are added to the ends of fitting arrays with intensities equal to *FIT_Y(1)* at the starting and *FIT_Y(end)* at the finishing point of the spectrum.

Fitting and adjustments

Following the endpoint correction, the points relating to the background are fitted with the 9^{th} order polynomial. In order to control the fitting behaviour, a correction condition has been considered. After finding the *SNR*, it is relatively simple to estimate the Peak-to-Peak (*PTP*) value of the noise. One important aspect that needs to be considered to obtain a precise background correction is that following this process, the resultant background corrected spectrum should not have any data lower than $\left(\frac{PTP}{2}+\varepsilon\right)$ where ε is related to the background correction error, which should not be more than the value of *PTP* itself. In the current algorithm, a simple loop validates this threshold for all the points of the spectrum. If

this condition fails, the coordinates of the minimum of the spectrum at the failed ranges are added to the fitting arrays and fitting process restarts until the $\left(\frac{PTP}{2}+\varepsilon\right)$ condition becomes valid at all the points of the spectrum. This process eliminates the possible fluctuation in the background estimation, which may otherwise arise due to the lack of background points in some sections of the spectrum.

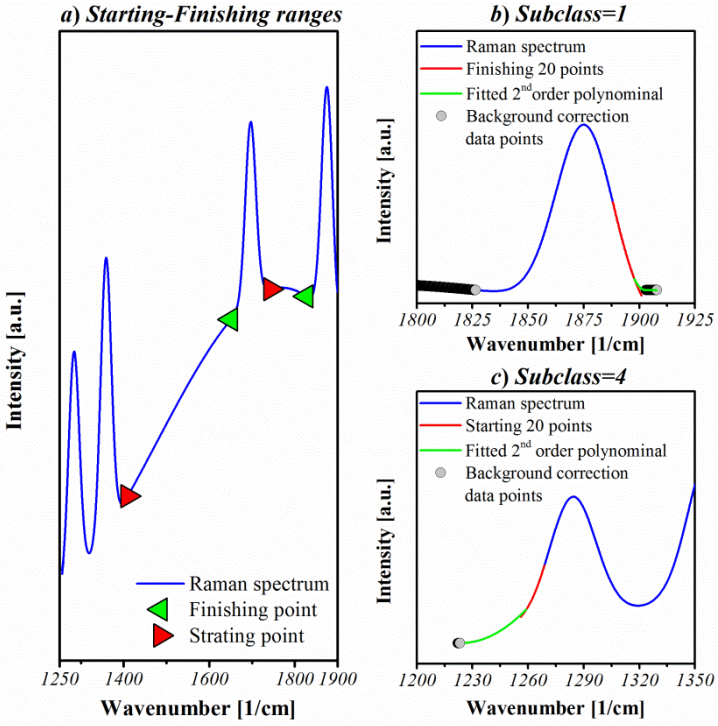

Figure 3.3. Endpoint effects for (Subclass=1 and 4), wherein **a)** shows the full original spectrum before adjusting the endpoints, and **b)** and **c)** show the magnified regions of the starting and the finishing points, respectively, after adjusting the endpoints.

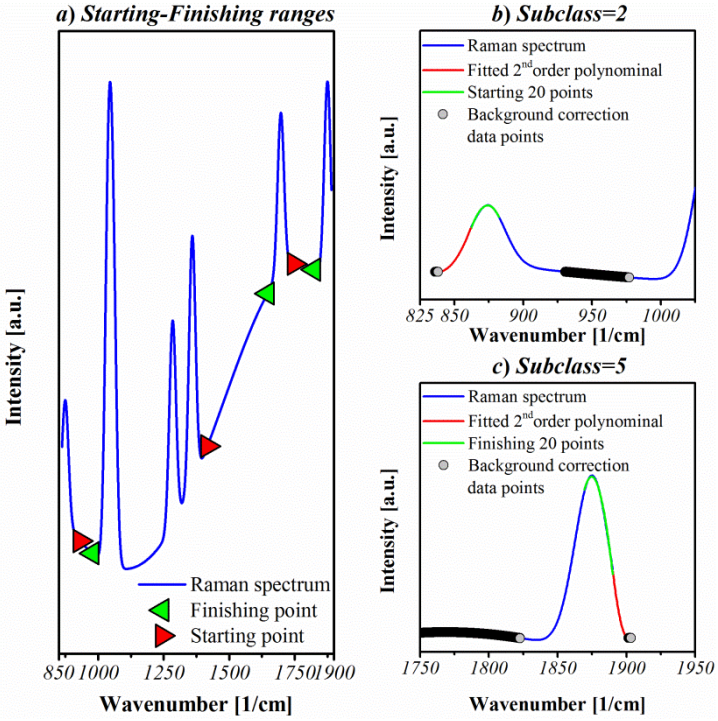

Figure 3.4. Endpoint effects for (Subclass=2 and 5), wherein **a)** shows the full original spectrum before adjusting the endpoints, and **b)** and **c)** show the magnified regions of the starting and the finishing points, respectively, after adjusting the endpoints.

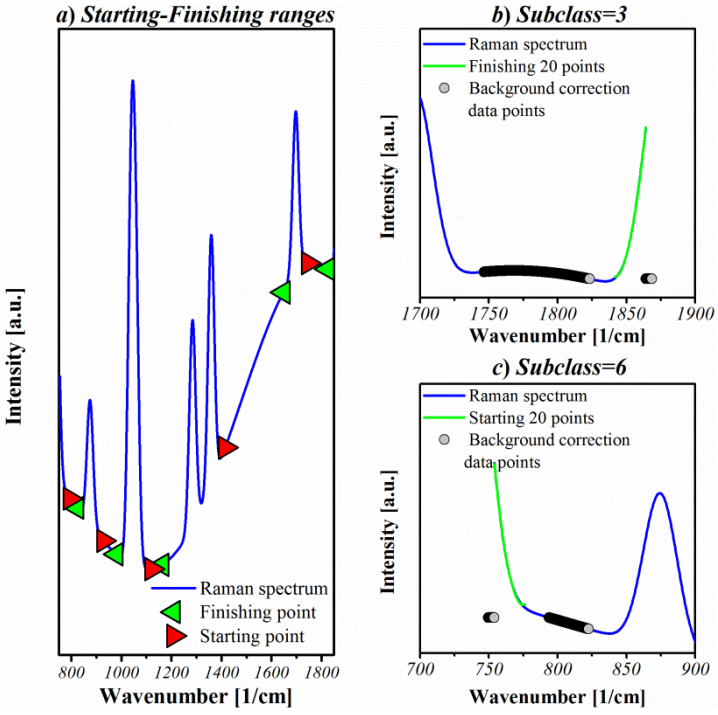

Figure 3.5. Endpoint effects for (Subclass=3 and 6), wherein **a)** shows the full original spectrum before adjusting the endpoints, and **b)** and **c)** show the magnified regions of the starting and the finishing points, respectively, after adjusting the endpoints.

3.3.4. Testing the accuracy of current algorithm

For testing the accuracy of the designed algorithm, statistical analyses have been carried out.

The processes include:

- Producing 900 spectra, each containing 10 Gaussian peaks of random characteristics (i.e. μ, σ, and intensity) with constant *SNR=60 dB*.
- Changing the number of Gaussian peaks from 2 to 30 with random characteristics (i.e. μ, σ, and intensity) and constant *SNR=60 dB*, with each condition applied for 200 times.
- Changing *SNR* of the spectrum from 10 to 130 *dB* with 10 Gaussian peaks of random characteristics (μ, σ, and Intensity), with each condition applied 200 times.

The spectrum after the background correction is compared with the original spectrum and Root Mean Squared Error (*RMSE*) values is calculated.

3.3.5. Experimental data

Chemicals: Rhodamine B, crystal violet and methyl red were purchased from Merck Chemicals and L-serine amino acid was purchased from Sigma-Aldrich. All chemicals were used without further modifications.

Preparation of e-beam evaporated substrates: The metal layers were deposited by a BalzersTM electron beam evaporator. The layer composed of 1000 Å Au with an underlying 100 Å Ti layer. The films were deposited sequentially by electron evaporation process onto the bare *AT*-cut quartz substrates. The purpose of the Ti layer is to assist with the adhesion of the Au layer to the substrate surface.

Raman scattering measurements: To obtain good Raman signals, gold substrates were immersed in 1 mM solutions of rhodamine B, crystal violet or methyl red for 1 h, followed by washing with deionized water (MilliQ) and air drying. In case of L-serine amino acid, the powder was directly placed on a flat gold substrate before Raman measurements. It is known that Au and Ag thin films and nanostructured substrates assist in increasing the Raman scattering cross-section of molecules by a surface enhanced Raman scattering (SERS) process[27-28]. The above samples containing different Raman active molecules were analysed using a Perkin Elmer Raman Station 200F (785 nm laser, spot size of 100 μm) with an

exposure time of 1 sec and 20 acquisitions, with instrumental background correction feature described.

3.4. Results and discussion

The performance of the current algorithm is summarized by stating the results of the calibration curve calculations and further explaining the results of each section outlined in the methods.

3.4.1 .Calibration curve

Figure 3.6 shows a single artificially synthesized Gaussian peak with different *SNR* values. The width of the Gaussian peak equals 40 units in this analysis. **Figure 3.7** shows the variation of correlation coefficient (*r*) with *SNR* and *CWT* scales for the artificially synthesized spectra outlined in **Figure 3.8**. To generate the calibration curve, the scale related to the highest correlation coefficient (*r*) obtained for Gaussian peaks exhibiting different *SNR* is plotted against the *SNR* values. A function can then be fitted through these points, where the *Best-Scale* for obtaining the 2^{nd} derivative of any spectra after finding its *SNR* can be estimated. The function which best fits this calibration curve is exponential in nature. The best fit function generates real numbers, while scales for *CWT* should contain only integer numbers. Hence, rounding towards positive infinity of this fitted function is considered as the calibration curve. Calibration curve for current example is shown in **Figure 3.9**.

There are three important issues in working with calibration curves:

- Changes in the number of signal data points can change the calibration curve.
- The numbers of scales in *CWT* should be same for all investigated spectra
- The calibration curve is dependent on the width of the peaks (in Gaussian peaks this is known as variance)

To address the first condition, the number of data points for each spectrum was fixed at 5000 points. This adjustment was carried out using cubic spline data interpolation. The scales for all transforms have been chosen in a constant array from 1 to 200. The variation of calibration curve for different variance of simulated Gaussian peak is shown in **Figure 3.9**. In the case of constant *SNR*, an increase in peaks width results in an increase in *Best-scale* number, a phenomenon that has been widely reported. In the previous report, different

situations influencing the derivative estimation of a signal using *CWT* was considered. So, in the current situation, by fixing data points and scale array lengths, the only user input will be the width estimation. In the case where a lower variance is selected, sometimes, part of the peak base is selected as background as well. In this case, background estimation through fitting of 9^{th} order polynomial, which could be corrected with the algorithm, is explained in *Section 3.3.9*. In the case where the variance estimations are high, the areas that relate to the background would be more confined due to the increase in *Best-Scale* values. This may result in false background estimation producing artificial humps in the corrected spectrum. This can be addressed by decreasing variance estimation number with user input. An important aspect of this is that if the average peak width in the spectrum lies within the same range of the estimated variance number, then this fixed number would address all similar situations.

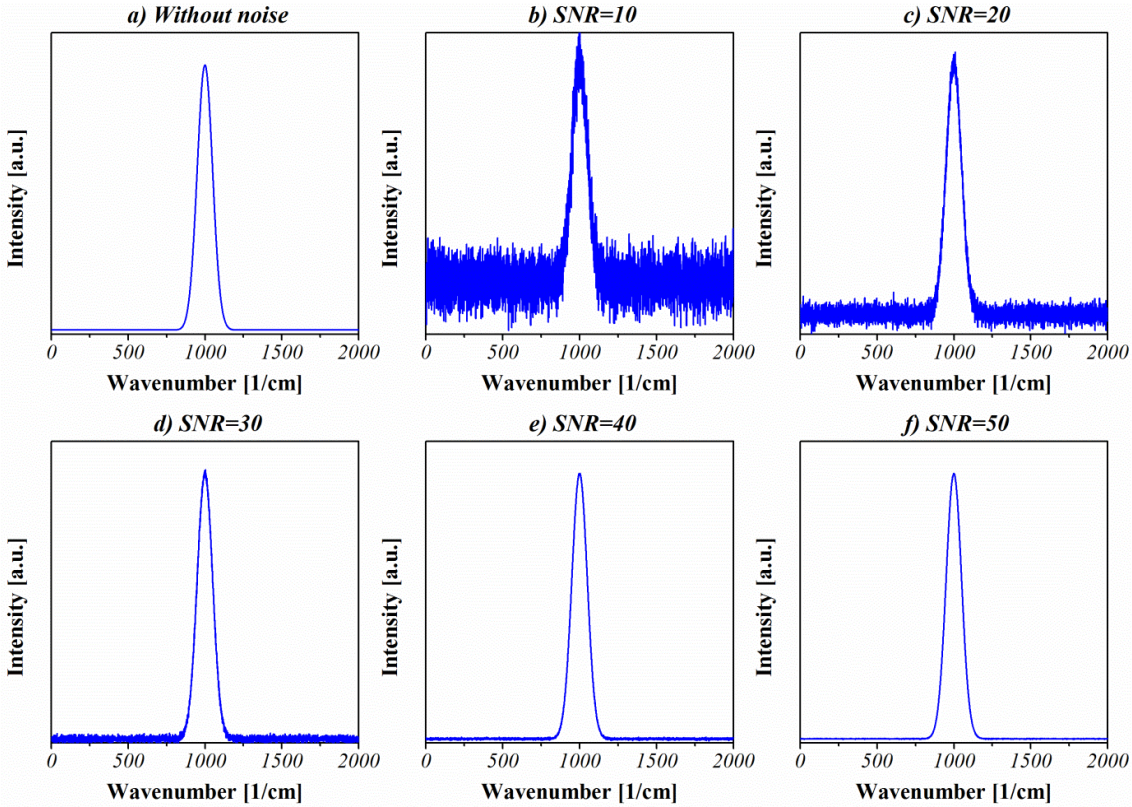

Figure 3.6. A Gaussian peak with different *SNR* values.

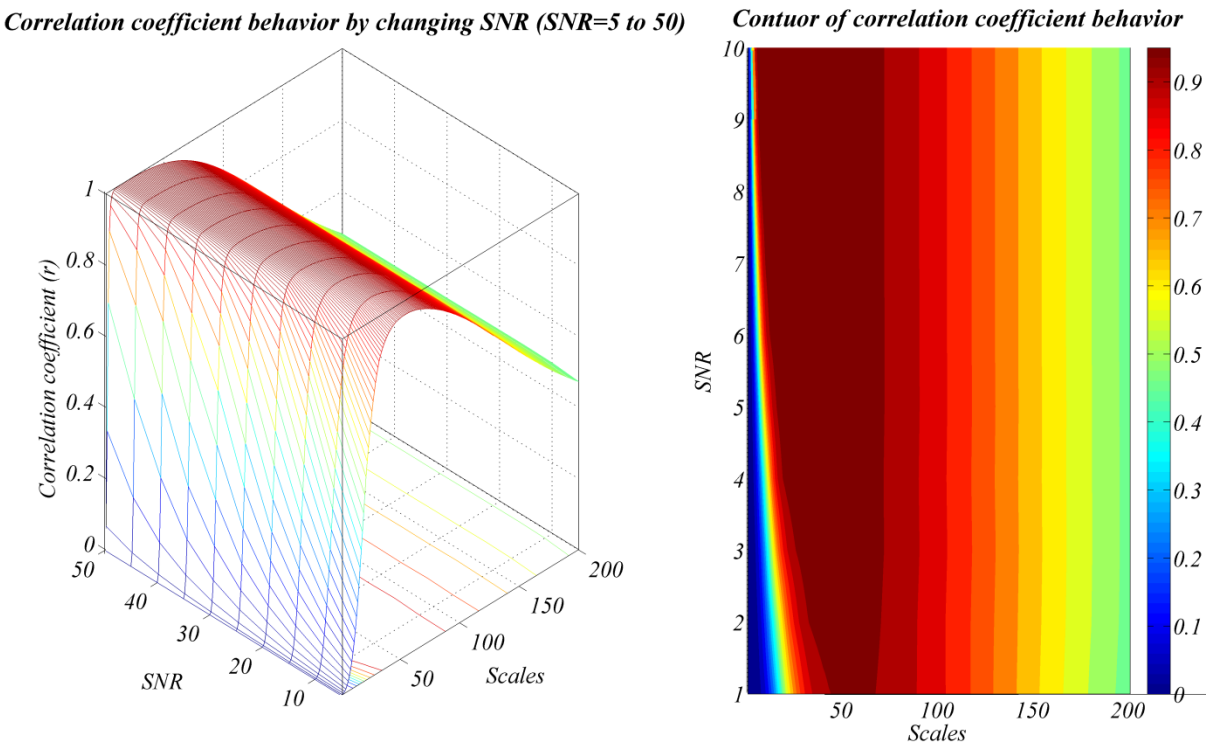

Figure 3.7. Variation of correlation coefficient with *SNR* and *CWT* scales.

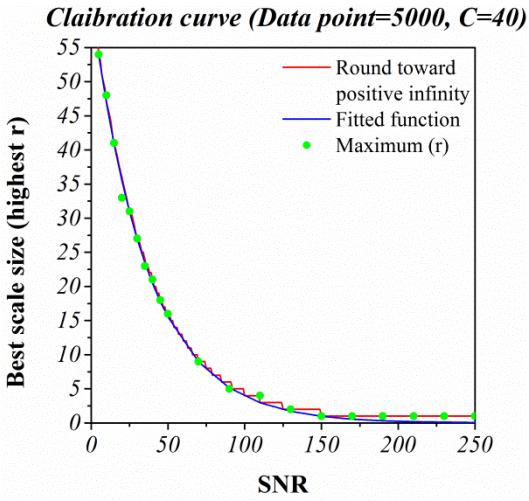

Figure 3.8. Calibration curve for signals in **Figure 3.6**.

In the investigated experimental results, keeping the variance number a constant value of 20 resulted in appropriate background estimations in most of cases, which is explained in the experimental results section.

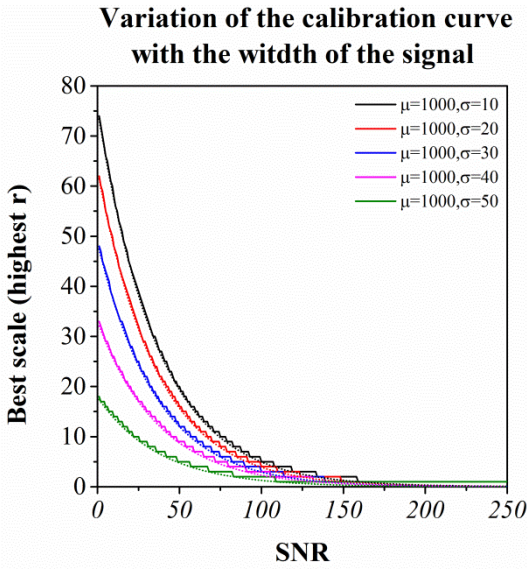

Figure 3.9. The effect of peak width on Best-Scale in different *SNR* values.

3.4.2. Estimating signal to noise ratio

SNR is an important factor to determine the *Best-Scale* values for estimating 2nd derivative of a spectrum. Due to the dependency of *Best-Scale* to *SNR*, it is of utmost importance to estimate *SNR* of a spectrum before estimating 2nd derivative. As previously mentioned, the first step for this calculation is de-convoluting or estimating the noise profile from the signal. One method to address this issue is to smooth a noisy signal and subtracting the de-noised signal from the spectrum that results in the noise profile. Although this approach is extensively used, there are issues associated with this approach. Primarily, in the case where there exists high level of denoising, if the signal has sharp peaks, the de-noised spectrum could reduce the intensity of these peaks. Subsequently, the noise profile derived from simple subtraction of the de-noised spectrum from the noisy spectrum would result in artificial peaks where sharp peaks occur in the spectrum. This error induces higher intensities in the noise profile within the ranges where sharp peaks are smoothed in the spectrum. On the other hand, in the case of low *SNR* values, the peaks with lower intensities are suppressed during the denoising step, which introduces errors in estimating the noise profile.

If noise is considered as a high frequency signal distributed evenly over the whole spectrum, a section of its profile could be used as a representative for the noise profile where this range is comparably larger than the average noise wavelength. In other words, two different sections of a noise profile should have similar *RMS* values with negligible variance if they are distributed evenly and have the same intensity in the overall range. An important

aspect that needs to be addressed is selecting the threshold for dividing the spectrum into measurable sections. This division window should be large enough to provide a significant sample of the noise profile for calculations and also small enough to make it possible to select a region that does not include peaks. After selecting the proper window size, the Standard Deviation (*STD*) for each window is calculated and the lowest value should correspond to a part of the signal which consists of noise and background without peaks. In the case where the selected window size is small enough, the background can be estimated using a simple linear fit. The results of the noise profile selection are shown in **Figure 3.10** for a spectrum with sigmoid shaped background with 10 peaks and initial *SNR* equal to 20.

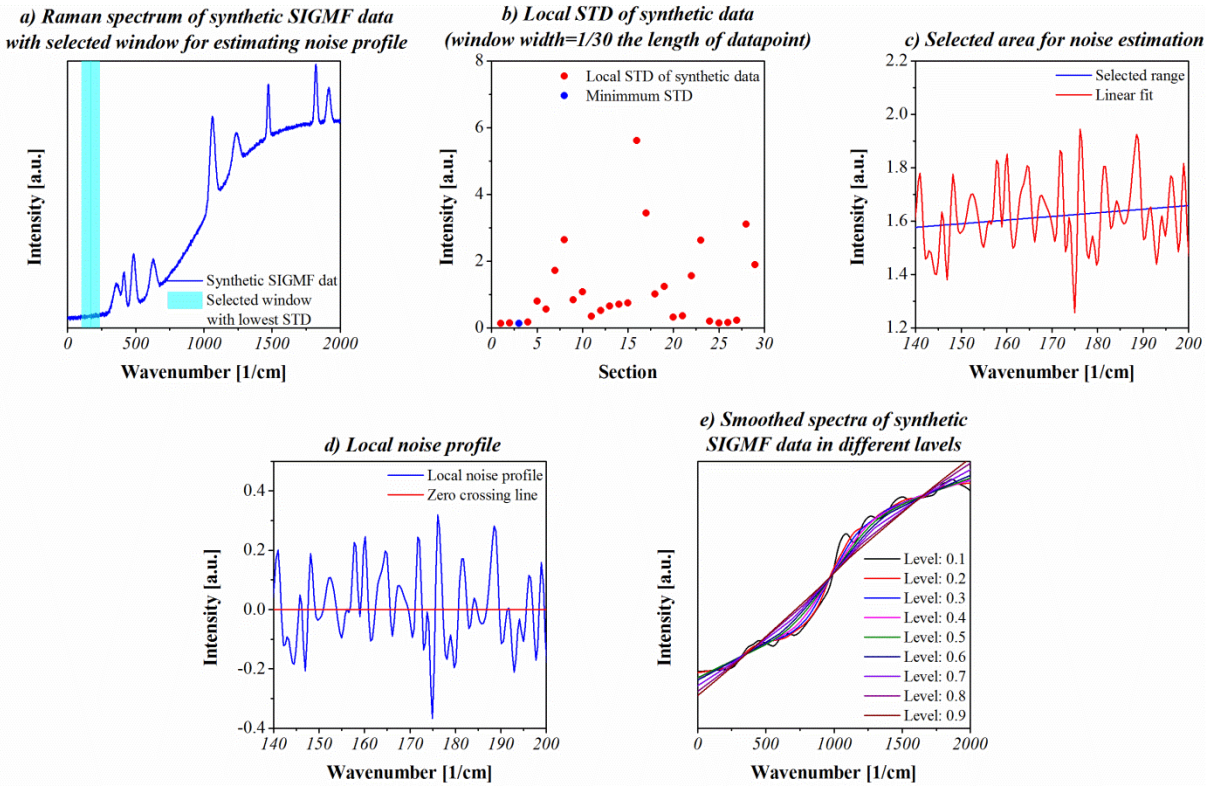

Figure 3.10. *SNR* estimation steps: **a)** Simulated Raman spectrum with 10 peaks randomly distributed on the signal with sigmoidal background, wherein shaded section represents window size for calculating *LSTD*; **b)** *STD* in different divided ranges of spectrum; **c)** Spectrum in minimum *LSTD*, wherein red line shows linear fitting of the spectrum in selected region to find background; **d)** Estimated noise profile by subtracting linear background and spectrum; and **e)** Different smoothing levels of the spectrum.

For estimating the accuracy of the current algorithm, testing was carried out using similar signal features (10 peaks randomly distributed on the signal with sigmoidal background) while changing two parameters: *SNR* value of the signal and the background

intensity. **Figure 3.11** represents the accuracy tests for *SNR* estimation algorithm wherein **Figure 3.11a** denotes the variation of *SNR* with smoothing, **Figure 3.11b** shows the effect of background intensity where background intensity ratio is calculated via dividing values of the intensity of highest peak in the spectrum with the background to intensity of the spectrum without the background; and **Figure 3.11c** shows the effect of change in the real *SNR* on the estimated *SNR* values by comparing between estimated *SNR* and the initial *SNR*.

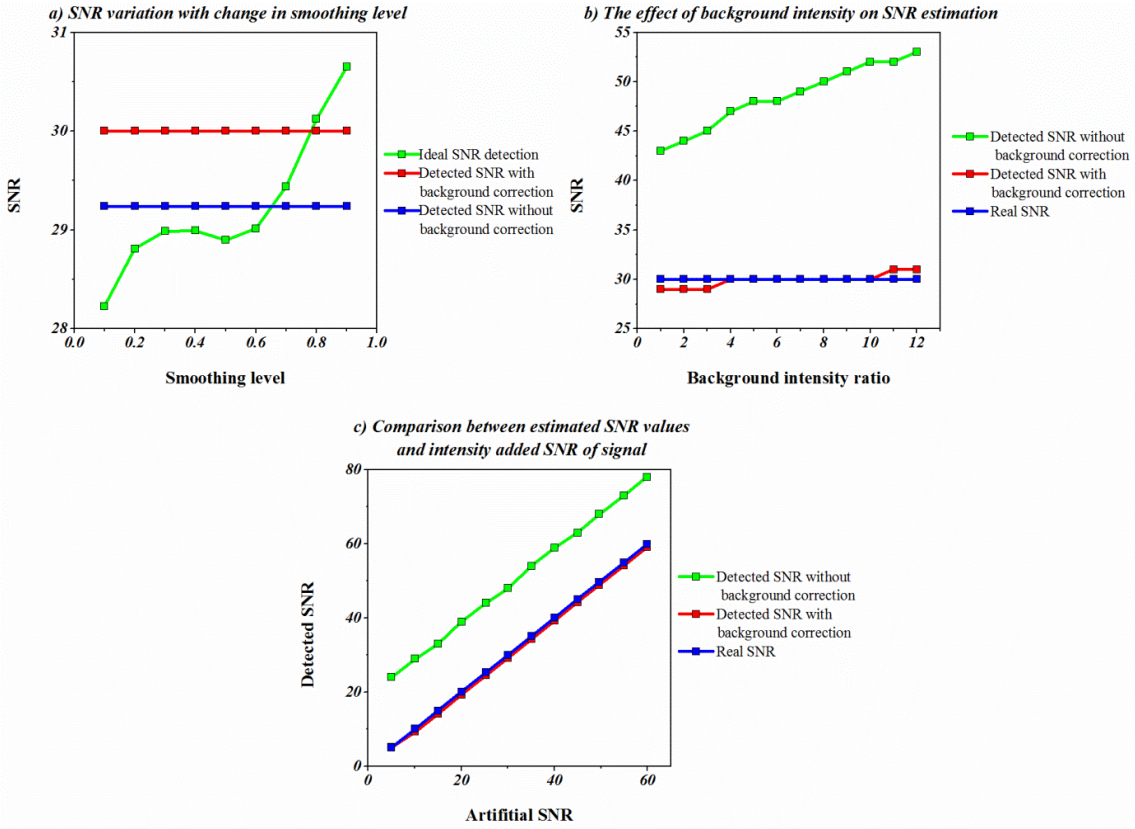

Figure 3.11. Testing of *SNR* estimation algorithm: **a)** *SNR* variation with smoothing level; **b)** Effect of background intensity on *SNR* estimation, wherein the intensity ratio is the ratio between intensity of the highest peak in initial background-free signal and max intensity of the added background; and **c)** Comparison between estimated *SNR* values and initially added *SNR* of signal.

In the case where the level of smoothing is low, certain wider peaks are considered as background, while, in the case where the levelling is higher, it tends towards a linear profile where most sections of the smoothed curve are located under the real background resulting in higher noise *PTP* values. Thus increasing the smoothing levels shows an increase in *SNR* values. Due to these changes, the average values of the *SNR*s derived in different smoothing levels could be a good estimation for the real *SNR* of the signal. In the current tested data

(**Figure 3.11a**), the initial *SNR* of the synthesized spectrum was 30 while the estimated *SNR* value was 29.3, which when rounded towards positive infinity (ceiling or '*Ceil'*) corroborates well with the initial *SNR* value. The intensity of background could also influence the estimated *SNR*. If the intensity of the background increases, peaks would be suppressed in the signal. Thus, smoothing curves tend to follow peak shapes in lower intensities which results in an increase in estimated *SNR*. If initial background correction is ignored in the algorithm, then it results in higher values as shown in **Figure 3.11b**. But in the current method for estimating *SNR*, with increasing intensity of the background (**Figure 3.11b**), estimated *SNR* is in good agreement with the initial *SNR* values. On comparing the initial and estimated *SNR* values, where these values were changed with a constant intensity ratio of 6, it resulted in the estimated *SNR* values to be closer to the real *SNR* values. Similar to the previous cases, if the initial background correction is ignored then the estimated *SNR* would have larger values than real *SNR* (**Figure 3.11c**).

3.4.3. 2nd derivative and end effect

Most spectra are discrete in nature, i.e. they do not always tend to be of zero intensity at the starting and finishing points (end effect). These points are considered as break points in the spectrum and during wavelet transformation, an artificial peak appears in these areas[29]. The 2nd derivative of the synthetic spectrum without applying end effect correction results in artificial peaks (**Figure 3.12b,** outlined in magenta colour). As previously stated, negative peaks in the 2nd derivative correspond to the place of the peaks in the spectrum. Due to the end effect there is an addition of two artificial peaks resulting in an error during the peak removal process. The 2nd derivative of any spectra is calculated using wavelet transform with *'Mexican Hat'* as mother wavelet, as described previously. The active regions of *'Mexican Hat'* wavelet is equal to [-5.a,5.a] where *a* represents the scale of transform. Thus, if the spectrum from both sides is extended in a way that the added points could have length wider than 5.a, the end effects would be confined to these regions. As the 2nd derivative of a signal is highly sensitive to any breaking points and sharp changes in slopes in the signal, the extending points should be added in a way that it follows its adjacent slope of the signal.

Following the estimation of *Best-Scale* (where the value for *a* can be determined), *10*a* points are added to the start and end of the signal based on the signal local slope at these junctions (**Figure 3.12c**). The active regions were doubled in this case to ensure that no trace

of end effects remains in the 2nd derivative. The corrected 2nd derivative of the spectrum is shown in **Figure 3.12d**.

Due to the existence of noise in the spectrum, the 2nd derivative of a spectrum, through numerical calculation, would result in a noisy spectrum (**Figure 3.13b**). This profile does not provide appropriate information that is required to determine the peak positions in the 2nd derivative of the spectrum. Estimating the 2nd derivative of the spectrum after end point correction using *CWT* in *Best-Scale* would still exhibit traces of noise in the spectrum that can be suppressed by simply squaring of the estimated 2nd derivative, as the intensity of the reminiscent noise is less than 1 (**Figure 3.13d**).

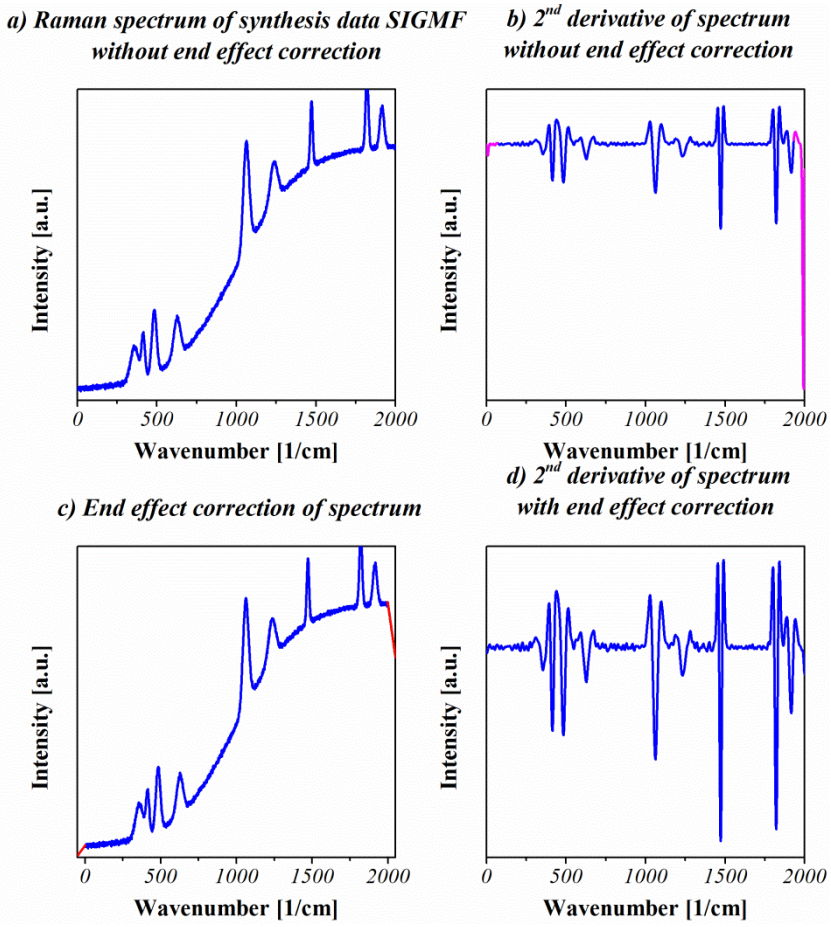

Figure 3.12. a) Synthetic spectrum (*SNR*=20, 10 peaks); **b)** 2nd derivative (wavelet transform, *Best-Scale*=17); **c)** Added points based on slopes of the spectrum at ending points; and **d)** 2nd derivative (wavelet transform, *Best-Scale*=17) with end point correction.

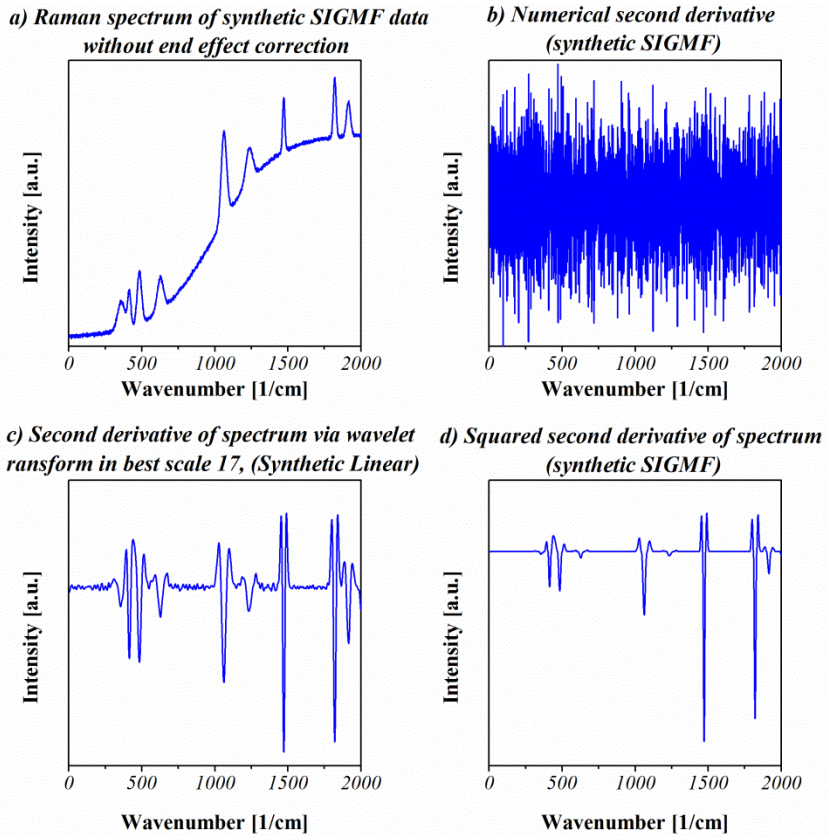

Figure 3.13. a) Synthetic spectrum with (*SNR*=20, 10 peaks); **b)** Numerical 2nd derivative; **c)** 2nd derivative (wavelet transform, *Best-Scale*=17); and **d)** Squared 2nd derivative to suppress noises.

3.4.4. Reasons for adding helping points based on the degree of separation

When distance between peaks becomes less than their width, the peaks overlap with each other. In the case when this phenomenon occurs, packing of peaks follows in one place. Under these conditions, estimating background points using 2nd derivative is a challenging process. If two peaks exist in a signal, based on their position and their *Full Width at Half Maximum* (*FWHM)*, the degree of separation (*R*) could be defined as a variable to show the overlap and peak conditions with respect to each other. If these peaks follow a Gaussian function, *FWHM* of each peak can be calculated through:

$$FWHM = 2\sqrt{2Ln2}\cdot\sigma \tag{3.12}$$

The degree of separation is defined as:

$$R = \frac{x_2 - x_1}{\frac{1}{2} * (FWHM_2 + FWHM_1)} \tag{3.13}$$

Smaller the value of *R*, the higher is the overlap of signals. This phenomenon is shown in **Figure 3.14** where the variation of *R* with position in two similar Gaussian peaks is explained. By an increase in the distance between signals, *R* is increased. If the spectrum is considered as not overlapping parts of Gaussian peaks, the 2nd derivative of the signal would show a positive peak by increasing peaks distance from each other. When two peaks are located within their *FWHM* range, this positive peak (**Figure 3.14b**) reaches its maximum value. By moving from these points, a minima extremum point is generated in 3rd derivative. If the areas of 2nd derivative of the spectrum between zero crossing points are considered, the location of this minimum point that lies in a positive area sandwiched between the two negative areas can be observed. The location of this minimum point can be established by considering the zero crossing 3rd derivative of the spectrum. If the intensity of this point passes half of the intensity of max adjacent point, it could be considered roughly as a part of the background.

This approximation results in adding points to the background arrays where 2nd derivative fails to estimate the background in the highly peak packed areas. Thus, instead of following an arbitrary shape, the fitting process progresses through these points. The location of these points could be a little higher than the base of the peaks, but, the iteration algorithm, described before will correct any overlapping due to added points from this section to the background arrays.

3.4.5. Background correction

After finding squared 2nd derivative of the synthesized spectrum, the peaks are removed from the spectrum by applying the algorithm described in previous sections. The areas between starting and ending points (represented as arrows in **Figure 3.15a**) are related to the background. These areas are selected for fitting and estimating the background of the signal. Following this process, the algorithm then finds the subclass of the starting and ending points. In this case, a subclass value of 0 for starting and 4 for ending points are detected (**Figure 3.15b and 3.15c**). The green dashed line is the first fitting estimation for background. As it can be clearly seen from **Figure 3.15d**, the background estimated curve crosses the spectrum at the end. In order to correct this issue, algorithm explained in *Section*

3.3.9 is applied. By adding points in this area after 314 loops, the final background is determined (represented as magenta colour). This process eliminates creation of artificial peaks due to fluctuation of estimated background in area where there are not enough points to fit in 9^{th} order polynomial. A simple subtraction of this curve from the original spectrum would result in the background corrected spectrum (**Figure 3.15e**).

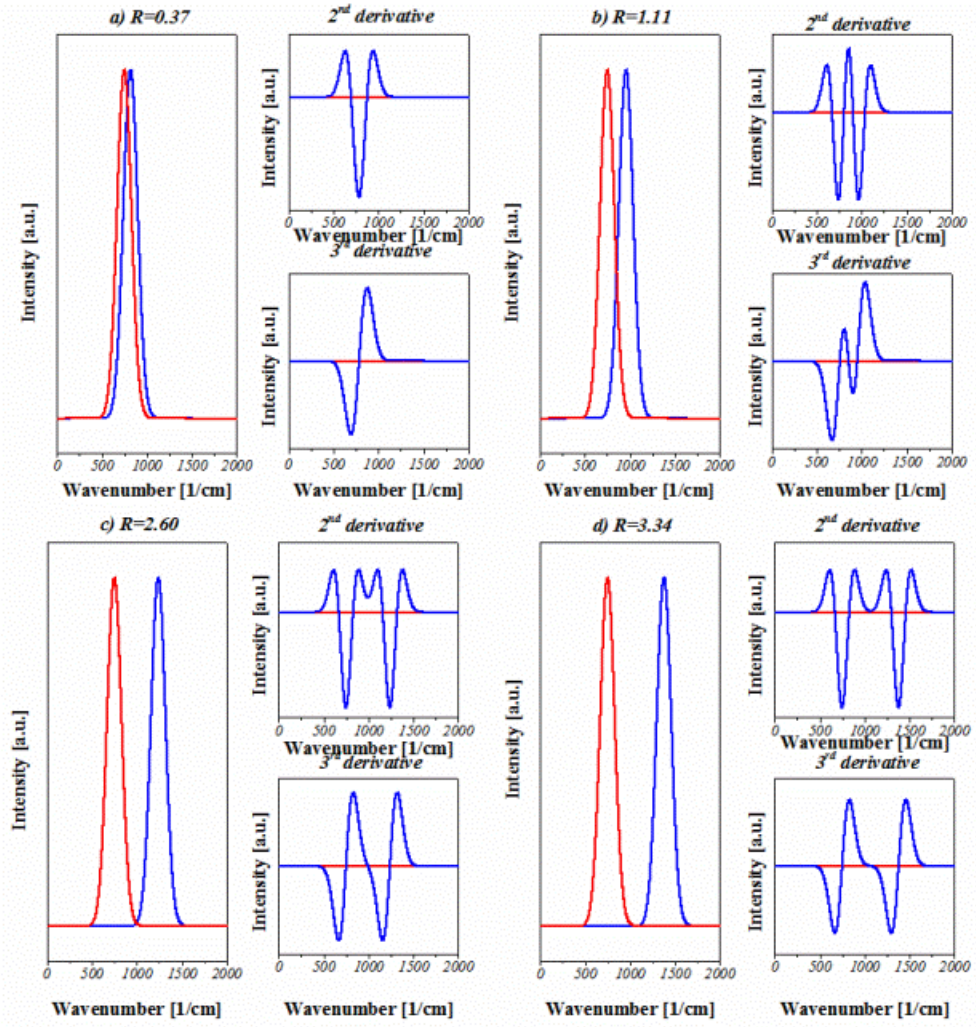

Figure 3.14. Overlapping Gaussian peaks and their second and third derivatives: **a)** R=0.37; **b)** R=1.11; **c)** R=2.6; and **d)** R=3.34.

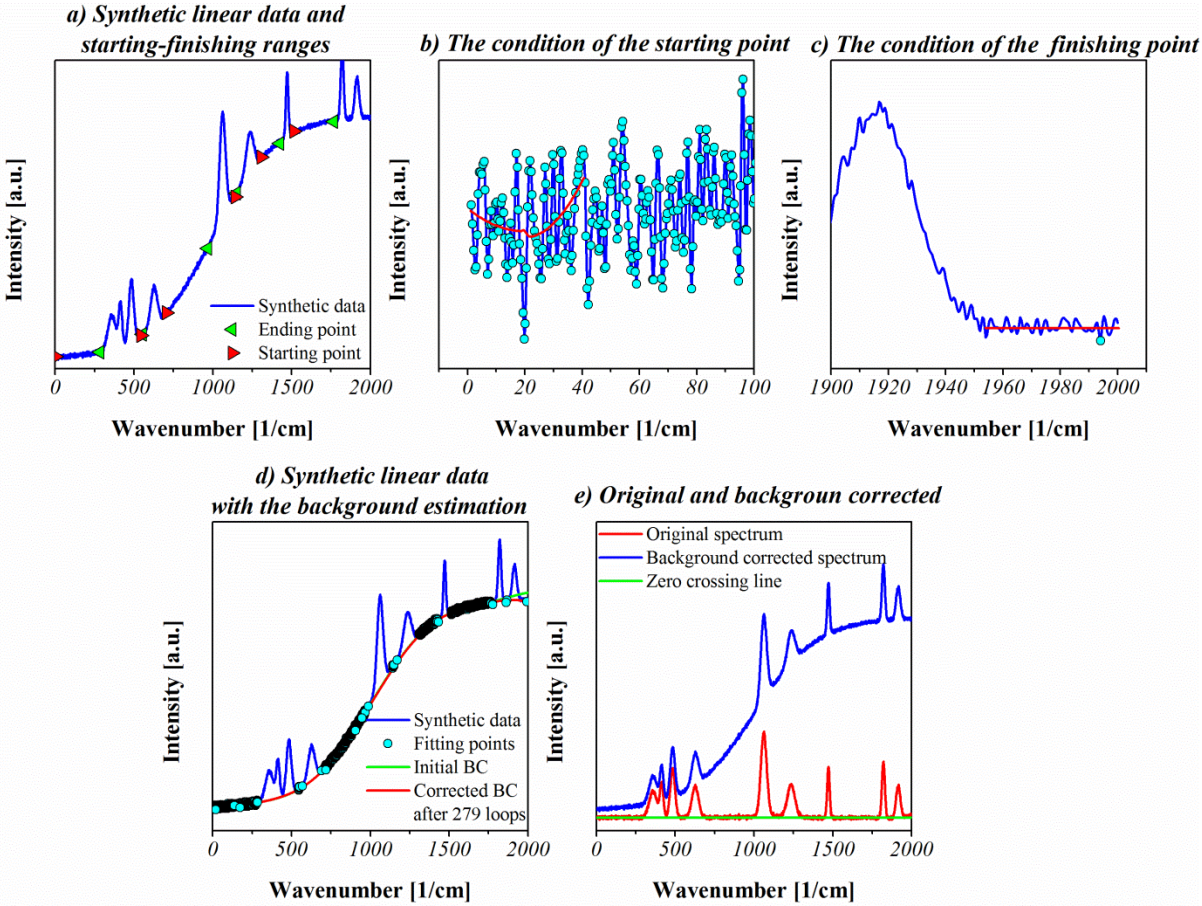

Figure 3.15. a) Spectrum with starting and finishing points of background; **b)** Starting condition of the spectrum (Subclass=0); **c)** Ending condition of the spectrum (Subclass=4); **d)** Background points and their fittings, wherein green dashed and magenta curves relate to starting fitting curve and corrected background after 314 loops, respectively; and **e)** Original spectrum with the background corrected one.

SNR estimation and background correction results for a spectrum with other types of background are shown in the Appendix A.

3.4.6. Testing the accuracy of proposed algorithm

Following 900 iterations testing of the proposed algorithm in *Section 3.3.10*, a comparison between the background-removed spectrum and original signal before adding background (initial signals) was carried out. *RMSE* for the comparison between background corrected spectra with their initial signals is outlined in **Figure 3.16a**. Based on a previous study by *Rowlands et al*, most of the best background corrections have so far reported an *RMSE* value of more than 0.1. The median of *RMSE* calculated in the current algorithm is about 0.075 which is less than 0.1 indicating that this algorithm could provide a good

approximation for background correction. The frequency changes of *RMSE* are charted in **Figure 3.16b**, which typically show that more than 94% of the points have an *RMSE* lower than 0.2, out of which more than 77% impressively lie below 0.1 *RMSE*, suggesting that this algorithm would have less than 6% error in all conditions of signal features. Hence, the algorithm used in the current study could be an excellent candidate for automation. Testing of the system with varying peaks number also shows that by an increase in the number of peaks in a spectrum, the median point of *RMSE* changes slowly at the start but changes rapidly after 20 peaks (**Figure 3.17**). This behaviour is a direct consequence of the decreasing number of background points in the spectrum.

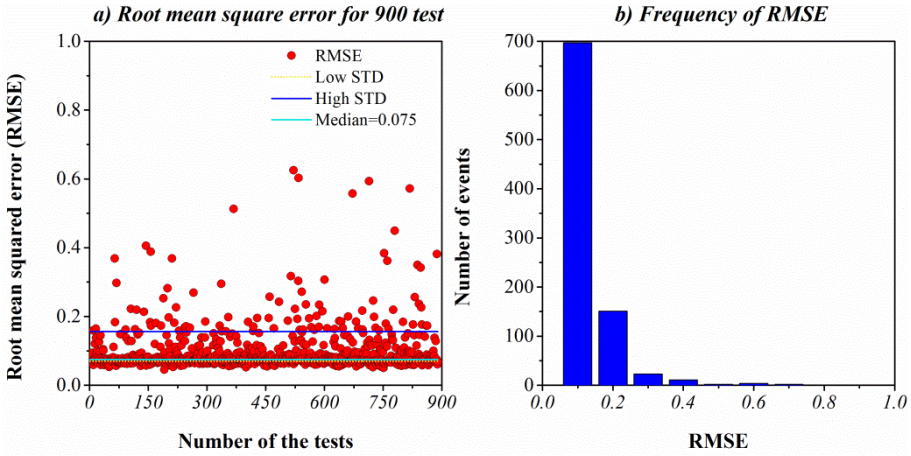

Figure 3.16. a) Root mean squared error (*RMSE*) variation during testing 900 times random spectra with 10 peaks; and **b)** Distribution of *RMSE* with number of tests.

As shown in *Section 3.1*, the values of *Best-Scale* exponentially increase with a decrease in *SNR* while an increase in the scale results in widening of the 2nd derivative peaks. Wider peaks confine the background points that can be selected between peaks. Thus, in lower *SNR*, *RMSE* has higher values, as shown in **Figure 3.18**. By an increase in *SNR*, values of *RMSE* initially show a drastic decrease, however after a while a slight increase is observed that becomes constant at higher values. The explanation for this behaviour is related to the exponential nature of the calibration curve and inaccuracies introduced by performing *CWT* on an essentially noiseless signal. Rounding the value towards positive infinity (*Ceil*) in calculating *Best-Scale* values is inevitable due to integer nature of the *CWT* scales. But it makes the *Best-Scale* constant at higher level of *SNR*. The slight increase after the initial decrease in *RMSE* could be related to this feature where for all *SNR* values larger than 80, the Best-Scale varies from 6 to 1.

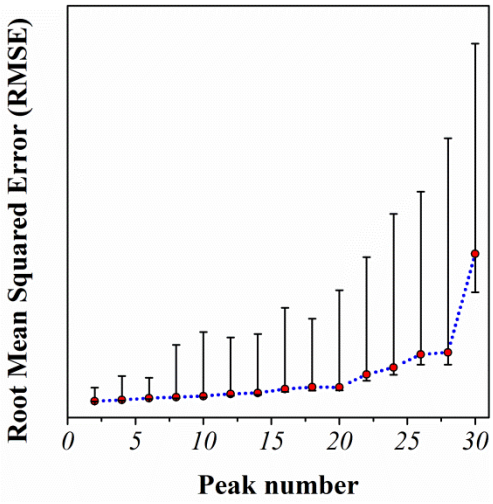

Figure 3.17. Variation of *RMSE* with peak number in the spectrum. Dot points show median of *RMSE*, and upper and lower error bars are related to *STD* of points with higher and lower *RMSE*, respectively.

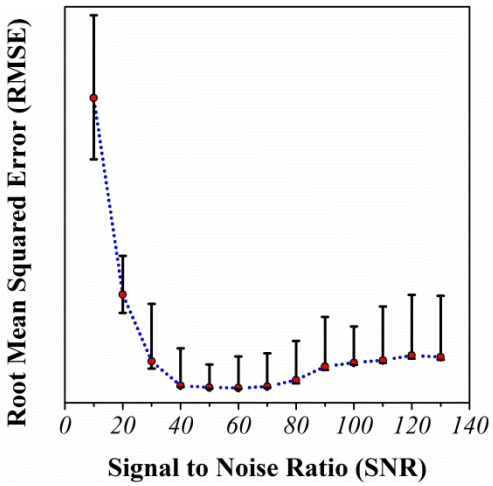

Figure 3.18. Variation of *RMSE* with *SNR* in the spectrum. Dot points show median of *RMSE*, and upper and lower error bars are related to *STD* of points with higher and lower *RMSE*, respectively.

To further check the conditions, where currently proposed algorithm might fail, extreme conditions were also chosen by employing either a very low *SNR* value of 5 (Figure 3.19), or large number of peaks corresponding to 30 (Figure 3.20), or a combination of both (Figure 3.21). The slight errors resulting from the conditions when *SNR* is significantly reduced or the number of peaks in a spectrum is significantly large, the current algorithm might introduce certain anomalies in the spectra. Therefore care must be taken while dealing with such situations.

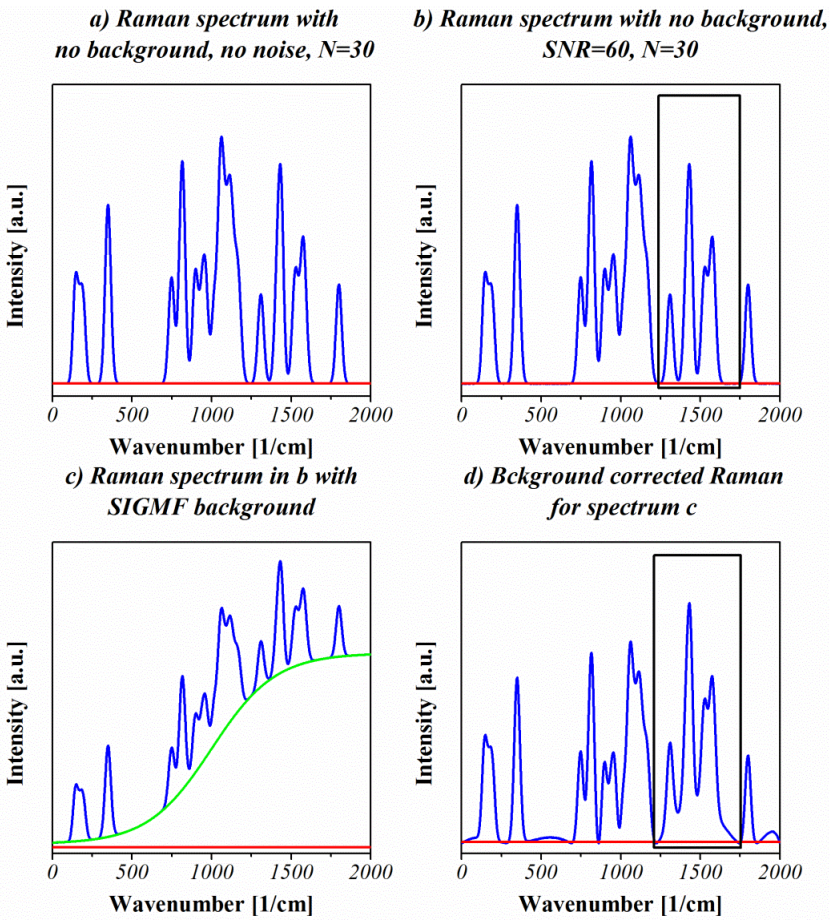

Figure 3.19. a) Raman spectrum without any background with 30 peaks and no noise, **b)** spectrum in **(a)** after introducing noise corresponding to *SNR*=60, **c)** spectrum in **(b)** after introducing a sigmoidal background, and **d)** background corrected spectrum of that shown in **(c)**. The rectangular boxes shown in **(b)** and **(d)** highlight the errors introduced during the background correction step.

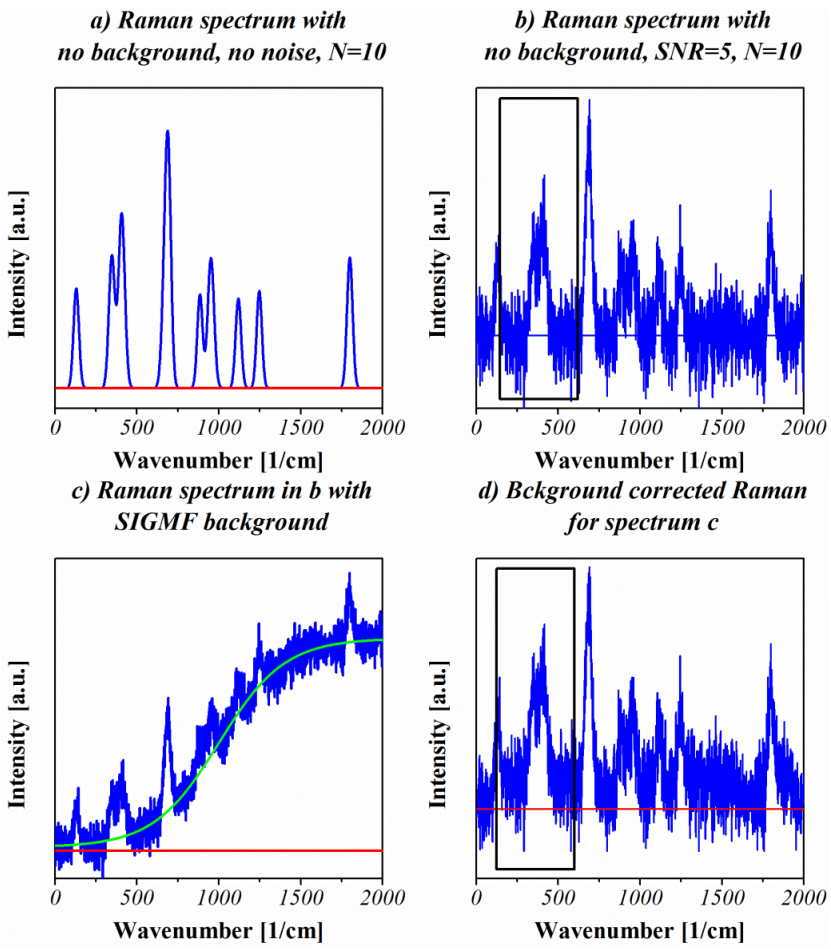

Figure 3.20. a) Raman spectrum without any background with 10 peaks and no noise, **b)** spectrum in **(a)** after introducing noise corresponding to *SNR*=5, **c)** spectrum in **(b)** after introducing a sigmoidal background, and **d)** background corrected spectrum of that shown in **(c)**. The rectangular boxes shown in **(b)** and **(d)** highlight the errors introduced during the background correction step.

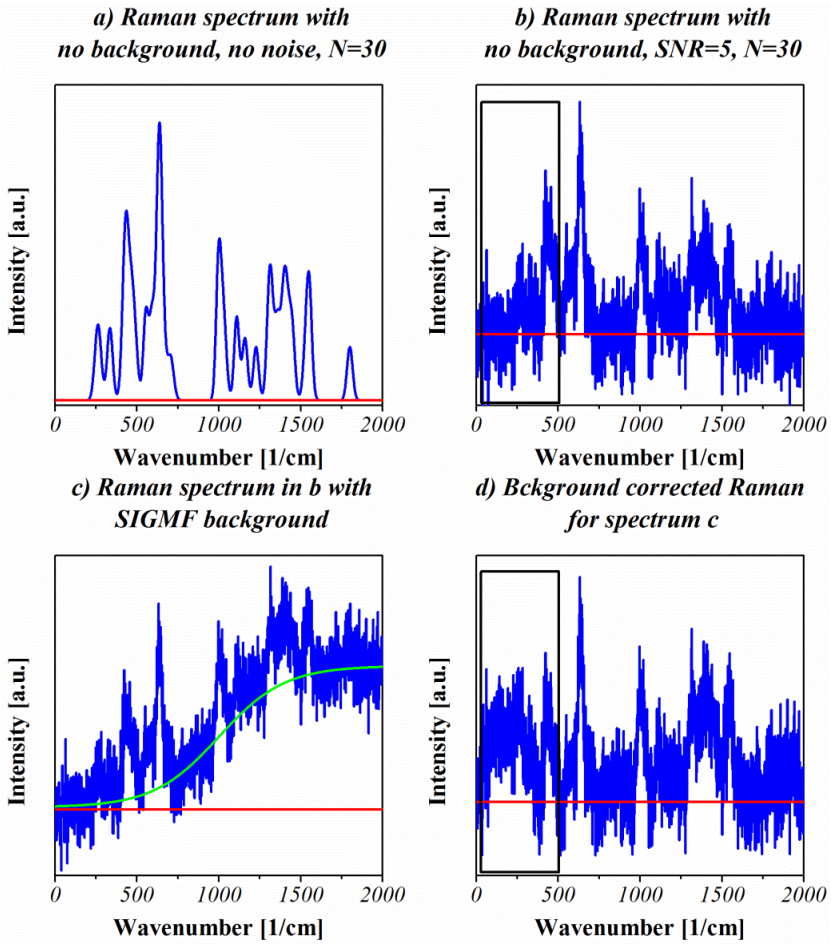

Figure 3.21. a) Raman spectrum without any background with 30 peaks and no noise, **b)** spectrum in **(a)** after introducing noise corresponding to *SNR*=5, **c)** spectrum in **(b)** after introducing a sigmoidal background, and **d)** background corrected spectrum of that shown in **(c)**. The rectangular boxes shown in **(b)** and **(d)** highlight the errors introduced during the background correction step.

3.4.7. Experimental results

Application of the current algorithm for background correction of four different noisy experimental systems (L-serine, Rhodamine B, Methyl-red and crystal violet) is outlined in **Figure 3.22**. Analysis of the performance of the algorithm in real data could not be done due to the inherent inability to obtain the experimental data without a background to compare with results. However, the proposed algorithm shows good performance in most cases, with the exception of a few minor errors resulting from the condensation of peaks (**Figure 3.22b**). Interestingly, the end effect errors are considerably less than the commonly reported studies

due to the ability of algorithm reported in this study to follow background feature in the end points.

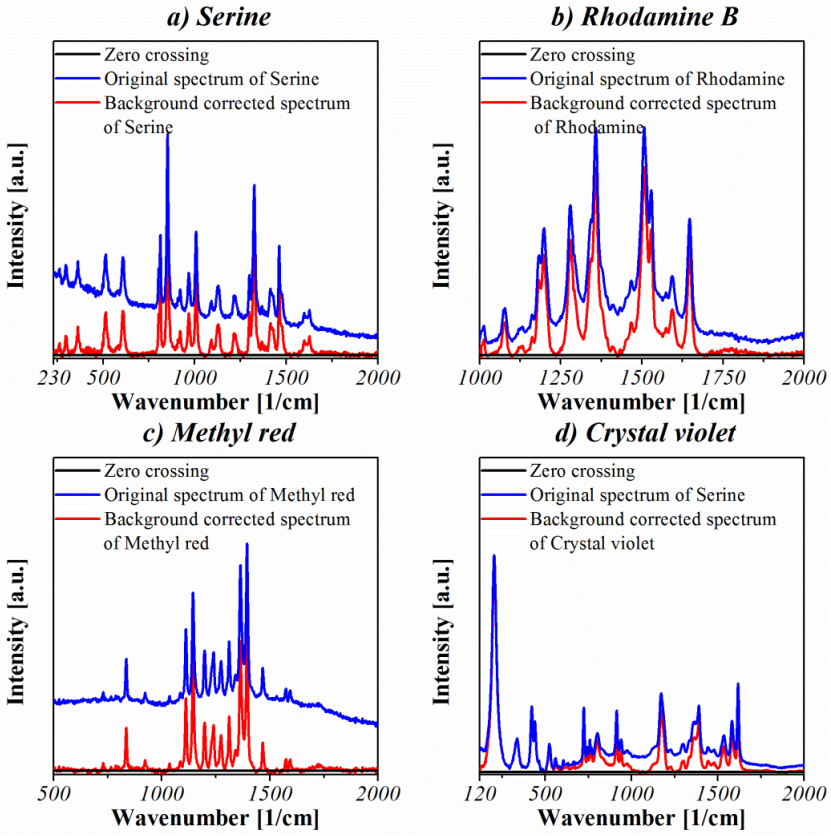

Figure 3.22. Examples of application of the current algorithm for experimentally obtained real Raman spectra: **a)** Serine amino acid; **b)** Rhodamine B; **c)** methyl red and **d)** crystal violet.

3.5. Conclusion

In conclusion, a new algorithm has been provided based on continuous wavelet transformation for baseline correction of Raman spectra with the ability to work with noisy signals without de-noising. The algorithm is benefitted from *CWT* thereby enabling to work directly with noisy signal, and *SRM* for enabling peak removal from the signal and finding the background shape. The *CWT* method eliminates the needs for smoothing the signal and also gives a good approximation to estimate peaks starting and finishing points due to its ability to calculate 2nd derivative of the noisy spectrum. On the other hand, using *SRM*, the peaks remain untouched and background estimation can be achieved using fitting of the remaining data points in the spectrum.

This algorithm has been tested for accuracy for each section of programming and has acceptable errors that make it applicable to most of the data analysis essential for Raman spectroscopy. The accuracy tests as well as experimental results showed that this algorithm could be implemented in the cases where automatic baseline detection is necessary. This approach could address the problems of background corrections on real data where the quality of spectra is low (e.g. biological low power Raman spectroscopy). Furthermore, based on accuracy tests, this approach has a minimal variance in the relative peak intensities during analyses.

References

1. Schulze, G.; Jirasek, A.; Yu, M. M. L.; Lim, A.; Turner, R. F. B.; Blades, M. W., *Applied Spectroscopy* **2005,** *59* (5), 545-574.
2. Ling, Y.-C.; Vickers, T. J.; Mann, C. K., *Applied Spectroscopy* **1985,** *39* (3), 463-470.
3. Kneen, M. A.; Annegarn, H. J., *Nuclear Instruments and Methods in Physics Research Section B: Beam Interactions with Materials and Atoms* **1996,** *109–110* (0), 209-213.
4. Dietrich, W.; Rüdel, C. H.; Neumann, M., *Journal of Magnetic Resonance (1969)* **1991,** *91* (1), 1-11.
5. Člupek, M.; Matějka, P.; Volka, K., *Journal of Raman Spectroscopy* **2007,** *38* (9), 1174-1179.
6. Donnelle, D.; Rust, B., *Computing in Science & Engineering* **2005,** *7* (2), 80-88.
7. Chrimes, A. F.; Khoshmanesh, K.; Stoddart, P. R.; Kayani, A. A.; Mitchell, A.; Daima, H.; Bansal, V.; Kalantar-zadeh, K., *Analytical Chemistry* **2012,** *84* (9), 4029-4035.
8. Plowman, B.; Ippolito, S. J.; Bansal, V.; Sabri, Y. M.; O'Mullane, A. P.; Bhargava, S. K., *Chemical Communications* **2009,** (33), 5039-5041.
9. Šćepanović, M.; Grujić-Brojčin, M.; Vojisavljević, K.; Bernik, S.; Srećković, T., *Journal of Raman Spectroscopy* **2010,** *41* (9), 914-921.
10. Pearson, A.; O'Mullane, A. P.; Bansal, V.; Bhargava, S. K., *Inorganic Chemistry* **2011,** *50* (5), 1705-1712.
11. Pearson, A.; O'Mullane, A. P.; Bhargava, S. K.; Bansal, V., *Inorganic Chemistry* **2012,** *51* (16), 8791-8801.
12. Fujimori, H.; Komatsu, H.; Ioku, K.; Goto, S.; Yoshimura, M., *Physical Review B* **2002,** *66* (6), 064306.

13. Wang, H.; Fu, Y.; Zickmund, P.; Shi, R.; Cheng, J.-X., *Biophysical Journal* **2005,** *89* (1), 581-591.
14. Shao, X.-G.; Leung, A. K.-M.; Chau, F.-T., *Accounts of Chemical Research* **2003,** *36* (4), 276-283.
15. Zhang, X. Q.; Zheng, J. B.; Gao, H., *Analyst* **2000,** *125* (5), 915-919.
16. Salomaa, I. K.; Kauppinen, J. K., *Applied Spectroscopy* **1998,** *52* (4), 579-586.
17. Chakrabarti, C.; Vishwanath, M.; Owens, R., *J VLSI Sign Process Syst Sign Image Video Technol* **1996,** *14* (2), 171-192.
18. Charles, C.; Leclerc, G.; Pireaux, J.-J.; Rasson, J.-P., *Surface and Interface Analysis* **2004,** *36* (1), 49-60.
19. Leung, A. K.-m.; Chau, F.-t.; Gao, J.-b., *Analytical Chemistry* **1998,** *70* (24), 5222-5229.
20. Sheng, Y.; Roberge, D.; Szu, H. H., *Optical Engineering* **1992,** *31* (9), 1840-1845.
21. Nie, L.; Wu, S.; Lin, X.; Zheng, L.; Rui, L., *Journal of Chemical Information and Computer Sciences* **2002,** *42* (2), 274-283.
22. Xiaoquan, L.; Hongde, L.; Zhonghua, X.; Qiang, Z., *Journal of Chemical Information and Computer Sciences* **2004,** *44* (4), 1228-1237.
23. Rojas, F. S.; Ojeda, C. B.; Pavon, J. M. C., *Talanta* **1988,** *35* (10), 753-761.
24. Morrey, J. R., *Analytical Chemistry* **1968,** *40* (6), 905-914.
25. Horvath, M. P.; Copeland, R. A.; Makinen, M. W., *Biophysical Journal* **1999,** *77* (3), 1694-1711.
26. Rowlands, C.; Elliott, S., *Journal of Raman Spectroscopy* **2011,** *42* (3), 363-369.
27. Wang, Y.; Yan, B.; Chen, L., *Chemical Reviews* **2012,** *113* (3), 1391-1428.
28. Li, Q..; Li, B..; Wang, Y., *RSC Advances* **2013,** *3* (32), 13015-13026.
29. Gregoire, J. M.; Dale, D.; van Dover, R. B., *Review of Scientific Instruments* **2011,** *82* (1),015105.

CHAPTER IV

Fabrication of ZnO and ZnO/Ag nano-arrays for SERS biosensing

In this chapter, to develop high quality, reproducible, stable and recyclable *SERS* substrates, the effects of synthesis parameters on the formation and properties of ZnO/Ag nano-arrays were studied. At few first sections of this chapter, a comprehensive study was performed to develop a reproducible and highly controllable synthesis method to produce well aligned ZnO nano-arrays. Then, different approaches were carried out to decorate the obtained ZnO nano-arrays with silver nanoparticles. Facile soft chemical synthesis strategies were employed to fabricate Raman-active and recyclable ZnO/Ag nanorod arrays as highly reproducible surface enhanced Raman scattering (*SERS*) substrates. The controlled Ag nanoparticle deposition parameters enabled decoration of uniform density of SERS-active hot-spots on ZnO nano-arrays on a large 1 cm × 1 cm substrate. These ZnO/Ag nano-arrays showed outstanding reproducibility towards acquiring SERS spectra of Rhodamine-B as a probe molecule at 30 random locations on a single substrate. The photocatalytic nature of ZnO/Ag semiconductor-metal heterojunction was exploited to endow these SERS substrates with reusability characteristics. The study shows that by controlling optimal metal loading on a semiconductor surface, high photocatalytic activity and SERS performance can be obtained.

Part of the work presented in this chapter has been published at:

Kandjani, A. E.; Mohammadtaheri, M.; Thakkar, A.; Bhargava, S.K.; Bansal, V.; ZnO/Ag nano-arrays as reusable SERS substrates with controllable 'hot-spots' for highly reproducible molecular sensing, *Journal of Colloid and Interface Science*, 436 (2014) pp. 251–257.

4.1. Introduction

In order to fabricate a reliable sensing platform, several criteria need to be considered in production processes. In SERS based platforms, control in the uniformity of the features of SERS active metals on the surface is one of the critical points, which should be considered to generate uniform Raman enhancement throughout the sample surface. Thus, structure, pattern and distances between active SERS materials need to be controlled to generate uniform 'hot spots' on the surface of the SERS based sensors[1]. This could be achieved by controlling the deposition of the SERS active metal structures on substrates.

Similarly, a reliable photocatalytic surface requires the reproducible design of surfaces with uniform distribution of semiconductor nanostructures[2]. Furthermore, they need to have high surface area with low surface defect density in order to increase the photocatalytic activity. Thus fabricating nano arrays of semiconductors with high photocatalytic activities like ZnO[3], TiO_2[4] and GaN[5] have attracted many researchers' attentions. Among these materials, ZnO is one of the materials that has the capability to make uniform nano-arrays with long range order via soft-chemical approaches. The semiconducting properties of ZnO nanostructures are largely dependent on their compositions, crystal structure, dimension, and morphology[6]. A better understanding of the chemical processes involved in the growth of one-dimensional ZnO nanostructures is essential for designing photocatalytic substrates with desired structural and functional properties.

Considering the SERS sensing and photocatalytic activities of semiconductor materials, combining these two properties can make each substrate having two functionalities. ZnO based materials, due to their high surface area, single crystalline nature and uniformity in nano-range scale, are among the best candidates for developing multifunctional substrates for applications requiring both SERS and photocatalysis.

In this chapter, important synthesis aspects for forming zinc oxide nano arrays were studied. In order to add the SERS functionality on ZnO based photocatalytic substrate, these fabricated nano arrays were then decorated with silver nanoparticles. Silver nanoparticles were decorated on the ZnO nano-arrays via photoreduction and

electroless plating methods. The effects of the synthesis variables on the final morphology and structure of the materials were studied. The developed materials were finally tested for their photocatalytic and SERS activities.

4.2. Materials and methods

Chemicals: All the chemicals were purchased from Sigma Aldrich and used as received. Deionized MilliQ water (18.2 MΩm) was used throughout the synthesis process. Si (001) substrates (1 cm × 1 cm) were employed for the growth of ZnO nano-arrays, which were cleaned using sequential washing and ultrasonication in acetone, ethanol and isopropanol before drying under nitrogen. Further, to eliminate any remaining organic traces from the Si surface, the substrates were exposed to UV-Ozone (UVO Cleaner Plus) for 10 min.

Fabrication of ZnO seed layers via sputtering method: Initially for testing ZnO nano-arrays fabrication, ZnO thin film was sputtered on the cleaned silicon wafer. The substrate temperature was kept at 500 °C and sputtering was carried out to fabricate 400 nm crystalline ZnO pin-hole free ZnO thin films. A thin film of photoresist was then coated on the substrates for eliminating possible scratches during the transport and dicing of the substrates. Finally, the substrates were diced into 1 cm × 1 cm pieces.

Fabrication of ZnO seed layers via sol-gel method: In addition to the sputtering method, a different method was also used to fabricate ZnO seed layer. In this method a uniform ZnO layer was coated on Si wafers via sol-gel process. Briefly, ethanolic solution of zinc acetate dehydrate was mixed with monoethanolamine (MEA) in equal weight ratio, followed by aging the mixture at 55 °C for 24 h and spin coating 300 µL of this solution on to Si wafers at 3500 rpm for 15 sec. The substrates were dried at 95 °C for 10 min and the spin coating procedure was repeated several times before annealing the substrates. The effect of sol-gel synthetic parameters on the formation and uniformity of zinc oxide nano-arrays were studied.

Fabrication of ZnO nanorod arrays: For the hydrothermal growth of ZnO nanorod arrays, 50 mL solution containing aqueous zinc nitrate hexahydrate and hexamine was transferred to sealed glass autoclaves. The substrates were floated on the top of the solution in the autoclaves such that the ZnO thin film side of the substrate faced the solution. The hydrothermal reaction was allowed to proceed at 95 °C, followed by

collecting the Si/ZnO nanorod array substrates and rigorous washing with deionized water before drying with N_2 gas under ambient conditions. The effects of the concentration of the precursor and period of the hydrothermal reaction on morphology of the ZnO nanorod arrays were studied.

Decoration of Si/ZnO nanorod arrays with Ag-NPs via photo-reduction: ZnO nanorod arrays (1 cm x 1 cm) were decorated with Ag-NPs using phto-reduction method. This involved the immersion of ZnO films into an aqueous solution of silver salt following by nitrogen purging for 30 min and finally illumination of the solution (mercury lamp, 354 nm) for 2h. For each sample, 9 mL of aqueous solution of silver salt ($AgNO_3$ and Ag_2SO_4) with 1 mL of propanol was prepared. The role of the propanol was to trap the possible oxidant radical forming during UV reduction process. The effect of the solution concentration on the decoration of ZnO arrays was studied. The schematic of ZnO/Ag (phototreduced) nano-arrays fabrication is shown in **Figure 4.1**.

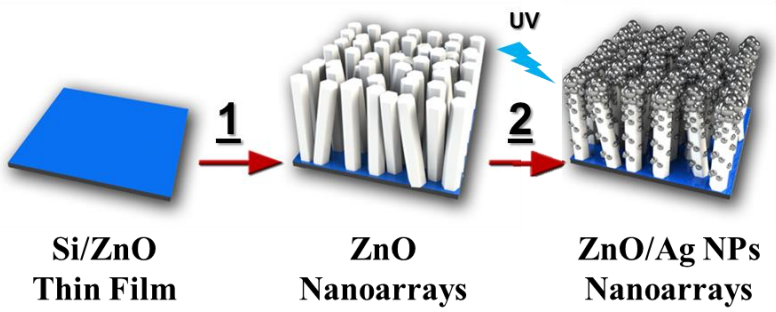

Figure 4.1. Schematic representation of fabrication of ZnO/Ag nano-arrays on a Si substrate which involves (1) hydrothermal growth of ZnO nano-arrays onto Si wafer spin-coated with ZnO thin film, (2) photocatalytic reduction of AgNPs using UV irradiation.

Decoration of Si/ZnO nanorod arrays with Ag-NPs via electroless plating: ZnO nanorod arrays (1 cm x 1 cm) were also decorated with Ag-NPs using an electroless deposition method, wherein initially ZnO was sensitized for 30 min with a 2 mL aqueous solution containing 0.3 mM $SnCl_2$ and 0.1 µL trifluoroacetic acid. After washing with water, the substrates were immersed in 2 mL of 3 mM aqueous $Pd(NO_3)_2$ for 10 min to form Pd nuclei that acted as seeds for silver plating in the next step. The density of AgNPs on the surface of Sn- and Pd-sensitized ZnO nanorod arrays was controlled by exposing these substrates initially to different concentrations

of 1 mL diaminesilver(I) complex ($[Ag(NH_3)_2]^+$), followed by addition of 1 mL of glucose solution (1 M) to reduce this complex at room temperature. The substrates were collected after 1, 3 and 6 min of reaction, washed with water and dried under N_2 gas prior to further use. Effects of the initial silver concentration, time of the synthesis as well as the effects of the sensitizing and catalytic steps on the decoration of the ZnO nano-arrays were studied. The schematic of ZnO/Ag (electroless plating) nano-arrays fabrication is shown in **Figure 4.2**.

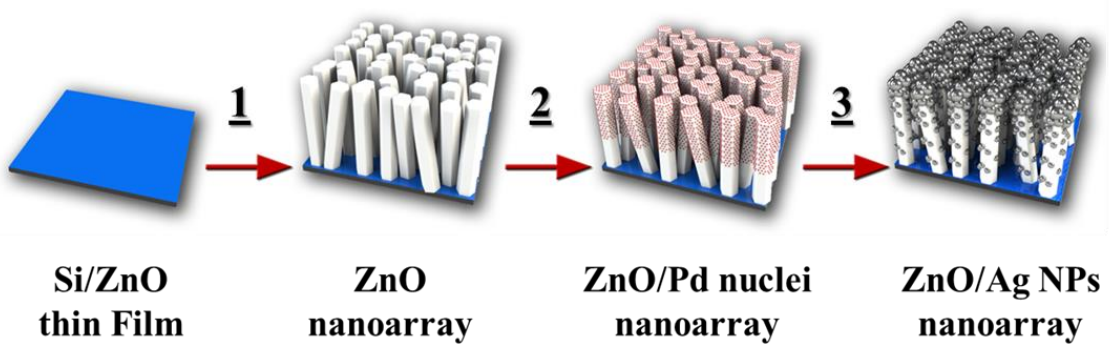

Figure 4.2. Schematic representation of fabrication of ZnO/Ag nano-arrays on a Si substrate which involves (1) hydrothermal growth of ZnO nano-arrays onto Si wafer spin-coated with ZnO thin film, (2) sensitization of ZnO nano-arrays with Sn and Pd, followed by (3) electroless plating of AgNPs onto ZnO nano-arrays.

Substrate characterization: Prepared substrates were characterized using different microscopic and spectroscopic techniques. Morphological studies were performed using field emission scanning electron microscope (SEM - FEI Nova NanoSEM), X-ray diffraction (XRD) patterns were collected using Bruker AXS X-ray diffractometer employing Cu-Kα radiation, X-ray photoelectron spectroscopy (XPS) surface analyses were carried out by a Thermo Scientific K-Alpha instrument using un-monochromatized Mg Kα radiation (photon energy 1253.6 eV) under vacuum better than 10^{-9} Torr, and XPS core levels were aligned to the adventitious C 1s binding energy (BE) of 285 eV.

Evaluation of SERS activity: Rhodamine B (RB) was selected as a model probe molecule to evaluate the SERS activity of the prepared substrates. RB was bound to the substrates by immersing substrates independently in 1 mL of 100 µM RB for 1 h in the dark, followed by rinsing the substrates with deionized water and air drying. Raman spectroscopy measurements were performed using Perkin Elmer Raman

Station 200F (785 nm laser) with a spot size of 100 µm, 5 sec exposure time and 10 acquisitions averaged with the background correction feature disabled. The backgrounds of Raman spectra were corrected using algorithm developed in *Chapter III*. Since ZnO is a wide band-gap semiconductor with an optical absorption edge of ~370 nm, 785 nm laser source was used for SERS studies so that the possibility of the degradation of RB molecules during Raman measurements could be avoided.

Evaluation of photocatalytic performance and substrate recyclability as a self-cleaning SERS biosensor: Photocatalytic activity of ZnO/Ag nano-arrays was tested by exposing substrates to 1 mL of 10 µM RB in the dark for 1 h before their exposure to UV irradiation in a time-dependent manner. The uniform UV exposure to the substrates was ensured by employing an 18 W, 370 nm LED (Edmund Optics) with attached heat sink (to avoid sample heating) 5 cm above the substrate. The time-dependent photodegradation of RB was determined by monitoring the change in the absorbance intensity of the RB using EnVision Multilabel Plate Reader (PerkinElmer). The photodegradation efficiency of ZnO/Ag nano-arrays was estimated as:

$$Photodegradation\ efficiency = \frac{(C_0 - C)}{C_0} \times 100 \qquad 4.1$$

wherein C_0 and C correspond to RB concentrations before and after irradiation, respectively.

SERS substrate recyclability studies were performed over three cycles. Each of these cycles involved immersion of ZnO/Ag nano-arrays in RB and collection of their SERS spectrum. This was followed by substrate cleaning through rinsing with deionized water, exposing the substrate to UV irradiation for 30 min to photodegrade RB, further rinsing with deionized water and air drying. Raman spectrum was collected again from the same substrate by re-exposing it to RB and the process was repeated three times to ensure recyclable SERS detection. The schematic of the sensing and recycling is shown in **Figure 4.3**.

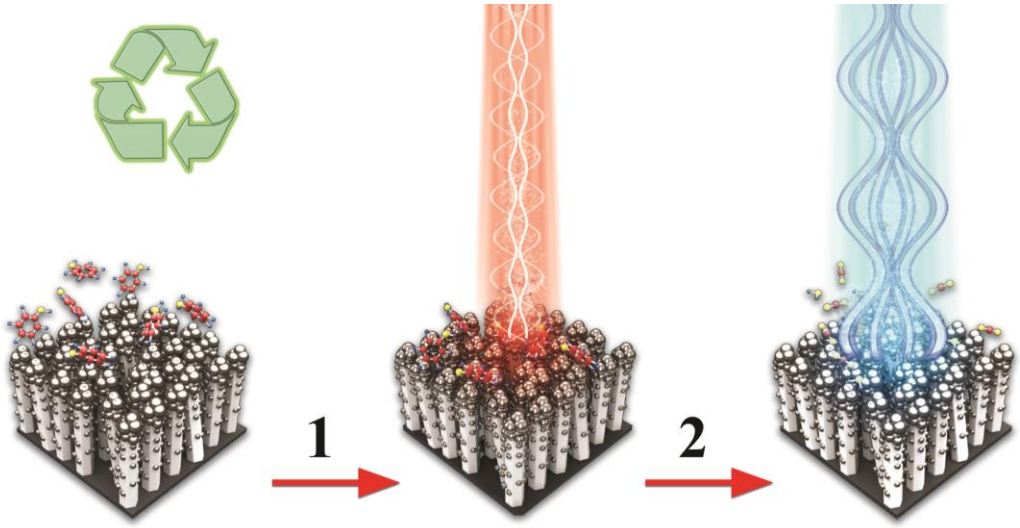

Figure 4.3. Schematic for 1) detection and 2) Photocatalytic removal of organic marker for regeneration of SERS sensor.

4.3. Zinc oxide nano-arrays

4.3.1. Mechanism

In the synthesis procedure of ZnO nano-arrays, hexamine (HMTA) and $Zn(NO_3)_2$ were used. In this synthesis form, Zn^{2+} ions are provided by zinc nitrate for fabrication of ZnO nano-arrays where oxygen atoms are sourced directly from water molecules. HMTA is a non-ionic cyclic tertiary amine. It has been shown that two Zn^{2+} ions can be bridged with HMTA forming tetradentate ligands, which act as bidentate ligands[7].

Furthermore, HMTA has high affinity toward non-polar surfaces of the ZnO crystals and acts as a capping agent and decreases the kinetics of the growth of these crystal planes. Therefore, anisotropical growth of zinc oxide occurs in [0001] crystallite direction[8]. It has been shown that HMTA hydrolyses in water and produces ammonia and formaldehyde. The formed ammonia can react with zinc ions to form zinc ammonium complexes as well as also zinc hydroxide. The reaction procedure can be summarized as below:

$$HMTA + 6H_2O \leftrightarrow 4NH_3 + 6HCHO \quad (4.2)$$

$$NH_3 + H_2O \leftrightarrow NH_4^+ + OH^- \quad (4.3)$$

$$Zn^{2+} + 4NH_3 \leftrightarrow [Zn(NH_3)_4]^{2+} \quad (4.4)$$

$$Zn^{2+} + 2OH^- \leftrightarrow Zn(OH)_2 \quad (4.5)$$

$$Zn(OH)_2 \rightarrow ZnO + H_2O \quad (4.6)$$

The production of ammonia in the solution due to hydrolysis of HMTA is a very slow process, thus, low amounts of OH^- ions are consumed gradually, and no sudden growth and precipitation can occur. This slow kinetics allows a rapid consumption of the solution reactants as well as prohibits the oriented growth of ZnO nanowires[9-10]. Formed ammonia has two roles in the reaction, providing basic environment necessary for $Zn(OH)_2$ formation and stabilization of Zn^{2+} ions through its coordinating with zinc ions. Zinc hydroxide can be converted into zinc oxide by providing appropriate heat. As all of the reactions related to forming $Zn(OH)_2$ are in equilibrium, the reaction can be controlled by synthesis variables, which are precursor ($Zn(NO_3)_2$) concentration, growth temperature and growth time. Precursor concentration controls the density of the nano-arrays while temperature and time control morphology and aspect ratio of the formed nano-arrays[11-12]. As decomposition of HMTA results in increase entropy, the reaction kinetics can be highly increased by increasing the temperature[13].

One of the main advantages of using soft chemical method for fabricating ZnO nano-arrays is that ZnO can be grown on to almost any substrate, such as Si wafer, paper[14], organic substrates[15] and even textile[16]. But most important point in all these methods is that the seeding layer should have a proper adhesion with the substrate. ZnO nano-array can also be grown on the surfaces such as gold without any seeding layer[11]. However, by using a seed layer the advantage is its capability to make a uniform and large-area growth of nano-arrays on any substrates. The main role of the seed layer in the growth of the nano-arrays is the growth of the ZnO nan-rods on the seed through heterogeneous growth. This heterogeneous growth, due to the existence of seed layer, is energetically more favourable because the existing seeds bypass the nucleation step.

The seed layer can be prepared by various methods, soft chemical methods (e.g sol-gel[17] and spin coating of ZnO colloidal nanoparticles[18]), sputtering[19] and laser ablation[20]. The orientation and also the density of the nano-arrays are highly dependent on the crystallinity of the seed layer. Most of the ZnO nano-arrays have preferential growth toward c-axis which results in their growth perpendicular to their substrate surface[21].

In sol-gel process, first $Zn(Ac)_2$ is hydrolysed in the absolute ethanol. The positively charged Zn complex can attach to the ethanolamine and with the aid of the water in the structure of zinc acetate, these complexes can form a frame for sol-gel. These structures then attach to each other via hydrogen bonding and form a net which is known as sol. After drying the sol, these complexes break apart and form ZnO crystallites with short ordering[22-23]. As the

complexes are decomposed at low temperature, short ordering of ZnO crystallites (amorphous structure) forms on the substrate. The thin film can be crystalized using proper heat treatment. Thus, crystallite size and structural ordering of materials can be controlled[24].

4.3.2. Effect of hydrothermal conditions

Effect of Zn^{2+} concentration: The sputtered ZnO thin films were used as seed layer for growth of ZnO nano-arrays. The concentration of the $Zn(NO_3)_2$ was varied from 1 mM to 100 mM. The synthetic conditions for fabricating ZnO nano-arrays were kept constant [$\frac{Zn(NO_3)_2}{HMAT} = 1$; Temperature=95 °C and Time=6 h]. As shown in **Figure 4.4**, the density of the nanorods of ZnO is increased with increasing $Zn(NO_3)_2$ concentration. By reaching to 12.5 mM concentration of Zn^{2+} ions in the hydrothermal solution a full coverage of ZnO nano-arrays can be achieved. Above this concentration, due to existence of the higher amount of precursors in the solution, the produced nanorods grow longer and thicker. At 50 mM, the grown nanorods tend to merge to each other and gradually form a dense layer of the ZnO film. At higher concentrations, these compact layers can also allow a secondary growth of layered ZnO nano structures in the form of thin film. At these high concentrations, the morphology of the ZnO nano-arrays completely changes into a thick film of ZnO structures.

Effect of hydrothermal time: After finding optimal concentration (12.5 and 25 mM) for forming ZnO nano-arrays, the effect of the synthesis time in forming ZnO nano-arrays was studied. The hydrothermally grown ZnO nano-arrays were collected at 1.5 h to 6 h as shown in **Figure 4.5**. The formation for the nano-arrays starts after 3 h of hydrothermal reaction while at lower $Zn(NO_3)_2$ concentration (12.5 mM), formed nano-arrays had smaller thickness as well as were thinner in diameter. For making the nano-arrays with average length of 2000 nm and width of 120 nm (Aspect ratio≈17), concentration of 25 mM $Zn(NO_3)_2$ and 6 h reaction time were chosen for fabricating hydrothermally grown ZnO nano-arrays.

4.3.3. Effect of seed layer

Edge effects in sputtering and sol-gel: As with the sputtering method, the whole wafer was put into the sputtering chamber with high temperature operation of 500 °C, resulting in highly crystalline ZnO thin films. After taking the sputtered ZnO wafer

out of the sputterer chamber, the wafers were diced with a wafer dicer into 1 cm × 1 cm pieces. By doing so a part of the sputtered thin film was always chipped off the substrate. This resulted into forming packed ZnO arrays in the edges of the samples which yielded into different morphologies at the edges of the samples compared to the rest of the substrates. On the other hand, using sol-gel for forming seed layer all corners and edges of the sample were coated uniformly, which resulted into synthesis of the uniform nano array structures throughout the surface of the samples. The morphology of the fabricated nano-arrays at the edges of the samples is shown in **Figure 4.6** for sol-gel and sputtered zinc oxide seed layers.

Effect of the number of coating cycles: The uniformity of nano-array is highly depended on the uniformity of the seeding layer. If the thickness of the sample changes in different parts of the substrate or even an island type of the seed layer is formed during the coating of the seed layer, the uniformity of the formed nano-arrays as well as their alignment changes randomly. By increasing the number of the coating this issue can be resolved as the isolated islands would be eliminated from the surface as the thickness of the seed layer will surpass the threshold needed for fabricating ZnO nano-arrays. The effect of the number of coatings used to make ZnO nano-arrays is shown in **Figure 4.7**. The results demonstrate that by applying 5 coating cycles, a well aligned sample can be fabricated. The synthesis conditions used to study the formation of ZnO nano-arrays of different number of coating cycles are 0.1 M $ZnAc_2$, weight ratio of $ZnAC_2$ to MEA equal to 1, aging temperature of 55 °C for 24 h, spin coated at 4000 rpm, dried at 70°C for 30 min and calcinated at 450 °C for 1 h.

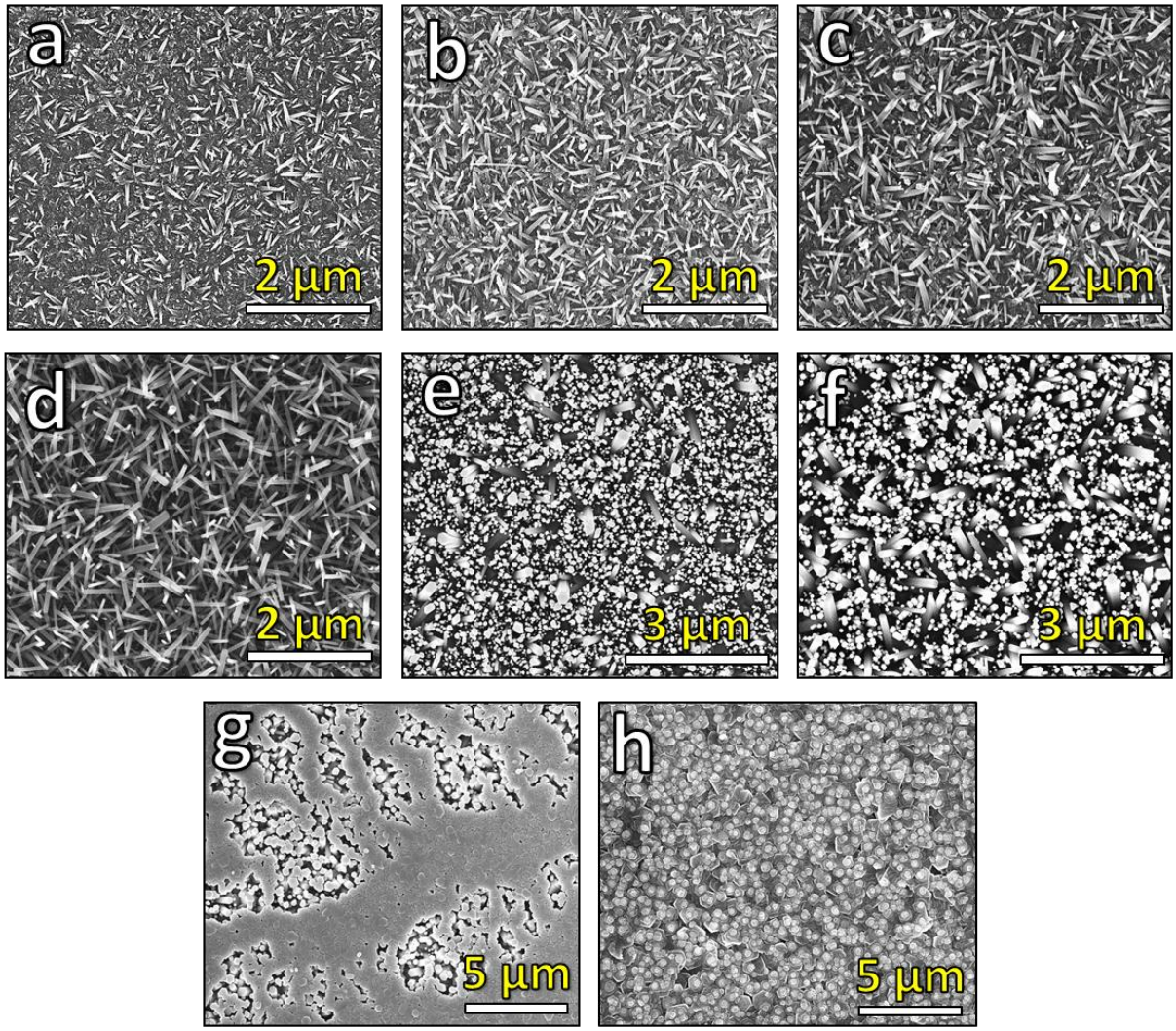

Figure 4.4. Hydrothermally grown ZnO nano-arrays on sputtered ZnO thin film (400 nm) for 6 h at 95 °C with initial $Zn(NO_3)_2$ concentrations of **a)** 1, **b)** 3, **c)** 5, **d)** 10, **e)** 12.5, **f)** 25, **g)** 50 and **h)** 100 mM.

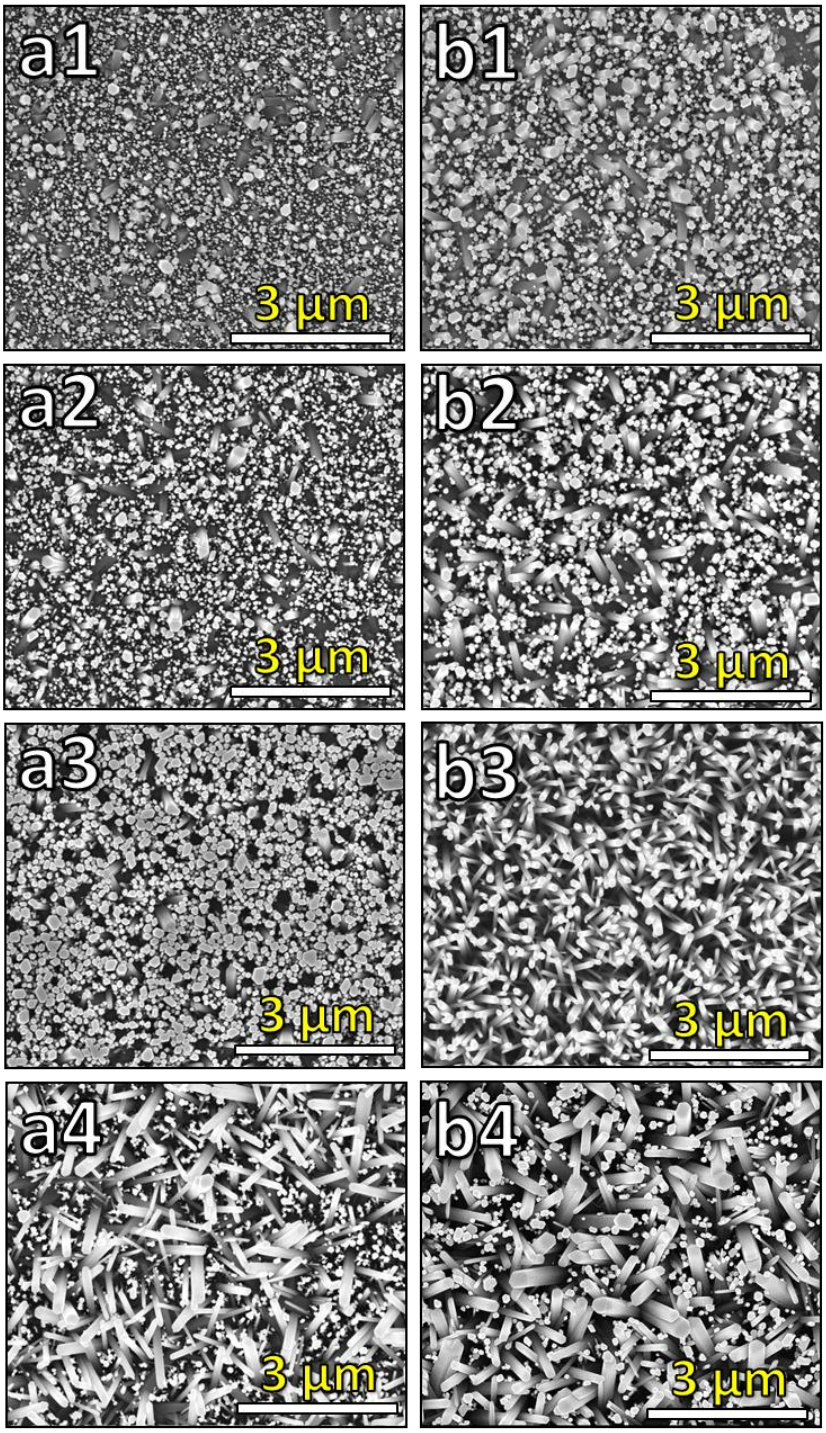

Figure 4.5. Hydrothermally grown ZnO nano-arrays on sputtered ZnO thin film (400 nm) at 95 °C with initial $Zn(NO_3)_2$ concentrations of **a)** 12.5 and **b)** 25 mM for 1) 1.5, 2) 3, 3) 4.5 and 4) 6 h.

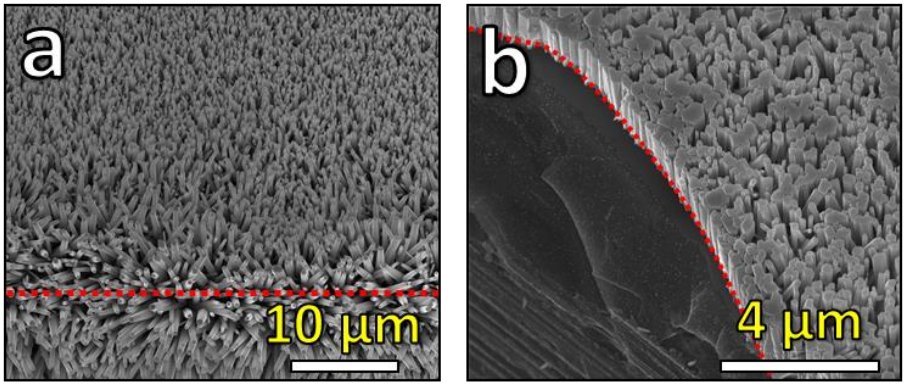

Figure 4.6. Edge effects in **a)** sol-gel and **b)** sputtered ZnO seed layers; red dashed lines show the position of the edge of the samples.

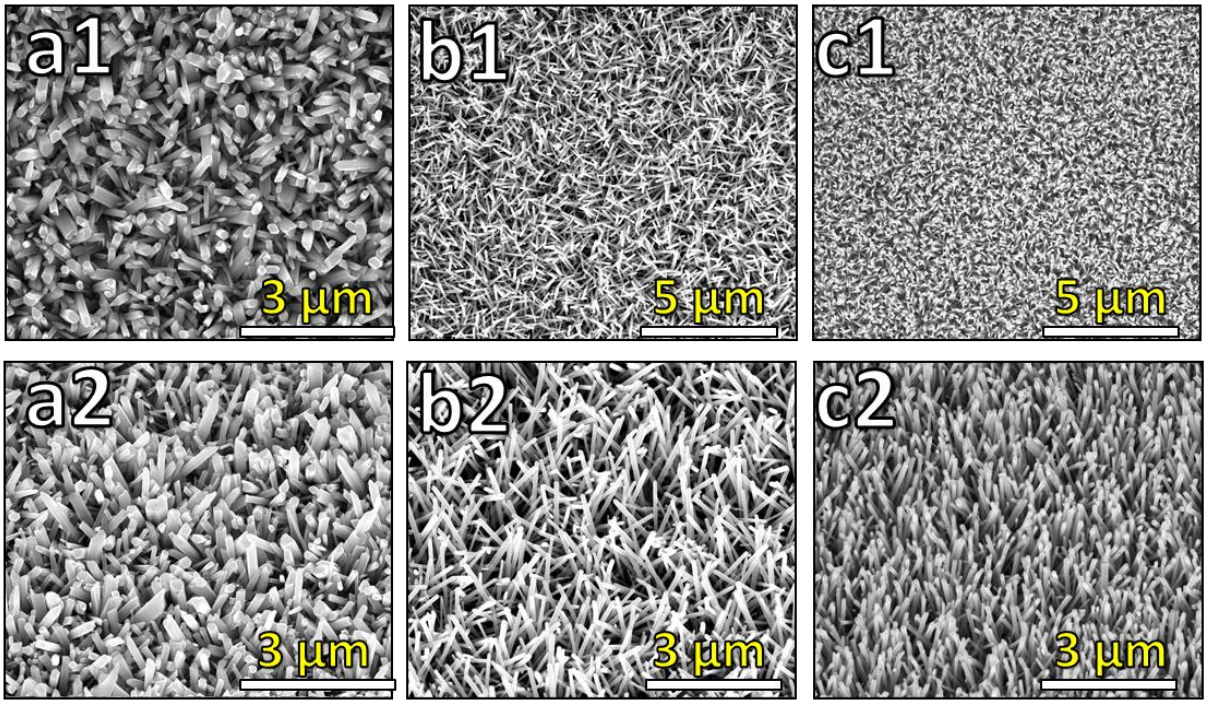

Figure 4.7. Effect of cycles of coating of ZnO seed layer on the hydrothermally grown ZnO nano-arrays for **a)** 1, **b)** 3 and **c)** 5 cycles of coatings [1) Top view and 2) angle (30°) view].

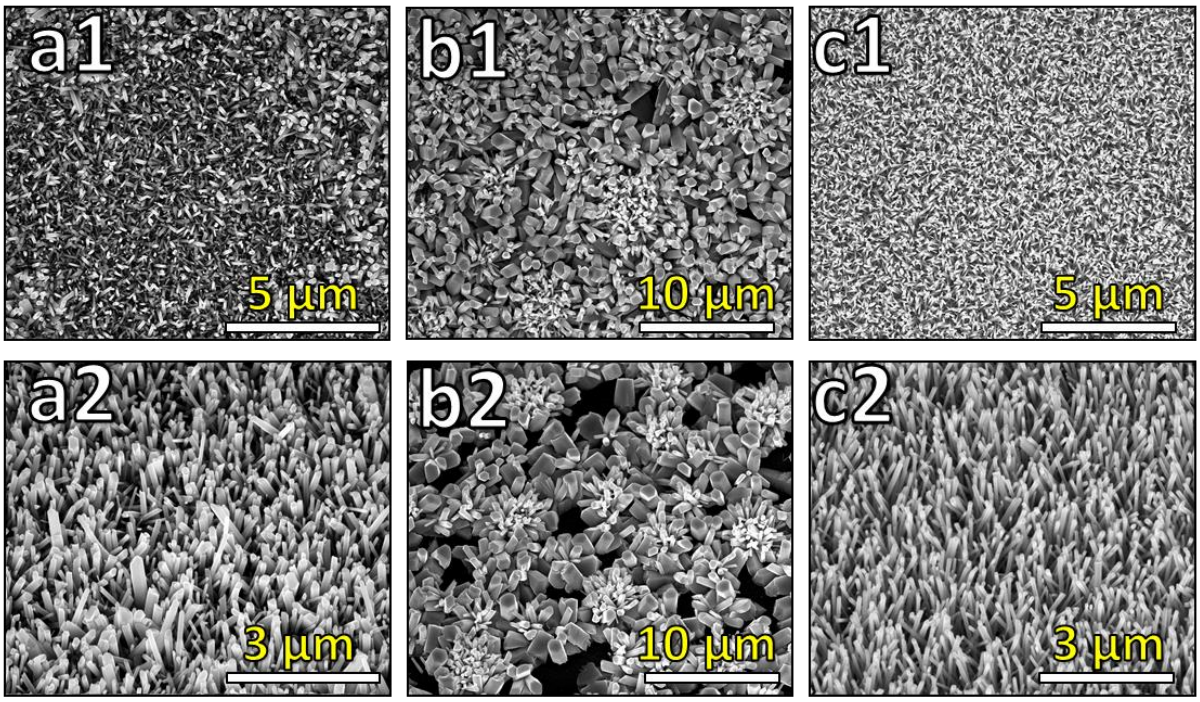

Figure 4.8. Effect of sol-gel concentration on the hydrothermally grown ZnO nano-arrays for **a)** 1, **b)** 10 and **c)** 100 mM of $Zn(AC)_2$ [1) Top view and 2) angle (30°) view].

Effect of $Zn(Ac)_2$ concentration: Uniformity and thickness of seed layer control the ZnO nano-array density as well as their growth and alignment[11, 18]. As shown in **Figure 4.8** when a sol-gel with low concentration was used for the fabrication of the seed layers, random arrays were produced. In addition, a number of areas with no or low density of nano-arrays on the surface of the substrate were observed. By increasing the concentration of $Zn(Ac)_2$ to 0.01 M, small islands of seed layer based thin films were observed to form, which after calcination were changed into flower type structures. When 0.1 M $Zn(Ac)_2$ concentration was used for the seed layer formation, completely uniform and well-ordered nano-arrays were observed on the substrate.

Effect of calcination temperature: Crystallinity of the substrate has a critical effect on the formation of the ZnO nano-arrays. Crystallinity of the seed layer can be increased by increasing the temperature and time of the calcination. By increasing the calcination temperature and allowing longer reaction time; diffusion of the atoms in the thin film can be controlled[24]. Increase in the diffusion rate in thin film are favoured as it results into more oriented crystallites on the surface which subsequently results into fabrication of ZnO nano-arrays with more even aspect ratio

and orientation. **Figure 4.9** and **4.10** show the effects of the heat treatment on the ZnO nano-arrays formation. As could be seen from these images, at low temperatures the nano-arrays have a random orientation and different aspect ratios throughout the sample surface. At 450 °C these nano-rods form well-aligned ZnO nano-arrays while maintaining their structural integrity. To understand the synthesis temperature effects three samples with three different calcination temperatures were synthesized, and their SEM images are shown in **Figure 4.11**. It can be observed that with an increase in the calcination temperature, the seed layers become much more uniform and the alignments of the nano-arrays are enhanced. At higher calcination temperatures (750 °C), due to increasing size of the crystallites in the thin film, the thicker nano rods with flatter tips are formed. Thus, 450 °C was chosen for synthesizing of uniform and cone tip shaped ZnO nano-arrays.

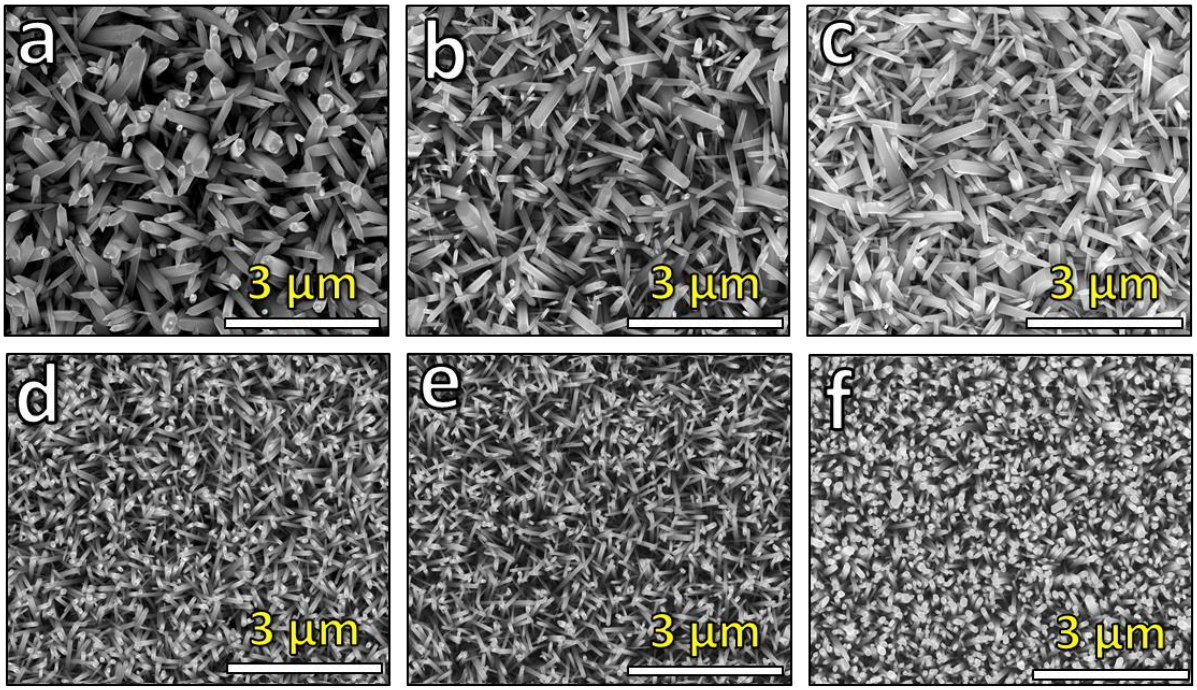

Figure 4.9. Effect of calcination temperature of the seed layer at **a)** 70, **b)** 150, **c)** 300, **d)** 450, **e)** 600 and **f)** 750 °C [Top view].

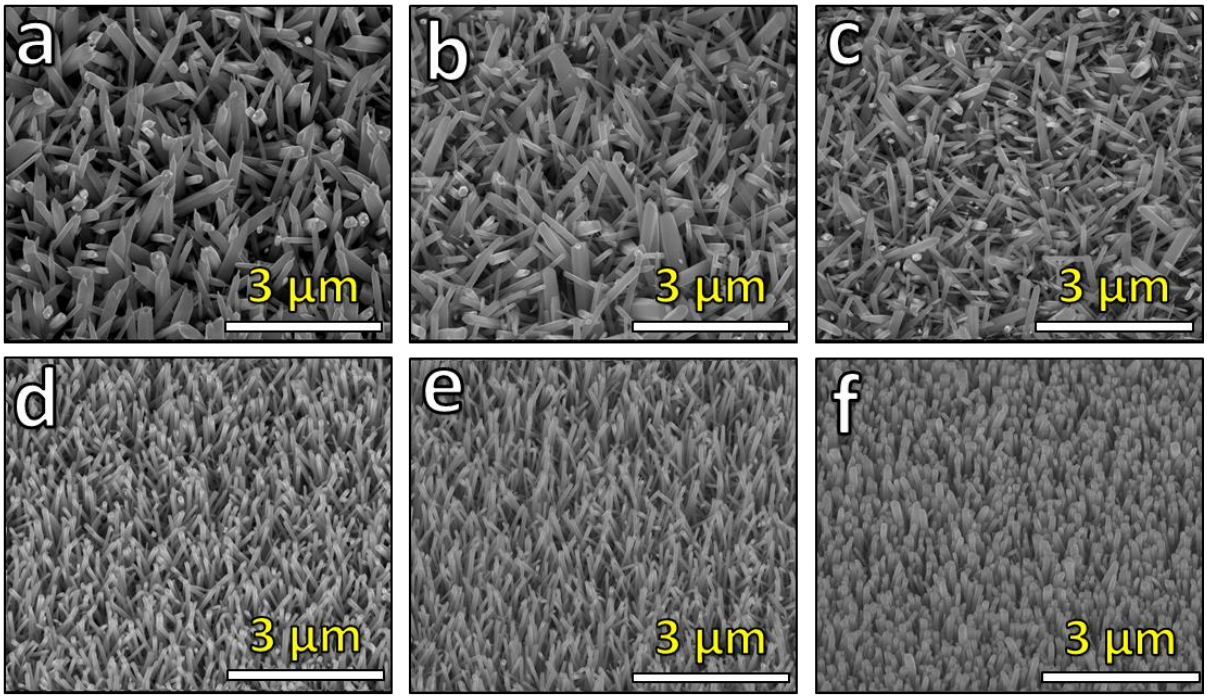

Figure 4.10. Effect of calcination temperature of the seed layer at **a)** 70, **b)** 150, **c)** 300, **d)** 450, **e)** 600 and **f)** 750 °C [Tilt (30 °C) view].

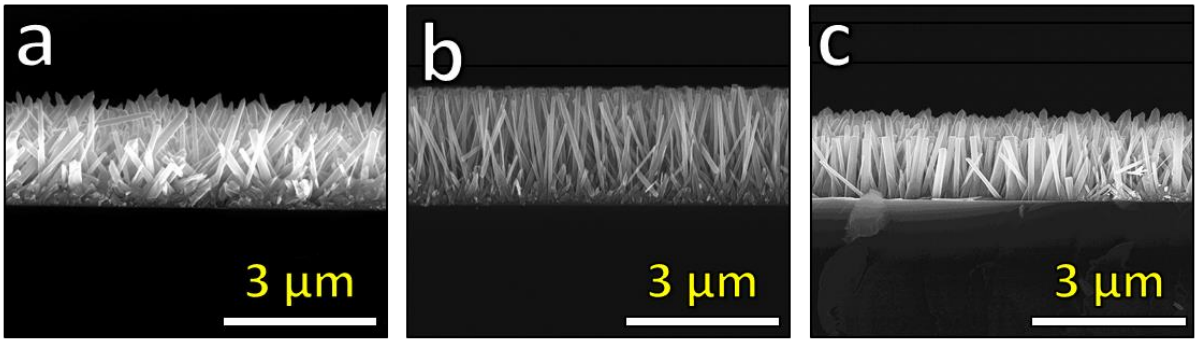

Figure 4.11. Effect of calcination temperature of the seed layer at **a)** 150, **b)** 450 and **c)** 750 °C [Side view].

4.4. Silver decoration

4.4.1. Mechanism

Photochemical synthesis of metallic silver: One of the methods for fabricating metallic nanoparticles is through a photoreduction process. In this method, nanoparticles are synthesized by direct photoreduction of metal-ions using intermediates generated through photo-chemical processes. These intermediates can be categorised as radical and excited molecules[25]. Several morphologies of nanoparticles with high control on size distribution have been reported using

photoreduction method for reducing silver nanoparticles[26]. This method provides many advantages[26] as:

- It is a clean and convenient technique for fabricating metallic nanoparticles.
- The formation and size of the nanoparticles can be easily controlled by tailoring the irradiation[27].
- It offers a great versatility enabling synthesis of metallic nanoparticles in various media.

The synthesis method which is used in this thesis was based on the reduction of the silver nitrate into silver nanoparticles. The mechanism can be summarized in four steps. Initially, photo-excitation produces radicals in the water which enables the electron transfer from media to Ag^+ ions generating Ag^0. These Ag^0 nuclei initiate formation of AgNPs. Using isopropanol in the solution during irradiation the alcohol can act as the radical scavenger and can increase the reduction of silver nanoparticles formation. The 2-propanol can change into a radical form which can help reduction of silver ions and finally changed into aldehydes. The reaction steps that occur in the reduction of the Ag^+ ions via photoreduction are summarized below[28].

$$Ag^+ + H_2O \xrightarrow{h\nu} Ag^0 + H^+ + \bullet OH \quad 4.7$$

$$Ag^+ + RCH2OH \xrightarrow{h\nu} Ag^0 + H^+ + R\dot{C}HOH \quad 4.8$$

$$nAg^0 \rightarrow (Ag^0)_n \quad 4.9$$

$$Ag^+ + R\dot{C}HOH \xrightarrow{h\nu} Ag^0 + H^+ + RCHO \quad 4.10$$

Although, the formation of pure metallic nanoparticles can occur by using photoreduction method alone, employing photocatalytic materials can be further enhanced the reduction process. That is under irradiation, semiconducting photocatalysts can increase production of the radicals in the solution. In addition, as pairs of electron and hole are generated during irradiation, the addition of the alcohol can act as a positively charged hole trap in the system and thus decrease the amount of oxidant radicals formation[29-30].

Silver mirror method: In 1835, Justus von Liebig invented a simple but versatile method for coating glasses to fabricate mirrors via a soft chemical method[31]. Since then this method has been used regularly, and with B. Tollens modification (1841-1918) it is considered as one of the best chemical methods for fabricating shiny silver

surfaces on many substrates[32]. The fundamental reactions in the Tollens process can be simplified as[33]:

$$Ag^{+} + 2OH^{-} \rightarrow Ag_2O \downarrow + H_2O \quad 4.11$$

$$Ag_2O + 4NH_3 + H_2O \rightarrow 2[Ag(NH_3)_2]^{+} + 2OH^{-} \quad 4.12$$

$$2[Ag(NH_3)_2]^{+} + RCHO + 2OH^{-} \rightarrow 2Ag^{0} \downarrow + RCOOH + 4NH_3 + H_2O \quad 4.13$$

There are two key aspects of in these reactions. By adding ammonia to colourless silver nitrate solution, a brownish precipitate of silver oxide forms in the solution. By continuing the addition of ammonia, the *Eq.4.12* is completed and silver oxide changes into diamminesilver(I) complex. As the $[Ag(NH_3)_2]^{+}$ is formed in the solution by increasing in pH, the standard redox potential of Ag^{+}/Ag changes from +0.799 V to +0.38 V. The reducing sugar's redox potential is -0.15 eV at pH 7 in water. Thus, the overall reaction rate is decreased enabling the abrupt formation of silver nanoparticles and make the growth rate predominant comparing with nucleation rate[34]. Using low silver concentration in the reaction results in decreasing the reduction rate. This leads to a decrease in the number of the initial nuclei which subsequently make a small number of bigger particles. The pH of the solution controls the amounts of $[Ag(NH_3)_2]^{+}$ formation and therefore the kinetics of the *Eq.4.13*. Thus, a change in the pH can alter the particle size as well as the kinetics of the reduction. Therefore, the amount of ammonia added to the solution should be kept fixed in order to achieve a reproducible synthesis procedure. Furthermore, as the reduction is based on the oxidation of sugar in the solution the concentration of the glucose in the solution was kept of 1M.

In electroless deposition of silver nanoparticles on ZnO nano-arrays, formed nanoparticles should have a high tendency toward making uniform decoration on the surface of ZnO nanorods. To achieve this, two different methods are suggested in the literature: sensitization and activation. In sensitization method, Sn^{2+} ions are bound to the surface of the substrate nanostructures. Thereby Sn^{2+} ions bound on the surface modify the surfaces of the negatively charged zinc oxide nanostructures into positively charged hydrophilic surfaces. Sn^{2+} can easily oxidize into Sn^{4+} and thus allows Ag ions to be reduced and decorate the surfaces[35]. This electroless plating process is an autocatalytic reaction. That is when a small nuclei of the material are formed on the surface of the substrate, the localized growth and deposition onto these areas start[36]. Thus the use of sensitization alone cannot result into a uniform decoration. To solve this problem, activation process is usually applied to the surface prior to the platting process. The sensitized surface is transformed into the solution containing

Pd^{2+} ions where the Pd small nuclei can decorate the surface by replacing the Sn^{2+} as shown in reaction 4.14[37]. This is possible as the two half cells of the reactions (Pd^{2+} +0.99 V and Sn^{2+} +0.15 V vs. SHE) allow the formation of Pd nuclei on the surface[38].

$$Sn^{2+} + Pd^{2+} \rightarrow Sn^{4+} + Pd^{0} \qquad 4.14$$

After the formation of these nuclei, the plating can then be performed on the surface where the Pd particles act as catalytic sides for the formation of even and uniform silver nanoparticle decoration.

4.4.2. Silver decoration via photoreduction

The effect of Ag ion concentration on the decoration of ZnO nano-arrays (sputtered seed layer) was first studied. In high Ag ion concentrations, silver does not tend to stick on the substrate as it produces big particles on the ZnO nano-arrays rather than decorating them uniformly. At 150 mM, most of the substrate gets covered with micron size silver flakes as shown in **Figure 4.12a**. Although the distribution of silver seems to be uniformly throughout the sample, the structure of zinc oxide is observed to be buried to be under the silver flakes and thus these structures do not fulfil the requirement of this study. By decreasing the concentration of Ag^{+} ions the micron size polyhedron particles are formed. At 15 mM and 1.5 mM Ag^{+} ion concentrations, these particles cover most of the substrate as shown in **Figure 4.12b and c**. Again, the decoration tends to happen on the tips of the nano-arrays and in some parts, the agglomeration of silver particles in the samples was observed. By further decreasing the ion concentration to 0.15 mM, a uniform decoration of Ag nano-particles on ZnO nano arrays was achieved as shown in **Figure 4.12d**. The decorating particles were different in the size as the bigger particles stand on the tip of the materials while the smaller particles are formed by reaching to the root of the nano rods.

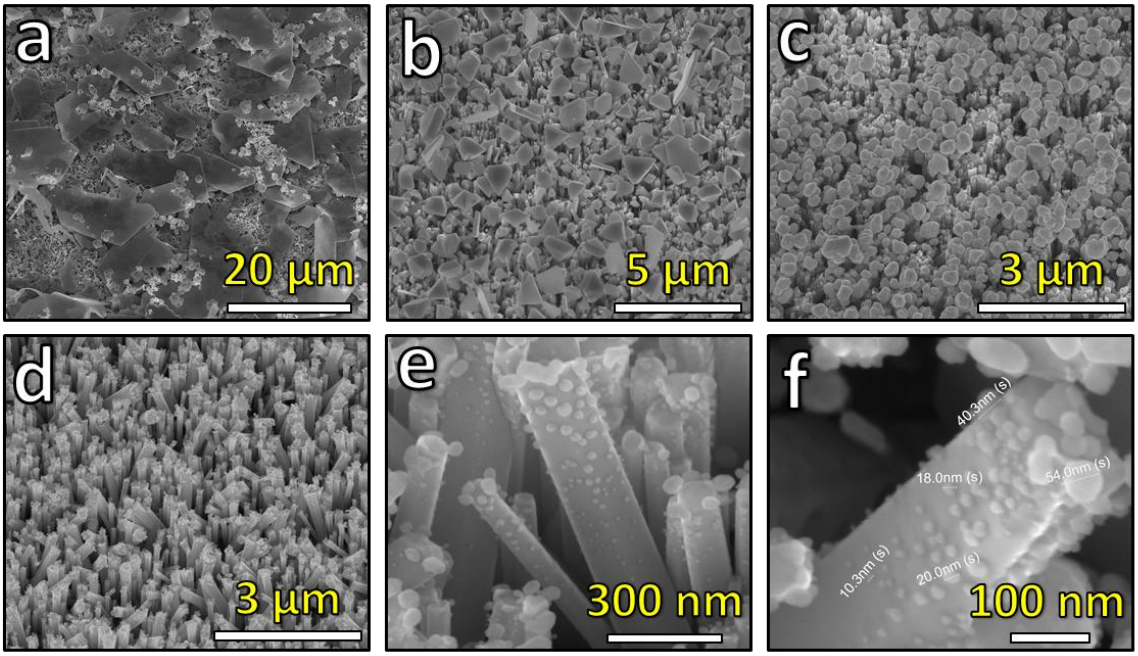

Figure 4.12. Effect of silver ion concentration on the decoration of ZnO nano-arrays for 2 h for samples prepared with **a)** 150, **b)** 15, **c)** 1.5, **d)** 0.15 mM and **e)** and **f)** 0.1 mM Ag^{+} ions.

As shown in **Figure 4.12 e** and **f** at 0.1 mM Ag+ ion concentration, the distance between the silver nano-particles on the ZnO rods is more than 20 nm in most of the cases. Also the coverage is not high, and a number of ZnO nano-rods are left without silver decoration. In concentration less than 0.15 mM, the particles are small and the coverage is poor. Low decoration densities as well as wide distance between decorated particles make low concentration inapplicable for SERS based sensing applications.

The decoration of Ag nano-particles was then carried out for ZnO nano-arrays grown through sol-gel method as shown in **Figure 4.13**. In all samples, silver nanoparticles tend to sit on the tip of the nano rods rather than other areas of the material. It has been shown that the face of (0001) in ZnO has the highest photocatalytic activities compared to other planes. This is the plane that corresponds to the top of the tips[39]. This phenomenon can be seen specifically in low temperature synthesis of ZnO arrays where the tip has a larger portion of the (0001) plane. In higher calcination temperatures, well alignment of the ZnO nano-arrays was achieved; however, as the size of the nano-arrays decreased, the silver nanoparticles formed on the tips thus a uniform coverage was not achieved.

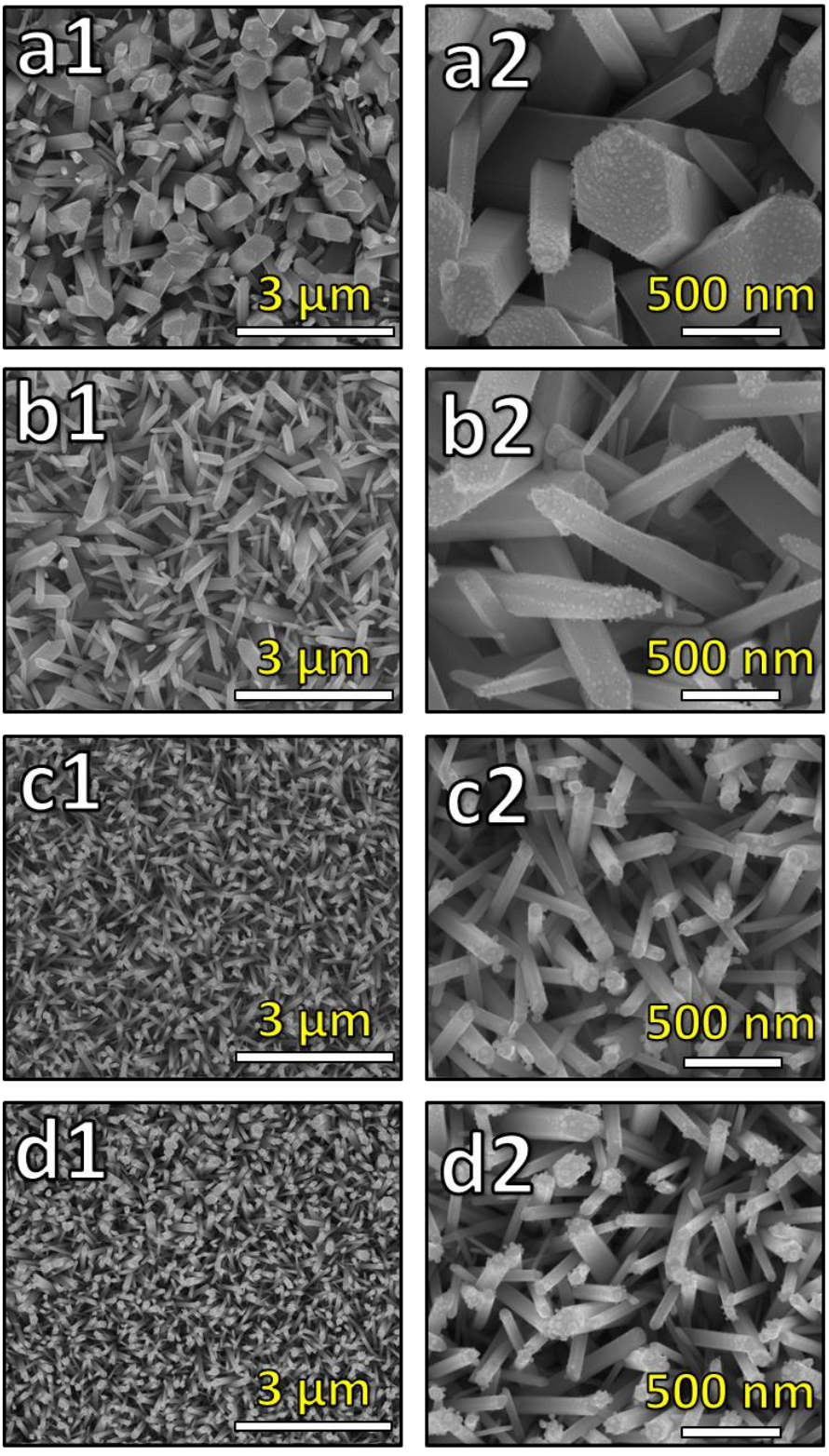

Figure 4.13. Silver decoration [0.15 mM, 2 h] of ZnO nano-arrays with different seed layer heat treated at **a)** 70, **b)** 150, **c)** 450 and **d)** 750 °C.

As explained in *Chapter I, Section 1.2.3*, by attaching the AgNPs to ZnO, an Ohmic junction can be produced between these materials. This can alter the photocatalytic activity of the samples. **Figures 4.14 a** and **b** show that pristine RB molecules do not degrade in the

absence of ZnO/Ag nano-arrays even after 6 h of UV illumination. However, RB bound to a ZnO/Ag nano-array surface [synthesized with sol-gel derived ZnO thin film calcined at 450 °C and subsequently decorated with 0.15 mM Ag^{+} ions] can be almost fully degraded under the same conditions. **Figure 4.14 c** compares the photodegradation efficiency of ZnO and ZnO/Ag nano-arrays. As could be seen from this figure, the photocatalytic activity of the ZnO nano-arrays were increased by decorating them with AgNPs. Increase in the photocatalytic activities due to the silver decoration confirms the electron transfer from semiconductor to silver nanoparticles, subsequently resulting in an increase in the electron-hole life time due to the formed heterojunction structures.

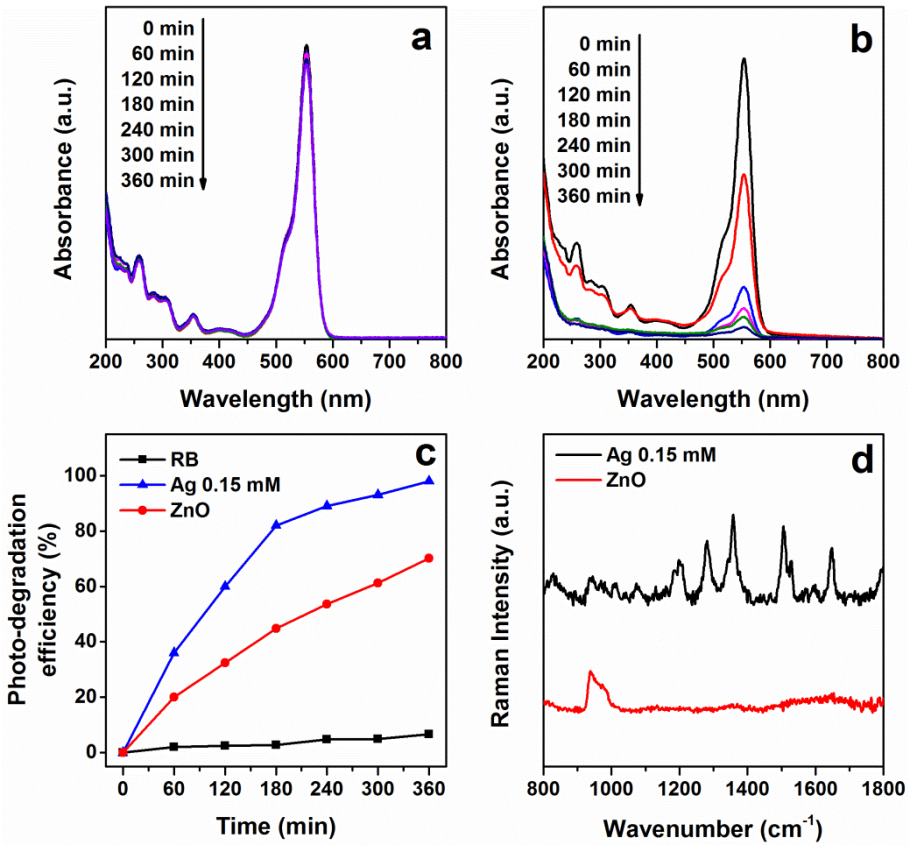

Figure 4.14. UV-visible absorbance spectra of RB with increasing illumination time in the **a)** absence and **b)** presence of ZnO/Ag prepared using 450 °C calcinated ZnO nano-arrays decorated with 0.15 mM AgNPs, **c)** photodegradation efficiency of ZnO and ZnO/Ag nano-arrays and **d)** SERS spectra for pure ZnO and ZnO/Ag nano-arrays.

Raman spectra presented in **Figure 4.14 d** show that zinc oxide nano-arrays alone does not have any enhancement. As explained in *Chapter I, Section 1.3.3*, it is possible to have a charge transfer from the marker to semiconductor. If this transfer happens in a semiconductor, the Raman signal of the marker enhances by only aid of

the semiconducting material[40]. Thus due to lack of Raman signals in the ZnO substrate, the charge transfer from organic to the semiconductor seems to have little or no effect. The Ag/ZnO nano-arrays show a slight increase in the Raman intensity of RB; however, the enhancement is not high enough to be used as a sensing substrate. This is mainly due to the fact that the distance between the silver nanoparticles is too high, and their surface densities are not sufficiently high to enable the formation of 'hot spots' on the ZnO nano-arrays.

4.4.3. Silver decoration via Tollens method

After fabrication of ZnO/Ag nano-arrays, a further attempt was carried out to make a better coverage of silver on the zinc oxide nano-arrays. Electroless plating shows a greater ability for decorating even large surfaces. This method has been used to obtain proper silver decoration on the ZnO nano-arrays. Top-view SEM images in **Figure 4.15** and higher magnification images in **Figure 4.16** show that Ag density in ZnO/Ag composite nanorod arrays can be controllably fine-tuned by varying the concentration of the diaminesilver(I) complex and the reaction time. In all the cases, silver can be observed deposited on the surface of ZnO nano-arrays in the form of quasi-spherical nanoparticles (AgNPs) instead of a thin film, which is preferred to achieve high SERS enhancement. It is also observed that the increase in the concentration of diaminesilver(I) complex as well as reaction time leads to a simultaneous increase in the AgNPs density and particle size. Although at the highest tested concentration (100 and 1000 mM), almost full coverage of ZnO nano-arrays with AgNPs is achieved, the increased reaction time of 6 min at these concentrations results in blocking the gaps between ZnO nanorods to such an extent that the overall constructions of the nano-arrays appear to fade away (**Figure 4.15 c3 and d3**). Conversely, at lower concentrations (1 and 10 mM), by increasing the reaction time, density of randomly distributed small AgNPs on ZnO nano-arrays can be uniformly increased. Additional side-view SEM images in **Figure 4.17** show that the density of AgNPs is achieved highest on the top of ZnO nanorods, which reduces towards the substrate.

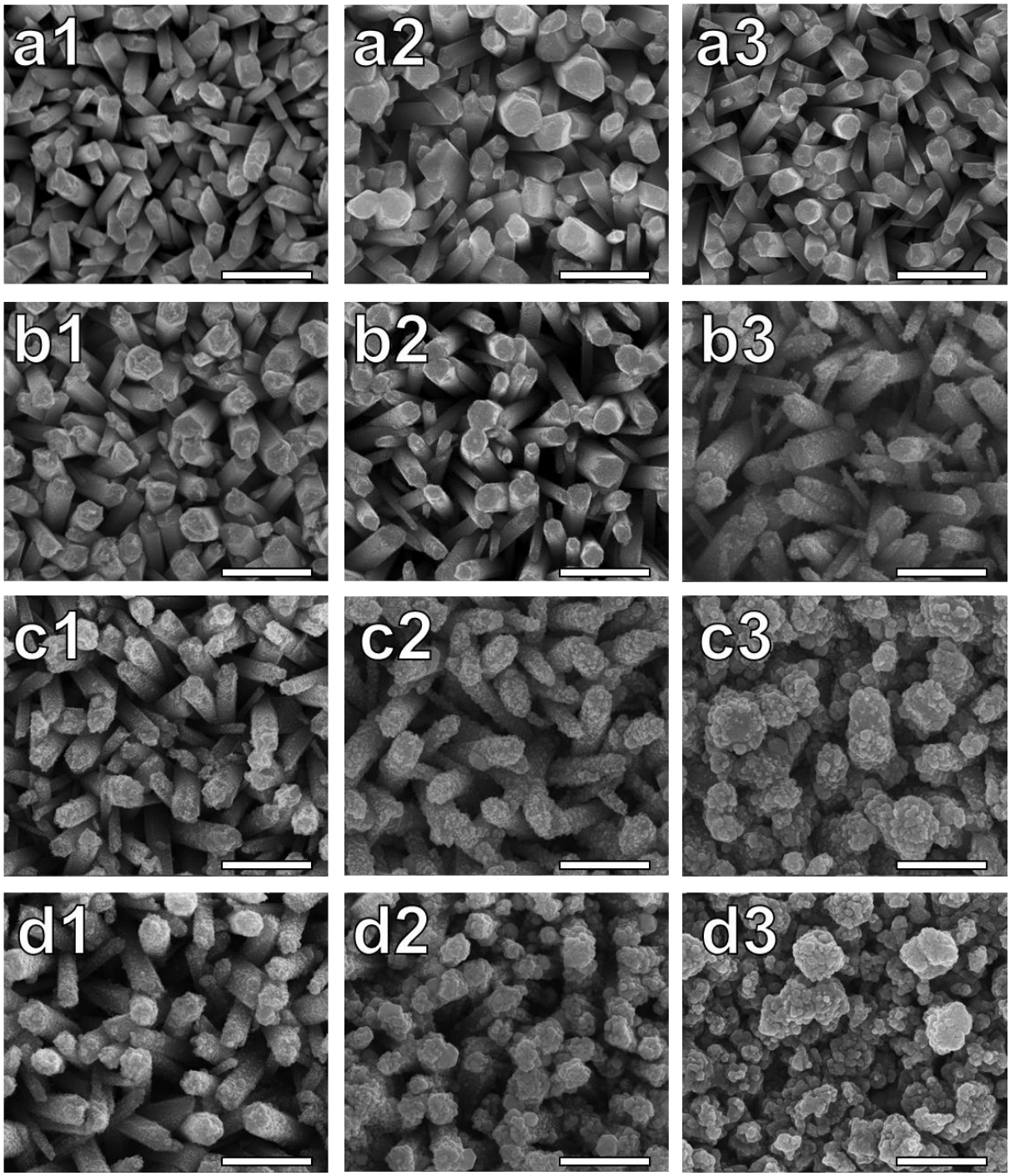

Figure 4.15. SEM images of ZnO/Ag composite nanorod arrays fabricated by reaction of ZnO nano-arrays with **a)** 1, **b)** 10, **c)** 100 and **d)** 1000 mM diaminesilver(I) complex for (**a1**, **b1**, **c1** and **d1**) 1 min, (**a2**, **b2**, **c2** and **d2**) 3 min and (a3, b3, c3 and d3) 6 min. Scale bars correspond to 1 µm.

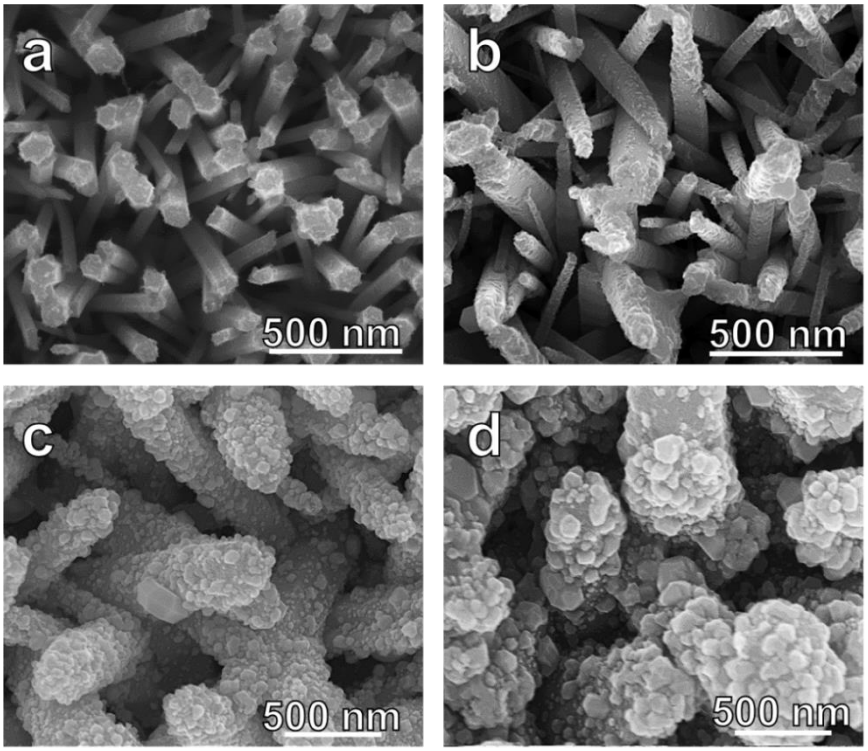

Figure 4.16. Additional SEM images of ZnO/Ag nano-arrays prepared using **a)** 1, **b)** 10, **c)** 100 and **d)** 1000 mM diaminesilver complex for 3 min reaction.

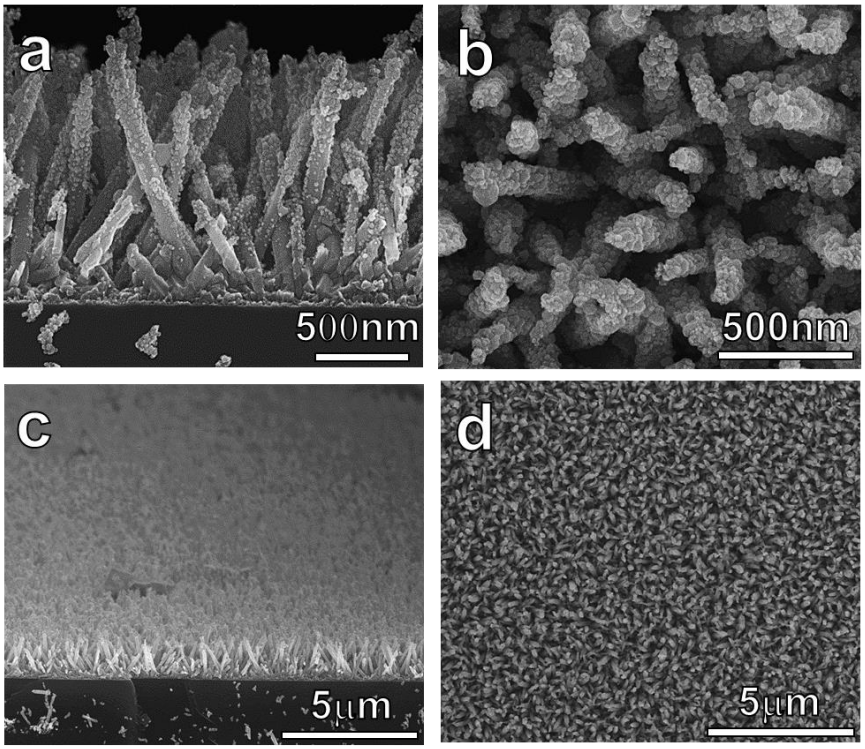

Figure 4.17. SEM images of ZnO/Ag nano-arrays prepared using 100 mM diaminesilver complex for 3 min reaction **a)** side-view, **b)** top-view, **c)** perspective-view at 10° sample tilt, and **d)** low magnification top-view images.

XRD patterns of ZnO/Ag nano-arrays as a function of increasing diaminesilver complex as well as AgNPs deposition time are shown in **Figure 4.18**. In all the samples, peaks corresponding to only wurtzite phase of ZnO (JCPDF 36-1451) without any other ZnO crystalline phases are observed. XRD patterns also show that with increasing concentration of diaminesilver precursor complex as well as AgNPs deposition time, peaks matching to (111) and (200) phase of face centred cubic silver (Ag^0) become pronounced (JCPDF 04-0783), thereby supporting the decoration of ZnO nano-arrays with AgNPs, as observed in the SEM images (**Figure 4.15** to **4.17**).

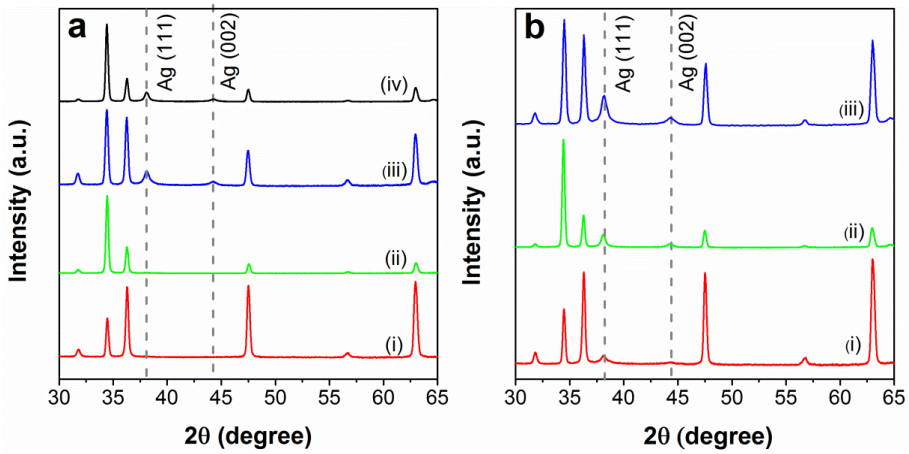

Figure 4.18. XRD patterns obtained from ZnO/Ag nanorod arrays **a)** as a function of diaminesilver concentration of (i) 1, (ii) 10, (iii) 100 and (iv) 1000 mM for 3 min reaction, and **b)** as a function of reaction time for (i) 1, (ii) 3 and (iii) 6 min for 1000 mM diaminesilver concentration. The lattice planes corresponding to Ag are indicated, while other peaks correspond to wurtzite phase of ZnO.

XPS was employed as a highly surface sensitive technique to follow the successful decoration of AgNPs on ZnO nano-arrays at each of the synthesis steps (**Figure 4.19**). For controllable loading of AgNPs on ZnO nanorods, it was found crucial to sensitize the ZnO surface by adsorbing Sn^{2+} ions. Successful binding of Sn^{2+} to ZnO surface is evident from characteristic Sn $3d_{5/2}$ core level BE at 486.7 eV that corresponds to Sn^{2+} (**Figure 4.19a** and **b**)[38]. When Sn^{2+}-adsorbed ZnO nano-array is exposed to an aqueous solution containing Pd^{2+} ions, the favourable difference in the standard reduction potentials of the two half cells of the reactions (Pd^{2+} +0.99 V and Sn^{2+} +0.15 V vs. SHE) allows deposition of Pd^0 nano-clusters on ZnO surface as per **Eq. 4.14**. Presence of this Pd^0 nanoparticle seed layer on the

surface of ZnO nanorods is evident from Pd 3d core level spectrum with characteristic $3d_{5/2}$ BE component at 335.2 eV (**Figure 4.19c**)[41]. These Pd seed particles can now act as nucleation sites for the uniform electroless deposition of AgNPs on ZnO in the next stage when Pd-activated ZnO substrates are exposed to diaminesilver(I) complex in the presence of a reducing agent such as glucose, as per the **Eq. 4.13**.

Ag 3d core level XPS spectrum obtained after reacting Pd-activated ZnO nano-arrays with diaminesilver(I) complex for 3 min shows two spin-orbital splitting pairs with Ag $3d_{5/2}$ BEs at 368 and 372 eV (**Figure 4.19d**). The lower BE feature shows that most of the reduced silver stays in the form of metallic Ag^0 (94.3%), while the higher BE feature of significantly lower intensity (5.7%) may be assigned to the potential surface oxidation of AgNPs bound onto ZnO surface[42].

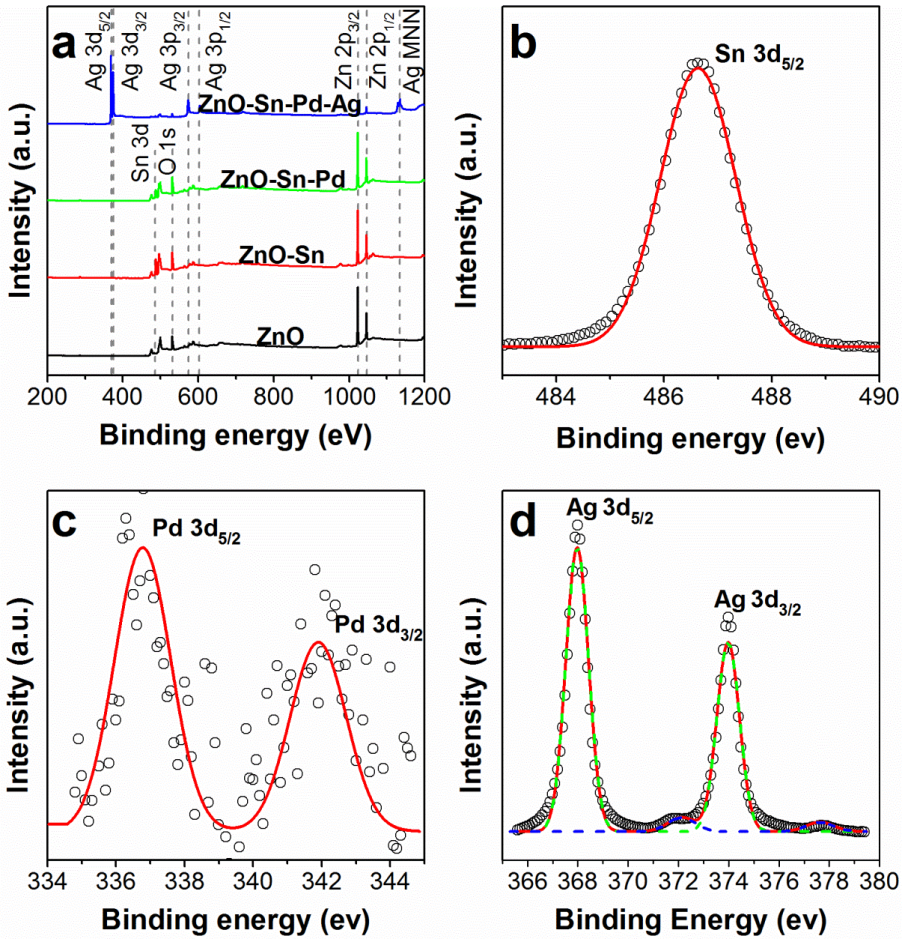

Figure 4.19. XPS spectra arising from ZnO/Ag nanorod arrays during different stages of Ag decoration **a)** general area scans from each synthesis step, **b)** Sn $3d_{5/2}$ core level from ZnO-Sn, **c)** Pd 3d core level from ZnO-Sn-Pd and **d)** Ag 3d core level from ZnO-Sn-Pd-Ag (ZnO/Ag).

To further evaluate the importance of the size and the density of AgNPs on ZnO surface in achieving high SERS response of the Raman marker molecule, the influence of the diaminesilver complex concentration as well as the reaction time on Raman intensity of RB was systematically investigated (**Figure 4.20**). By increase in starting silver plating concentration (**Figure 4.20a**) as well as Ag decoration time (**Figure 4.20b**), the intensities of the Raman signals corresponding to vibrational modes of RB from νCH (1192 cm^{-1}) and νCC (1355, 1503, 1580, and 1652 cm^{-1}) show a consistent increase[40]. This is expected as an increase in the size and density of AgNPs on ZnO nano-arrays is likely to increase the number of 'hot-spots', thereby leading to enhanced SERS activity[43]. To further obtain an estimate of the relative efficiencies of different designed surfaces towards SERS enhancement, the highest intensity Raman peak of RB at 1355 cm^{-1} was compared across different samples (**Figure 4.20c**). It is evident that both the AgNPs plating time and the concentration of diaminesilver complex play an important role in SERS enhancement in the tested range. While insignificant SERS enhancement was observed when either 1 or 10 mM diaminesilver complex were used for AgNPs decoration on ZnO nano-arrays, 100 and 1000 mM concentrations led to significant SERS enhancement across all the plating durations. Additionally, control experiments involving evaluation of Sn^{2+} and Pd^{0} sensitized ZnO surfaces were performed, which didn't provide any Raman enhancement for RB molecules.

To understand the SERS response behaviour of ZnO/Ag nano-arrays, we may briefly consider different phenomena that may contribute to Raman enhancement of RB dye in a ZnO/Ag system. These include (i) electromagnetic enhancement due to the optical excitation of the surface plasmon resonance of AgNPs with incident laser beam, (ii) charge transfer between attached RB molecules attached to excited AgNPs[44], and (iii) potential charge transfer between RB molecules and ZnO. In the latter case, it has recently been observed that charge transfer may occur from continuous states in the conduction band of the semiconductor to the adjacent analyte molecule, leading to Raman enhancement[40]. As evident from **Figure 4.20a** and **b**, RB molecules adsorbed on pristine ZnO nano-arrays do not show a measurable Raman signature. Therefore, it appears that in the SERS substrates reported in the current study, two former aspects make predominant contribution to the Raman enhancement, while the charge transfer mechanism between the organic analyte and semiconductor ZnO remains negligible. In the general context of metal-facilitated Raman

enhancement, it is now increasingly recognized that the distance between metal nanoparticles plays an important role in Raman enhancement, wherein an average inter-particle distance of less than 10 nm is observed to create SERS 'hot-spots'[45]. As evident from SEM images in **Figure 4.15**, at lower silver plating concentrations of 1 and 10 mM, small AgNPs that are far apart from each other by more than 10 nm are produced. Conversely, at higher silver plating concentrations (100 and 1000 mM), the increase in the AgNPs plating time causes a remarkable increase in the density of 'hot-spots'. This high density of hot spots appears to be responsible for significant SERS enhancement observed in **Figure 4.20c**.

It is now well-recognized that while the SERS response of different analyte molecules can be significantly increased by a variety of nanomaterial engineering approaches[46], achieving a reproducible SERS response from the same substrate is still a major challenge[1]. This is predominantly because it is challenging to produce large dimension (~1 cm x 1 cm) nanostructured surfaces that show uniformity across a large surface area. ZnO nano-arrays is one of the few nanostructured surfaces that can be reproducibly produced over large surface areas[47], as shown in **Figure 4.21**. Although individual ZnO nanorods in nano-arrays may appear to be randomly tilted from 0-30 degree (**Figure 4.15**), this distribution is uniform throughout 1 cm x 1 cm substrate surface. Moreover, the average width of these nanorods (150-300 nm) is far smaller than the incident laser beam (100 µm diameter), which ascertains that when the Raman laser beam hits the ZnO nano-arrays, it excites ~500 nanorods, thereby leading to a reproducible SERS enhancement. The high reproducibility of one of these SERS substrates is evident from the comparison of Raman spectra of RB at 30 different randomly selected positions (**Figure 4.20d**). The maximum relative standard deviation (RSD) of this substrate was calculated to be 0.132, which indicates that ZnO/Ag nano-arrays reported here are suitable to be classified as highly reproducible SERS active substrates.

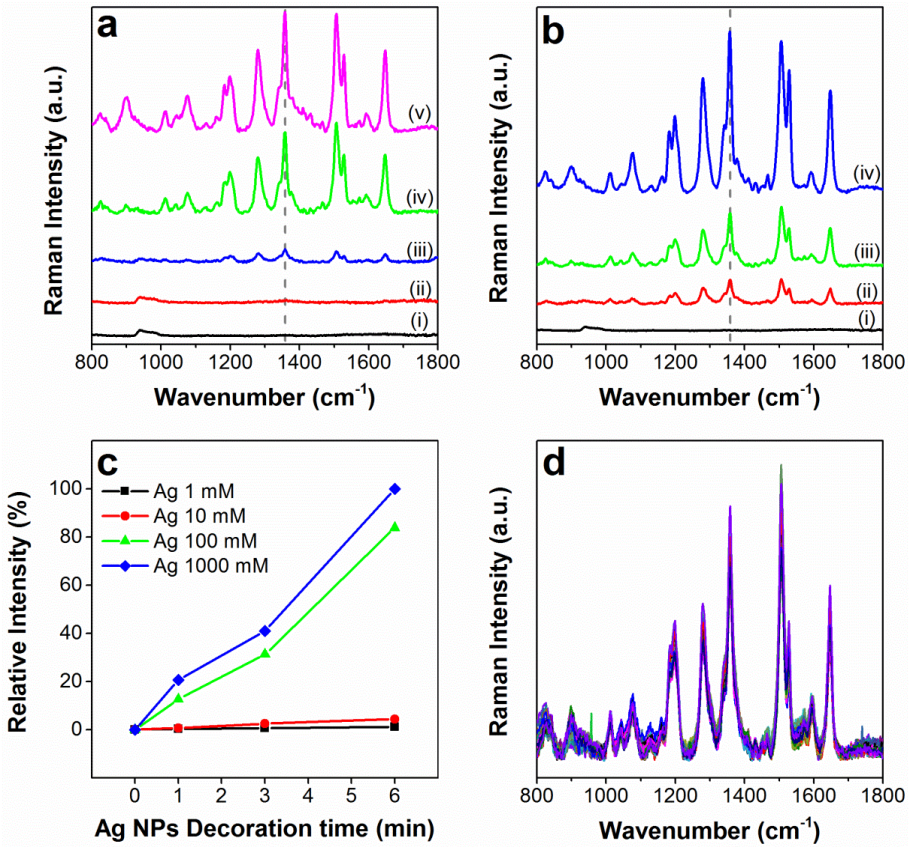

Figure 4.20. SERS spectra of RB molecules obtained from ZnO/Ag nano-arrays prepared by exposing ZnO substrates **a)** for 3 min to (i) 0, (ii) 1, (iii) 10, (iv) 100 and (v) 1000 mM diaminesilver complex and **b)** to 100 mM diaminesilver complex for (i) 0, (ii) 1, (iii) 3 and (iv) 6 min; **c)** relative intensity of the characteristic RB Raman band at 1355 cm^{-1} as a function of silver precursor concentration and AgNPs decoration time and **d)** 30 overlapping SERS spectra of RB molecules randomly collected from a single ZnO/Ag substrate prepared using 1 mM diaminesilver complex for 3 min.

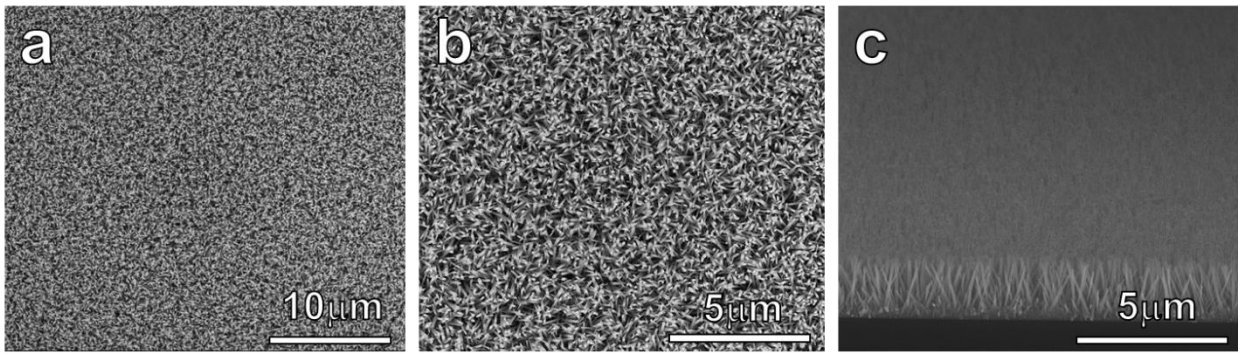

Figure 4.21. SEM images of ZnO nano-arrays at **a)** lower and **b)** and **c)** higher magnification, wherein **b**) shows the top-view image and **c**) shows a perspective image at 10° sample tilt.

Further, since metal-decorated semiconductor nanoparticles are well known for their photocatalytic activity, we explored the potential recyclability of ZnO/Ag nano-arrays to allow multiple SERS sensing events on a single substrate. **Figure 4.22a** and **b** show that although pristine RB molecules do not degrade in the absence of ZnO/Ag nano-arrays even after 6 h of UV illumination, RB bound to a ZnO/Ag nano-array surface can be almost fully degraded within the same time frame. **Figure 4.22c** compares the photodegradation efficiency of different ZnO/Ag nano-arrays. At the lower concentration of AgNPs in ZnO/Ag nano-arrays, the photodegradation efficiency of the system increases over that of pristine ZnO nano-arrays; however a drastic reduction in the photocatalytic activity is observed at higher concentration of AgNPs in ZnO/Ag nano-arrays. Mechanistic aspects of metal-loading dependent change in photocatalytic performance of semiconductors have been previously elucidated by our group and others, wherein an optimal metal loading is found critical to obtain high photocatalytic performance[48-49]. In case of photo-excited ZnO/Ag nano-arrays, at low AgNPs concentrations, metallic particles bound to ZnO semiconductor can increase the electron/hole life time by facilitating transfer of electrons from conduction band of ZnO to AgNPs. Conversely, if the size of the decorated AgNPs passes a threshold, these metallic particles can act as the recombination sites for electron/hole pairs, thereby reducing the photo-efficiency of the system[50].

Comparison of the SERS performance (**Figure 4.20**) and photodegradation efficiency (**Figure 4.22**) of different ZnO/Ag nano-arrays shows that while SERS performance of the substrates continuously improves with increasing AgNPs concentration, the highest concentration of AgNPs does not necessarily show the best photodegradation efficiency. Therefore, the ZnO/Ag nano-arrays substrate prepared using 100 mM diaminesilver complex for 3 min was chosen as an optimum substrate for SERS recyclability studies (**Figure 4.22d**). Reproducible SERS spectra could be obtained from the same substrate at least up to three cycles after being able to completely regenerate the ZnO/Ag nano-array substrate through its simple exposure to UV irradiation for 30 min. Although attempts have been previously made to regenerate SERS substrate through various solution-based approaches, the oxidation of AgNPs into silver oxides during substrate regeneration has been a limiting factor in the development of reproducible and regenerable SERS substrates[51]. It is known that UV irradiation in the absence of significant amount of ozone can protect silver against

oxidation[51]. Therefore, photocatalytic recycling of metal-decorated semiconductors appears to be a facile technique to develop regenerable SERS active substrates.

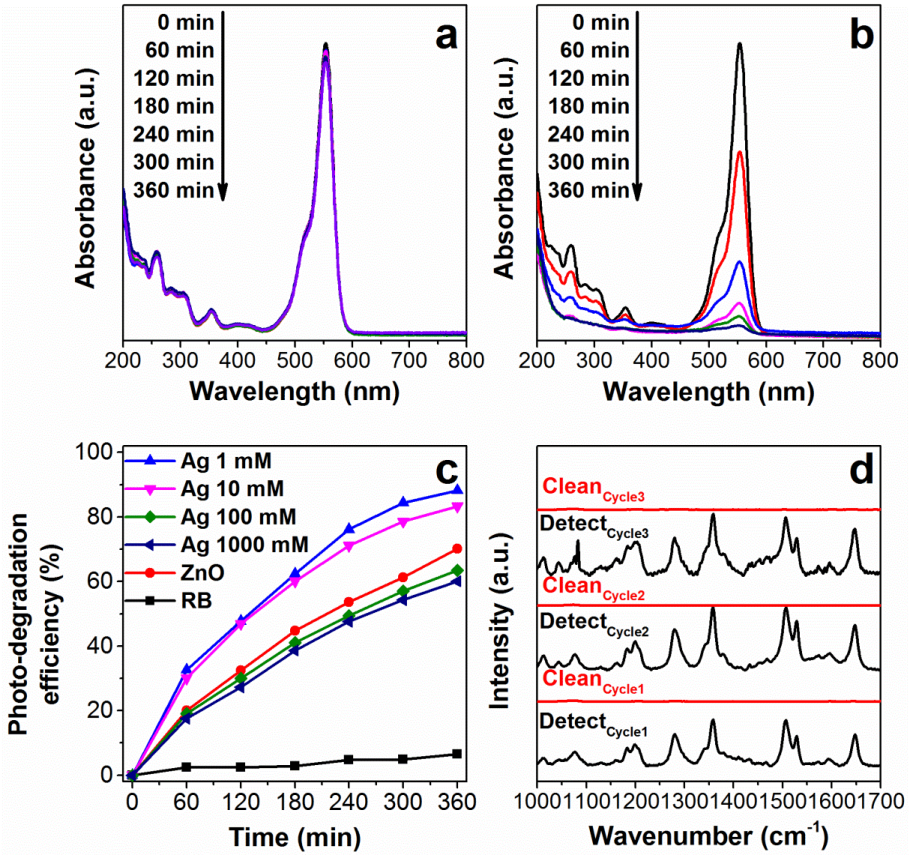

Figure 4.22. UV-visible absorbance spectra of RB with increasing illumination time in the **a)** absence and **b)** presence of ZnO/Ag prepared using 1 mM diaminesilver complex for 3min, **c)** photodegradation efficiency of different ZnO/Ag nano-arrays prepared after 3 min of AgNPs deposition and **d)** recyclability studies showing SERS spectra of RB on a single ZnO/Ag nano-array substrate through three cycles of SERS detection and substrate photo-cleaning.

4.5. Conclusion

This study demonstrates a facile soft chemical approach for the fabrication of ZnO/Ag nanorod arrays on silicon wafers. The effects of the synthesis parameters on the formation of aligned ZnO nano-arrays were studied thoroughly. Also, the capability of the silver decoration formation on ZnO nano-arrays using photoreduction and Tollens methods were studied comprehensively. The photocatalytic properties of ZnO semiconductor, combined with the SERS capabilities of AgNPs endow multifunctionality to these materials. The use of ZnO topology with nanorod arrays serves two purposes. The first among these is to allow

development of SERS-active Ag surfaces that remain uniform within the dimension of the exciting Raman laser beam (100 µm), thereby resulting in reproducible SERS response. The second being the high surface area of ZnO nanorods that maximizes the photocatalytic cleaning ability of SERS substrates during repeated molecular sensing events. Overall, these nanoengineered ZnO/Ag hybrid nano-arrays show outstanding performance towards reproducible SERS-based detection of analyte (RSD=0.132) while also showing an ability to be photo-cleaned between multiple SERS detection events on a single substrate. It is noted that an optimum decoration of AgNPs onto ZnO nano-arrays is critical to form reproducible SERS 'hot-spots' while achieving optimum cleaning attributes, thereby allowing an appreciable SERS response as well as SERS substrate recyclability.

Reference

1. Lin, X.-M.; Cui, Y.; Xu, Y.-H.; Ren, B.; Tian, Z.-Q., *Analytical and Bioanalytical Chemistry* **2009,** *394* (7), 1729-1745.
2. Lee, S.-Y.; Park, S.-J., *Journal of Industrial and Engineering Chemistry* **2013,** *19* (6), 1761-1769.
3. Udom, I.; Ram, M. K.; Stefanakos, E. K.; Hepp, A. F.; Goswami, D. Y., *Mater. Sci. Semicond. Process.* **2013,** *16* (6), 2070-2083.
4. Park, H.; Park, Y.; Kim, W.; Choi, W., *Journal of Photochemistry and Photobiology C: Photochemistry Reviews* **2013,** *15* (1), 1-20.
5. Maeda, K.; Domen, K., *Chem. Mater.* **2009,** *22* (3), 612-623.
6. Ozgur, U.; Hofstetter, D.; Morkoc, H., *Proceedings of the IEEE* **2010,** *98* (7), 1255-1268.
7. Ahuja, I. S.; Yadava, C. L.; Singh, R., *J. Mol. Struct.* **1982,** *81* (3–4), 229-234.
8. Sugunan, A.; Warad, H.; Boman, M.; Dutta, J., *J. Sol-Gel Sci. Technol.* **2006,** *39* (1), 49-56.
9. Sunandan, B.; Joydeep, D., *Science and Technology of Advanced Materials* **2009,** *10* (1), 013001.
10. Ashfold, M. N. R.; Doherty, R. P.; Ndifor-Angwafor, N. G.; Riley, D. J.; Sun, Y., *Thin Solid Films* **2007,** *515* (24), 8679-8683.
11. Xu, S.; Lao, C.; Weintraub, B.; Wang, Z. L., *J. Mater. Res.* **2008,** *23* (08), 2072-2077.
12. Xu, S.; Adiga, N.; Ba, S.; Dasgupta, T.; Wu, C. F. J.; Wang, Z. L., *ACS Nano* **2009,** *3* (7), 1803-1812.
13. Govender, K.; Boyle, D. S.; Kenway, P. B.; O'Brien, P., *J. Mater. Chem.* **2004,** *14* (16), 2575-2591.

14. Nagaraju, G.; Hwan Ko, Y.; Su Yu, J., *Mater. Lett.* **2014,** *116* (0), 64-67.
15. Qin, Y.; Wang, X.; Wang, Z. L., *Nature* **2008,** *451* (7180), 809-813.
16. Xu, B.; Cai, Z., *Appl. Surf. Sci.* **2008,** *254* (18), 5899-5904.
17. Baruah, S.; Dutta, J., *J. Sol-Gel Sci. Technol.* **2009,** *50* (3), 456-464.
18. Teng, M.; Min, G.; Mei, Z.; Yanjun, Z.; Xidong, W., *Nanotechnology* **2007,** *18* (3), 035605.
19. Liu, S.-Y.; Chen, T.; Wan, J.; Ru, G.-P.; Li, B.-Z.; Qu, X.-P., *Appl. Phys. A* **2009,** *94* (4), 775-780.
20. Jijun, Q.; Xiaomin, L.; Weizhen, H.; Se-Jeong, P.; Hyung-Kook, K.; Yoon-Hwae, H.; Jae-Ho, L.; Yang-Do, K., *Nanotechnology* **2009,** *20* (15), 155603.
21. Boyle, D. S.; Govender, K.; O'Brien, P., *Chem. Commun.* **2002,** (1), 80-81.
22. Kandjani, A. E.; Shokuhfar, A.; Tabriz, M. F.; Arefian, N. A.; Vaezi, M. R., *Journal of Optoelectronics and Advanced Materials* **2009,** *11* (3), 289-295.
23. Shokuhfar, A.; Samei, J.; Esmaielzadeh Kandjani, A.; Vaezi, M. R., *Defecs and diffusion forum* **2008,** *273-276*, 626-631.
24. Kandjani, A. E.; Tabriz, M. F.; Moradi, O. M.; Mehr, H. R. R.; Kandjani, S. A.; Vaezi, M. R., *J. Alloys Compd.* **2011,** *509* (30), 7854-7860.
25. Sakamoto, M.; Fujistuka, M.; Majima, T., *Journal of Photochemistry and Photobiology C: Photochemistry Reviews* **2009,** *10* (1), 33-56.
26. Quang Huy, T.; Van Quy, N.; Anh-Tuan, L., *Advances in Natural Sciences: Nanoscience and Nanotechnology* **2013,** *4* (3), 033001.
27. Sato-Berrú, R.; Redón, R.; Vázquez-Olmos, A.; Saniger, J. M., *Journal of Raman Spectroscopy* **2009,** *40* (4), 376-380.
28. Hada, H.; Yonezawa, Y.; Yoshida, A.; Kurakake, A., *The Journal of Physical Chemistry* **1976,** *80* (25), 2728-2731.
29. Wood, A.; Giersig, M.; Mulvaney, P., *The Journal of Physical Chemistry B* **2001,** *105* (37), 8810-8815.
30. Bamwenda, G. R.; Tsubota, S.; Nakamura, T.; Haruta, M., *Journal of Photochemistry and Photobiology A: Chemistry* **1995,** *89* (2), 177-189.
31. Liebig, J., *Justus Liebigs Annalen der Chemie* **1856,** *98* (1), 132-139.
32. Browne, C. A., *J. Chem. Educ.* **1942,** *19* (6), 253.
33. Yin, Y.; Li, Z.-Y.; Zhong, Z.; Gates, B.; Xia, Y.; Venkateswaran, S., *J. Mater. Chem.* **2002,** *12* (3), 522-527.
34. V. Goia, D.; Matijevic, E., *New J. Chem.* **1998,** *22* (11), 1203-1215.

35. Wei, X.; Roper, D. K., *J. Electrochem. Soc.* **2014,** *161* (5), D235-D242.
36. Cha, S. H.; Koo, H.-C.; Kim, J. J., *J. Electrochem. Soc.* **2005,** *152* (6), C388-C391.
37. Koo, H.-C.; Kim, S. Y.; Cho, S. K.; Kim, J. J., *J. Electrochem. Soc.* **2008,** *155* (9), D558-D562.
38. Shukla, S.; Seal, S.; Akesson, J.; Oder, R.; Carter, R.; Rahman, Z., *Appl. Surf. Sci.* **2001,** *181* (1–2), 35-50.
39. Jang, E. S.; Won, J. H.; Hwang, S. J.; Choy, J. H., *Adv. Mater.* **2006,** *18* (24), 3309-3312.
40. Musumeci, A.; Gosztola, D.; Schiller, T.; Dimitrijevic, N. M.; Mujica, V.; Martin, D.; Rajh, T., *JACS* **2009,** *131* (17), 6040-6041.
41. Brun, M.; Berthet, A.; Bertolini, J. C., *J. Electron. Spectrosc. Relat. Phenom.* **1999,** *104* (1–3), 55-60.
42. Ochanda, F.; Jones, W. E., *Langmuir* **2005,** *21* (23), 10791-10796.
43. Tang, H.; Meng, G.; Huang, Q.; Zhang, Z.; Huang, Z.; Zhu, C., *Adv. Funct. Mater.* **2012,** *22* (1), 218-224.
44. Smith, W. E., *Chem. Soc. Rev.* **2008,** *37* (5), 955-964.
45. Stranahan, S. M.; Willets, K. A., *Nano Lett.* **2010,** *10* (9), 3777-3784.
46. Marquestaut, N.; Martin, A.; Talaga, D.; Servant, L.; Ravaine, S.; Reculusa, S.; Bassani, D. M.; Gillies, E.; Lagugné-Labarthet, F., *Langmuir* **2008,** *24* (19), 11313-11321.
47. Xu, S.; Wang, Z., *Nano Research* **2011,** *4* (11), 1013-1098.
48. Pearson, A.; Jani, H.; Kalantar-zadeh, K.; Bhargava, S. K.; Bansal, V., *Langmuir* **2011,** *27* (11), 6661-6667.
49. Pearson, A.; O'Mullane, A. P.; Bansal, V.; Bhargava, S. K., *Inorg. Chem.* **2011,** *50* (5), 1705-1712.
50. Cárdenas-Lizana, F.; Gómez-Quero, S.; Idriss, H.; Keane, M. A., *J. Catal.* **2009,** *268* (2), 223-234.
51. Han, Y.; Lupitskyy, R.; Chou, T.-M.; Stafford, C. M.; Du, H.; Sukhishvili, S., *Anal. Chem.* **2011,** *83* (15), 5873-5880.

CHAPTER V

Hg(II) sensing with ZnO/Ag nano-arrays

Mercury being one of the most toxic heavy metals has long been a focus of concern due to its gravest threats to human health and environment. Although multiple methods have been developed to detect and/or remove dissolved mercury, many require complicated procedures and sophisticated equipment. In this chapter, a simple surface enhanced Raman spectroscopy (SERS) active ZnO/Ag nano-arrays is described, which can detect Hg^{2+}, remove Hg^{2+} and can be fully regenerated; not just from Hg^{2+} contamination when heat-treated, but also from the SERS marker when exposed to UV as a result of the self-cleaning ability of this heterojunction photocatalyst. The sensors are as well highly selective because of the unique way mercury (among other chemicals) interacts with Ag nanoparticles.

Part of the work presented in this chapter has been patented:

Bhargava, S. K. ; Bansal, V. ; **Kandjani, A. E. ;** Sabri, Y.M.; System for detection and removal of mercury; *AusPat*; 2013903747.

Part of the work presented in this chapter has been submitted to:

Kandjani, A. E.; Sabri, Y.M.; Mohammad-Taheri, M.; Bansal, V.; Bhargava, S.K.; Detect, remove and re-use: a new paradigm in sensing and removal of Hg (II) from wastewater via SERS-active ZnO/Ag nano-arrays; *Environmental Science & Technology*, (Submitted).

5.1. Introduction to mercury pollution

Mercury is poisonous in small quantities, yet it could be found in most geological materials and minerals. It is naturally present in the form of inert HgS however once industrial processes are undertaken; mercury in the elemental and ionic forms are formed. These industrial processes have resulted in increased mercury concentration in the surrounding environment. As this form of mercury toxicity is highly depended on to its concentration, it has become an issue of concern. As estimated by United Nations Environment Programme (UNEP) Global Mercury Report, around 6500 tonnes of mercury was released into the air from natural and anthropogenic sources in 2010[1-3] alone. The natural sources are mainly volcanic eruptions, erosion and fire[4-5]. The highest anthropgenic portion originates from coal-fired power plants and mining industries. These industries are continuously producing increased mercury based wastes that has contributed heavily to anthropogenic mercury pollution. **Figure 5.1** shows major mercury emission contributors from around the globe. As could be seen the emission of mercury continuing to increase in countries like China and Australia[5-7].

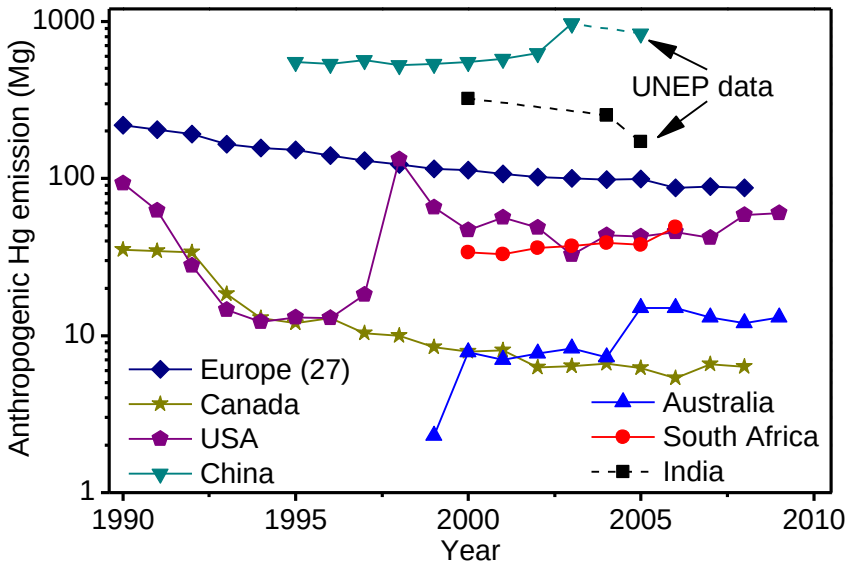

Figure 5.1. Hg emission contributors around the world[6].

Due to the fact that the type and amount of the toxic mercury released is highly depended on local mercury release conditions, it makes it difficult to understand the complexity of the natural transformations and environmental pathways of mercury. However, mercury is usually found in three different forms in the environment. These three forms are

elemental, ionic and organic mercury. Around 90% of the emitted mercury is in the elemental form which is the least toxic followed by ionic and organic being the most toxic to humans. It is well known that the elemental form of mercury follows a reaction cycle in the atmosphere and converts to organic form which accumulates in fish and enters the food chain as depicted in **Figure 5.2**[8-9]. Moreover, usage of contaminated water is another source for mercury intoxication[8]. The highly toxic and bioaccumulative methylmercury compounds (MeHg) can build up in living tissue and increase in concentration up the food chain[10-11].

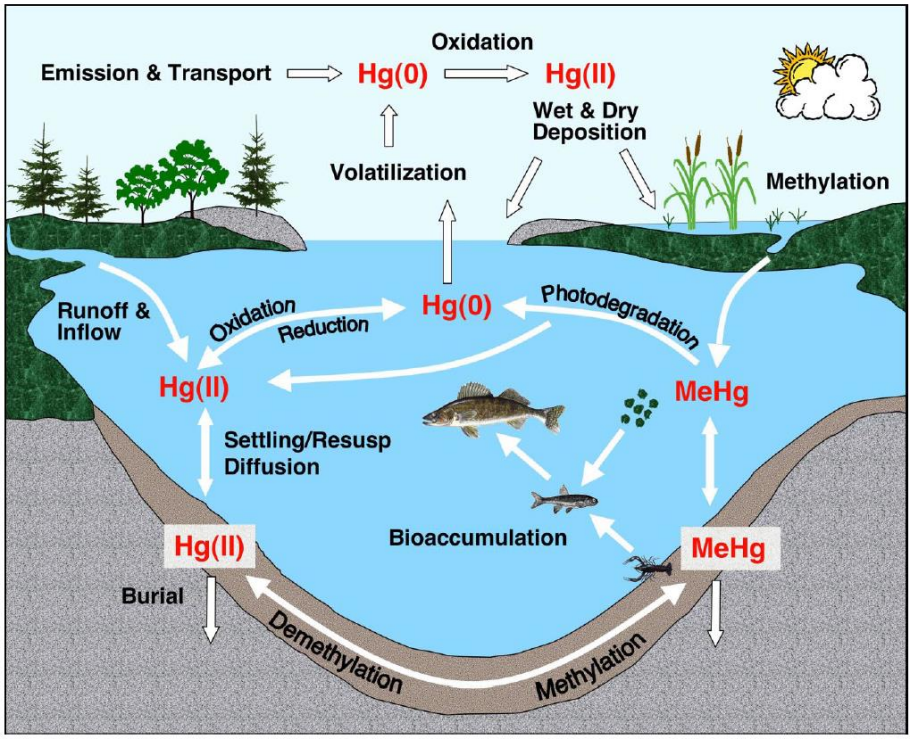

Figure 5.2. Mercury pollution - transport and cycle[9].

The devastating health effects of mercury poisoning can be appreciated from the observed incidents reported in the past. The first incident reported on mercury contamination was from 1932 to 1968 which occurred in Minamata bay in Japan[12-13]. Copious amount of mercury waste was spilled into the lake in Minamata which resulted in mercury entering into the ecosystem as MeHg and subsequently bioaccumulated in fish living in the lake. As the lake was the main food source for the people, a neurological syndrome in adults (often called the Minamata Disease) and mental retardation, seizures, and cerebral palsy in foetuses appeared as a result of MeHg that had accumulated in the fish being uptaken. On less tragic incident, low dose exposure of mercury has resulted in permanent cardio and neurological problems[14-16]. In most of these reports, mercury contamination was mainly due to consumption of sea food and contaminated drinking water.

Briefly, mercury can absorb in the human body through three paths, namely, gastrointestinal, skin and lung tracts[17]. It can make impairment of kidney and pulmonary function, chest pain and dyspnousea[15]. In addition, there are several reports establishing the linear correlation between the loss of intelligent quotient (IQ) and amounts of MeHg consumption[18-19]. All these important side-effects of industrialization have made mercury remediation as one of the most important topics in materials, clinical and environmental studies.

It is therefore, of no surprise that a series of global rules and regulations are continuously being issued by U.S. Environmental Protection Agency (USEPA) and readily being accepted by agencies such as the UNEP and the EU directive in controlling Hg emission from the industrial sources[2]. Furthermore, the water-quality criterion is also becoming stringent due to the realisation of the extreme toxicity of mercuric ions on human health. In fact, in Jan 2013 a preliminary multi-national reduction treaty involving delegates from 140 countries around the world has accepted the UNEP plans to reduce anthropogenic mercury emissions[1].

5.2. Mercury ions sensing and removal

Currently, there are several analytical methods to determine the concentration of soluble Hg^{2+} ions in water, including inductively coupled plasma mass spectroscopy (ICP-MS)[20], cold vapor atomic absorption spectroscopy (CVAAS)[21], electrochemical methods[22], and high-performance liquid chromatography[23]. However, most of these detection systems require highly precise sample preparation, expensive experimental equipment and have long turnaround times, which make them unsuitable for remote or in-the-field applications. Therefore, there is an ever increasing demand for the development of portable, fast, sensitive and selective Hg^{2+} sensors for industrial and environmental sustainability[24].

To address this issue, several alternative methods have been reported in literature based on colorimetric (UV-Vis, fluorescence, etc.)[25-27] and surface enhanced Raman spectroscopy (SERS)[28-30] techniques as potential cost-effective and simple approaches for Hg^{2+} detection in wastewater treatment processes. Among the range of methods reported, the SERS method is one of the most promising and is based on the interaction of Hg^{2+} ions either with SERS markers or with SERS active metal nanostructures. This method has the potential to achieve high sensitivity (ppb to ppt) as well as selectivity towards Hg^{2+} ions[29-33].

Most of the SERS based Hg^{2+} ions sensing studies are focused on using SERS active metallic nanoparticles; however, only few reports allow selective, sensitive and reliable Hg^{2+} sensing using SERS active thin-films[34-35]. Developing sensing methods based on thin-films rather than using colloidal nanoparticles has the advantage of eliminating the filtering step of the mercury-contaminated nanoparticles from wastewater following the detection step, thus reducing the cost and complexity of the wastewater treatment processes. In order to establish SERS active thin-films as a reliable and reproducible analytical tool, substrates with a homogeneous topology and high affinity towards the target toxin are required[36-37].

The major challenge in determining Hg^{2+} concentration in wastewater treatment plants is the removal of the soluble mercury ions. Several methods have been reported for Hg^{2+} ions removal from wastewater, including activated carbon sorption[38-39], ion-exchange[40] and photo-reduction[41-43]. The photo-reduction technique has been reported to be highly promising where by reducing Hg^{2+} ions into the low-water soluble elemental mercury (Hg^0) form, the toxin can be safely collected from the solution[44]. Photoreduction of Hg^{2+} can be performed using photocatalytic materials, where photogenerated electrons from the semiconductor are transferred to the divalent Hg^{2+} ions, subsequently reducing them to Hg^0. Thus, by a simple yet novel nano-engineering approach employing a photocatalytic substrate in combination with SERS-active, mercury-sensitive metallic nanoparticles, a combined functionality of SERS detection and photocatalytic Hg^{2+} removal can be acquired. Also, this photocatalytic/SERS multifunctionality allows the sensing layer to be cleaned from any organic traces using photo-degradation of attached organic molecules. This could lead to the ability of repeated cleaning of SERS marker molecules from the surface of SERS-active metal nanostructures, therefore, recovering their functionality.

When it comes to mercury sensing and removal processes, the major hurdle is the inability to achieve regeneration and therefore, re-use of the mercury amalgamated materials after their exposure. Previously, it has been shown that mercury amalgamated metallic surfaces can be potentially regenerated using low temperature heat-treatment processes[45-47]. Furthermore, the use of oxide based semiconductors with relatively high-temperature stability allows heat treatment processes to be carried out, thus enabling an additional functionality of surface regeneration through thermal removal of adsorbed mercury. Therefore, these substrates can be regenerated completely via removing SERS marker and amalgamated mercury by photodegradation and low temperature heat-treatment, respectively. This chapter provides the first account of a SERS-active ZnO/Ag nano-arrays system that can detect Hg^{2+}, remove Hg^{2+} and can be fully regenerated to perform multiple sensing events.

5.3. Materials and methods

Chemicals: All chemicals were purchased from Sigma Aldrich or Merck and used as received. Si (001) substrate (1cm × 1 cm) was chosen for growth of ZnO nano-arrays and cleaned using a standard procedure; initially, the wafer was ultra-sonicated consecutively in acetone, ethanol, isopropyl alcohol (IPA) and dried by nitrogen. To eliminate any remaining organic traces from the surfaces, they were cleaned for a period of 10 minutes with UV-Ozone (UVO Cleaner Plus). Deionized water (18.2 MΩm) was used throughout the synthesis process.

ZnO seeding with sol-gel: In order to prepare the seeding layer prior to ZnO array growth, the substrates were coated with three layers of zinc oxide via sol-gel process[48]. For sol-gel preparation, a previously reported protocol was used. Briefly, a 15 ml ethanol solution containing 0.1 M zinc acetate with an equal weight ratio of monoethanolamine (MEA) was prepared. This solution was then kept at 55 °C for 24 h (this step is referred to as ageing). The prepared solution was then deposited on to Si substrates using a spin coater operating at 4000 rpm for a period of 15 seconds. The prepared samples were dried at 95 °C for 10 min followed by annealing at 450 °C for 1 h.

Hydrothermal growth of ZnO nano-arrays: In order to grow ZnO nano-arrays, an aqueous solution containing 25 mM of zinc nitrate hexahydrate and equimolar hexamine was first prepared (also referred to as the nutrient solution). Approximately 50 mL of the nutrient solution was transferred to sealed glass autoclaves. The substrate was then placed face down at the top of the nutrient solution surface. The autoclaves were kept at 95 °C for a period of 6 h. The substrates were then removed from the autoclave, washed several times with water before being dried using dry nitrogen gas at room temperature.

Silver plating: The silver nanoparticles were decorated on ZnO nano-arrays by electroless deposition method. First; ZnO nano-arrays were sensitized with $SnCl_2$ aqueous solution (0.3 mM) prepared with trifluroacetic acid (1 µL for 10 mL solution) for 30 min. After sensitization step, the substrates were washed with water. Palladium seeding particles were then deposited on the ZnO nano-arrays by immersing the substrates into a solution containing 3 mM palladium nitrate for a period of 15 minutes. The deposited palladium nuclei act as seeding particles for silver plating. Finally, silver nanoparticles were deposited on the prepared substrates using Tollen's reagent method. Initially, 1 M diaminesilver(I) cation $[(Ag(NH_3)_2)^+]$ solution was prepared by adding a proper amount of 2.8% ammonium solution to aqueous silver nitrate solution until a transparent solution is observed. This stock solution

was afterwards diluted to a 100 mM concentration. Each of the prepared substrates was then immersed in separate 2 mL solutions containing 1 mL of 100 mM silver complex solution and 1 mL of aqueous 1 M glucose solution[49]. The synthesis was carried out by keeping the substrates in solution for a period of only 3 min at room temperature.

Analytical and characterization methods: Prepared samples were characterized with several different microscopic and spectroscopic techniques. Morphological studies were performed by FEI Nova NanoSEM field emission electron microscope (SEM). X-ray photoelectron spectroscopy (XPS) surface analyses were carried out using a Thermo Scientific K-Alpha instrument (un-monochromatized Mg Kα radiation, photon energy of 1253.6 eV at vacuum better than 10-9 Torr). Chemical bonding were aligned with adventitious carbon (C1s) binding energy of 285 eV. Inductively coupled plasma mass spectrometry (ICP-MS) analysis were carried out using Agilent 7700 series ICP-MS for measuring the amount of mercury ions in the solution after sensing and removing experiments. Raman measurements were conducted with Perkin Elmer Raman Station 200F (785 nm laser, spot size of 100 mm) with an exposure time of 5 s and 10 acquisitions, with background correction feature disabled. The backgrounds of SERS spectra were corrected based on our previous algorithm[50] as discussed in *Chapter III*. Perkin Elmer 2104 Multilabel Reader EnVision was used to investigate the photocatalytic efficiency when removing Rhodamine B (RB) from the substrate surface. All error bars (standard error of the mean) in the figures related to Raman experiments have been obtained following 10 different tests of the same sample.

SERS based mercury detection: The mercury detection experiments were performed by placing the prepared samples in glass vials containing 2 mL solution with Hg^{2+} concentrations of 10, 50, 100, 500, 1000, 5000 and 10000 ppb. Each solution containing identical substrates was then immediately placed in a dark room for a period of 1 h at room temperature. The substrates were then removed from solution, washed several times with water and transferred to the SERS marker dye solutions. To evaluate the sensing properties of the substrate, RB was selected as a probe molecule for SERS tests. The substrates were immersed in RB solutions with a concentration of 0.1 mM for a period of 1 h in order to ensure that surface adsorption equilibrium was reached. The substrates were then taken out of the RB solution, rinsed with deionized water and dried with dry nitrogen. SERS activities of the designed substrates were measured using Raman spectroscopy.

Photocatalytic degradation of SERS marker: Following mercury detection experiments, the photocatalytic degradation of organic traces from the substrate was carried out by placing

these substrates into 2 mL water and exposing them to UV light for a period of 1 h. In order to achieve even and constant intensity of UV light all over the surface while performing photocatalytic tests, 370 nm LED Area Light-Edmund optics was placed 5 cm above the samples with a heat sink connected to the LED to avoid any heat transfer to the samples. The complete removal of the RB marker was confirmed using Raman spectroscopy following the UV experiments. The substrates were then rinsed with deionized water, vacuum dried at room temperature and reused for further mercury removal/detection experiments. The photocatalytic efficiency for RB degradation in the current system was estimated using Eq. 5.1:

$$X = \frac{(C_0 - C)}{C_0} \times 100 \qquad 5.1$$

where C_0 and C are concentrations of dye before and after irradiation, respectively. In the current study, the photocatalytic degradation kinetics of a 10 µM RB solution was carried out using a blank (no catalyst), ZnO and ZnO/Ag nano-arrays.

Photocatalytic removal of mercury ions: As well as the removal of the SERS markers, the photocatalytic activity function of the prepared substrates was also employed to remove mercury from water following the detection/regeneration process. This was performed by exposing different samples (i.e. E-beam evaporated silver thin-film, zinc oxide and zinc oxide/silver nano-arrays) to 2 mL solution with a Hg^{2+} ion concentration of 10 ppm under UV irradiation for a period of 2 h. The Hg^{2+} ion removal kinetics were determined by taking 100 µL aliquots from the solution at five different time points over a period of 2 hours and analysing them using ICP-MS.

Surface regeneration following Hg exposure: In order to regenerate the Hg contaminated samples, the RB dye was first removed using the photocatalytic degradation method. The substrates were then placed in a vacuum at an operating temperature of 150°C for a period of 2 h to completely remove all of the amalgamated mercury. The complete removal of Hg from the substrate surface was confirmed using XPS analysis. The samples were observed to be repeatable (full regeneration) over three cycles following the detection of Hg^{2+} ions from a 5 ppm solution.

Selectivity of the developed nano-arrays towards Hg^{2+}: In order to evaluate the selectivity of the prepared ZnO/Ag nano-arrays, they were tested in a solution containing 1 ppm of Zn^{2+}, $Ca^{2+,}$ Mg^{2+}, Mn^{2+}, Cu^{2+}, Pb^{2+}, Fe^{2+} and Al^{3+} cations in the presence of 1 ppm Hg^{2+}.

5.4. Results and discussions

Figure 5.3 shows the synthesis procedures of ZnO/Ag nano-arrays (**a**) as well as the sensing/removing and regeneration steps (**b**). Briefly, ZnO seed layer was initially synthesized via sol-gel reaction method as reported in my previous work (**Figure 5.3-a1**)[48]. Then, ZnO nano-arrays were grown via soft hydrothermal method (**Figure 5.3-a2**). The synthesized ZnO nano-arrays were then sensitized with Sn^{2+} ions before adding Pd^{2+} ions in order to reduce them to Pd^{0} nanoparticles on the ZnO nano-arrays (**Figure 5.3-a3**). Finally, silver nanoparticles were synthesized via an electroless plating technique (**Figure 5.3-a4**). These steps have been explained in details in *Chapter IV*. The procedure of the sensing, removal and regeneration is shown in **Figure 5.3-b**. The first stage involved the exposure of the developed ZnO/Ag substrates to a solution containing various concentrations of Hg^{2+} ions for a period of 1 h followed by immersion into Rhodamine B (RB) solution (100 µM, 2 mL) for 1 h as shown in **Figure 5.3-b1**. The substrates were then tested using Raman spectroscopy (**Figure 5.3-b2**) and the intensity variation of the characteristic RB Raman band at 1358 cm^{-1} was used to determine the concentration of the Hg^{2+} ions in solution. Subsequently, to regenerate these Hg contaminated substrates, it was necessary to first remove the adsorbed RB from the surface. The RB removal was carried out by photocatalytic degradation by using the Hg contaminated ZnO/Ag arrays as the photocatalyst (**Figure 5.3-b3**). Following this stage, the full mercury removal from the solution was performed (if required) by immersing the ZnO/Ag nano-arrays back into the Hg^{2+} containing solution and performing photocatalytic mercury reduction. Finally, the adsorbed mercury on the ZnO/Ag nano-arrays could be recovered while regenerating the surface by using heat treatment at 150°C under vacuum for a period of 2 h (**Figure 5.3-b4**).

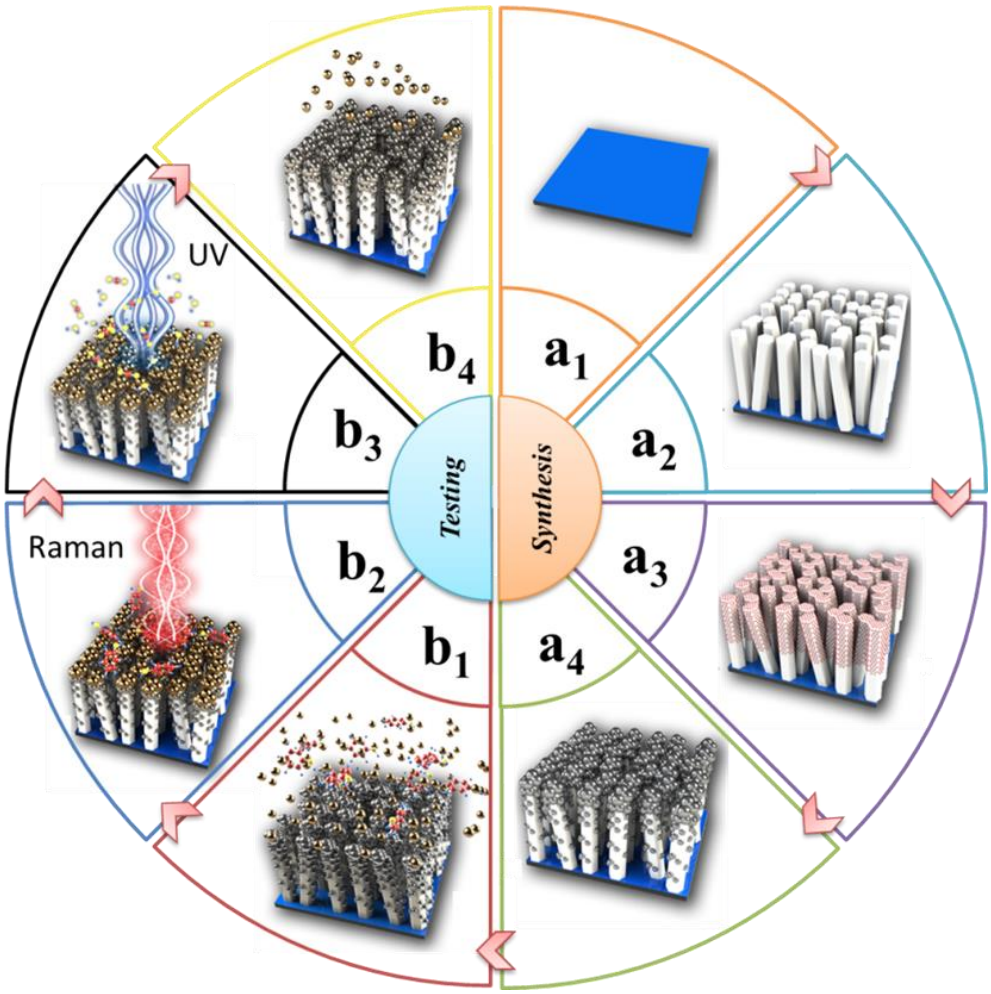

Figure 5.3. Detailed (**a**) synthesis and (**b**) sensing, removal and regeneration processes, starting with **a1**) synthesizing ZnO seed layer via sol-gel technique, **a2**) ZnO hydrothermal array growth, **a3**) decoration of the nano-arrays with palladium nanoparticles by charge exchange between Sn^{2+} and Pd^{2+} at the surface of the ZnO nano-arrays, **a4)** performing silver electroless plating decorating the ZnO arrays; followed by, **b1)** adsorption of Hg^{2+} ions on ZnO/Ag nano-arrays and subsequent adsorption of Raman marker on the arrays, **b2)** Raman detection of marker on mercury contaminated ZnO/Ag nano-arrays, **b3)** photocatalytic degradation of marker dye and finally, **b4)** removing mercury contamination from the ZnO/Ag nano-arrays by using heat treatment under vacuum as the regeneration step.

The SEM images of the synthesized ZnO/Ag nano-arrays before and after silver plating are shown in **Figure 5.4a** and **b**, respectively. The low magnification SEM images of the ZnO and ZnO/Ag nano-arrays (**Figure 5.4c** and **d**) show a uniform formation of nano-arrays and decorated silver nanoparticles throughout the surface of the sample. Furthermore,

as shown in **Figure 5.4e** and **f** the aspect ratio of the ZnO rods was determined to be 20 (average height of 2 µm and diameter of 100 nm).

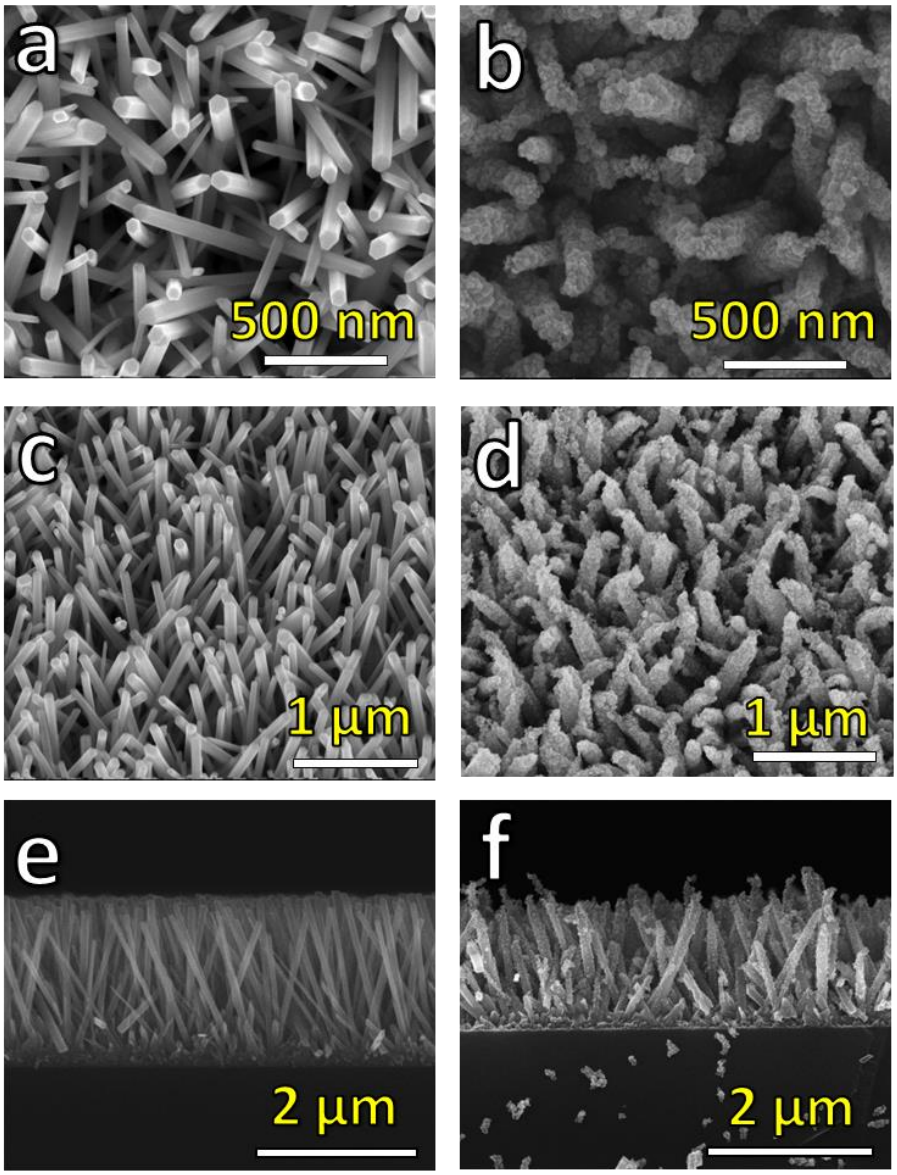

Figure 5.4. a) ZnO nano-arrays; **b)** Silver decorated ZnO nano-arrays; **c)** and **d)** low magnification of the obtained arrays; **e)** and **f)** side view of the obtained arrays.

The XRD analyses shown in **Figure 5.5** confirm the formation of metallic silver on ZnO nano-arrays with no other crystalline impurities.

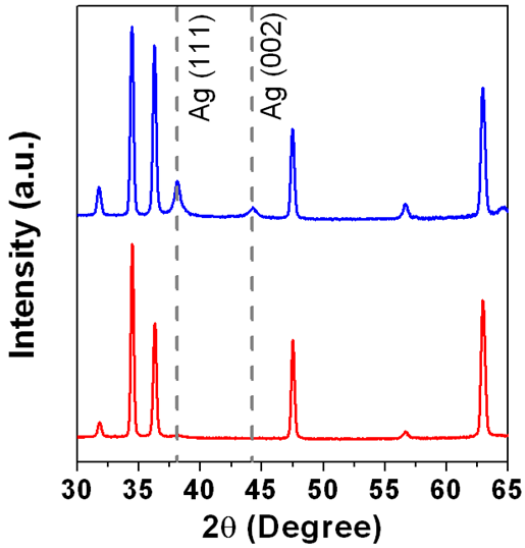

Figure 5.5. XRD patterns of ZnO (JCPDF 36-1451) and ZnO/Ag (JCPDF 04-0783) nano-arrays.

The prepared samples were tested for their mercury sorption and removal capabilities by exposing them to a solution containing Hg^{2+} at a concentration of 10 ppm placed either in the dark or under UV irradiation. In these tests, two control substrates, namely, e-beam evaporated silver thin-films and ZnO nano-arrays were used to compare with the developed ZnO/Ag nano-arrays. As observed in **Figure 5.6a**, the evaporated silver thin-film underwent mercury sorption on its surface via amalgamation which is a common phenomenon for gold and silver surfaces[51-52]. Furthermore, a similar Hg sorption behaviour was observed regardless of placing the samples in the dark or under UV irradiation as expected due to the metallic nature of silver thin-film. On the other hand, ZnO nano-arrays do differ in nature depending on whether they are placed in the dark or under UV irradiation. ZnO as a wide band-gap semiconductor can be excited by UV irradiation, which results into formation of electron/hole pairs, which can enhance the reduction of Hg^{2+} ions in solution to elemental mercury (Hg^0)[42]. The small removal of Hg^{2+} by the ZnO nano-arrays observed in the dark condition could be due to the high surface area of ZnO nano-arrays as well as the available high-energy surface defects with high electron densities[53]. In the case of ZnO/Ag nano-arrays in the dark, mercury sorption was observed to be higher than the ZnO nano-arrays and e-beam evaporated Ag thin-film due to the formation of high surface area Ag nanoparticles and their relatively higher affinity towards mercury.

Under UV irradiation, the mercury removal efficiency of ZnO/Ag nano-arrays was observed to be slightly lower relative to ZnO nano-arrays. It is well known that the

combination of noble metal nanoparticles with semiconductors produces heterojunction which results in an increase in lifetime of photo-generated electron/hole pairs subsequently increasing the photocatalytic activity of the composite[54-55]. However this phenomenon highly depends on the size and coverage density of the decorated noble metal nanoparticles[56-58]. In this study, in spite of the combination of ZnO and Ag nanoparticles, the formation of large Ag nanoparticles with high coverage on the ZnO nano-arrays surfaces seems to have dampened the photocatalytic efficiency. This phenomenon can be explained mainly due to the increase in electron/hole recombination sites in the decorated silver nanoparticles thus reducing the mercury sorption efficiency. Although, this is a negative property for this system when operated under UV irradiation, the mercury removal efficiency was observed to be significantly higher than the dark condition.

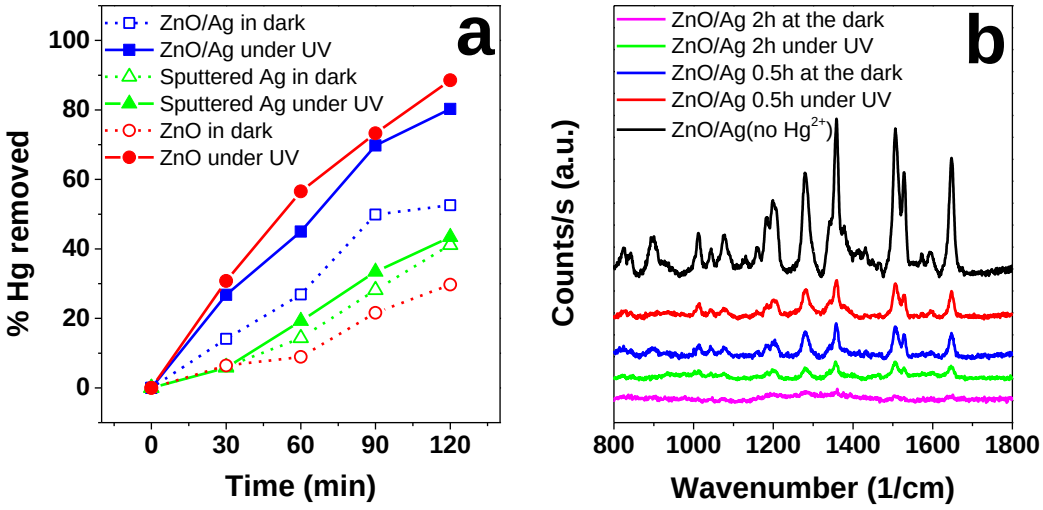

Figure 5.6. a) ICP-MS analysis of mercury ions removed from a solution containing 10 ppm Hg^{2+} tested in dark and under UV irradiation and **b)** SERS spectra of RB collected from a ZnO/Ag nano-arrays based substrate following its exposure to a 10 ppm Hg^{2+} solution in dark and under UV irradiation for a period of 0.5 h and 2 h.

There are two Raman based methods for the detection of Hg^{2+} ions in solution. The first method is based on the interaction of Hg^{2+} with a Raman marker (e.g. DNA-enzyme[33, 59-60] or T-Hg^{2+}-T pairs[34, 61-62]) where Hg^{2+} acts as a bridge between marker molecules. The increase in Hg^{2+} concentration would result in a higher number of linked markers, inducing stronger perturbations, which results in the increased Raman intensity of the features related to the markers. The second method is based on the interaction between Hg^{2+} ions with the SERS active noble metal nanoparticles[29, 63]. This type of interaction forms a mercury/active metal shell on the surface of these nanoparticles causing a reduction in the Raman intensity

related to the Raman marker molecules[29]. Raman signals of RB on ZnO/Ag nano-arrays are shown in **Figure 5.6b.** It can be observed that whether the ZnO/Ag nano-arrays are exposed to Hg^{2+} ions under dark or UV irradiation, an increase in mercury exposure period results in a decrease in the Raman intensity of the RB. However, the Raman intensity for the samples tested in the dark underwent a further decrease in comparison to the samples tested under UV irradiation. This result is postulated to be due to the photocatalytic activity of ZnO under UV irradiation, which enhances the reduction of Hg^{2+} into Hg^{0} which drops out of the solution and subsequently reduces the amount of available Hg^{2+} ions that can be adsorbed on the surface of the decorated silver nanoparticles.

It is important for a device to reach ultra-low detection limits when sensing Hg^{2+} ions in the solution. Since the number of Hg^{2+} ions in any one solution is limited, a device with a lower surface area can be used for the detection of low concentrations of mercury otherwise all the Hg^{2+} ions will be depleted on to the Ag nanoparticles if a larger area is used. The depletion of Hg^{2+} ions is undesired as it results in a reduction in the Raman intensity which is dependent on the coverage of mercury shell that is formed on the decorated Ag nanoparticles. If the coverage of these shells formed on the device is less than the saturation limit of the device, then the formed mercury shells will not be uniform and therefore, the uncertainty in the reported Hg^{2+} concentration will increase. Thus, the geometric surface area (GSA) of the sensor becomes highly important in determining the concentration of Hg^{2+} ions in the solution. For studying the effect of GSA on the mercury sorption capacity of the developed surfaces, two sets of sensors with GSA of 1 cm^2 and 0.25 cm^2 were synthesized and tested in solutions containing different Hg^{2+} concentrations (0–10 ppm, 2 mL, 1 h immersion). It was found that the sensor with the smaller GSA underwent less Hg^{2+} ions sorption on its surface at each tested mercury concentration relative to the sensor with the larger GSA as shown in **Figure 5.7a.** ICP-MS data showed that for the lowest Hg^{2+} concentration of 10 ppb, the 1 cm^2 device removed 100% while the 0.25 cm^2 removed ~30% of the total Hg^{2+} ions. On the other hand, when testing solutions containing a Hg^{2+} concentration of 10 ppm, the sensor with GSA of 0.25 cm^2 was completely covered with mercury shell (saturated). Therefore, using this device to detect ppm range concentrations would not be reliable as all Raman signals would be completely dampened. Hence, the lower the Hg^{2+} concentration that needs to be detected, the lower the GSA required making this method of detection feasible to detect ultra-low concentrations of Hg^{2+} in solution with the detection limit only restricted by how low the sample GSA can be fabricated while still usable with a Raman instrument.

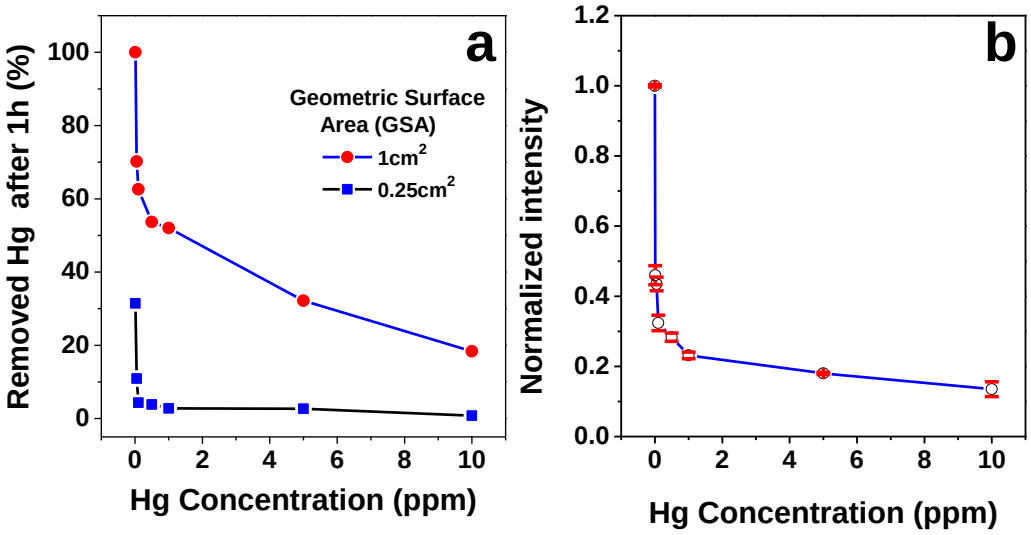

Figure 5.7. a) ICP-MS data showing Hg^{2+} ion removal efficiency of ZnO/Ag nano-arrays having geometric surface areas (GSA) of 1 cm^2 and 0.25 cm^2 from a solution contaminated with 10 ppm Hg^{2+} ions; and **b)** relative intensity of the characteristic RB Raman band at 1358 cm^{-1} as a function of Hg^{2+} ion concentration (10, 50, 100, 500, 1000, 5000 and 10000 ppb) using ZnO/Ag nano-arrays based SERS substrates (GSA=0.25 cm^2).

The sensitivity data of the sensor with the smaller GSA is shown in **Figure 5.7b** based on relative intensity of the characteristic RB Raman band at 1358 cm^{-1} which was obtained on a control ZnO/Ag nano-array without any Hg^{2+} exposure. As could be seen, the Raman spectrum of RB in the presence of 10 ppb shows more than 50% decrease in the intensity. Therefore, the detection limit of the developed ZnO/Ag nano-array for sample with smaller GSA towards Hg^{2+} ions was calculated to be in the sub ppb range (~0.45 ppb) using the three times the standard deviation of the blank method.

One of the most important yet rarely reported parameters when it comes to chemical detection using Raman on thin-films is the consistency of the sensing device over the different areas of the surface. Similarly, in the current study, it is important to obtain a uniform mercury shell throughout the ZnO/Ag nano-arrays surface in order to obtain a repeatable result regardless of the position on the surface being analysed with Raman spectroscopy. **Figure 5.8a** shows Raman mapping for scanning area of 150 × 150 μm^2 based on the characteristic RB Raman band at 1358 cm^{-1} from a sensor device having a geometric surface area (GSA) of 0.25 cm^2 of the ZnO/Ag nano-arrays without Hg^{2+} exposure. It may be observed that the intensity of the selected characteristic RB Raman band throughout the surface is uniform having an RSD of less than 4%. The uniformity of the ZnO/Ag nano-arrays was also tested after exposure to a solution containing an Hg^{2+} concentration of 1 ppm

for a period of 1 h. Although the RSD of the Raman signal was observed to increase to 16.55% post-mercury exposure (**Figure 5.8b**), the signal was observed to be uniform throughout the device's surface area. The increase of the RSD to 16.55% was mainly due to the decrease in the Raman intensity (due to the presence of mercury) and therefore, the low signal to noise ratio (*SNR*) associated with deteriorating Raman signal. The Raman spectra for these samples were background corrected using smoothing free algorithm while special attention was given to prevent changing any signal features (relative intensities and signal position) obtained when comparing the data[50].

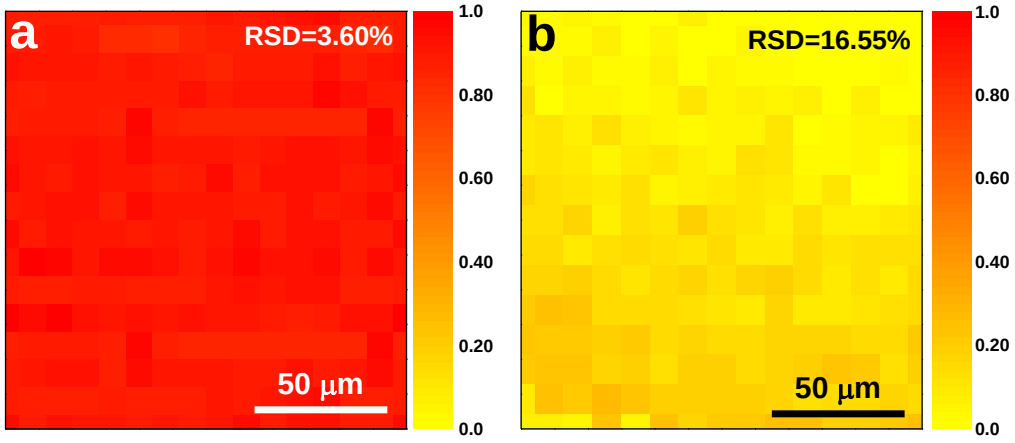

Figure 5.8. a) Raman mapping for scanning area of 150 × 150 μm^2 based on the characteristic RB Raman band at 1358 cm^{-1} from a sensor device having a geometric surface area (*GSA*) of 0.25 cm^2 of the ZnO/Ag nano-arrays without Hg^{2+} exposure; **b)** after exposing to a Hg^{2+} concentration of 1 ppm.

The first regeneration step of the developed ZnO/Ag nano-arrays via RB photocatalytic degradation was studied using UV-Vis spectroscopy while its second regeneration step was carried out using XPS analysis of Hg 4f core level during the heat treatment process. The photocatalytic degradation efficiency of ZnO and ZnO/Ag nano-array substrates towards RB is shown in **Figure 5.9**. The silver decorated sample showed lower photocatalytic activities. This phenomenon is completely explained in *Chapter IV, Section 4.4.3*. It was found that the ZnO and ZnO/Ag nano-arrays underwent ~100% and ~70% degradation of the 10 µM RB, respectively. The UV-Vis intensity related to RB (at ~550 nm) on ZnO/Ag nano-arrays is shown in **Figure 5.9b** and found to decrease with increasing irradiation time. In a sensing event, only a monolayer of RB is expected to deposit on the ZnO/Ag nano-array surfaces following Hg^{2+} exposure thus the time required to remove the

RB layer via photocatalysis would also be much less than that required to degrade a 10 µM RB solution.

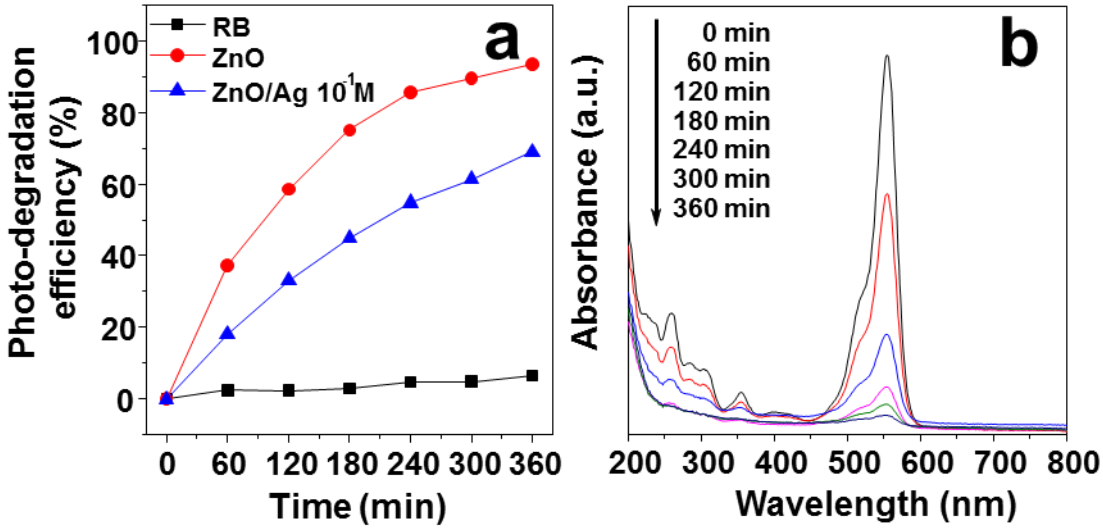

Figure 5.9. a) Photodegradation efficiency of RB using blank (no photocatalyst), ZnO and ZnO/Ag systems and **b)** UV-Vis absorbance spectra of RB by increase in the illumination time in the presence of ZnO/Ag nano-arrays.

The second regeneration step involving the removal of mercury following removal of the dye is an essential step in regaining the sensing and removal properties of the developed ZnO/Ag nano-arrays. It has been previously shown[45, 47] that mercury could be completely removed from noble metal surfaces using thermal desorption. However, as Ag nanoparticles undergo oxidation in the presence of heat and oxygen in air, the thermal desorption step was performed in the vacuum which also helped in preventing oxidation and accelerating the regeneration step. XPS analysis of Hg 4f core level spectra was used to determine the extent of surface regeneration as shown in **Figure 5.10a.** It may be observed that a mere 2 h heat treatment of the ZnO/Ag nano-arrays at an operating temperature of 150°C was required to completely remove all the amalgamated mercury from the surface.

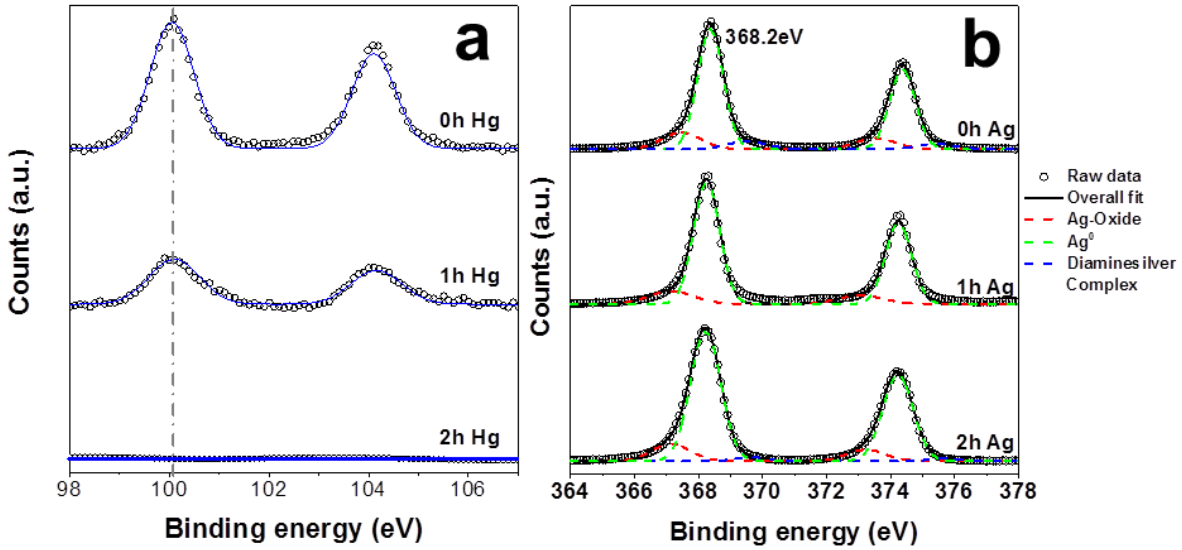

Figure 5.10. a) Hg 4f and **b)** Ag 3d XPS spectra of ZnO/Ag nano-arrays after RB degradation followed by heat treatment in the vacuum.

The surface regeneration experiments were carried out over three cycles, the data of which is shown in **Figure 5.11a.** It can be observed that the Raman signal of the RB carried out after each cycle has similar intensities thus indicating that the developed surfaces can be fully regenerated repeatedly following Hg^{2+} sensing/removal events. **Figure 5.11b** further shows the overlayed Raman spectra obtained as-such from the regenerated surfaces over the three sensing cycles without applying any spectral background correction, thus demonstrating the extent by which the developed surfaces can be regenerated to allow repeatable SERS sensing events. In addition; the XPS data corresponding to Ag 3d core level (**Figure 5.10b**) indicated that no significant chemical shifting had occurred. As glucose reduced silver nanoparticles can stand oxidation better than unprotected silver nanoparticles, the deconvoluted peaks can be assigned to Ag^0 as the main surface component with small quantities of AgO and surface bounded Ag ammonia complex[64]. The results indicated that Hg desorption had occurred during heat treatment of the developed ZnO/Ag nano-arrays[49].

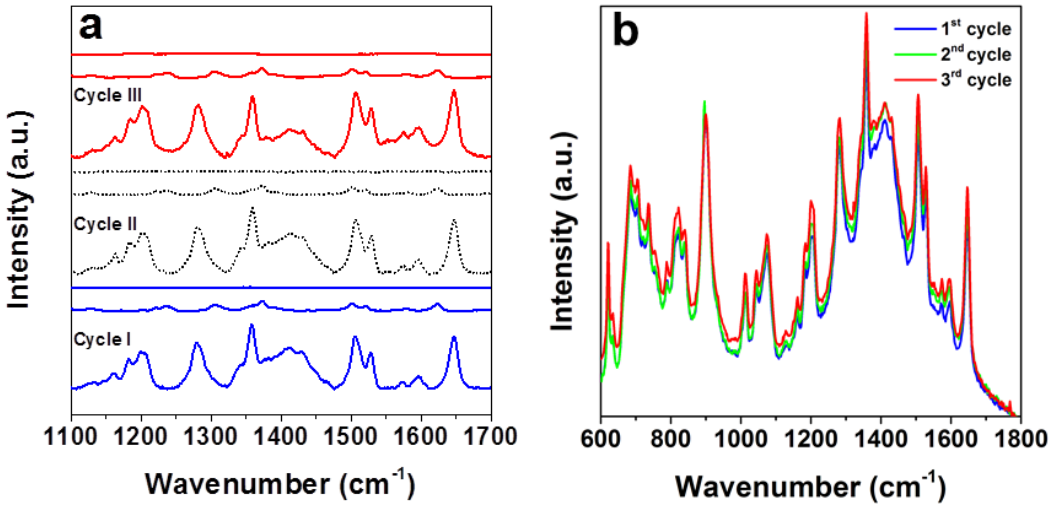

Figure 5.11. a) SERS enhancement of RB for developed substrates before and after Hg^{2+} exposure (5 ppm) and after removing RB and amalgamated mercury from the system with three successful regeneration cycles and **b)** Overlayed SERS spectra of one sample after three complete regeneration cycles without any background corrections being applied.

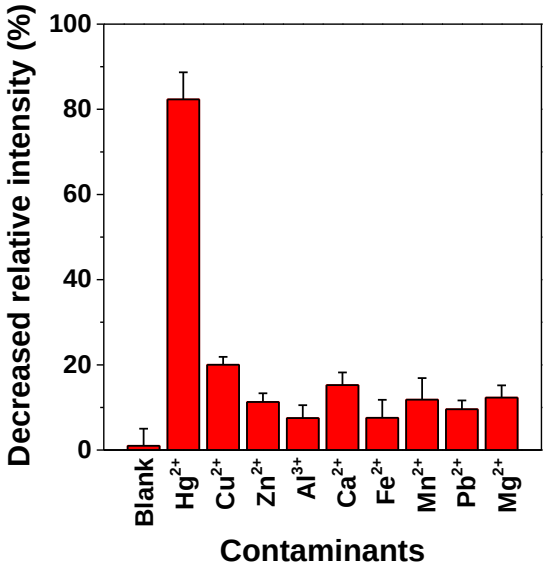

Figure 5.12. Selectivity of the ZnO/Ag nano-arrays towards Hg^{2+} (on the characteristic RB Raman band at 1358 cm^{-1}) in the presence of other metal ion species in a solution containing 1 ppm of each cation for an exposure period of 1 h.

In order to evaluate the selectivity of the prepared ZnO/Ag nano-arrays, they were tested in a solution containing 1 ppm of Cu^{2+}, Zn^{2+}, Ca^{2+}, Fe^{2+}, Mn^{2+}, Pb^{2+}, Mg^{2+} and Al^{3+} cations (**Figure 5.12**). It is observed that the decrease in Raman signal in the presence of

Hg^{2+} ions is significantly higher than any other cations thus demonstrating the specificity of the developed ZnO/Ag nano-arrays towards Hg^{2+} ions.

5.5. Conclusion

In summary, fabrication of a highly sensitive and selective SERS based device has been demonstrated, which can a) be used for SERS based Hg^{2+} detection, with the added multifunctionality of photocatalytic activity that can b) be used for the removal of Hg^{2+}, and c) can be regenerated and re-used over many cycles. The multifunctional nature, simplicity and small size of the developed ZnO/Ag nano-arrays based device allows for ease in mobility making this sensor suitable candidate for real time detection of ultra-low concentrations of Hg^{2+}. Finally, the high affinity of the developed ZnO/Ag nano-arrays towards Hg^{2+} and its excellent regeneration rate allows for removal of Hg^{2+} ions from the most highly concentrated solution and its reusability following a sensing/removal event.

References

1. *Global Mercury Assessment 2013: Sources, Emissions, Releases and Environmental Transport*; DTI/1636/GE; United Nations Environment Programme (UNEP): Switzerland, **2013**.
2. *EPA's Roadmap for Mercury*; EPA-HQ-OPPT-2005-0013; USA, **2006**.
3. *Mercury Study Report to Congress*; EPA-425/R-97-006; U.S. Environmental Protection Agency (EPA): 1997.
4. Qiu, J., *Nature* **2013,** *493* (7431), 144-145.
5. Streets, D. G.; Devane, M. K.; Lu, Z.; Bond, T. C.; Sunderland, E. M.; Jacob, D. J., *Environmental Science & Technology* **2011,** *45* (24), 10485-10491.
6. Ippolito, S. J.; Sabri, Y. M.; Bhargava, S. K., *Measuring Gas Phase Mercury Emissions from Industrial Effluents*. John Wiley & Sons, Inc.: New Jersey, **2012**;
7. Park, K. S.; Seo, Y. C.; Lee, S. J.; Lee, J. H., *Powder Technol.* **2008,** *180* (1–2), 151-156.
8. Harris, H. H.; Pickering, I. J.; George, G. N., *Science* **2003,** *301* (5637), 1203.
9. Engstrom, D. R., *Proceedings of the National Academy of Sciences* **2007,** *104* (42), 16394-16395.
10. Schaefer, J. K.; Rocks, S. S.; Zheng, W.; Liang, L.; Gu, B.; Morel, F. M. M., *Proceedings of the National Academy of Sciences* **2011**.
11. Schaefer, J. K.; Morel, F. M. M., *Nature Geosci* **2009,** *2* (2), 123-126.
12. Gilbertson, M.; Carpenter, D. O., *Environ. Res.* **2004,** *95* (3), 240-246.

13. Kudo, A.; Fujikawa, Y.; Miyahara, S.; Zheng, J.; Takigami, H.; Sugahara, M.; Muramatsu, T., *Water Sci. Technol.* **1998,** *38* (7), 187-193.
14. Grandjean, P.; Murata, K.; Budtz-Jørgensen, E.; Weihe, P., *The Journal of Pediatrics* **2004,** *144* (2), 169-176.
15. Magos, L.; Clarkson, T. W., *Ann. Clin. Biochem.* **2006,** *43* (4), 257-268.
16. Davidson, P. W.; Myers, G. J.; Weiss, B., *Pediatrics* **2004,** *113* (Supplement 3), 1023-1029.
17. Syversen, T.; Kaur, P., *J. Trace Elem. Med Biol.* **2012,** *26* (4), 215-226.
18. Myers, G. J.; Davidson, P. W.; Cox, C.; Shamlaye, C. F.; Palumbo, D.; Cernichiari, E.; Sloane-Reeves, J.; Wilding, G. E.; Kost, J.; Huang, L.-S.; Clarkson, T. W., *The Lancet* **2003,** *361* (9370), 1686-1692.
19. Counter, S. A.; Buchanan, L. H., *Toxicol. Appl. Pharmacol.* **2004,** *198* (2), 209-230.
20. A. Moreton, J.; Trevor Delves, H., *J. Anal. At. Spectrom.* **1998,** *13* (7), 659-665.
21. Ghaedi, M.; Reza Fathi, M.; Shokrollahi, A.; Shajarat, F., *Anal. Lett.* **2006,** *39* (6), 1171-1185.
22. Nolan, M. A.; Kounaves, S. P., *Anal. Chem.* **1999,** *71* (16), 3567-3573.
23. Harrington, C. F., *TrAC, Trends Anal. Chem.* **2000,** *19* (2–3), 167-179.
24. Li, M.; Gou, H.; Al-Ogaidi, I.; Wu, N., *ACS Sustainable Chemistry & Engineering* **2013,** *1* (7), 713-723.
25. Jiang, C.; Guan, Z.; Rachel Lim, S. Y.; Polavarapu, L.; Xu, Q.-H., *Nanoscale* **2011,** *3* (8), 3316-3320.
26. Guo, X.; Qian, X.; Jia, L., *JACS* **2004,** *126* (8), 2272-2273.
27. Lee, J.-S.; Han, M. S.; Mirkin, C. A., *Angew. Chem. Int. Ed.* **2007,** *46* (22), 4093-4096.
28. Chen, Y.; Wu, L.; Chen, Y.; Bi, N.; Zheng, X.; Qi, H.; Qin, M.; Liao, X.; Zhang, H.; Tian, Y., *Microchimica Acta* **2012,** *177* (3-4), 341-348.
29. Ren, W.; Zhu, C.; Wang, E., *Nanoscale* **2012,** *4* (19), 5902-5909.
30. Ganbold, E. O.; Park, J. H.; Ock, K. S.; Joo, S. W., *Bull. Korean Chem. Soc.* **2011,** *32* (2), 519-523.
31. Li, P.; Liu, H.; Yang, L.; Liu, J., *Talanta* **2013,** *106* (0), 381-387.
32. Duan, J.; Yang, M.; Lai, Y.; Yuan, J.; Zhan, J., *Anal. Chim. Acta* **2012,** *723* (0), 88-93.
33. Han, D.; Lim, S. Y.; Kim, B. J.; Piao, L.; Chung, T. D., *Chem. Commun.* **2010,** *46* (30), 5587-5589.
34. Du, Y.; Liu, R.; Liu, B.; Wang, S.; Han, M.-Y.; Zhang, Z., *Anal. Chem.* **2013,** *85* (6), 3160-3165.

35. Zhang, L.; Chang, H.; Hirata, A.; Wu, H.; Xue, Q.-K.; Chen, M., *ACS Nano* **2013,** *7* (5), 4595-4600.
36. Lin, X.-M.; Cui, Y.; Xu, Y.-H.; Ren, B.; Tian, Z.-Q., *Analytical and Bioanalytical Chemistry* **2009,** *394* (7), 1729-1745.
37. Banholzer, M. J.; Millstone, J. E.; Qin, L.; Mirkin, C. A., *Chem. Soc. Rev.* **2008,** *37* (5), 885-897.
38. Namasivayam, C.; Kadirvelu, K., *Carbon* **1999,** *37* (1), 79-84.
39. Kadirvelu, K.; Kavipriya, M.; Karthika, C.; Vennilamani, N.; Pattabhi, S., *Carbon* **2004,** *42* (4), 745-752.
40. Dąbrowski, A.; Hubicki, Z.; Podkościelny, P.; Robens, E., *Chemosphere* **2004,** *56* (2), 91-106.
41. Wang, X.; Pehkonen, S. O.; Ray, A. K., *Electrochim. Acta* **2004,** *49* (9–10), 1435-1444.
42. Dou, B.; Chen, H., *Desalination* **2011,** *269* (1–3), 260-265.
43. Prairie, M. R.; Evans, L. R.; Stange, B. M.; Martinez, S. L., *Environmental Science & Technology* **1993,** *27* (9), 1776-1782.
44. Khalil, L. B.; Rophael, M. W.; Mourad, W. E., *Applied Catalysis B: Environmental* **2002,** *36* (2), 125-130.
45. Morris, T.; Sun, J.; Szulczewski, G., *Anal. Chim. Acta* **2003,** *496* (1–2), 279-287.
46. Sabri, Y. M.; Ippolito, S. J.; Tardio, J.; Bhargava, S. K., *The Journal of Physical Chemistry C* **2011,** *116* (3), 2483-2492.
47. Sabri, Y. M.; Ippolito, S. J.; Tardio, J.; Atanacio, A. J.; Sood, D. K.; Bhargava, S. K., *Sensors and Actuators B: Chemical* **2009,** *137* (1), 246-252.
48. Kandjani, A. E.; Tabriz, M. F.; Moradi, O. M.; Mehr, H. R. R.; Kandjani, S. A.; Vaezi, M. R., *J. Alloys Compd.* **2011,** *509* (30), 7854-7860.
49. Yabu, H.; Hirai, Y.; Shimomura, M., *Langmuir* **2006,** *22* (23), 9760-9764.
50. Kandjani, A. E.; Griffin, M. J.; Ramanathan, R.; Ippolito, S. J.; Bhargava, S. K.; Bansal, V., *Journal of Raman Spectroscopy* **2013,** *44* (4), 608-621.
51. Levlin, M.; Ikävalko, E.; Laitinen, T., *Fresenius' Journal of Analytical Chemistry* **1999,** *365* (7), 577-586.
52. Sabri, Y. M.; Ippolito, S. J.; Atanacio, A. J.; Bansal, V.; Bhargava, S. K., *J. Mater. Chem.* **2012,** *22* (40), 21395-21404.
53. Michelle, J. S. S.; Kester, W. J. W.; Irene, Y., *J. Phys.: Condens. Matter* **2012,** *24* (30), 305001.
54. Pearson, A.; Bhargava, S. K.; Bansal, V., *Langmuir* **2011,** *27* (15), 9245-9252.

55. Pearson, A.; Jani, H.; Kalantar-zadeh, K.; Bhargava, S. K.; Bansal, V., *Langmuir* **2011,** *27* (11), 6661-6667.
56. Cárdenas-Lizana, F.; Gómez-Quero, S.; Idriss, H.; Keane, M. A., *J. Catal.* **2009,** *268* (2), 223-234.
57. Yoo, S. J.; Jeon, T.-Y.; Lee, K.-S.; Park, K.-W.; Sung, Y.-E., *Chem. Commun.* **2010,** *46* (5), 794-796.
58. Subramanian, V.; Wolf, E. E.; Kamat, P. V., *JACS* **2004,** *126* (15), 4943-4950.
59. Ma, W.; Sun, M.; Xu, L.; Wang, L.; Kuang, H.; Xu, C., *Chem. Commun.* **2013,** *49* (44), 4989-4991.
60. Lee, J.; Jun, H.; Kim, J., *Adv. Mater.* **2009,** *21* (36), 3674-3677.
61. Li, F.; Wang, J.; Lai, Y.; Wu, C.; Sun, S.; He, Y.; Ma, H., *Biosens. Bioelectron.* **2013,** *39* (1), 82-87.
62. Kang, T.; Yoo, S. M.; Yoon, I.; Lee, S.; Choo, J.; Lee, S. Y.; Kim, B., *Chemistry – A European Journal* **2011,** *17* (7), 2211-2214.
63. Senapati, T.; Senapati, D.; Singh, A. K.; Fan, Z.; Kanchanapally, R.; Ray, P. C., *Chem. Commun.* **2011,** *47* (37), 10326-10328.
64. Mikhlin, Y. L.; Vishnyakova, E. A.; Romanchenko, A. S.; Saikova, S. V.; Likhatski, M. N.; Larichev, Y. V.; Tuzikov, F. V.; Zaikovskii, V. I.; Zharkov, S. M., *Appl. Surf. Sci.* **2014,** *297* (0), 75-83.

CHAPTER VI

Nano-patterned ZnO/AgTCNQ as a novel p-n junction photocatalyst

Colloidal lithography (CL) has been evolved as an alternative to conventional photo and electron-beam lithographic techniques to pattern the surfaces within nano range resolution. As this technique can produce controlled patterning of semiconductor and metallic nanomaterials on various surfaces, this technique has the potential for many optoelectronic applications. In this chapter, a novel colloidal lithography method was developed to fabricate organic/inorganic p-n heterojunctions with desired spacing and coverage density. Two different uniform sized polystyrene (PS) beads (500 nm and 1500 nm) were synthesized using dispersion polymerization and they were used as colloidal templates on the Zinc oxide substrate to make the mask. Electron Beam assisted silver deposition onto these PS templates and subsequent etching of PS, led to the formation of silver patterns of nano-stars on the ZnO thin film. TCNQ vapour was allowed to react with the silver patterns for the growth of AgTCNQ organic semiconductor on the surface of ZnO thin film. The effects of the synthesis temperature, the size of the PS bead on the distance, and surface coverage of the AgTCNQ patterns on the ZnO structure were studied. The synthesized p-n heterojunctions were tested for their photocatalytic degradation ability of an organic dye Rhodamine B and it was found that these p-n semiconductors act as efficient photocatalysts by increasing the electron-hole life time.

A part of this chapter has been prepared as a manuscript for submission:

Kandjani, A. E.; Ramanathan, R.; Mohammadtaheri, M.; Bhargava, S.K.; Bansal, V.; Nano-patterning of AgTCNQ/ZnO p-n heterojunction: the controlled junction population via colloidal lithography; *Advanced Materials*, (To be submitted).

6.1. Introduction to surface patterning: necessities and applications

Nowadays, fabrication of well controlled nanostructures based on their size, position, shape and structure is one of the main challenges. Although common lithography techniques provide an approach to fabricate patterned structures, due to their expensive, low-throughput, and low resolution (limited to micron size) limitations, these techniques are not applicable to make nano patterned surfaces for advanced applications. Electron-beam lithography (EBL) technique can produce the nano level precision, but this method is much expensive and the fabrication time increases exponentially with increase in the area of the patterning[1-2]. Recently, a host of non-conventional lithographic techniques has been introduced such as soft imprint lithography as an alternative; however, these techniques still require masks or masters to form patterns, similar to the conventional or nano lithographic techniques[3-7]. Self-assembly techniques such as Langmuir–Blodgett monolayers and liquid crystalline structures of surfactants are the commonly used methods to make either the master or mask for designing nano-patterns[8-10].

Among these techniques, ***colloidal lithography*** (*CL*) has been demonstrated to be a cheap, convenient and precise method to fabricate patterned surfaces (scalable for feature size below 100 nm) on a wide range of substrates of different surface chemistry[11]. Uniform sized colloidal particles are used as sacrificial templates that function as a monodispersed (particles with narrow particle size distribution) sacrificing materials are used as a mask component in this technique. Silica, polymethyl methacrylate (PMMA) and polystyrene (PS) particles are the commonly used colloidal particles, and these particles can be synthesized via wet chemical methods such as emulsion polymerisation (e.g. PMMA[12] and PS[13-14]) or sol-gel (e.g. silica[15]) methods. These uniform sized colloidal materials can have sizes within the range of tens of nanometres to tens of micrometres. Due to their size monodispersity, they can be assembled into 2D or 3D periodic arrays or patterns, which are referred as ***photonic crystals***. These arrays can be used as a mask for preparation of templates for surface patterning of different structures via etching or deposition methods[16-17].

6.1.1. Synthesis of monodispersed polymer beads

The fabrication of monodispersed polymeric beads can be achieved via different approaches, including: micro-emulsion polymerization[18], emulsifier-free emulsion polymerization[19], seed emulsion polymerization[20] and dispersed polymerization[13, 21-22]. First two methods are the common methods for the synthesis of uniform sized polymeric particles but their yield is very low and these particles are not stable over long time. Seed emulsion polymerisation is generally used for synthesizing large particles (more than 10 µm), but it is a tedious process as well as difficult to control the size. The dispersion polymerization is a single step process to generate uniform sized spherical polymeric particles with dimensions between 0.1 to 15 µm. In this method, polymerization of a monomer is carried out in the presence of a dissolved polymeric stabilizer in the reaction medium. The solvent should dissolve both the monomer and the steric polymeric stabilizer; however, the as-formed polymeric particles should be insoluble in the same solvent. Thus, the reaction medium consists of a homogenous solution of the monomer, initiator and also the dispersant. The soluble dispersant polymer has a crucial effect in controlling the size of polymeric particles formation. This dispersant polymer adsorbs onto the surface of the as-formed nuclei particles and acts as steric stabilizer, which controls the size of the particles as well as increase the stability. In addition to the dispersant polymer, monomer concentration, initiator concentration, and synthesis temperature play an important role in determining the size, size distribution, and molecular weight of the formed particles[23]. This technique has been utilized to form the monodispersed PS spheres in this thesis. The synthesis procedure is shown in **Figure 6.1**, schematically.

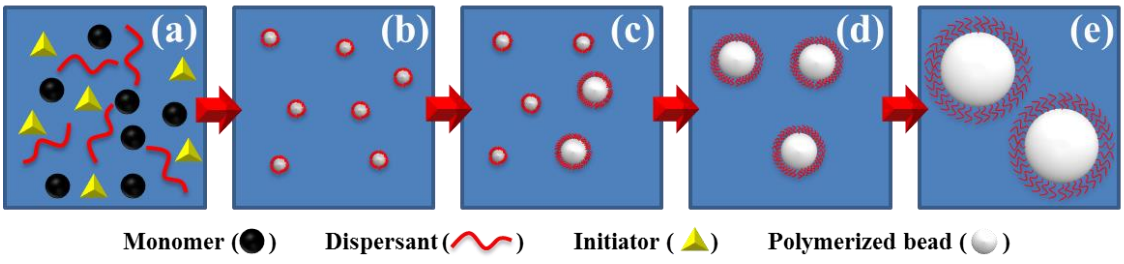

Figure 6.1. Schematic model for the growth of monodispersed polystyrene microspheres.

As shown in **Figure 6.1**, the dispersion polymerization for synthesis of uniform sized polystyrene particles consists of five stages[23]:

a) The continuous solution phase of the starting materials, including: monomer, dispersant and initiator.

b) By heating of the mixture, the free radicals of the initiator form and make small nuclei of the polymeric materials.

c) Growth of the small nuclei makes larger particles until the adsorbed polymer layer sterically restricts the growth further.

d) When all particles reach to the point that they have enough stabilizer polymers on their surface, they become sterically stabilized. This point is called as ***critical point***.

e) After reaching to the critical point, nucleation and particle formation do not occur in the solution. The growth after this point is mostly based on diffusive capture of oligomers. This reaction stops when all of the monomer is consumed.

Thus, the formed particles are sterically-stabilized by dispersant polymer and the number of formed particles remains constant.

6.1.2. Colloidal particles at the air/water interface

When a colloidal particle is located at the interface of water and air, it reduces the surface free-energy of the water and amphiphilicity of the particle controls its position at the air-water interface. As shown in **Figure 6.2a**, when a spherical colloidal particle floats at the interface of water and air, the particle is immersed into the water to a certain depth. The immersion factor (***Z***) can be defined as the deviation from symmetrical immersion depth. The normalized immersion factor (Z_0) can be calculated as $Z_0=Z/R$ where R denotes the particle radius**.** Thus the energy between materials at the interface can be calculated as:

$$E_{bead/air} = \gamma_{bead/air}.2\pi R^2(1+Z_0) \quad 6.1$$

$$E_{bead/water} = \gamma_{\frac{bead}{water}}.2\pi R^2(1-Z_0) \quad 6.2$$

$$E_{air/water} = \gamma_{\frac{air}{water}}.\pi R^2(1-Z_0^2) \quad 6.3$$

The *Eq. 6.3* is related to the energy gained by reduction in the interface of air/water by floating of the colloidal sphere[24].

The total interface energy E_{total}, is the accumulation of the three energies and the size of the sphere and can be written as:

$$E_{total} = Z_0^2 + 2(a-b)(Z_0+1) - 1 \quad 6.4$$

$$a = \frac{\gamma_{bead/air}}{\gamma_{air/water}} \quad 6.5$$

$$b = \frac{\gamma_{bead/water}}{\gamma_{air/water}} \quad 6.6$$

As could be seen from *Eq. 6.4*, the total energy equation forms energy well. The colloidal particle would stay at the interface if the energy of particle with Z_0 does confine in the energy well as:

$$-1 < \frac{\gamma_{bead/air} - \gamma_{bead/water}}{\gamma_{air/water}} < 1 \quad 6.7$$

If *Z=1*, the particle is completely in the air phase and when *Z=-1* then the particle is completely immersed[25].

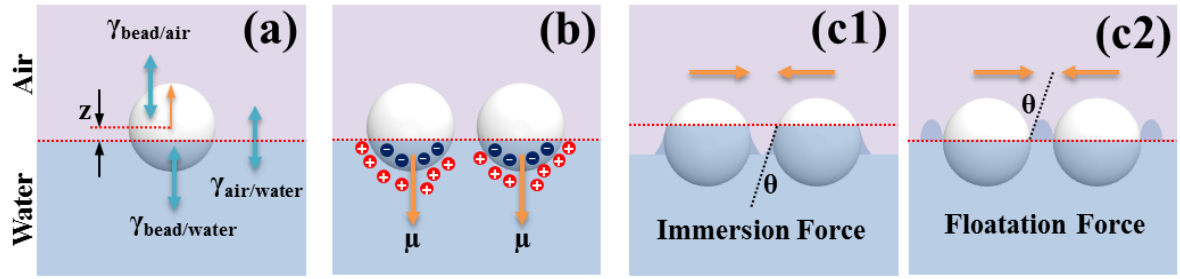

Figure 6.2. a) Geometry of a particle floating on the interface; **b)** accumulation of the surface charges on the suspended particles which disperse particles; **c)** formation of attractive capillary forces.

For polystyrene beads on the air/water interface[26]:

$$a = \frac{\gamma_{PS/air}}{\gamma_{air/water}} = 0.49 \quad 6.8$$

$$b = \frac{\gamma_{bead/water}}{\gamma_{air/water}} = 0.14 \quad 6.9$$

Which results into $E_{total,min}=0.14$ where $E_{air}=1.96$ ($Z=1$) and $E_{water}=0.64$ ($Z=-1$). This clearly shows that the sphere has minimum energy when it sits on the surface and for moving

the colloidal particle to the water phase or air phase, excessive energy is needed, and thus the particle gets trapped at the interface[26].

As colloidal particle sits on the surface, a surface charge layer is created on the part of the particle which is on the surface, as shown in **Figure 6.2b**. The surface charge of the colloidal particle and the structured arrangement of water molecules constitute a dipole[25, 27]. When two particles of same surface charge approach each other, due to the identicle charge and non-symmetrical charge distribution of the water molecules, the particles remain dispersed without undergoing any further aggregation. If the particles are fabricated using a steric surfactant, the dipole forces are negligible.

Between the interface of the two particles, once an attractive capillary force is created this leads to a decrease in the surface energy due to the interface distortion. ***Immersion*** and ***floating*** are the two major types of capillary forces as shown in the **Figure 6.2c** and these attractive forces are long range nature[24, 28-29]. Thus between particles, three major forces are created on the interface: *attractive* **capillary forces** and **van der Waals forces** and *repulsive* **dipole forces**. The controlled interplays among these forces play the key role in assembling these particles into close packed structures or patterned structures.

6.1.3. Close-pack colloidal arrays and colloidal lithography

Most of the available techniques for formation of the close-packed monolayer of colloidal monodispersed particles can be divided into two major groups: ***direct assembly*** on the surface of the solid substrate of interest and ***interface mediated*** methods[30]. The interface mediated methods have several advantages over the direct assembly method. As mentioned in the previous section, the particles stay as a monolayer on the interface. Second, particles on the surface of the liquid have more mobility and hence close packing can be achieved by increasing the surface pressure at the air-water interface. Third, the type of the substrate is not as critical as in the direct assembly method. In this thesis, interface mediated method has been utilised for the formation of polystyrene particle monolayers[30]. If colloids are added to the interface the capillary forces make the particles stick together leading to brightly colored patches on the surface that indicate the formation of the densely packed monolayer. The particles on the surface can be forced to form closely packed patches. One of the main techniques to achieve this is the use of Langmuir-Blodgett trough[8, 11, 31-32]. In this technique the particles on the interface are swept by hydrophobic troughs and are forced to form a close

packed 2D solid structures formation. After the formation of the close packed monolayer, these monolayer can be transferred to any substrate using a dip coater or manually. In addition of using Langmuir troughs for packing the colloids on the interface, considering the charge of the colloidal particles, in small scales these colloids can be forced to form a close packed layers using ionic surfactant[33]. If packed 2D colloidal mask is needed to be used for covering large areas, use of Langmuir-Blodgett trough is the best possible method reported in the literature. On the other hand the use of surfactant assist method is more restricted to smaller surfaces.

6.2. Silver tetra-cyanoquinodimethane (AgTCNQ)

As mentioned in the previous section, the close-packed colloidal particles were used as a sacrificial mask to make patterned semiconducting p-n junctions between Zinc oxide and silver-7,7,8,8-Tetracyanoquinodimethane (AgTCNQ). TCNQ is a p-type organic semiconductor, having the electron affinity of 2.88 eV and it has been used in many optoelectronics applications[34-35]. It can be reduced into two forms such as $TCNQ^{\bullet-}$ and $TCNQ^{2-}$ as shown in **Figure 6.3**[36] due to its affinity to accept the electrons. These ionized forms of TCNQ can easily co-ordinate with metal ions to form ***coordination polymeric*** (CPs) and ***metal-organic*** (MOFs) frameworks. The MOFs are produced by reaction between transition metal with TCNQ molecules. Due to the insolubility of the TCNQ based MOFs in common solvents, re-crystallization to obtain the single crystal becomes very difficult, which restricts the study of their structure. Among the metal-TCNQ structures, AgTCNQ and CuTCNQ have attracted most interest. These materials show low band-gap p-type behaviour. Also, they show an interesting hysteresis loop in their I-V curves which makes them good candidates for resistive switching memories[37-39]. Nano-wire or nano-rod structures of these metal TCNQ structures enable them to behave as good candidates for field emission applications[37, 40]. Other novel applications have also been recently found for these materials, mostly through ongoing investigations in our group. For instance, AgTCNQ has been shown to be a highly active antibacterial material[41]. Both of these materials have been used for catalytic and photocatalytic applications[42-43]. Also recently, CuTCNQ/ZnO heterojunction has been used as a p-n organic/inorganic humidity gas sensor[44].

AgTCNQ and CuTCNQ molecule can be synthesized via different methodologies:

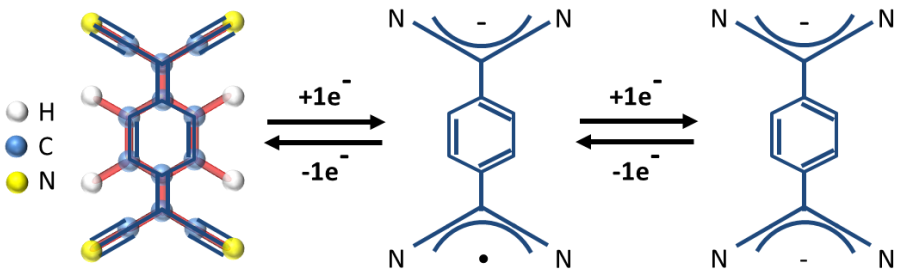

Figure 6.3. Structure of TCNQ and its ionic forms.

Electrochemical Methods: $TCNQ^0$ is partially soluble in acetonitrile and addition of Ag or Cu thin films or particles to this solution lead to the formation of metal-TCNQ structures. Dissolved $TCNQ^0$ molecules are adsorbed onto the surface of metal and the resultant charge transfer process makes metal and TCNQ ions. These ions can migrate to the solution and also they can form transition metal-TCNQ (M-TCNQ) frames. As CuTCNQ and AgTCNQ have low solubility in acetonitrile, nanorods and nanowires of CuTCNQ and AgTCNQ, respectively, can be formed using this method. The aspect ratio of these formed MOF nano-arrays can be controlled by varying the concentration of $TCNQ^0$ in the solution as well as time of the reaction[45-46].

Chemical vapour deposition (CVD): An alternative method for the synthesis of AgTCNQ and CuTCNQ nanostructures is the gas-solid reaction between $TCNQ^0$ vapour and the transition metal. In this method, TCNQ vapour has enough energy to allow charge transfer reaction on the surface of the metal substrate to form M-TCNQ. The temperature has a critical importance in controlling the formation and the growth of M-TCNQ structures. The higher the temperature the faster the growth that can happen, and larger nanowires can be formed. The morphology of materials is controlled by the thickness and size of the metallic materials in addition to the time and temperature. If the thickness of the metallic material is reduced below 200 nm, thin film of the M-TCNQ can be formed[47-48] rather than forming nanowires or nanorods.

The heterojunction semiconducting devices, as explained in *Chapter 1 - Section 1.2.2.2*, have gained researchers' interests due to their unique band structure properties. As a metal-organic semiconductor, AgTCNQ has not been explored to be a part of heterojunction and their applications. In this chapter, a novel method has been suggested for the formation of p-n heterojunction between AgTCNQ nano-wires and ZnO thin film. I is shown here that colloidal lithography based nano-patterning technique not only allows the fabrication of a

well-controlled p-n junction, but also it allows control over the density and location of the junctions at the nano scale levels. This technique can easily be extended to the formation of other interesting well-controlled heterojunction structures.

6.3. Materials and methods

Chemicals: All chemicals were purchased from Sigma Aldrich or Merck and used as received. Si (001) substrate (1 cm × 1 cm) was chosen for growth of ZnO nano-arrays and cleaned using a standard procedure; initially, the wafer was ultra-sonicated consecutively in acetone, ethanol, isopropyl alcohol (IPA) and dried by nitrogen. To eliminate any remaining organic traces from the surfaces, they were cleaned for a period of 10 minutes with UV-Ozone (UVO Cleaner Plus). Deionized water (18.2 MΩm) was used throughout the synthesis process.

ZnO thin film with sol-gel: The substrates were coated with three layers of zinc oxide via sol-gel process. For sol-gel preparation, a previously reported protocol was used[49]. Briefly, a 15 mL ethanol solution containing 0.1 M zinc acetate with an equal weight ratio of monoethanolamine (MEA) was prepared. This solution was then kept at 55 °C for 24 h (this step is referred to as ageing). The prepared solution was then deposited on to Si substrates using a spin coater operating at 4000 rpm for a period of 15 seconds. The prepared samples were dried at 95 °C for 10 min, this process was repeated 5 times to make sure that ZnO film was coated evenly on the samples. Then, these substrates were annealed at 450 °C for 1 h.

Monodispersed polystyrene (PS): PS beads were synthesized using a dispersion polymerization technique[13]. Initially, 20 mL of styrene monomer were washed with ammonia (28%) solution to remove the inhibitor from the monomer. The purified styrene was dissolved in 20mL ethanol/water solution in a three neck round bottom flask and was purged with nitrogen to remove any oxygen and avoid unwanted polymerization. PVP was added to the solution as a steric surfactant. Azobisisobutyronitrile (AIBN, $[(CH3)_2C(CN)]_2N_2$) was used as an initiator. 28 mg of AIBN was dissolved in 20mL ethanol and then purged with nitrogen for 10 min. The AIBN was injected to the solution which was kept at the temperature of 70 °C at 1500 rpm. The synthesis was kept in the N_2 atmosphere and constant temperature and stirring for 24 h. The formed PS monodispersed particles were centrifuged and washed with ethanol and water several times and redispersed in ethanol. The synthesis variables for formation of 500 and 1500 nm monodispersed spheres are listed in **Table 6.1**.

Variable	500 nm	1500 nm
Ethanol	36 mL	40 mL
Water	4 mL	---
Styrene	2 mL	2 mL
AIBN	28 mg	28 mg
PVP	800 mg	200 mg

Table 6.1. Synthesis conditions for producing 500 and 1500 nm monodispersed PS spheres.

Monolayer formation: The prepared monodispersed PS colloids in ethanol were used for forming the masks on the ZnO substrates. In this regard, a plastic standard petridish containing deionised water was used to form a water/air interface. Then, 30 µL of prepared PS solution was injected slowly to the interface. The formation of brightly-colored patched sections shows the formation of monolayer. Then, 10 µL of sodium dodecyl sulphate (SDS) solution (20 mg/mL) was added to the interface in order to make the monolayer completely compact. This helps to get more packed monolayer surfaces on the interface. The formed monolayer was transferred onto ZnO substrate from the interface.

Synthesis of ZnO/Ag nano-star patterns: 300 nm thick Ag thin film was deposited using E-beam evaporation system on the dried PS monolayer on ZnO thin film. Then the PS and excessive silver were washed away from the substrate using a lift-off procedure using tetrahydrofuran (THF).

Synthesis of ZnO/AgTCNQ: As-fabricated ZnO/Ag star patterns were placed in a furnace 5 mm above the TCNQ powder. The setup was purged continuously with 120-150 sccm argon for controlled temperature and time periods. **Figure 6.4** shows the synthesis procedure schematically.

Evaluation of photocatalytic activity: Photocatalytic activities of these hetereojunctions were tested by exposing these substrates to 1 mL aqueous solutions of 10 µM RB (in dark for 1 h) before their exposure to UV irradiation. The uniform UV exposure to the substrates was ensured by employing an 18 W, 370 nm LED (Edmund Optics) with attached heat sink (to avoid sample heating) 3 cm above the substrate. The photocatalytic degradation of RB was followed by monitoring the decrease in the absorbance of the RB (UV-Vis peak at 654 nm) using Varian Cary 50

Bio UV/ Visible Spectrophotometer. The photodegradation efficiency of ZnO/Ag nano-arrays was estimated as:

$$Photodegradation\ efficiency = \frac{(C_0 - C)}{C_0} \times 100 \qquad 6.10$$

wherein C_0 and C correspond to RB concentrations before and after irradiation, respectively.

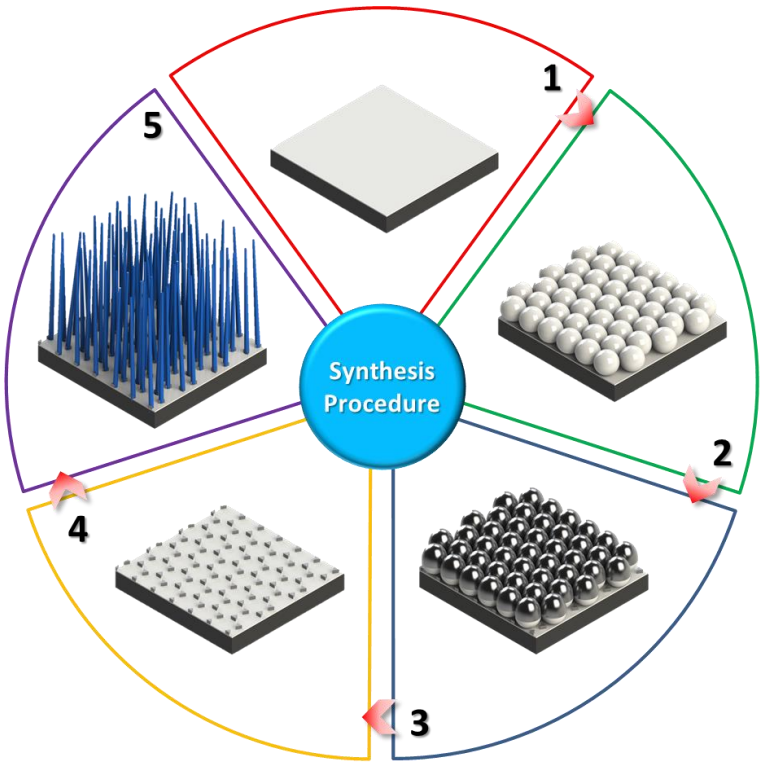

Figure 6.4. Synthesis procedure for controlled ZnO/AgTCNQ nano-arrays:

1) synthesis of ZnO thin film via Sol-gel method;
2) Monolayer of PS nano-arrays on ZnO thin film;
3) E-beam evaporation of silver layer;
4) Lift-off of PS arrays and formation of Ag star-shape patterns on ZnO thin film;
5) CVD growth of AgTCNQ nano-arrays and formation of ZnO/AgTCNQ heterojunction.

6.4. Formation of PS monolayers and ZnO/Ag nano-star patterns

The SEM images of the synthesized PS beads are shown in **Figure 6.5**. As could be seen from this figure, the synthesized polystyrene beads are uniform with average sizes of 500 and 1500 nm. These beads were used for fabricating a mask on ZnO thin films.

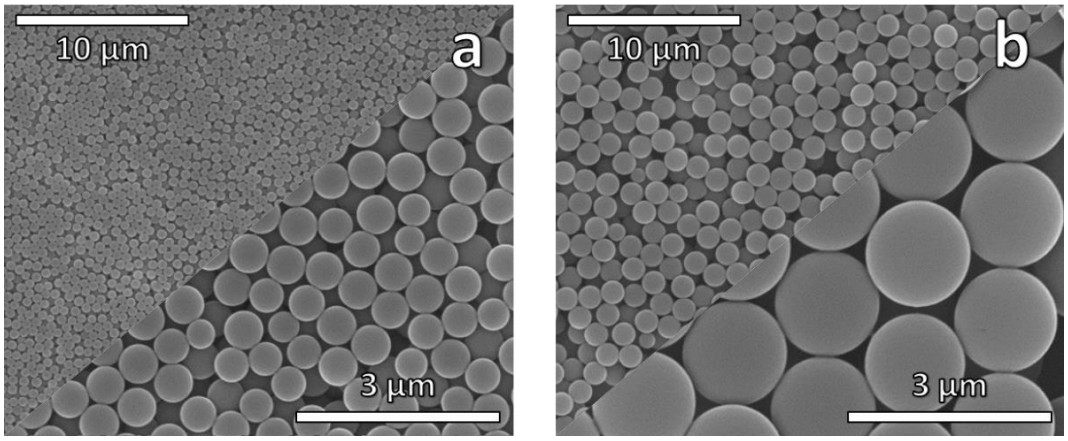

Figure 6.5. SEM images of the synthesized **a)** 500 nm and **b)** 1500 nm polystyrene monodispersed spheres.

Figure 6.6 shows the SEM image of the packed monolayer of polystyrene particles and these particles were packed hexagonally. The few pin holes formed in the monolayer were due to inhomogeneous packing. Very few sections have second layer, which was mainly due to the diffusion of few PS particles inside the solution during their injection into the water/air interface.

During the EB mediated silver deposition onto the substrates, the close-packed PS monolayer acts as a nano-sized mask. This phenomenon results into deposition of silver on PS and also on the ZnO thin film through the orifices created between hexagonal packed PS spheres as shown in **Figure 6.7** schematically.

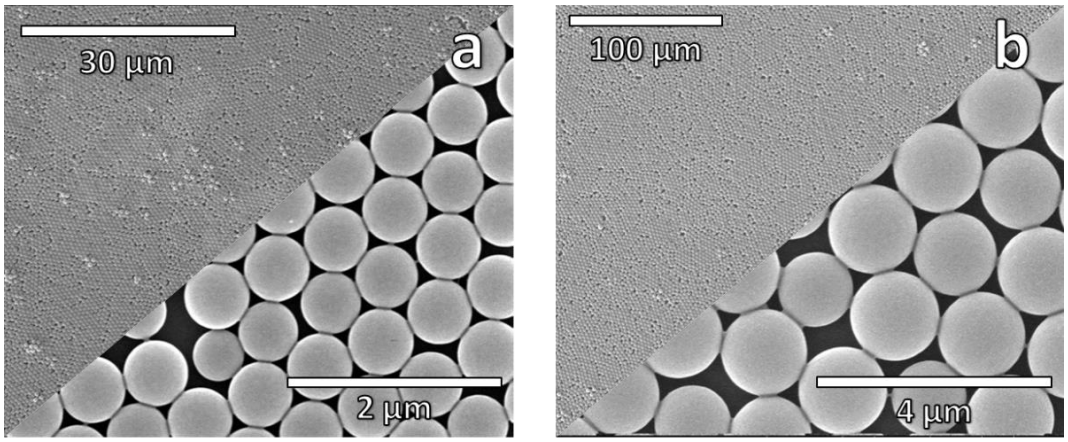

Figure 6.6. SEM images of the monolayer formed by **a)** 500 nm and **b)** 1500 nm PS beads.

During THF etching, THF diffuses inside of the structure and dissolves the PS beads. As the evaporation thickness is less than the diameter of the PS beads, the formed layer of the

silver on the PS detached from the structure during lift-off process and only locations which silver is attached to the surface of the zinc oxide thin film remain of the substrate.

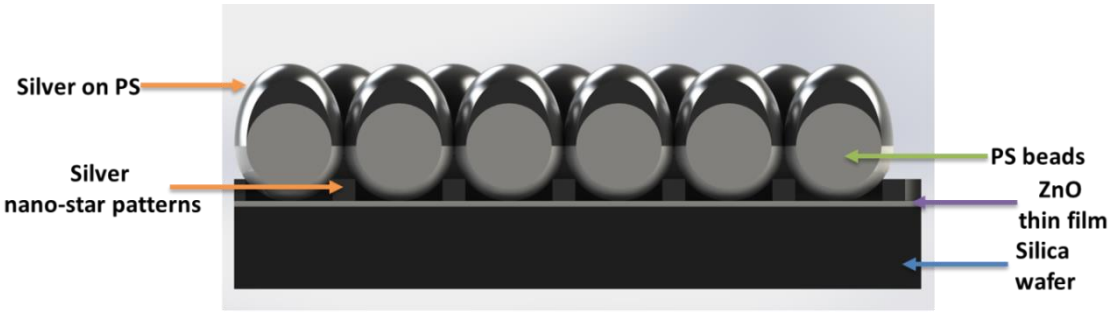

Figure 6.7. Schematic shows the cross section for formation of star shaped islands.

Figure 6.8 shows the formation of the ZnO/Ag nano-star patterns. The individual silver sites on the surface usually show a quasi-triangular shape and are arranged in a space group P6mm array due to the hexagonal packing of the colloidal crystal mask. This forms nano-star patterns of silver on ZnO thin film. Due to the packing fault in the monolayer formation, there are some random shapes on the structure as well. However, the majority of the structure is patterned with nano-star features.

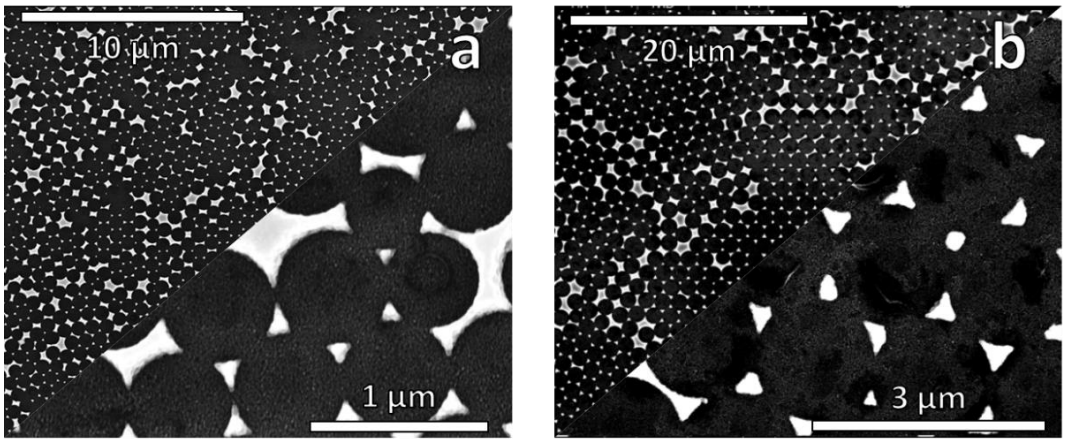

Figure 6.8. SEM images of the produced ZnO/Ag nano-star patterns using **a)** 500 nm and **b)** 1500 nm packed PS masks.

For confirming the repeatability and height of the produced nano-star patterns after lift-off process, AFM imaging was carried out as shown in **Figure 6.9**. AFM results clearly showed the formation of the star morphologies on ZnO thin films with consistent dimensions, distance and height. For sample prepared using 1500 nm PS beads, the distances are much more uniform and the height of the silver features is almost 300 nm. The samples produced

with smaller PS masks have star features but the height and dimensions are not as uniform as the bigger PS masks. This is mainly due to the packing faults in the smaller particles. As could be seen from **Figure 6.8** and **6.9**, the triangular features in small particles are smaller than the big spheres due to smaller orifices in the packed monolayer of PS spheres. The smaller the orifice, the more sensitive it is to the size of the adjacent spheres in the evaporation system, and thus it cannot form features of exactly the same height with sharp edges. Small distortions in smaller particles packing can result into large packing fault which makes the distances and orientation of the evaporated features more sensitive to the alignment of spheres in the masks produced from smaller spheres. **Figure 6.10** shows phase image of the ZnO/Ag star patterns using smaller spherical particles. Area surrounded with the star features have cellular structure which is related to the formed zinc oxide thin films in these areas.

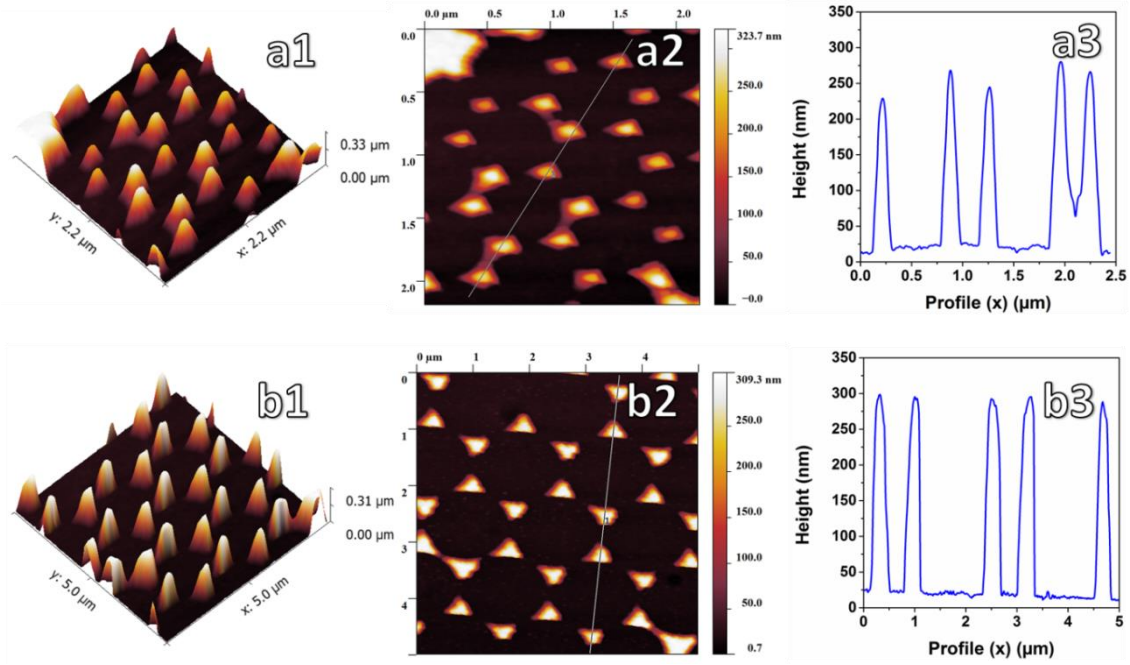

Figure 6.9. AFM images and height profiles of ZnO/Ag nano-star patterns using **a)** 500 nm and **b)** 1500 nm packed PS masks.

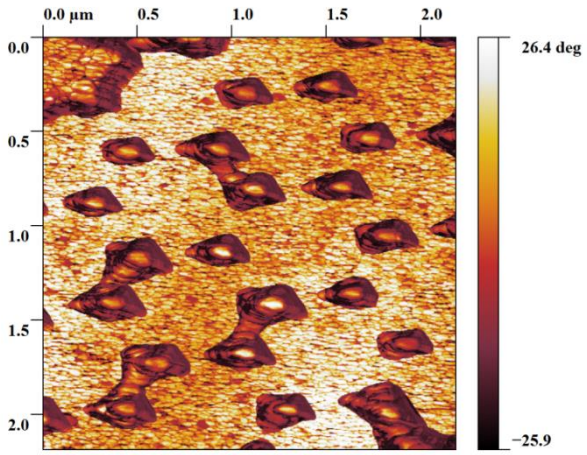

Figure 6.10. AFM phase image of ZnO/Ag nano-star patterns using 500 nm.

Figure 6.11 shows the EDX profile of the ZnO/Ag nano-star patterns. As could be seen from this image the evaporated silver is present in the defined places, and it did not result in random distribution during THF etching. The place and intensities in the larger PS masks are more accurate and sharper due to the fact that the formed features are bigger and distances between the features are micron size that resulted in forming sharper and more distinct peaks in these areas. **Figure 6.11a2** and **b2** show the position of Ag nano-star patterns on the ZnO thin film. The optimum points of the peaks are in the central points of the triangles where the height of the silver would be maximal. In these points Si-Kα spectra show a minimal intensity peak point while Ag-Lα reaches to its maximum amount. As Zn and O is just for ZnO layers which are in the form of thin film it cannot be detected properly by line scanning. To address the ZnO issue and confirm its existence on the surface, EDX spectrum from the overall surface of the sample was collected where it clearly shows the existence of Zn, O, Si and Ag in the system. It should be noted that due to the smaller sizes of the nano-star patterns in the 500 nm PS mask, the amount of the material is much less than the structures made by 1500 nm PS mask, which results in more noisy signal in line mapping of the smaller nano-star patterns.

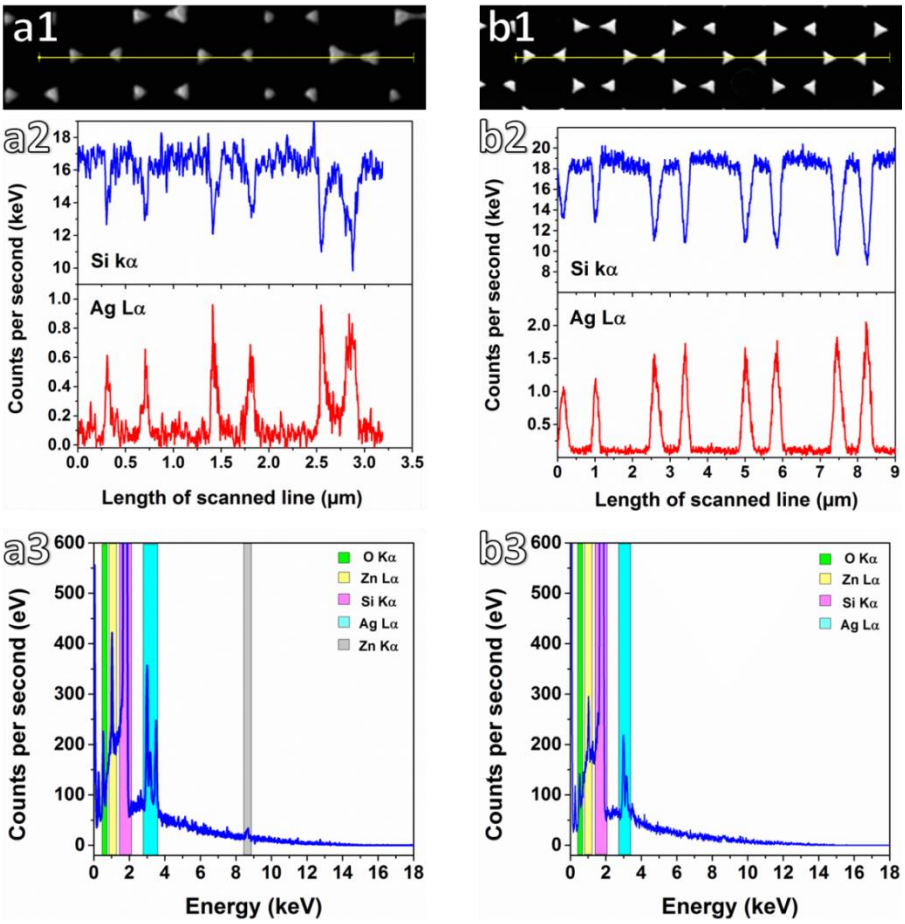

Figure 6.11. EDX linear profile and spectrum of ZnO/Ag nano-star patterns using **a)** 500 nm and **b)** 1500 nm packed PS masks.

6.5. ZnO/AgTCNQ arrays

Figure 6.12 shows the SEM images of the AgTCNQ arrays produced by chemical vapour deposition (CVD). TCNQ vapour was allowed to interact with Ag substrate for the adsorption of TCNQ onto the surface of the Ag structures. If the temperature is sufficient enough, TCNQ can be reduced into $TCNQ^{\bullet -}$ and react with Ag to form AgTCNQ. It is clear that by increasing the temperature, the aspect ratio of the AgTCNQ is increased, which results in the higher surface area[50] ideal for making heterojunctions with high interfacial area. Although the average length of the wires are 17, 26 and 36 μm for synthesis temperature of 160, 180 and 200 °C, the wires still have similar thicknesses of 150 to 300 nm.

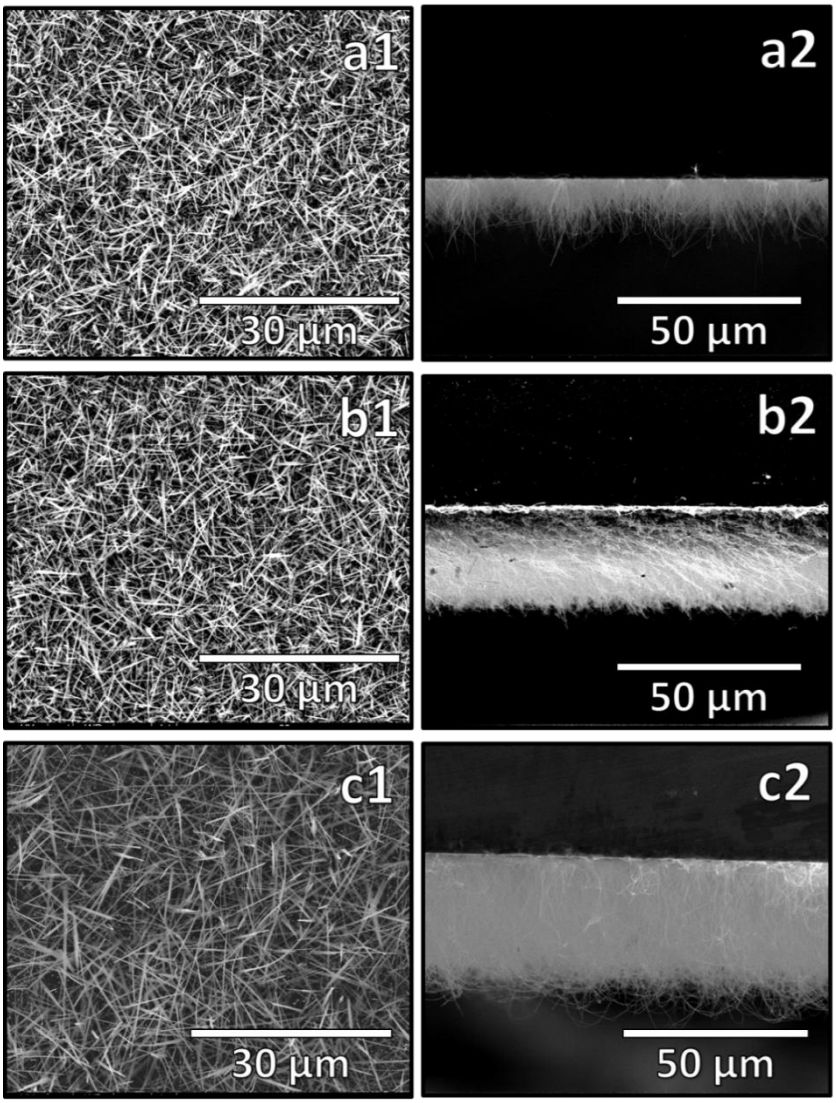

Figure 6.12. Effect of CVD temperature on the formation of AgTCNQ from nano-star patterns (500 nm PS mask): **a)** 160, **b)** 180 and **c)** 200 °C for 1 h.

Figure 6.13 shows the formation of AgTCNQ from Ag nano-star patterns on the ZnO thin film. Due to the formation of large silver triangles in larger PS mask features, much longer wires of AgTCNQ were produced. Thus, the patterning shows the ability in the control of the coverage and also aspect ratio of AgTCNQ (**Figure 6.13-a1** and **b1**). Also, SEM images from the surface of the samples show the starting growth points of the AgTCNQ in these structures. As shown in this image, the AgTCNQ wires are initiated from the star patterns and from each pattern one or multiple AgTCNQ wires can grow (**Figure 6.13-a2** and **b2**). Slightly thicker wires are grown in the smaller pattern (**Figure 6.13-a3** and **b3**) but main difference is in the length of the wires. From **Figure 6.13-a2** and **b2** the structural control which could be gain via colloidal lithography can be recognised. The distance of the junction

as well as the population of the junction can be controlled via using this technique, which could help the design of engineered heterojunction devices.

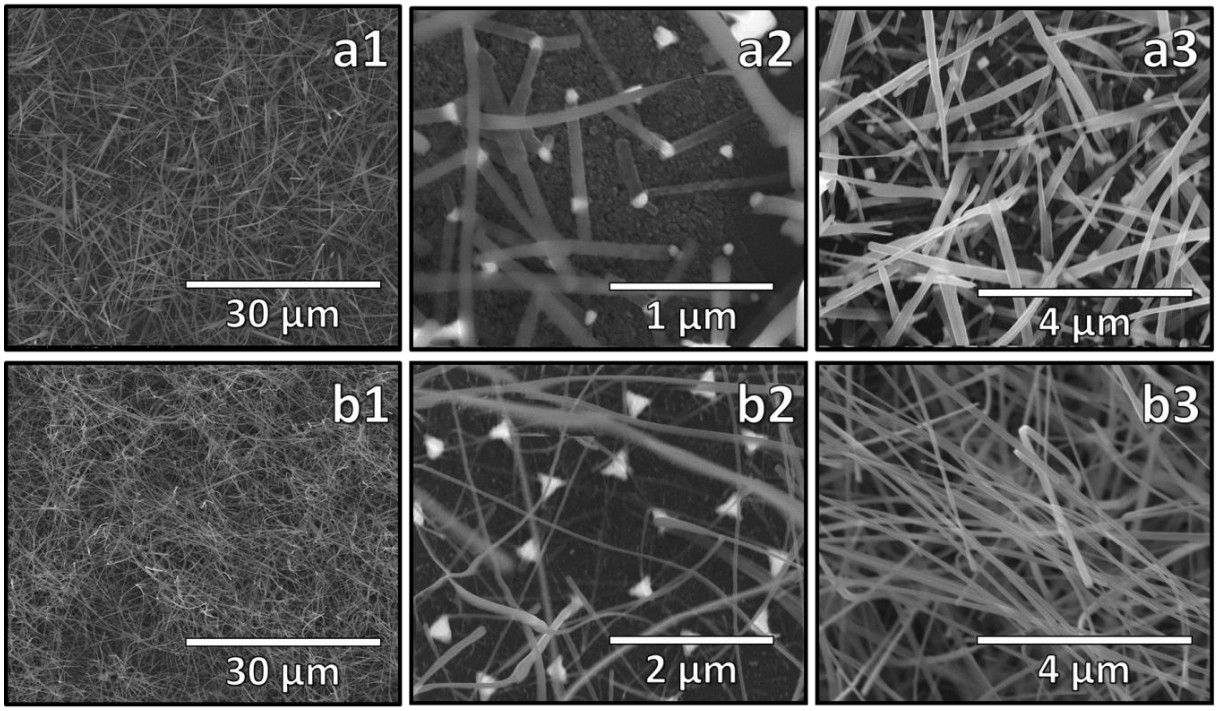

Figure 6.13. Growth of AgTCNQ at 200 °C for 1h from nano-star patterns **a)** 500 nm and **b)** 1500 nm PS masks: 1) low magnification, 2) origin of the nanowires and 3) AgTCNQ wires.

To get further insight to AgTCNQ formation, EDX mapping was carried out on samples fabricated using 1500 nm PS masks. As shown in **Figure 6.14-b1**, for the ZnO-Ag nano-star patterns the map confirms the location of the silver stars on the surface based on Ag Lα. In addition, the places where Ag patterns are located the color concentration for Si Kα reduces drastically (**Figure 6.14-c1**). In the case of the EDX spectrum the existence of Ag, Si, Zn, O and adventitious N and carbon is evident as shown in **Figure 6.14-d1**. As AgTCNQ nanowires are long with smaller diameters, during SEM most of them tend to move around in contact with the electron beam for long time. As mapping is a long process, in the AgTCNQ samples, the uniform distribution of the Ag and N on the surface confirms the formation of AgTCNQ (**Figure 6.14-b2** and **c2**). Moreover, EDX spectrum of the sample shows a huge increase in the intensity of the nitrogen peak which is related to the nitrogen of AgTCNQ molecule in the synthesized material (**Figure 6.14-d2**).

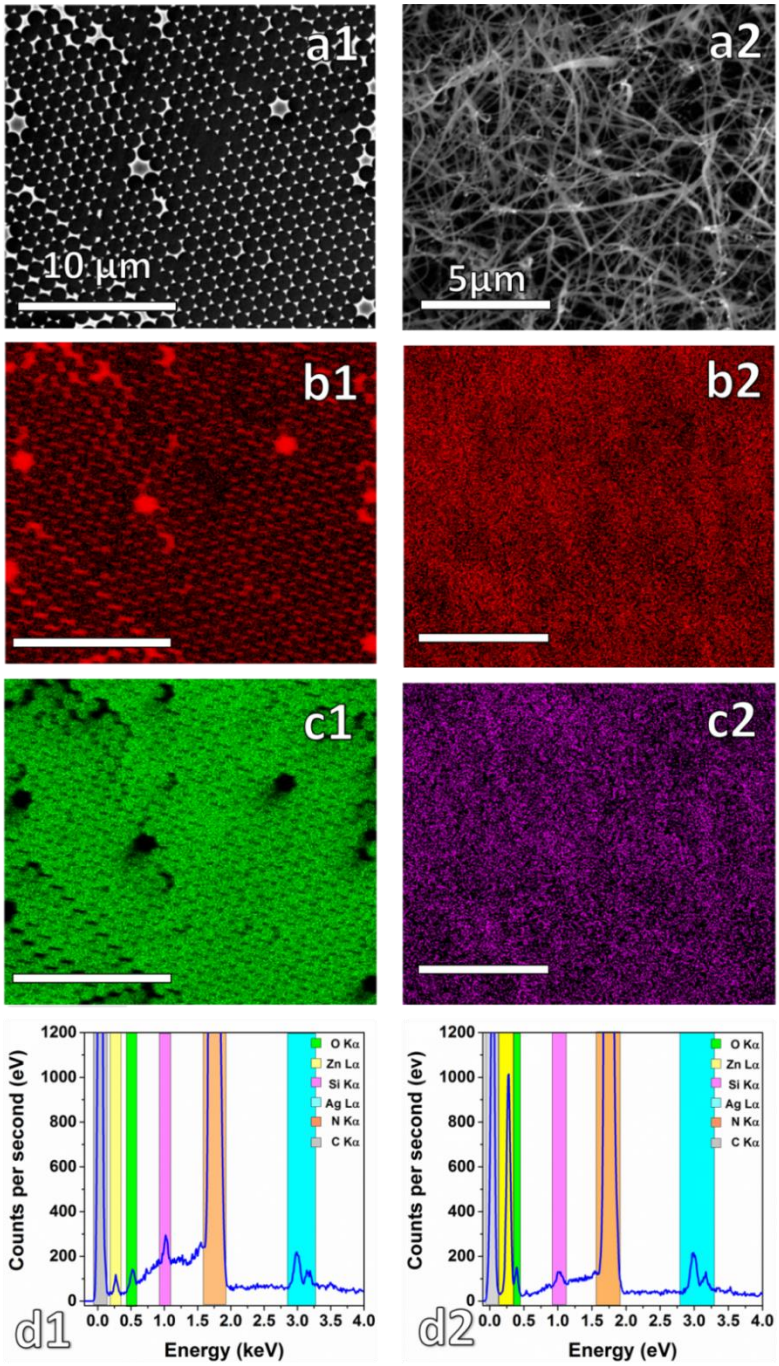

Figure 6.15.

a1) SEM image of ZnO-Ag nanostar pattern fabricated from 500nm PS mask;

b1) EDX mapping of the **a1** surface for Ag Lα ;

c1) EDX mapping of the **a1** surface for Si kα;

d1) EDX spectrum from surface of **a1**;

a2) SEM image of ZnO-AgTCNQ of same surface at 200°C for 1h;

b2) EDX mapping of the **a2** surface for Ag Lα ;

c2) EDX mapping of the **a2** surface for N kα;

d2) EDX spectrum from surface of **a2**.

Raman spectra of samples are shown in **Figure 6.15**. For $TCNQ^0$, three characteristic vibration modes at ca. 1200 cm^{-1} (C═CH bending), 1450 cm^{-1} (C−CN wing stretching) and 1600 cm^{-1} (C═C ring stretching) were detected by Raman spectroscopy[50]. It has been shown that when TCNQ becomes $TCNQ^{\bullet-}$, due to the charge transfer between metallic structures and TCNQ molecule, vibration mode located at 1450 cm^{-1} is red shifted 70 cm^{-1}, which is the main characteristic for confirming the formation of AgTCNQ in all structures.

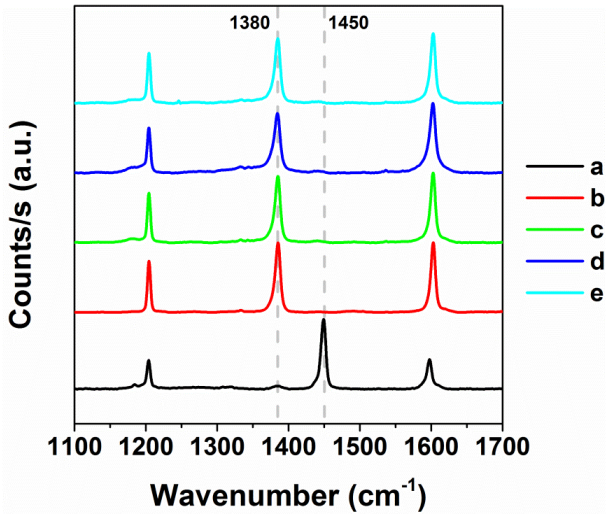

Figure 6.15. Raman spectra of **a)** TCNQ powder, **b)** Zno-AgTCNQ 160 °C, **c)** Zno-AgTCNQ 180 °C and **c)** ZnO-AgTCNQ 200 °C fabricated from 500 nm Ag nano-stars and **d)** ZnO-AgTCNQ 200 °C fabricated from 1500 nm Ag nano-stars.

XPS studies were carried out to show the formation of ZnO in the thin film and also charge transfer between TCNQ and Ag stars. For XPS study the background of the XPS spectra were corrected using Shirley algorithm. The chemical shifts were carried out by aligning core level binding energies (BEs) with adventitious C 1s BE of 285 eV. The peaks were deconvoluted using a Gaussian–Lorentzian function. As shown in **Figure 6.16**, the binding energy for Zn $2p_{3/2}$ is located at 1022.8 eV which is related to the Zn^{2+} in the ZnO structure. As could be seen from this figure, the ZnO spectrum in the ZnO-AgTCNQ is noisier and has lower intensity than ZnO thin film which is mainly due to the dense AgTCNQ nanowire frames formation on top of ZnO thin film. It has been reported that when TCNQ reacts with the structure of a transition metal, due to the charge transfer between TCNQ and the metallic structure and binding between N and metallic atom to form metal-TCNQ structure, the N1s core level binding energy would change with respect to pure $TCNQ^0$. $TCNQ^0$ molecules have characteristic N 1s core level BE at 399.1 eV along with a shake-up feature at 2.4 eV higher BE[51]. Conversely, in AgTCNQ a significant shift in N 1s core level is expected to occur. The BE from 399.1 eV in $TCNQ^0$ shifts to 398.4 eV. The energy difference between shake-up and the main peak also shows a decrease. This phenomenon confirms the formation of AgTCNQ in the structure[41, 51].

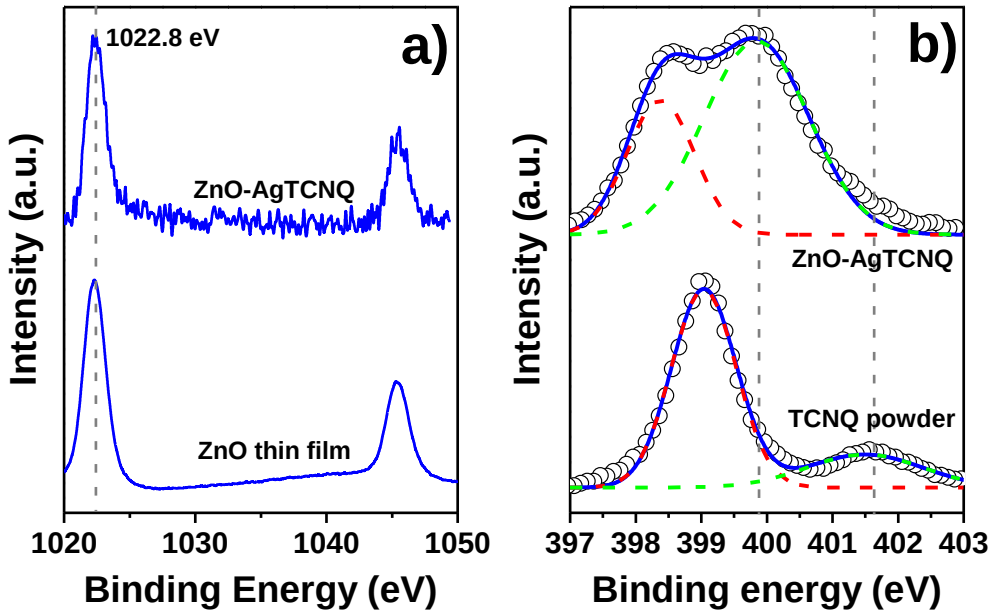

Figure 6.16. XPS spectra of different materials showing **a)** Zn 2p and **b)** N 1s core levels.

The prepared samples, fabricated using smaller PS mask, were further tested for their photocatalytic degradation ability towards rhodamine B (RB) dye. As shown in **Figure 6.17a** and **g**, the degradation rate of RB is not high as RB was degraded only partially (<15%) without the catalytic surfaces. With ZnO nano-thin film catalysts, free radicals can be generated on UV-excitation that can attack the molecules of the RB close to the surface of the catalyst (**Figure 6.17b** and **g**). When silver nano-star patterns are formed on the surface of zinc oxide thin film, as discussed in *Chapter IV, Section 4.4.3*, due to the thickness of the silver stars (300 nm) these patterned sites act like recombination sites consuming the photo-excited charges, thereby, reducing the photo-activities. During TCNQ CVD process, AgTCNQ arrays grow form Ag nano-stars and subsequently forms a p-n heterojunction with ZnO thin film. AgTCNQ has a narrow band-gap of 0.3 eV with work function of 1.7 eV[52] while ZnO is an n-type semiconductor with band-gap of 3.37 eV and work function of 5.3 eV[53]. When AgTCNQ and ZnO attach to each other as explained in *Chapter 1, Section 1.2.2.2*, a depletion layer can be produced at the interface which helps in separating the electron and hole and thus increasing the life time of electron-hole pair. This results into high activity of the samples in ZnO/AgTCNQ samples as shown in **Figure 6.17 d-f** and **g**. The photoactivity of the samples is increased slightly with increase in the synthesis temperature which relates to the increase in the size of the AgTCNQ nano-arrays. These results clearly show the photocatalytic application of the AgTCNQ and ZnO p-n heterojunctions.

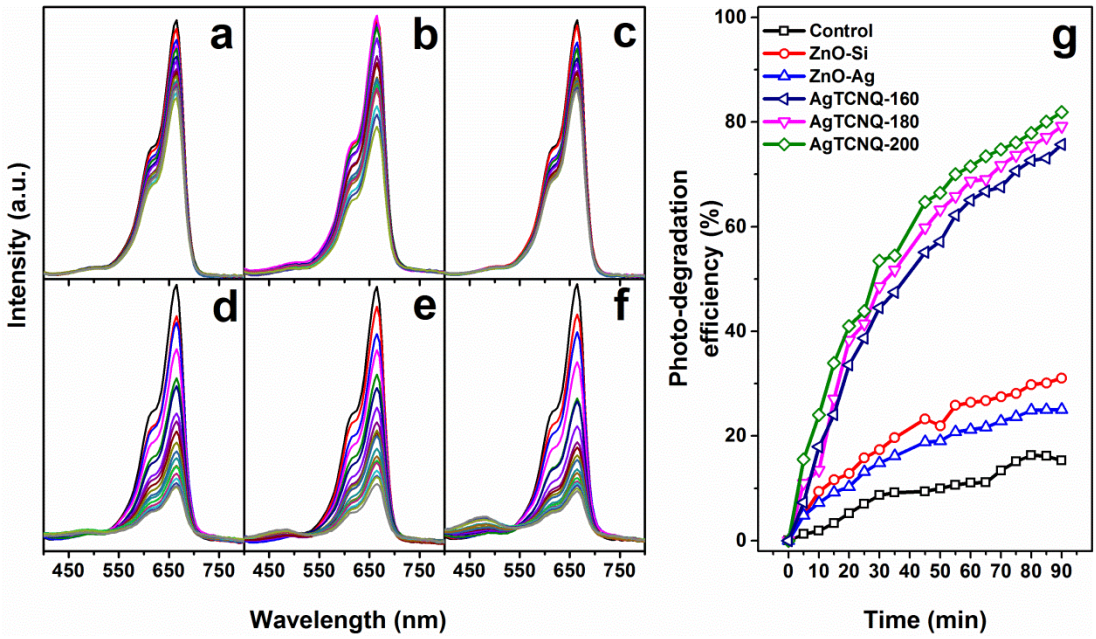

Figure 6.17. UV-visible absorbance spectra of RB with increasing illumination time in the **a)** absence of any photocatalytic surfaces, **b)** ZnO thin film, **c)** ZnO-Ag nano-star pattern, **d)** ZnO-AgTCNQ [160 °C, 2h] , **e)** ZnO-AgTCNQ [180 °C, 2h] , **f)** ZnO-AgTCNQ [200 °C, 2h] and **g)** corresponding photodegradation efficiency of the samples.

6.6. Conclusion

In this chapter, a novel approach was developed to fabricate ZnO/AgTCNQ heterojunction materials with control in junction position and also the growth of the materials. The results show that the colloidal lithography can be used to control the fabrication process of well-defined p-n junction devices. With this method thin film zinc oxide was decorated with silver nano-star patterns with thickness of 300 nm that changed into AgTCNQ nanowire arrays by reacting TCNQ vapour with silver patterns. AgTCNQ was formed to have aspect ratios of more than 100. SEM images illustrated the nucleation of the AgTCNQ wires from the patterns. The produced AgTCNQ nano-arrays make heterojunction with ZnO thin film, which increases the photocatalytic activities of the synthesized materials.

References

1. Abu Hatab, N. A.; Oran, J. M.; Sepaniak, M. J., *ACS Nano* **2008,** *2* (2), 377-385.
2. Weisheng, Y.; Zhihong, W.; Yang, Y.; Longqing, C.; Ahad, S.; Kimchong, W.; Xianbin, W., *Journal of Micromechanics and Microengineering* **2012,** *22* (12), 125007.

3. Quist, A.; Pavlovic, E.; Oscarsson, S., *Analytical and Bioanalytical Chemistry* **2005,** *381* (3), 591-600.
4. Mrksich, M.; Whitesides, G. M., *Trends Biotechnol.* **1995,** *13* (6), 228-235.
5. Dias, A.; Kingsley, D.; Corr, D., *Biosensors* **2014,** *4* (2), 111-136.
6. Kaufmann, T.; Ravoo, B. J., *Polymer Chemistry* **2010,** *1* (4), 371-387.
7. Tian, D.; Song, Y.; Jiang, L., *Chem. Soc. Rev.* **2013,** *42* (12), 5184-5209.
8. Tao, A. R.; Huang, J.; Yang, P., *Acc. Chem. Res.* **2008,** *41* (12), 1662-1673.
9. Kim, S.-H.; Lee, S. Y.; Yang, S.-M.; Yi, G.-R., *NPG Asia Mater* **2011,** *3*, 25-33.
10. Li, F.; Josephson, D. P.; Stein, A., *Angew. Chem. Int. Ed.* **2011,** *50* (2), 360-388.
11. Acharya, S.; Hill, J. P.; Ariga, K., *Adv. Mater.* **2009,** *21* (29), 2959-2981.
12. Harkins, W. D., *JACS* **1947,** *69* (6), 1428-1444.
13. Unciti-Broceta, A.; Johansson, E. M. V.; Yusop, R. M.; Sanchez-Martin, R. M.; Bradley, M., *Nat. Protocols* **2012,** *7* (6), 1207-1218.
14. Zhang, H.; Liu, D.; Shahbazi, M.-A.; Mäkilä, E.; Herranz-Blanco, B.; Salonen, J.; Hirvonen, J.; Santos, H. A., *Adv. Mater.* **2014**, n/a-n/a.
15. Goethals, E. C.; Elbaz, A.; Lopata, A. L.; Bhargava, S. K.; Bansal, V., *Langmuir* **2012,** *29* (2), 658-666.
16. Yu, Y.; Zhang, G., *Colloidal Lithography*. **2013**;
17. Tang, Z.; Wei, A., *ACS Nano* **2012,** *6* (2), 998-1003.
18. Gan, L. M.; Chew, C. H.; Lye, I.; Imae, T., *Polym. Bull.* **1991,** *25* (2), 193-198.
19. Sharifi-Sanjani, N.; Soltan-Dehghan, M.; Naderi, N.; Ranji, A., *J. Appl. Polym. Sci.* **2004,** *94* (5), 1898-1904.
20. Shim, S.-E.; Cha, Y.-J.; Byun, J.-M.; Choe, S., *J. Appl. Polym. Sci.* **1999,** *71* (13), 2259-2269.
21. Bamnolker, H.; Margel, S., *J. Polym. Sci., Part A: Polym. Chem.* **1996,** *34* (10), 1857-1871.
22. Tseng, C. M.; Lu, Y. Y.; El-Aasser, M. S.; Vanderhoff, J. W., *J. Polym. Sci., Part A: Polym. Chem.* **1986,** *24* (11), 2995-3007.
23. Kawaguchi, S.; Ito, K., *Dispersion Polymerization*. Springer Berlin Heidelberg: **2005**; Vol. 175.
24. Chan, D. Y. C.; Henry jr, J. D.; White, L. R., *J. Colloid Interface Sci.* **1981,** *79* (2), 410-418.

25. Li, Q.; Jonas, U.; Zhao, X. S.; Kappl, M., *Asia-Pacific Journal of Chemical Engineering* **2008,** *3* (3), 255-268.
26. Sheppard, E.; Tcheurekdjian, N., *J. Colloid Interface Sci.* **1968,** *28* (3–4), 481-486.
27. Pieranski, P., *Phys. Rev. Lett.* **1980,** *45* (7), 569-572.
28. Kralchevsky, P. A.; Nagayama, K., *Langmuir* **1994,** *10* (1), 23-36.
29. Kralchevsky, P. A.; Nagayama, K., *Adv. Colloid Interface Sci.* **2000,** *85* (2–3), 145-192.
30. Vogel, N.; Weiss, C. K.; Landfester, K., *Soft Matter* **2012,** *8* (15), 4044-4061.
31. Vogel, N.; de Viguerie, L.; Jonas, U.; Weiss, C. K.; Landfester, K., *Adv. Funct. Mater.* **2011,** *21* (16), 3064-3073.
32. Tao, A.; Kim, F.; Hess, C.; Goldberger, J.; He, R.; Sun, Y.; Xia, Y.; Yang, P., *Nano Lett.* **2003,** *3* (9), 1229-1233.
33. Oh, J. R.; Moon, J. H.; Yoon, S.; Park, C. R.; Do, Y. R., *J. Mater. Chem.* **2011,** *21* (37), 14167-14172.
34. Coropceanu, V.; Cornil, J.; da Silva Filho, D. A.; Olivier, Y.; Silbey, R.; Brédas, J.-L., *Chem. Rev.* **2007,** *107* (4), 926-952.
35. Giergiel, J.; Wells, S.; Land, T. A.; Hemminger, J. C., *Surf. Sci.* **1991,** *255* (1–2), 31-40.
36. Ji, H.-X.; Hu, J.-S.; Guo, Y.-G.; Song, W.-G.; Wan, L.-J., *Adv. Mater.* **2008,** *20* (24), 4879-4882.
37. Liu, H.; Liu, Z.; Qian, X.; Guo, Y.; Cui, S.; Sun, L.; Song, Y.; Li, Y.; Zhu, D., *Crystal Growth & Design* **2009,** *10* (1), 237-243.
38. Heintz, R. A.; Zhao, H.; Ouyang, X.; Grandinetti, G.; Cowen, J.; Dunbar, K. R., *Inorg. Chem.* **1998,** *38* (1), 144-156.
39. Liu, Y.; Ji, Z.; Tang, Q.; Jiang, L.; Li, H.; He, M.; Hu, W.; Zhang, D.; Jiang, L.; Wang, X.; Wang, C.; Liu, Y.; Zhu, D., *Adv. Mater.* **2005,** *17* (24), 2953-2957.
40. Soumen, M.; Uday Narayan, M.; Shreyasi, P.; Kalyan Kumar, C., *Nanotechnology* **2013,** *24* (46), 465601.
41. Davoudi, Z. M.; Kandjani, A. E.; Bhatt, A. I.; Kyratzis, I. L.; O'Mullane, A. P.; Bansal, V., *Adv. Funct. Mater.* **2014,** *24* (8), 1047-1053.
42. Pearson, A.; O'Mullane, A. P.; Bhargava, S. K.; Bansal, V., *Inorg. Chem.* **2012,** *51* (16), 8791-8801.
43. Pearson, A.; O'Mullane, A. P.; Bansal, V.; Bhargava, S. K., *Inorg. Chem.* **2011,** *50* (5), 1705-1712.

44. Wang, K.; Qian, X.; Zhang, L.; Li, Y.; Liu, H., *ACS Applied Materials & Interfaces* **2013,** *5* (12), 5825-5831.
45. Ren, L.; Xian, X.; Yan, K.; Fu, L.; Liu, Y.; Chen, S.; Liu, Z., *Adv. Funct. Mater.* **2010,** *20* (8), 1209-1223.
46. Nafady, A.; O'Mullane, A. P.; Bond, A. M., *Coord. Chem. Rev.* **2014,** *268*, 101-142.
47. Xiao, K.; Tao, J.; Puretzky, A. A.; Ivanov, I. N.; Retterer, S. T.; Pennycook, S. J.; Geohegan, D. B., *Adv. Funct. Mater.* **2008,** *18* (19), 3043-3048.
48. Liu, H.; Wu, X.; Chi, L.; Zhong, D.; Zhao, Q.; Li, Y.; Yu, D.; Fuchs, H.; Zhu, D., *The Journal of Physical Chemistry C* **2008,** *112* (45), 17625-17630.
49. Kandjani, A. E.; Tabriz, M. F.; Moradi, O. M.; Mehr, H. R. R.; Kandjani, S. A.; Vaezi, M. R., *J. Alloys Compd.* **2011,** *509* (30), 7854-7860.
50. Gucciardi, P. G.; Trusso, S.; Vasi, C.; Patane, S.; Allegrini, M., *Phys. Chem. Chem. Phys.* **2002,** *4* (12), 2747-2753.
51. Tseng, T.-C.; Urban, C.; Wang, Y.; Otero, R.; Tait, S. L.; Alcamí, M.; Écija, D.; Trelka, M.; Gallego, J. M.; Lin, N.; Konuma, M.; Starke, U.; Nefedov, A.; Langner, A.; Wöll, C.; Herranz, M. Á.; Martín, F.; Martín, N.; Kern, K.; Miranda, R., *Nat Chem* **2010,** *2* (5), 374-379.
52. Liu, H.; Zhao, Q.; Li, Y.; Liu, Y.; Lu, F.; Zhuang, J.; Wang, S.; Jiang, L.; Zhu, D.; Yu, D.; Chi, L., *JACS* **2005,** *127* (4), 1120-1121.
53. Zheng, Y.; Zheng, L.; Zhan, Y.; Lin, X.; Zheng, Q.; Wei, K., *Inorg. Chem.* **2007,** *46* (17), 6980-6986.

CHAPTER VII

Conclusion and Future Works

In this chapter, the summary of the work presented in the thesis and potential avenues for future works are provided.

7.1. Summary of work

Development in the semiconductor based technologies is reliant on newly emerging developments in the synthesis approaches and introducing novel functionalities and applications to semiconducting materials. The photocatalytic ecotoxic pollutant removal is one of the interesting application fields of semiconductors. There is a high demand to fabricate semiconductors with more versatile processing technologies to obtain higher photo-activities in waste-water treatment. The vast inorganic and organic groups of semiconductors need a strategic plan to optimise the photocatalytic activities of these semiconductors. Although, there are some rules of thumb in selecting proper semiconducting materials for photocatalytic reactions, such as: band-gap, electron-hole pair lifetime and chemical stabilities, the possibilities are still numerous. In addition, the properties of semiconductors can be easily modified and improved by making different types of composites. Formation of junctions between semiconductor/semiconductor and semiconductor/metal has shown tremendous effect in influencing the photocatalytic activities of the semiconductors. Also, the catalytic activities, especially photocatalytic activities, are highly depended on the structure, morphology and surface area of the catalyst. Therefore, there are a number of unexplored possibilities in fabrication of photocatalytic materials with high activities, which makes this field of the study a hot topic among various research disciplines.

In addition to the photocatalytic activities of semiconductors, metallic nano-materials can add further functionalities to semiconductors. If properly chosen and synthesized, these materials can be used as sensing platforms for SERS and optical sensing. Thus, combining semiconductor with these materials can provide the multifunctionality of sensing and self-cleaning/ pollutant removal properties. As the metallic nanomaterials are extremely versatile in their properties, we are facing with numerous possibilities. The combination of semiconductor/metallic materials can bring novel applications to address sensing and removal of the environmental and biological toxins.

Through this PhD thesis, I have tried to address some of the problems and research questions in regard to the fabrication and application of semiconductor heterojunction materials for sensing, self-cleaning and toxic heavy metal removal from the waste water. Additionally, as the SERS sensing was the main approach for sensing procedure in this thesis,

I have suggested a novel approach to address the background issue while acquiring Raman spectra to be able to obtain more trustworthy data from SERS sensors. The objectives and summary of the finding of the current thesis is summarized in the following section.

7.1.1. Designing novel background correction technique for SERS sensing

In SERS sensing platforms, the sensing approach can be carried out using two different approaches of peak position change and intensity change. In the former case, the chemical reaction between SERS marker and the target material can alter the position and peak arrangement of the marker Raman features, and thus this technique is used for characterisation of different species. In the latter form, the concentration of the target material is sensed via change in the intensities of the acquired Raman spectrum of the target material. In both cases, the existence of the background can inject huge errors in the sensing approaches. In the first case, the background can suppress the featuring peaks of target material while in the second, having different background feature results in inconsistent sensing results. Thus, the need for appropriate algorithm for background correction is one of the main necessities in SERS sensing. As most of the available techniques are utilizing smoothing in their background correction methods and considering the fact that noise removal can introduce more complex errors to the background correction the challenge is to find an algorithm that provides the ability of the background correction without smoothing.

For addressing this issue an algorithm has been provided in this thesis where smoothing free background correction can be carried out for SERS spectra. This algorithm combines the signal removing background correction technique with wavelength transform technique. In this method, the locations of the peaks are detected via finding derivative of wavelet transform of noisy Raman spectrum. After finding the position, start and ending points of peaks in the spectrum, the signal removing background correction method is used to find the background of the spectrum and extract background corrected spectrum from it. This algorithm showed good capabilities in the background correction of the experimental Raman spectra without denoising them. The statistical studies confirmed the *RMSE* of the proposed approach less than 0.2 over 900 samples which makes this method as one of the best reported techniques known the background correction of Raman spectra. This software can provide a proper base for background correction of SERS spectra for sensing approaches.

7.1.2. Fabrication of ZnO/Ag nano-arrays for SERS based sensors

As the SERS sensors require highly controlled and extremely expensive production processes to be able to make reliable, reproducible sensing platforms, it is a highly expensive spectroscopy technique. As SERS is mainly used for sensing organic molecules and compounds, the removal of the organic molecules from the SERS active surface can regenerate the surface and sensing ability of the structures. The regeneration process can be done through combining photocatalytic activities of semiconductors with SERS sensors. In this way the regeneration of the surface of the SERS sensor can be carried out via photocatalytic degradation of organic traces. This can change the cost of the fabrication and testing in the sensing technologies. Although this technique can be used for regenerating the SERS surfaces, there still remains a big challenge for fabricating the SERS sensors as they should have highly controlled surface and topologies. The general approaches for fabricating these surfaces include expensive methods of lithography. Thus, there is a need for a more general approach with the ability to maintain the reproducibility of the sensing data.

In this thesis, ZnO nano-arrays were chosen for fabricating semiconducting surfaces for recyclable SERS substrate. The main reason for choosing this structure was the formation of high aspect ratio, well aligned ZnO nano-structures where the diameter of the ZnO nano-rods were 150 nm in average and the length 2µm. The effects of the synthesis parameters on the arrays alignment and size were studied completely. In addition to studying the facile synthesis method for ZnO substrates, a chemical method of even decoration of ZnO nano-arrays with silver nanoparticles was introduced in here. To gain an acceptable SERS sensing results, the produced nano-arrays were decorated with silver nanoparticles with control in their size and coverage. This fabrication process resulted into formation of ZnO/Ag nano-arrays with decent SERS response as well as good photocatalysis performance. These sensors were also employed for Hg^{2+} sensing in waste water. As the Hg^{2+} can make amalgam with silver, the SERS properties of the silver nanoparticles are subsequently changed. This fact is used for sensing heavy metal ions in the liquid. The results showed that the provided system can also be used for mercury removal using photocatalytic activities of the zinc oxide nano-arrays. Thus, the produced structures can be used for sensing mercuric ion as well as removal of this toxin from the solution, which has not been reported before.

7.1.3. Controlling the junction place and formation in inorganic/organic p/n hetero junction of ZnO/AgTCNQ

TCNQ is one of the widely investigated organic semiconductors. It can make a metal-organic framework by charge transferring with transition metals and forming metal-TCNQ organic semiconductors. AgTCNQ is one of the widely studied TCNQ derived materials where it has been studied for its switching and field emission properties. But interestingly, there are far fewer reports about the junction formation between this semiconducting organic material and other semiconductors available in the literature. The formation of the junction and also the possibilities that this interesting junction can bring is still a mystery. Due to the gap in this field, proper study of the junction formation and control in the synthesis of the material and final properties requires further research.

In addition, in most of the studies involving in the formation of the TCNQ-based p/n junctions, the position and population of the junctions were randomly attained or designed by lithography techniques. One of the fields of the lithography is colloidal lithography. Although, technique has been successfully used for fabricating optical and SERS based sensors; there are no studies in regard to the control of the junction position and population using colloidal lithography.

In this thesis, I have shown a facile method for fabricating silver patterns on zinc oxide films with nanoscale accuracy via colloidal lithography. Silver/ZnO which is a metal/semiconductor heterojunction could easily be changed into p/n semiconductors heterojunction by converting silver metal to a charge transfer organic semiconductor AgTCNQ. In this case a p/n junction could be formed with controlling the junction positions and also the population. The fabricated p/n junctions were tested for their photocatalytic activities, which showed improved performance over ZnO/Ag junctions.

7.2. Future work

Considering the vast possibilities that the work contained within this thesis could be applied to, a select number of suggested investigations for the future have been briefly discussed for each section explained in *Section 7.1*.

7.2.1. Designing novel background correction technique for SERS sensing

- As the nature of the peaks in most of the spectroscopy techniques are Lorentzian-Gaussian feature, the developed algorithm from the current PhD work can be further modified to fit with other available spectroscopic techniques like XRD, FTIR, etc.
- The algorithm can be easily incorporated into software where the convoluted peaks can be deconvoluted using wavelet transform after background correction. This technique can make a huge step forward in making an automatic program for different spectroscopic techniques like photoluminescence, XPS, etc. This can be resulted from the ability of the wavelet transformation to be carried out in continuous dilation and thus from second order, this dilation can extract the exact location of the peaks in the overlapped peaks.
- In addition to the deconvolution abilities, it has been shown that wavelet transform can act as a signal-processing filter due to transforming the signal in different frequencies. Thus, wavelet transform technique can be used for denoising the spectra. This can make another enhancement to the background corrected signals.

7.2.2. Fabrication of ZnO/Ag nano-arrays for SERS based sensors

- Zinc oxide is a highly active photocatalyst, but it is unstable and could be dissolved in acidic or high basic solutions. Thus, coating the zinc oxide with alternative photocatalyst (e.g. TiO_2) with higher photo-activities can make the nano-array of zinc oxide applicable for different media.
- Forming junction between zinc oxide and other p-type semiconductors such as CuI and Cu_2O can increase the lifetime of electron and hole and increase the photocatalytic activity of the fabricated structures.
- Silver is a good SERS active metal. However, it is susceptible to oxidation in the air, which changes the response of the sensor after a while. This can limit the regeneration cycles of the sensor. Thus, modifying silver with other materials using techniques such as galvanic replacement, core/shell structure and alloying with more noble metals like gold can address this problem. Also, the material selection and

composition can be chosen in a way that it enhances the SERS activities of the structures.

- Silver as the selective metal towares mercury ion detection studies, was employed only for three cycles. However, in order to confirm the developed sensor's full regeneration capability and long term stability, it is necessary to undergo further studies involving more regeneration cycles (>10 cycles) and long term testing (> 6 months) to truly confirm its useability for industrial applications. That is, it is well known that thermal removal of Hg in order to regenerate the system can oxidize the Ag surface thus reducing its Raman activity. In this thesis, to avoid this oxidation high vacuum heating chamber was used. But changing the Ag to more noble metallic structure can overcome the need for high vacuum thermal treatment using the mentioned methods in the previous section. In this case, long term life cycle can be achieved for these sensors.

7.2.3. Controlling the junction place and formation in inorganic/organic p/n hetero junction of ZnO/AgTCNQ

- The formation of AgTCNQ on ZnO thin film was studied in this thesis. This is only a starting point for the formation and control of these junctions. The TCNQ can be altered to other types of charge transfer materials like tetrafluoro tetracyanoquinodimethane ($TCNQF_4$) and tetracyanoanthraquinodimethane (TCNAQ). These materials have different charge transfer behaviour compared to pure TCNQ. Also they can make metal-organic molecule exactly the same way as AgTCNQ. Thus they could result into better junctions with increased electron-hole life time of zinc oxide structures.
- As AgTCNQ is a low band-gap semiconductor and ZnO is a wide band-gap semiconductor, the AgTCNQ and ZnO heterojunction with some modifications can be used in solar-cells.

Appendices

- **Supporting information for chapter III: Background correction algorithm and *SNR* estimation for other types of backgrounds**
- **Curriculum vitae**

Appendix A: Supporting information for chapter III

Detailed background correction algorithm

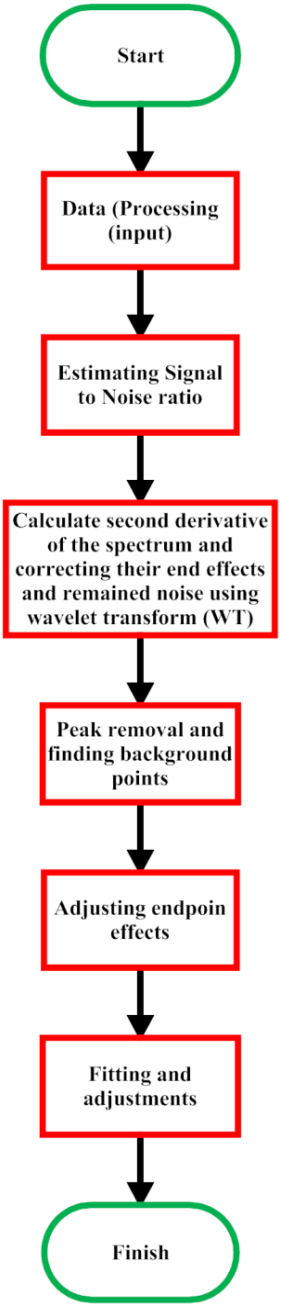

Figure S1 General Algorithm of background correction.

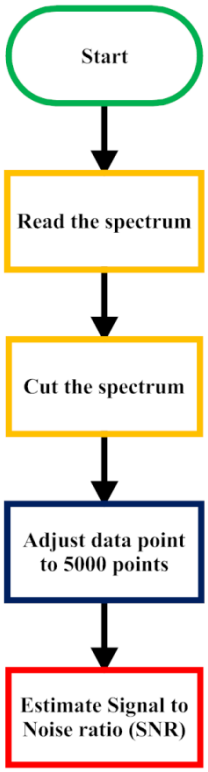

Figure S2 Detailed flow chart for Data processing (input).

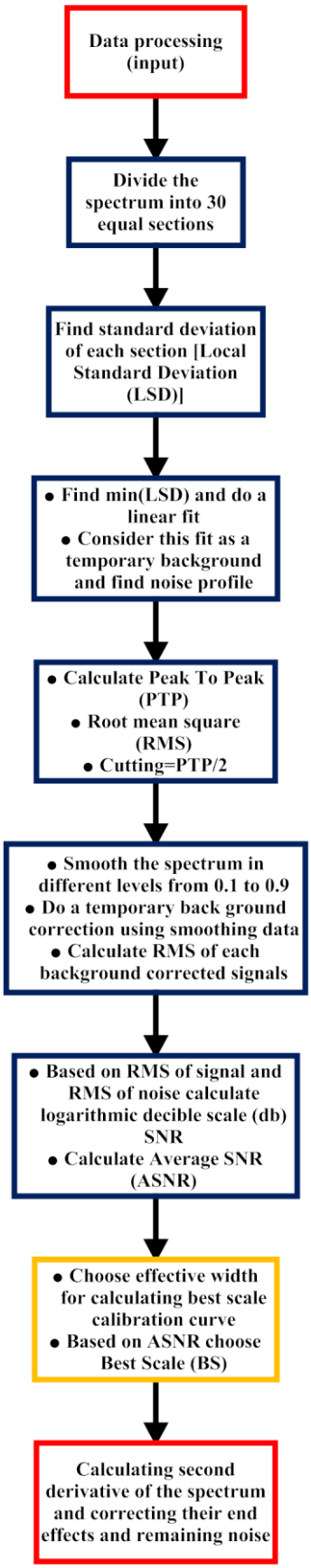

Figure S3 Detailed flow chart for *Estimating Signal to Noise Ratio (SNR).*

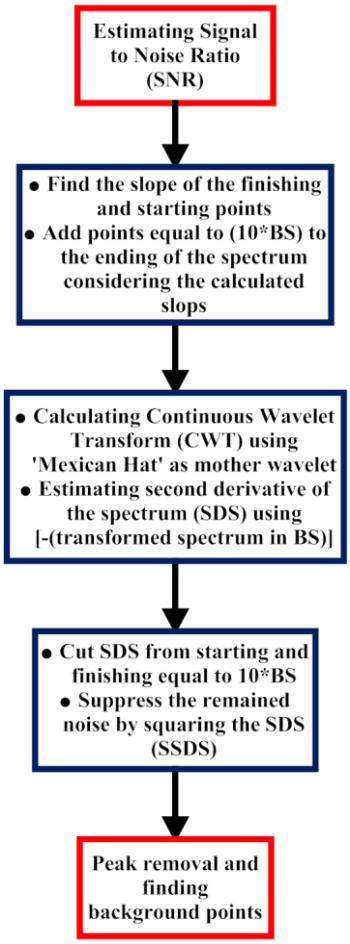

Figure S4 Detailed flow chart for *Calculating 2nd derivative of the spectrum and correcting their end effects and remained noise*.

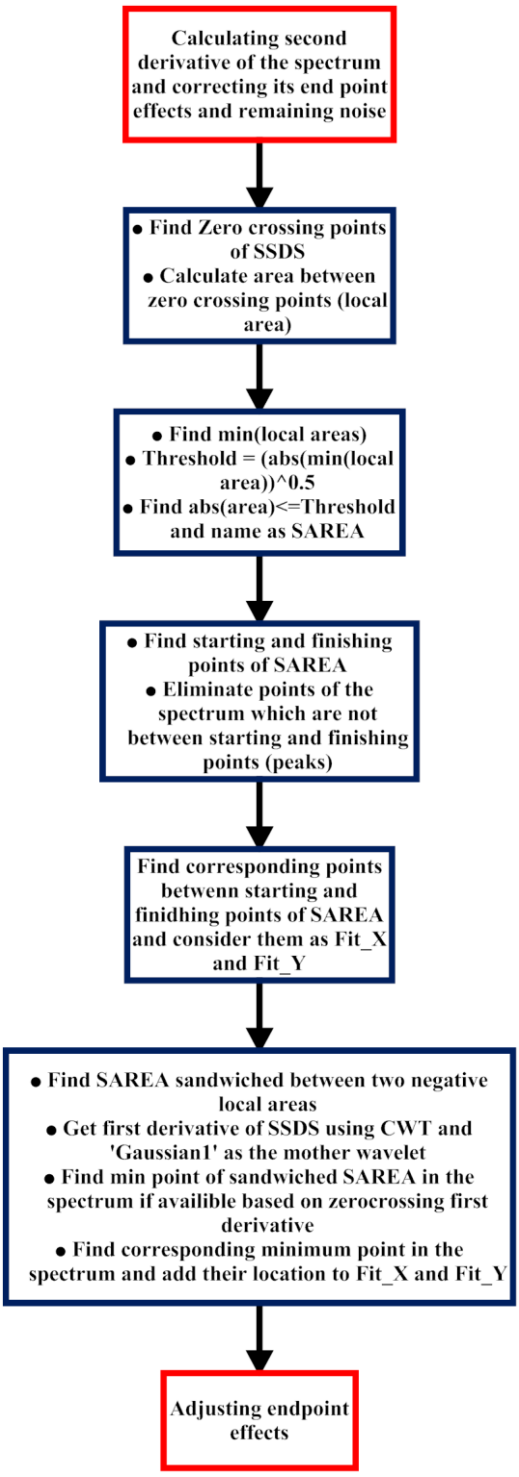

Figure S5 Detailed flow chart for *Peak removal and finding background points.*

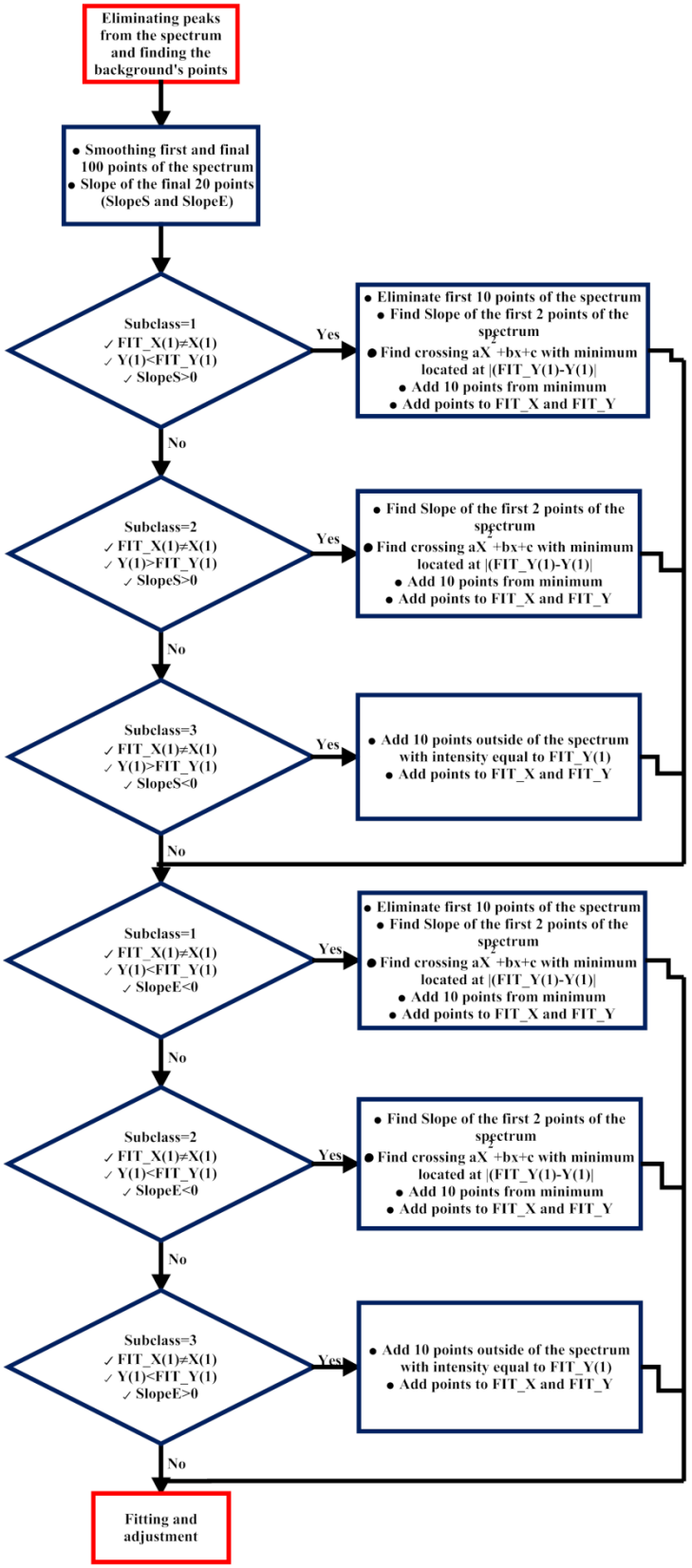

Figure S6 Detailed flow chart for *Adjusting endpoint effects.*

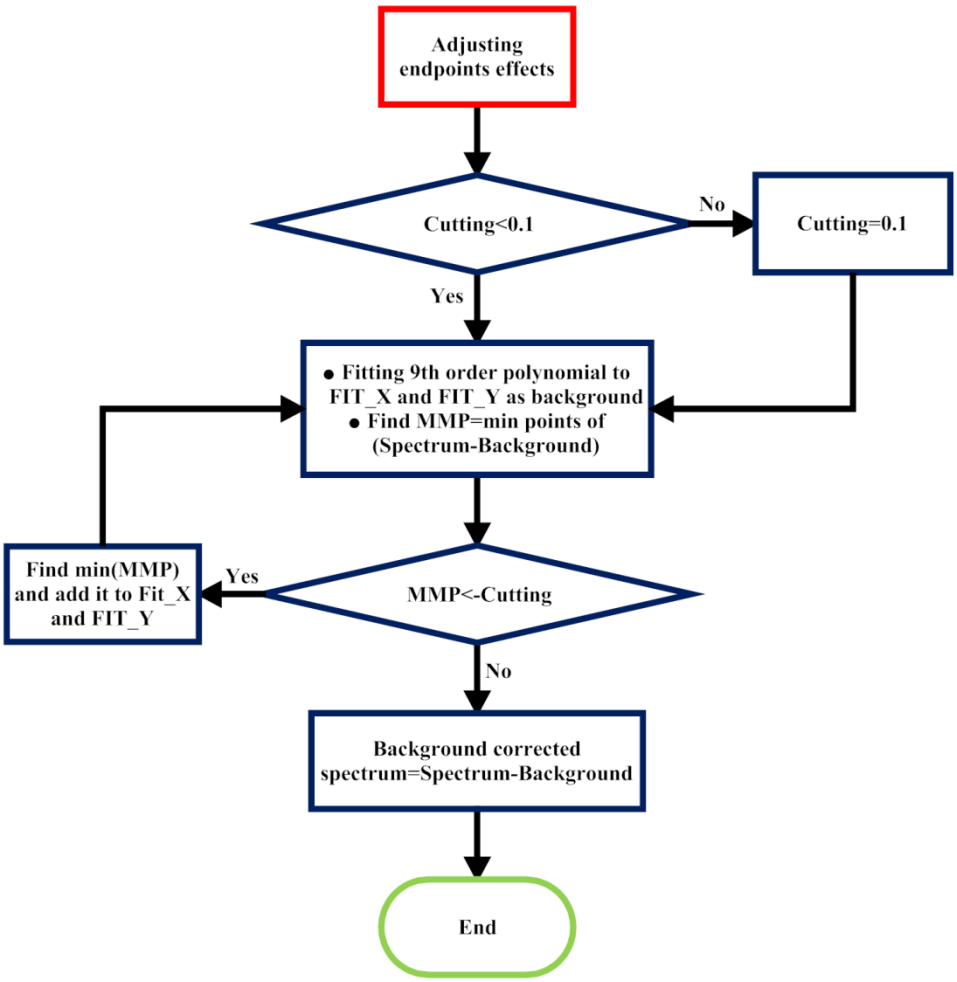

Figure S7 Detailed flow chart for *Fitting and adjustments*

SNR estimation for other types of backgrounds

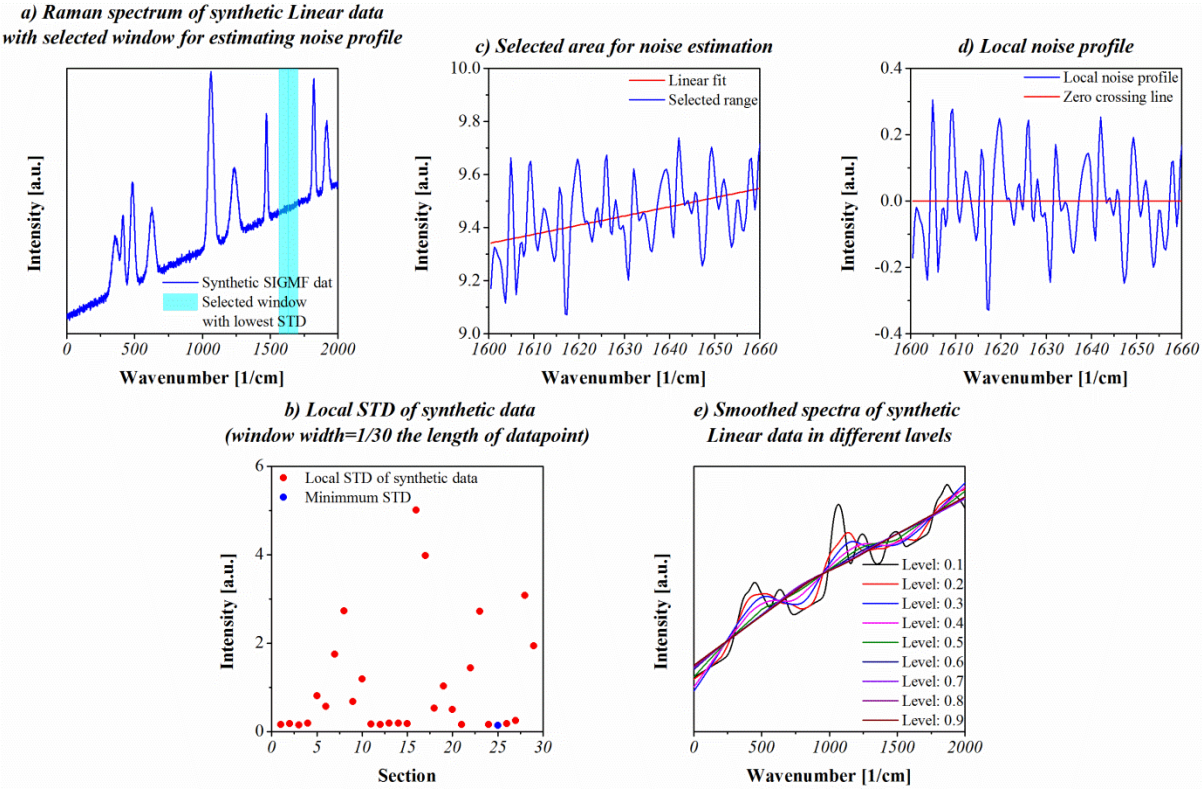

Figure S8 *SNR* estimation steps: **a)** Simulated Raman spectrum with 10 peaks randomly distributed on the signal with the linear background wherein shaded section represents window size for calculating *LSTD*; **b)** *STD* in different divided ranges of spectrum; **c)** Spectrum in minimum *LSTD* wherein red line shows linear fitting of the spectrum in selected region to find background; **d)** Estimated noise profile by subtracting linear background and spectrum; and **e)** Different smoothing levels of the spectrum.

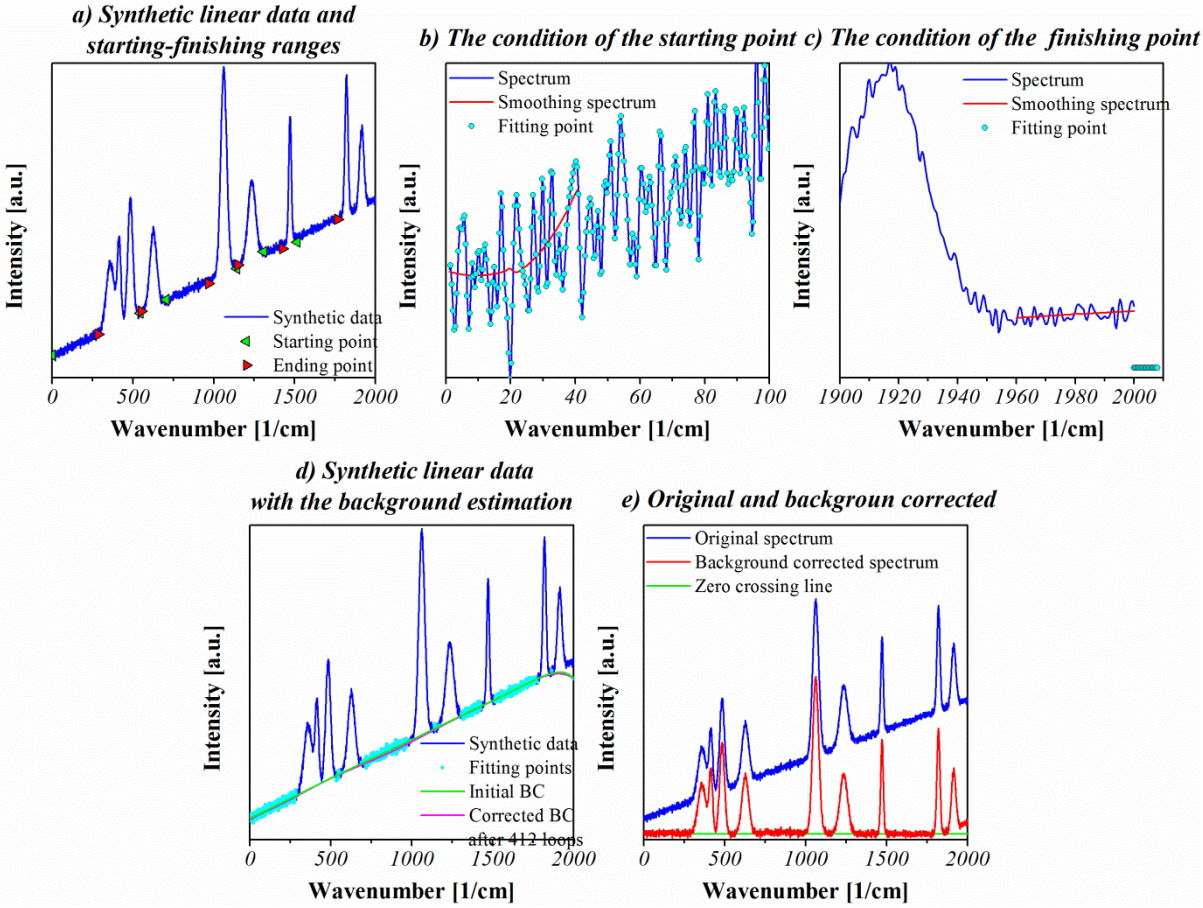

Figure S9 a) Spectrum with starting and finishing points of background; **b)** Starting condition of the spectrum (Subclass=0); **c)** Finishing condition of the spectrum (Subclass=6); **d)** Background points and their fittings (green dashed and magenta curves relate to starting fitting curve and corrected background after 412 loops, respectively); and **e)** Original spectrum with the background corrected one.

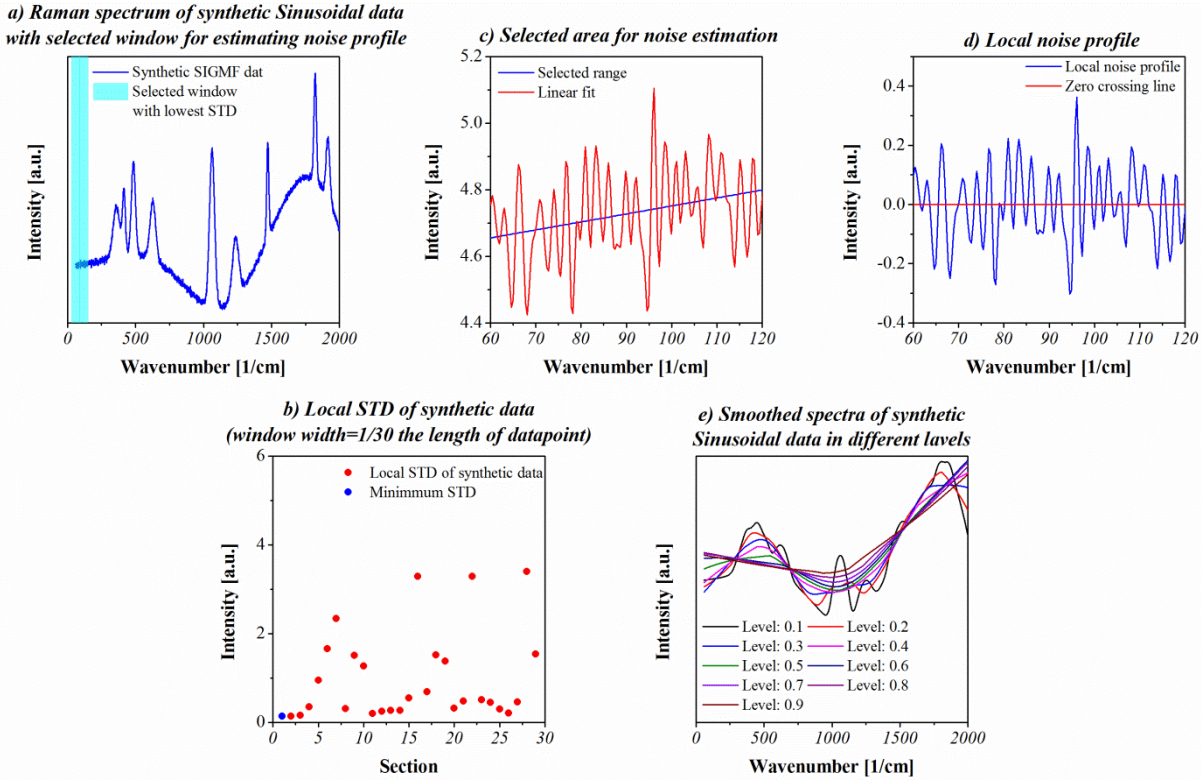

Figure S10 *SNR* estimation steps: **a)** Simulated Raman spectrum with 10 peaks randomly distributed on the signal with the sinusoidal background wherein shaded section represents window size for calculating *LSTD*; **b)** *STD* in different divided ranges of spectrum; **c)** Spectrum in minimum *LSTD* wherein red line shows linear fitting of the spectrum in selected region to find background; **d)** Estimated noise profile by subtracting linear background and spectrum; and **e)** Different smoothing levels of the spectrum.

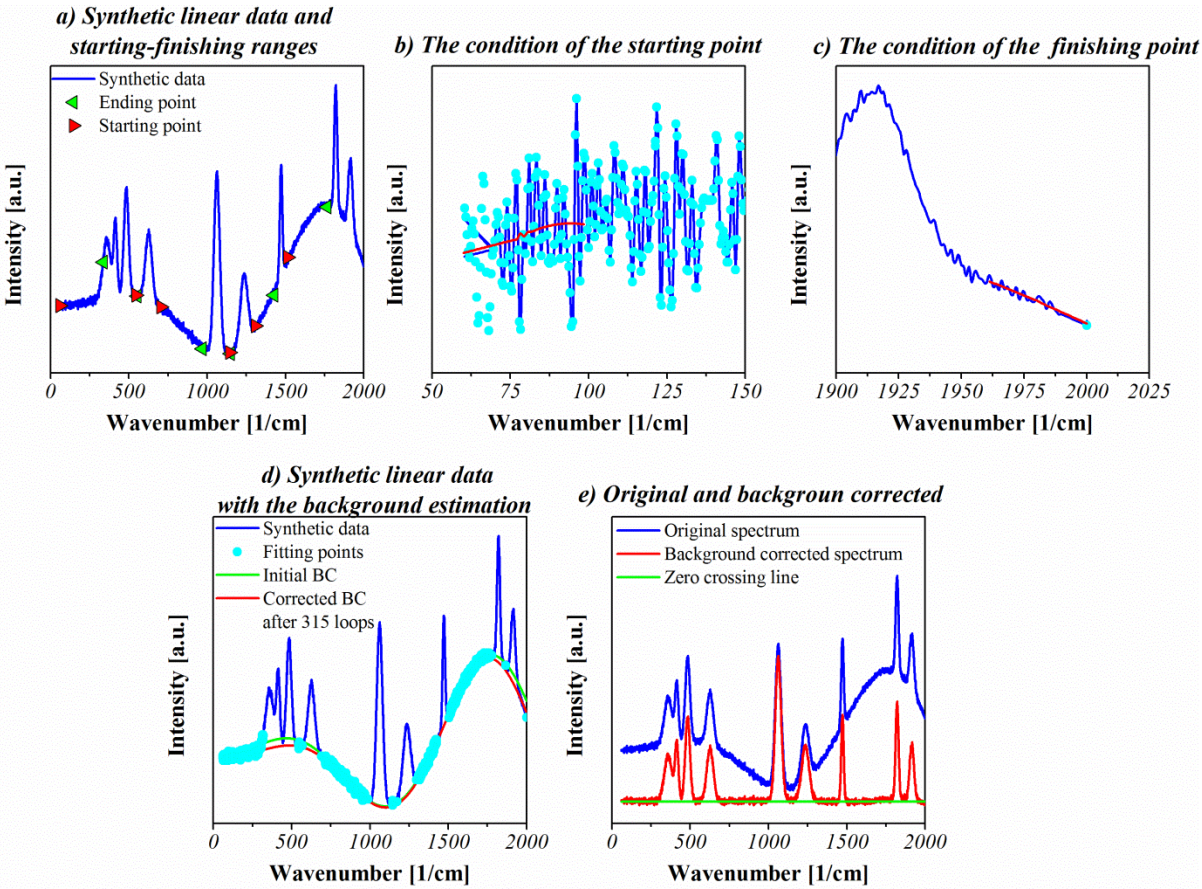

Figure S11 a) Spectrum with starting and finishing points of background; **b)** Starting condition of the spectrum (Subclass=3); **c)** Finishing condition of the spectrum (Subclass=4); **d)** Background points and their fittings (green dashed and magenta curves relate to starting fitting curve and corrected background after 589 loops, respectively); and **e)** Original spectrum with the background corrected one.

Appendix B: Curriculum vitae

Publication Record:

I have in total **47 refereed publications** to my credit, which include 1 book chapter, 28 refereed articles in international journals, 1 Australian and 1 PCT International Patent and 16 refereed papers in international conferences. In addition to these, 2 more refereed journal publications have been communicated, which are currently under peer review process. A list of these publications is provided below:

Publication Record during PhD:

Published Referred Journal Articles during PhD:

No	Title	Journal's Name	Date	Volume Page No.	Authors
1	*Detect, remove and re-use: a new paradigm in sensing and removal of Hg (II) from wastewater via SERS-active ZnO/Ag nano-arrays*	Environmental Science and Technology	2014	DOI: 10.1021/es503527e	**Kandijani, A. E.** ; Sabri, Y. M., Mohammadtaheri, M., Bansal V., Bhargava S. K.,
2	*ZnO/Ag nanoarrays as reusable SERS substrates with controllable 'hot-spots' for highly reproducible molecular sensing*	Journal of Colloid and Interface Science	2014	436 (2014) pp. 251–257	**Kandjani, A.E**, Mohammadtaheri, M., Thakar A., Bhargava S. K., Bansal V.
3	*Low temperature fabrication of alkali metal-organic charge transfer complexes on cotton textile for optoelectronics and gas sensing*	Langmuir (Accepted for Cover Image)	2014	DOI:10.1021/la501446b	Ramanathan, R., Walia, S., **Kandjani, A.E.**, Balendhran, S., Mohammadtaheri, M., Bhargava, S. K., Kalantar-Zadeh, K., Bansal, V.
4	*Synergistic influence of polyoxometalate surface corona towards enhancing the antibacterial performance of tyrosine-capped Ag nanoparticles*	Nanoscale (Cover image)	2014	6 (2) , pp. 758-765	Daima, H.K., Selvakannan, P.R., **Kandjani, A.E.,** Shukla, R., Bhargava, S.K., Bansal, V.
5	*3-D nanorod arrays of metal-organic KTCNQ semiconductor on textiles for flexible organic electronics*	RSC Advances	2013	3 (39), pp. 17654-17658	Ramanathan, R., **Kandjani, A.E.**, Walia, S., Balendhran, S., Bhargava, S.K., Kalantar-Zadeh, K., Bansal, V.
6	*Hybrid Antibacterial Fabrics with Extremely High Aspect Ratio Ag/AgTCNQ Nanowires*	Advanced Functional Materials (Cover Image)	2013	Article in Press	Davoudi, Z.M., **Kandjani, A.E.,** Bhatt, A.I., Kyratzis, I.L., O'Mullane, A.P., Bansal, V.
7	*Alkali ratio control for lead-free piezoelectric thin films utilizing elemental diffusivities in RF plasma*	CrystEngComm	2013	15 (36) , pp. 7222-7229	Nili, H., **Kandjani, A.E.,** Plessis, J.D., Bansal, V., Kalantar-Zadeh, K., Sriram, S., Bhaskaran, M.
8	*A new paradigm for signal processing of Raman spectra using a smoothing free algorithm: Coupling continuous wavelet transform with signal removal method*	Journal of Raman Spectroscopy	2013	44 (4) , pp. 608-621	**Kandjani, A.E**., Griffin, M.J., Ramanathan, R., Ippolito, S.J., Bhargava, S.K., Bansal, V.

Filed Australian patents during PhD:

No	Title	Inventors	Number
1	*A background correction method for a spectrum of a target sample*	Bansal, V. ; **Kandjani, A.E** ; Griffin, M. J. ; Ramanathan, R.	2013 PCT/AU2013/001472
2	*System for detection and removal of mercury*	Bhargava, S. K. ; Bansal, V. ; **Kandijani, A. E.** ; Sabri, Y. M.	2013 Au: 2013903747

Presentations in peer reviewed International Conference:

No.	Title	Title and Place of Assembly	Date	Authors
1	*A soft chemical method for fabricating recyclable SERS substrate with ZnO/Ag photocatalyst/SERS system*	Advanced Materials World Congress, Izmir, Turkey	16-19 September 2013	**Kandjani, A.E**, Mohammadtaheri, M., Thakar A., Bhargava S. K., Bansal V.

Submitted or under preparation Journal Articles from PhD:

No	Title	Journal's Name	Status	Authors
1	*Controlling the photocatalytic activities of ZnO/AgTCNQ with colloidal lithography*	Advanced Materials	Under preparation	**Kandjani, A.E**, Ramanathan, R., Bhargava S. K., Bansal V.
2	*Effects of the template size on the colloidal lithography driven ZnO/AgTCNQ organic/inorganic junctions*	Advanced Materials	Under preparation	**Kandjani, A.E**, Bhargava S. K., Bansal V.

Publication Record prior to PhD:

Published Referred Journal Articles prior to PhD:

No	Title	Journal's Name	Date	Volume Page No.	Authors
1	*Characteristics of the breakup and fragmentation of an electrohydrodynamic melt jet*	Particuology	2012	10 (3), pp. 255-265	Khoshnevis, A., Tabriz, M.F., Hemayatkhah, M., **Kandjani, A.E.**, Milani, J.M., Esmaeilzadeh, E., Eslamian, M., Vaezi, M.R.
2	*Effects of the pH of initial solution on hydrothermally synthesized TiO 2 nanoparticles*	International Journal of Engineering, Transactions B: Applications	2012	25 (2) , pp. 131-135	Vaezi, M.R., Arefian, N.A., Tabriz, M.F., **Kandjani, A. E.**
3	*Wall effect in 3D simulation of same sized particles packing*	International Journal of Engineering, Transactions B: Applications	2012	25 (2), pp.137-141	Tabriz, M.F., Salehpoor, P., **Kandjani, A.E.,** Vaezi, M.R.

4	*Linear optical properties of ZnO nano particles synthesized by electrohydrodynamics atomization (EHDA) method*	Journal of Materials Science: Materials in Electronics	2012	23 (2) , pp. 384-389	Tabriz, M.F., Mehr, H.R.R., Moradi, O.M., **Kandjani, A.E.,** Esmaeilzadeh, E., Kandjani, S.A.
5	*A comparison between hydrothermally prepared Co3O4 via H2O2 assisted and calcination methods*	Journal of Ceramic Processing Research	2011	12 (3), pp. 327-331	Hashemi Amiri, S.E., Vaezi, M.R., **Kandjani, A.E.**
6	*An investigation on linear optical properties of dilute Cr doped ZnO thin films synthesized via sol-gel process*	Journal of Alloys and Compounds	2011	509 (30) , pp. 7854-7860	**Kandjani, A.E.,** Tabriz, M.F., Moradi, O.M., Mehr, H.R.R., Kandjani, S.A., Vaezi, M.R**.**
7	*The use of artificial neural network (ANN) for modeling optical properties of hydrothermally synthesized ZnO nanoparticles designed based on Doehlert method*	Journal of Optoelectronics and Advanced Materials	2010	Vol. 12, pp. 380–386	**Kandjani, A.E.,** Arefian N.A., Farzalipour Tabriz M., Salehpoor P., Ahmadi Kandjani S., Vaezi M.R.
8	*Synthesis and Characterization of TiO2 Nanoparticles via Chemical Bath Deposition (CBD) Method*	Journal of Nano Research	2010	Vol. 11, pp. 35-38	Shokuhfar A., Hassanjani-Roshan A., Vaezi M.R., Kazemzadeh S.M., **Kandjani A. E.**, Nasiri-Tabrizi B.
9	*Neural networks simulation of photocatalytic degradation of Acid Red 27 with SnO2 nanoparticles*	Materials Science – Poland	2010	Vol. 28, pp. 377-390	**Kandjani A.E.**, Salehpoor P., Tabriz M.F., Arefian N.A., Vaezi M.R.
10	*Photocatalytic decoloration of Acid Red 27 in presence of SnO_2 nanoparticles*	Water Science and Technology	2010	Vol. 62, pp. 1256 -1264	**Kandjani A.E.**, Tabriz, M.F., Arefian N.A., Vaezi M.R., Halek F., Sadrnezhaad S.K.
11	*Optical properties of Sol-Gel prepared nano ZnO. The effects of modifier and hydrolysis agent*	Journal of Optoelectronics and Advanced Materials	2010	Vol. 12, pp. 1421 - 1426	**Kandjani A.E.**, Tabriz, M.F., Arefian N.A., Vaezi M.R., Ahmadi Kandjani S.
12	*Powder Production via Electrohydrodynamic-Assisted Molten Metal Jet Impingement into a Viscous Medium*	Journal of Powder Technology	2010	Vol. 203, pp. 518–528	**Kandjani A.E.**, Khoshnevis A., Hemayatkhah M., Esmaeilzadeh E., Vaezi M.R., Eslamian M.
13	*Optical and magnetic properties of Co_3O_4/ZnO Core/Shells*	Journal of Optoelectronics and Advanced Materials	2010	Vol. 12, pp. 2057 - 2062	**Kandjani A.E.,** Hashemi Amiri S.E., Vaezi M.R., Sadrnezhaad S.K.
14	*Log-normal and mono-sized particles' packing into a bounded region*	International Journal of Engineering	2009	Vol. 22, pp. 57-62	Tabriz, M.F., Salehpoor P., **Kandjani A.E.,** Vaezi M.R.
15	*Optical properties of Sol-Gel prepared nano ZnO: The effects of aging period and synthesis temperature*	Journal of Optoelectronics and Advanced Materials	2009	Vol. 11, pp. 289–295	**Kandjani A.E.,** Shokuhfar A., Tabriz, M.F.,, Arefian N.A., Vaezi M.R.

16	*Investigation of reaction conditions on alchothermal synthesis of ZnO nanoparticles*	Defect and Diffusion Forum	2008	Vols. 273-276 pp. 198-203	**Kandjani A.E.,** Vaezi M.R., Shokuhfar A., Tabriz M.F**.**
17	*Sonochemical Synthesis of SnO/ZnO Nano-Composite: The Effects of Temperature and Sonication Power*	Defect and Diffusion Forum	2008	Vols. 273-276 pp. 34-39	Shokuhfar A., Vaezi M.R., Arefian N.A., **Kandjani A.E.**, Tabriz M.F.
18	*Effect of synthesis temperature on the morphology of ZnO nanoparticles obtained via a novel chemical route*	Defect and Diffusion Forum	2008	Vols. 273-276 pp. 192-197	Samei J., Shokuhfar A., **Kandjani A. E.,** Vaezi M.R.
19	*Synthesis of ZnO Nanoparticles via Sol-Gel Process Using Triethanolamine as a Novel Surfactant*	Defect and Diffusion Forum	2008	Vols. 273-276 pp. 626-631	Shokuhfar A., Samei J., **Kandjani A. E.,** Vaezi
20	*Sonochemical synthesis of ZnO nanoparticles: The effect of temperature and sonication power (Hot paper of the year)*	Materials Research Bulletin	2008	Vol. 48 pp. 645-654	**Kandjani A.E.,** Tabriz M.F., Pourabbas B.
21	*Synthesis of Zn2TiO4 and ZnTiO3 nanocomposite by CBD method*	Materials Science – Poland	2007	Vol. 25 pp. 1109-1117	Vaezi M.R., **Kandjani A.E.**, Nikzad L., Arefian N.A., Alibeigi S., Tabriz M. F., Ghassemi S.H., Samei J.
22	*Particle size distribution effect on 3D packing of nano particles into a bounded region*	International Journal of Engineering	2007	Vol. 20 pp. 281-291	Tabriz, M.F., Salehpoor P., **Kandjani A.E.,** Vaezi M.R., Sadrnezhaad S.K.

Referred Book Chapter:

No.	Book	Editor	Chapter Name	Authors	Status	Publisher
1	*Artificial Neural Networks - Application*	Chi Leung Patrick Hui	*Application of Artificial Neural Network in Optical Properties of Nanosemiconductors*	Tabriz, M.F., Salehpoor P., **Kandjani A.E.**	ISBN: 978-953-307-188-6 DOI: 10.5772/15399	InTech

Refereed Conference Publications:

No.	Title	Title and Place of Assembly	Date	Authors
1	*Modeling linear optical properties of hydrothermally synthesized ZnO nanoparticles with artificial neural network*	3rd Conference on Nanostructures Kish island-Iran	10-12 Mar. 2010	**A. E. Kandjani,** N.A. Arefian, M. Farzalipour Tabriz, P. Salehpoor, S. Ahmadi Kandjani, M.R. Vaezi
2	*Formation mechanisms of ZnO shells on the surface of CdS nanoparticles in CdS/ZnO Core/Shells*	2nd International Congress on Nanoscience and Nanotechnology Tabriz, Iran	28-30 Oct. 2008	**A. E. Kandjani**, M. Farzalipour Tabriz, S. Baharlouyi, N.A. Arefian, M.R. Vaezi

3	*Molecular Dynamics Simulation of Cooling Rate Effect on Formation of CuZr Nanostructured Alloy*	2nd International Congress on Nanoscience and Nanotechnology Tabriz, Iran	28-30 Oct. 2008	M. Farzalipour Tabriz, P. Salehpoor, **A. E. Kandjani**, M.R. Vaezi, S.K. Sadrnezhaad
4	*Photocatalytic degradation mechanisms and kinetics of Acid Red 27 dissolved in water in presence of nano SnO_2*	2nd International Congress on Nanoscience and Nanotechnology Tabriz, Iran	28-30 Oct. 2008	N.A. Arefian, **A. E. Kandjani**, M. Farzalipour Tabriz, M.R. Vaezi, S.K. Sadrnezhaad
5	*Synthesis of Nano Zinc oxide particles using 2metoximetanole as surfactant via chemical bath deposition (CBD)*	1st National net-based conference on materials engineering Tabriz, Iran	1-3 May 2007	J. Samei, **A. E. Kandjani**, M.R. Vaezi, A. Shokuhfar
6	*Synthesis of nano zinc oxide via hydrothermal: and investigation on the effects of surfactant and solution's pH*	1st National net-based conference on materials engineering Tabriz, Iran	1-3 May 2007	P. Sowti, **A. E. Kandjani**, M.R. Vaezi, A. Shokuhfar
7	*The effects of synthesis temperature on the final morphologies and particle sizes of ZnO/SnO nanocomposites*	1st National net-based conference on materials engineering	1-3 May 2007	N. A. Arefian, **A. E. Kandjani,** A. Shokuhfar, M.R. Vaezi,
8	*Synthesis of ZnO nanoparticles via novel solvothermal route*	1st National conference on Ceramics Meybod-Iran	20-21 Feb. 2008	**A. E. Kandjani**, A. Shokuhfar, M. Farzalipour Tabriz, M.R. Vaezi,
9	*An Investigation on the effects of synthesis variables on the synthesis of CdS/ZnO core/shells*	1st National conference on New Materials Karaj-Iran	10-13 June 2008	**A. E. Kandjani**, M. Farzalipour Tabriz, S. Baharlouyi, N.A. Arefian, M.R. Vaezi
10	*Synthesis of ZnS nanoparticles: an investigation on the effects of synthesis period and temperature*	1st National conference on New Materials Karaj-Iran	10-13 June 2008	**A. E. Kandjani**, M. Farzalipour Tabriz, A. Pourandarjani, F. Tazesh, M.R. Vaezi
11	*Investigation of reaction conditions on alchothermal synthesis of ZnO nanoparticles*	2nd International Conference on Diffusion in Solids and Liquids Algarve, Portugal	4-6 July 2007	A. Shokuhfar, M.R. Vaezi, **A. E. Kandjani**, M. Farzalipour Tabriz
12	*Sonochemical Synthesis of SnO/ZnO Nano-Composite: The Effects of Temperature and Sonication Power*	2nd International Conference on Diffusion in Solids and Liquids Algarve, Portugal	4-6 July 2007	A. Shokuhfar, M.R. Vaezi, N. A. Arefian, **A. E. Kandjani**, M. Farzalipour Tabriz
13	*Effect of synthesis temperature on the morphology of ZnO nanoparticles obtained via a novel chemical route*	2nd International Conference on Diffusion in Solids and Liquids Algarve, Portugal	4-6 July 2007	J. Samei, A. Shokuhfar, **A. E. Kandjani**, M.R. Vaezi
14	*Synthesis of ZnO Nanoparticles via Sol-Gel Process Using Triethanolamine as a Novel Surfactant*	2nd International Conference on Diffusion in Solids and Liquids Algarve, Portugal	4-6 July 2007	A. Shokuhfar, J. Samei, **A. E. Kandjani**, M.R. Vaezi
15	*Effects of particle size distribution on 3D random loose packing of powders into a bounded region*	2nd Tehran International Congress on Manufacturing Engineering Tehran, Iran	10-13 Dec. 2007	M. Farzalipour Tabriz, P. Salehpoor, **A. E. Kandjani**, M.R. Vaezi

Research/Academic experience

- Research assistant at Materials and Energy Research Center (MERC), Iran, 2007-2011.
- Member of Iran's National Elites Foundation, 2011 till now.

Honours/Awards

- Accepted as member of Iran's National Elites Foundation (2009)
- RMIT Post graduate award (2011)

- Perkin Elmer Prize for most outstanding contribution to the field of Fourier transform infrared spectroscopy post graduate students (2013)
- The Deputy Pro Vice-Chancellor Research and Innovation Postgraduate Research International Conference award (2013)
- Professor CNR Rao Postgraduate Research Excellence Award in Materials Science for the most outstanding postgraduate research student working in the field of materials science (2014).

Published journal cover images: